T.C.
IŞIK UNIVERSTIY
SCHOOL OF GRADUATE STUDIES

MASTER THESIS
DEPARTMENT OF ELECTRICAL AND ELECTRONICS ENGINEERING
ELECTRICAL AND ELECTRONICS ENGINEERING PROGRAM

Bilal ANTAKI

INTELLIGENT HEALTH MONITORING IN 6G NETWORKS: MACHINE LEARNING-ENHANCED VLC-BASED MEDICAL BODY SENSOR NETWORKS

SUPERVISOR
Asst. Prof. Dr. Farshad MIRAMIRKHANI

İSTANBUL, September 2025

T.C.
IŞIK UNIVERSITY
SCHOOL OF GRADUATE STUDIES

MASTER THESIS
DEPARTMENT OF ELECTRICAL AND ELECTRONICS ENGINEERING
ELECTRICAL AND ELECTRONICS ENGINEERING PROGRAM

Bilal ANTAKI
(23ELEC5003)

INTELLIGENT HEALTH MONITORING IN 6G NETWORKS: MACHINE LEARNING-ENHANCED VLC-BASED MEDICAL BODY SENSOR NETWORKS

SUPERVISOR
Asst. Prof. Dr. Farshad MIRAMIRKHANI

İSTANBUL, September 2025

T.C.
IŞIK UNIVERSITY
SCHOOL OF GRADUATE STUDIES

MASTER'S THESIS
DEPARTMENT OF ELECTRICAL AND ELECTRONICS ENGINEERING
ELECTRICAL ENGINEERING PROGRAM

Bilal ANTAKI
(23ELEC5003)

INTELLIGENT HEALTH MONITORING IN 6G NETWORKS: MACHINE LEARNING-ENHANCED VLC-BASED MEDICAL BODY SENSOR NETWORKS

Date: 01/09/2025

Thesis Supervisor: Asst. Prof. Dr. Farshad MIRAMIRKHANI / Işık University

Jury Members:

Prof. Dr. Onur KAYA / Işık University

Assist. Prof. Sina ALP / Istanbul Okan University

İSTANBUL, September 2025

ÖZET

6G AĞLARINDA AKILLI SAĞLIK İZLEME: MAKİNE ÖĞRENMESİ DESTEKLİ VLC TABANLI MEDİKAL VÜCUT SENSÖR AĞLARI

Yapay Zeka (YZ) destekli kablosuz haberleşmedeki son gelişmeler, elektromanyetik girişim kaygıları nedeniyle geleneksel Radyo Frekansı (RF) sistemlerinin kısıtlamalarla karşılaştığı hastaneler gibi kritik ortamlarda Altıncı Nesil (6G) teknolojilerinin benimsenmesini hızlandırmaktadır. Mevcut LED tabanlı aydınlatma altyapısını kullanan Görünür Işık Haberleşmesi (VLC), yüksek hızlı veri iletimi ve azaltılmış elektromanyetik girişim (EMI) gibi ikili avantaj sunmaktadır. Ancak, klinik ortamlardaki hasta hareketleri sinyal alımında önemli değişkenliğe neden olmakta ve kanal özelliklerini dinamik olarak değiştirmektedir. Bu araştırma, farklı hastane senaryolarında VLC tabanlı Medikal Vücut Sensör Ağları (MBSN) kanallarını modellemek için ortama özgü ışın izleme ile Makine Öğrenmesi (ML) tekniklerini birleştiren yenilikçi bir metodoloji sunmaktadır. İlk katkı, önceden çevresel veriye ihtiyaç duymadan gerçek zamanlı olarak hedef sembol hata oranlarını (SER) koruyabilen Q-öğrenme güdümlü uyarlanabilir modülasyon algoritmasının uygulanmasını içermektedir. İkinci bileşen, değişken hastane koşullarında yol kaybı ve Kök Ortalama Kare (RMS) gecikme yayılımını tahmin etmek için bir Uzun Kısa Süreli Bellek (LSTM) modeli tasarlamayı kapsamaktadır. Üçüncü katkı, doğru hasta konumlandırması için altı farklı algoritmayı—Doğrusal Regresyon, Destek Vektör Regresyonu, K-En Yakın Komşu, Çok Katmanlı Algılayıcı (MLP), LSTM ve Geçitli Tekrarlayan Birimler—değerlendiren kapsamlı bir ML tabanlı konum tahmin çerçevesi sunmaktadır. Bugüne kadar, bu çalışma tıbbi ortamlarda ışın izlemeli Kanal Darbe Yanıtı (CIR) modellemesini ML güdümlü analizle birleştiren ilk çalışma olarak görünmektedir. Simülasyon bulguları, Q-

öğrenme modelinin güvenilir bir şekilde SER hedeflerini karşıladığını ve spektral verimliliğin (SE) eşik seviyesine yakın koşullarda optimale yakın performans gösterdiğini ortaya koymaktadır. Ayrıca, LSTM tabanlı tahminler, Yoğun Bakım Ünitesi (YBÜ) senaryosunda D1 konumundaki sensörün hem yol kaybı (1.6797 dB) hem de RMS gecikme yayılımı (1.0567 ns) için en büyük Kök Ortalama Kare Hatasını (RMSE) ürettiğini göstermektedir. Buna karşılık, Aile Tipi Hasta Odasında (ATHO) D3 sensörü, yol kaybında (1.0652 dB) ve gecikme yayılımında (0.7657 ns) en yüksek RMSE değerlerini vermekte ve gerçekçi çalışma koşullarında güçlü tahmin performansını doğrulamaktadır. Konum tahmini için MLP, optimal mimari olarak öne çıkmakta, ATHO'da birleşik D1-D2-D3 sensör konfigürasyonları için 58.6 cm'lik metre altı doğruluk elde etmekte, bireysel sensörler 63.5 cm (D1), 75.0 cm (D2) ve 73.1 cm (D3) değerleri vermekte, daha karmaşık YBÜ ortamında ise MLP, D1-D2-D3 için 217.1 cm'lik klinik olarak kabul edilebilir hassasiyeti korumakta, eşleştirilmiş konfigürasyonlar 202.1 cm (D1-D2) ve 216.3 cm (D1-D3) elde etmekte, tüm bunları sıralı modellere kıyasla %35-48 hesaplama gereksinimi azaltması ve %37-89 daha hızlı hiperparametre optimizasyonu ile sunarak sağlık tesislerinde gerçek zamanlı hasta takibi için en pratik çözüm olmaktadır.

Anahtar Kelimeler: Uyarlanabilir Modülasyon, Kanal Modellemesi, Kanal Parametre Tahmini, Makine Öğrenmesi (ML), Görünür Işık Haberleşmesi (VLC).

ABSTRACT

INTELLIGENT HEALTH MONITORING IN 6G NETWORKS: MACHINE LEARNING-ENHANCED VLC-BASED MEDICAL BODY SENSOR NETWORKS

Recent advancements in Artificial Intelligence (AI)-enabled wireless communication are accelerating the adoption of Sixth Generation (6G) technologies in critical environments such as hospitals, where traditional Radio Frequency (RF) systems face limitations due to electromagnetic interference concerns. Visible Light Communication (VLC), which utilizes existing LED-based lighting infrastructure, offers the dual advantage of high-speed data transmission and reduced electromagnetic interference (EMI). However, patient movement within clinical environments introduces considerable variability in signal reception and alters channel characteristics dynamically. This research introduces an innovative methodology that merges site-specific ray tracing with Machine Learning (ML) techniques to model VLC-based Medical Body Sensor Network (MBSN) channels across different hospital scenarios. The first contribution involves implementing a Q-learning-driven adaptive modulation algorithm capable of maintaining target symbol error rates (SER) in real time without requiring prior environmental data. The second component involves designing a Long Short-Term Memory (LSTM) model to estimate path loss and Root Mean Square (RMS) delay spread under time-varying hospital conditions. The third contribution presents a comprehensive ML-based position estimation framework that evaluates six different algorithms—Linear Regression, Support Vector Regression, K-Nearest Neighbors, Multilayer Perceptron (MLP), LSTM, and Gated Recurrent Units—for accurate patient localization. To date, this appears to be the first study that integrates ray-traced Channel Impulse Response (CIR) modeling with ML-driven analysis in medical environments. Simulation

findings indicate that the Q-learning model reliably meets SER targets, with spectral efficiency (SE) performing close to optimal at near-threshold conditions. Additionally, the LSTM-based predictions reveal that in the Intensive Care Unit (ICU) scenario, the sensor at position D1 produces the largest Root Mean Square Error (RMSE) for both path loss (1.6797 dB) and RMS delay spread (1.0567 ns). Conversely, in the Family-Type Patient Room (FTPR), sensor D3 yields the highest RMSE for path loss (1.0652 dB) and delay spread (0.7657 ns), confirming strong predictive performance under realistic operational conditions. For position estimation, MLP emerges as the optimal architecture, achieving sub-meter accuracy of 58.6 cm for combined D1-D2-D3 sensor configurations in FTPR, with individual sensors yielding 63.5 cm (D1), 75.0 cm (D2), and 73.1 cm (D3), while in the more complex ICU environment, MLP maintains acceptable precision of 217.1 cm for D1-D2-D3, with paired configurations achieving 202.1 cm (D1-D2) and 216.3 cm (D1-D3), all while offering 35-48% reduction in computational requirements and 37-89% faster hyperparameter optimization compared to sequential models, making it the most practical solution for real-time patient tracking in healthcare facilities.

Keywords: Adaptive Modulation, Channel Modeling, Channel Parameter Estimation, Machine Learning (ML), Visible Light Communication (VLC).

ACKNOWLEDGEMENT

I would like to express my sincere gratitude to my advisor, Asst. Prof. Dr. Farshad Miramirkhani, for his invaluable guidance, encouragement, and insightful feedback throughout the course of this thesis. His mentorship has not only shaped the direction and quality of my research but also contributed greatly to my academic growth. It has been an honor and a privilege to work under his supervision.

I am also deeply grateful to the members of my thesis committee for their time, constructive comments, and thoughtful suggestions, which helped enhance and refine this work.

I extend my heartfelt thanks to my family for their unwavering love, patience, and belief in me. Their support has been a source of strength and motivation throughout this journey.

Finally, I would like to thank my friends for their encouragement, understanding, and companionship, which made this challenging yet rewarding experience more memorable and fulfilling.

Bilal ANTAKI

TABLE OF CONTENTS

PAGE NO:

LIST OF FIGURES

LIST OF TABLES

ABBREVIATIONS LIST

4G: Fourth Generation

5G: Fifth Generation

6G: Sixth Generation

ACK/NACK: Acknowledgement / Negative Acknowledgement

AI: Artificial Intelligence

ANN: Artificial Neural Network

AOA: Angle of Arrival

AR: Augmented Reality

AUWC: Acoustic Underwater Communication

BER: Bit Error Rate

CIR: Channel Impulse Response

cm: Centimeter

CQI: Channel Quality Indicator

CSI: Channel State Information

DCO-OFDM: DC-biased Optical Orthogonal Frequency Division

DNN: Deep Neural Network

DQN: Deep Q-Network

ECG: Electrocardiograph

ELM: Extreme Learning Machine

EMI: Electromagnetic Interference

FL: Federated Learning

FNN: Feedforward Neural Network

FSO: Free Space Optics

FTPR: Family-Type Patient Room

GA: Genetic-Algorithm

Gbps: Gigabits per second

GHz: Gigahertz

GPS: Global Positioning System

GRUs: Gated Recurrent Units

H2H: Hospital-to-Home

HPO: Hyperparameter Optimization

ICU: Intensive Care Unit

IIoT: Industrial Internet-of-Things

IM/DD: Intensity Modulation / Direct Detection

IMU: Inertial Measurement Units

IoMT: Internet of Medical Things

IoT: Internet of Things

IPS: Indoor Positioning System

IR: Infrared

IRS: Intelligent Reflecting Surface

ISAC: Integrated Sensing and Communication

ISI: Inter-Symbol Interference

IWDs: Intelligent Wearable Devices

KF: Kalman Filter

kHz: Kilohertz

KNN: K-Nearest Neighbors

KPIs: Key Performance Indicators

LBS: Location-Based Services

LEDs: Light-emitting Diodes

LoS: Line of Sight

LR: Linear Regression

LSTM: Long Short-Term Memory

M-ANN: Memory-augmented ANN

m: Meter

MAE: Mean Absolute Error

MAPE: Mean Absolute Percentage Error

MBSNs: Medical Body Sensor Networks

MCS: Modulation and Coding Scheme

MDPs: Markov Decision Processes

MIMO: Multiple Input Multiple Output

ML: Machine Learning

MLP: Multilayer Perceptron

MPSK: M-ary Phase Shift Keying

MTL: Multitask Learning Multiplexing

NLoS: Non-Line of Sight

ns: Nanosecond

OFDM: Orthogonal Frequency Division Multiplexing

OLLA: Outer Loop Link Adaptation

OOK: On-Off Keying

OWC: Optical Wireless Communication

PAM: Pulse Amplitude Modulation

PD: Photodetector

PL: Path Loss

PPG: Photoplethysmograph

PPM: Pulse Position Modulation

PWM: Pulse Width Modulation

QAM: Quadrature Amplitude Modulation

QoS: Quality of Service

REM: Radio Environment Map

RF: Radio Frequency

RF: Random Forest

RFF: Random Fourier Features

RL: Reinforcement Learning

RMS: Root Mean Square

RMSE: Root Mean Square Error

RNNs: Recurrent Neural Networks

RSRP: Reference Signal Received Power

RSS: Received Signal Strength

RSS: Received Signal Strength

s: Second

SAEs: Sparse Autoencoders

SE: Spectral Efficiency

SER: Symbol Error Rate

SLFNs: Single Layer Feedforward Networks

SMBO Sequential Model-Based Optimization

SNR: Signal-to-Noise Ratio

SVM: Support Vector Machine

SVR: Support Vector Regression

TDOA: Time Difference of Arrival

TOA: Time of Arrival

UV: Ultraviolet

UVC: Ultraviolet Communication

V-VLC: Vehicular Visible Light Communication

VL: Visible Light

VLC: Visible Light Communication

VLP: Visible Light Positioning

VR: Virtual Reality

WBANs: Wireless Body Area Networks

WCkNN: Weighted-Coefficients k-Nearest Neighbors

WSNs: Wireless Sensor Networks

XR: Extended Reality

CHAPTER 1

1. INTRODUCTION

The continuous evolution of wireless communication—especially with the integration of Artificial Intelligence (AI)—is driving the need for a corresponding shift in communication infrastructure and technologies (Z. Zhang et al., 2019; Letaief et al., 2019; Giordani et al., 2020). While Fifth Generation (5G) networks are currently being deployed on a global scale, significant attention from both academic and industrial sectors has turned toward exploring the capabilities and development pathways of Sixth Generation (6G) systems (Mettiti & Oumsis, 2022; Letaief et al., 2019; Chowdhury et al., 2020). Despite the significant improvements 5G offers over fourth generation (4G) systems, it remains constrained by shortcomings in reliability, latency, bandwidth, and data rates. Consequently, 6G is being developed to address these challenges (C. Wang et al., 2023).

Optical Wireless Communication (OWC) has come forward as a promising candidate for 6G and future network architectures (C. Wang et al., 2023). OWC encompasses all forms of optical transmission through unguided media and is categorized by its operational frequency range (Uysal et al., 2016; Chowdhury et al., 2018). Given the ongoing spectrum scarcity in wireless communications, optical transmission offers an effective remedy by delivering extremely high bandwidth over an unlicensed, regulation-free spectrum, along with high data rates and minimal transmission loss (Garg & Nain, 2021; Chowdhury et al., 2018). Additionally, OWC systems offer advantages such as low energy consumption, seamless integration with existing lighting infrastructures, robust security, and resistance to electromagnetic interference (EMI) (K. Wang et al., 2022; Chowdhury et al., 2018). These characteristics make OWC particularly suitable for RF-restricted settings like hospitals (Sohn

et al., 2020; Dhatchayeny et al., 2019). One practical form of OWC is Visible Light Communication (VLC), which corresponds to the 390–750 nm wavelength range and leverages widely available light-emitting diodes (LEDs). These LEDs convey data by modulating light at a very high frequency, unnoticeable to the bare human eye or lighting quality (Uysal et al., 2016). Since LEDs are common in indoor environments and can function both as transmitters and lighting sources, VLC-based systems can be implemented at a relatively low cost (Mapunda et al., 2020; Karunatilaka et al., 2015).

Due to its unique physical layer characteristics, VLC outperforms radio frequency (RF)-based systems in several aspects (Cho et al., 2021). One notable advantage is that light cannot penetrate opaque objects, making VLC inherently secure. This property positions VLC as an ideal complement to RF-based indoor systems, such as Medical Body Sensor Networks (MBSNs) (Julien-Vergonjanne et al., 2016; Cho et al., 2021; Arfaoui et al., 2020). In recent years, interest in OWC-enabled MBSNs has grown significantly, particularly within healthcare environments. For instance, many hospitals already utilize tetherless infrared (IR) links for communication between body-worn sensors and monitoring devices (Donmez et al., 2021).

Key performance indicators (KPIs) used to assess 6G wireless networks encompass metrics such as spectrum and energy efficiency, peak and user-perceived data rates, area or space traffic capacity, connectivity density, latency, and mobility (C. Wang et al., 2023). For VLC-based MBSNs, specific standards have been defined for mobile IR devices positioned near patients in fixed Line-of-Sight (LoS) configurations (ISO/IEEE International Standard Health Informatics-Point-of Care Medical Device Communication-Transport Profile-Infrared, 2004). Additionally, IR transmitters and incoherent light sources like LEDs must comply with established eye safety regulations (Photo-Biological Safety of Lamps and Lamp Systems (Identical With CIE S009), 2006; Safety of Laser Products Part 1: Equipment Classification and Requirement, 2007).

Determining key 6G system requirements, such as latency and data rate, necessitates accurate wireless channel modeling. This is typically done by deriving the channel impulse response (CIR) through advanced ray tracing techniques (Miramirkhani & Uysal, 2015; Lichtenegger et al., 2019). Once the CIR is available, parameters like the Root Mean Square (RMS) Delay Spread can be estimated. Traditionally, such estimations rely on signal processing methods, including pilot-based channel estimation. However, machine learning has recently gained traction in this area due to its capability to model complex, nonlinear relationships and its potential to outperform traditional techniques under certain conditions (H. W. Lee & Choi, 2023; Kao & Wu, 2022; Ji & Thompson, 2023; Jebur et al., 2021).

Machine Learning (ML) algorithms are increasingly being applied to improve the performance of VLC-enabled MBSNs (Chi et al., 2020). VLC systems often encounter challenges stemming from nonlinear distortions, including the inherent nonlinearity in LED outputs, receiver photo-detectors, high-frequency attenuation, and various environmental influences (Ying et al., 2015; KS et al., 2023). ML techniques offer effective solutions to these issues by enhancing functions such as channel estimation, jitter correction, position tracking, modulation recognition, phase estimation, and system security (X. Wu et al., 2019; Saxena et al., 2023; Chi et al., 2020). Furthermore, ML approaches are employed to identify and address security vulnerabilities in Internet of Things (IoT)-based systems, thereby strengthening data privacy and system integrity (Alwahedi et al., 2024). In healthcare settings, integrating ML with distributed-edge and cloud computing enables more efficient data transmission, faster response times, and real-time analysis of sensor data (Alnaim & Alwakeel, 2023; Shehab et al., 2022; Dharmarathne et al., 2024).

In medical settings, patient movement leads to signal strength fluctuations, which presents challenges for implementing VLC-based systems—despite their reliability, high bandwidth, and secure communication capabilities. However, smart transmitter designs that dynamically adjust system parameters based on

real-time channel variations can significantly improve performance. VLC systems continue to find valuable applications in healthcare. For instance, Machine Learning techniques can effectively forecast the Radio Environment Map (REM) in VLC-enabled networks, helping maintain consistent signal coverage in highly reliable environments such as hospitals (Serpi & Politi, 2023).

Deploying wireless systems in hospitals is constrained by EMI risks, privacy, and the non-stationary, geometry-dependent optical channel caused by human motion and wavelength-dependent surface reflectance. We address these by combining site-specific ray tracing with ML: (i) Q-learning for real-time, CSI-free adaptive modulation to meet SER targets; (ii) LSTM models for path loss and RMS delay-spread estimation under time-varying conditions; and (iii) an MLP-based position-estimation pipeline designed specifically for two hospital scenarios.

To generalize our work to all hospitals, all relevant room types and layouts will be considered during development and evaluation, including intensive care units, emergency wards, operating rooms, corridors, nursing stations, and family type rooms, with variation in geometry, surface materials, lighting spectra and placement, and typical human activity. This coverage and evaluation protocol aims to produce models that transfer reliably across diverse hospital settings.

If successful, the system will enable EMI-safe, privacy-aware patient monitoring that maintains target SER in real time, achieves sub-meter localization in typical single-bed rooms, and estimates channel parameters to preserve QoS, all using commodity LED luminaires and body-worn photodiodes; training for RL occurs offline with online adaptation from observations without prior CSI, and the estimation and positioning models run within documented compute budgets on edge hardware, to aim for a clear and accurate track from simulation to practical implementation.

This proposal directly targets TÜBİTAK's priority areas in artificial intelligence and next-generation communication (6G), aligning with Türkiye's

policy to initiate 6G preparations and to domestically develop enabling technologies for intelligent, connected healthcare. The aim is to advance the capabilities of VLC in MBSNs, specifically addressing adaptive modulation, path loss (PL) estimation, RMS delay spread estimation, as well as patient position estimation for enhanced communication reliability in 6G health monitoring systems. The structure of the proposal is shown in Figure 1.1.

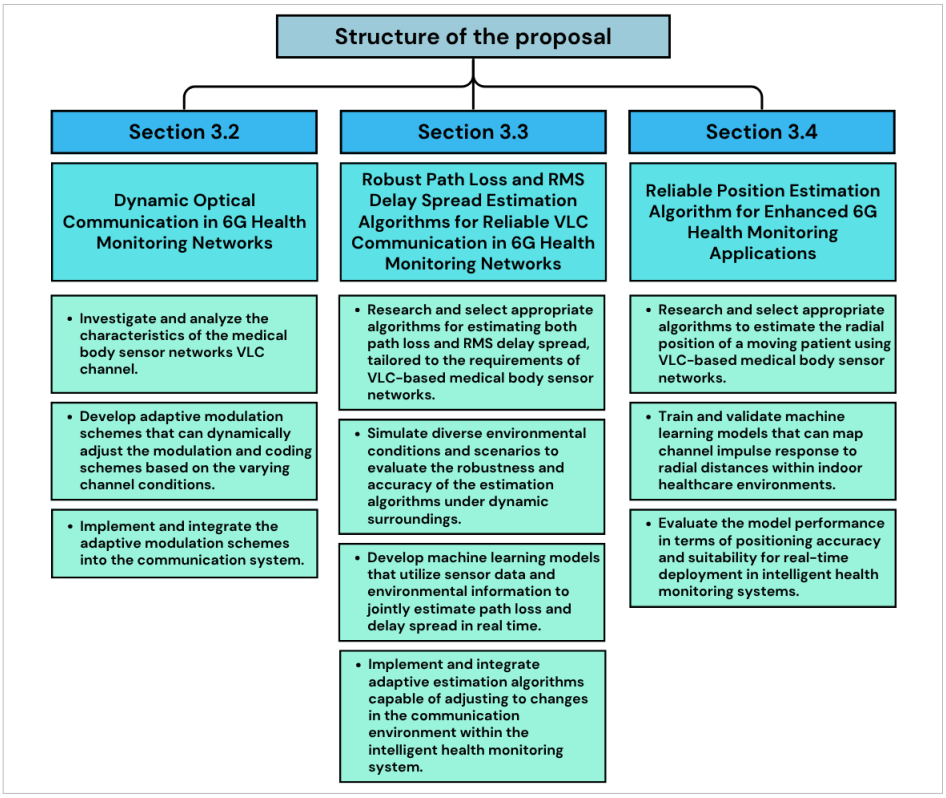

Figure 1.1 Structure of the Proposal

CHAPTER 2

2. LITERATURE SURVEY

2.1. ENABLING COMMUNICATION AND NETWORKING TECHNOLOGIES FOR 6G IN HEALTHCARE

Although 5G represents a significant improvement over 4G systems, it still falls short in meeting the demands of emerging applications. Current services increasingly require capabilities beyond what 5G can offer, including worldwide coverage, extremely high data rates, ultra-low latency, dense device connectivity, robust security, minimal power usage, and enhanced energy efficiency (C. Wang et al., 2023). As the wireless communication landscape evolves rapidly, overcoming 5G's shortcomings has become essential, reinforcing the need for 6G development. Presently, 6G remains in its exploratory phase, with numerous countries and standardization bodies outlining their development roadmaps (Pillai, 2024). Both 5G and 6G services are characterized by distinct KPIs, and Table 2.1 highlights the advancements required in KPIs to meet the performance expectations of 6G compared to 5G (Strinati et al., 2019; Slalmi et al., 2020).

The 6G vision encompasses a range of application scenarios, each imposing specific performance demands on communication systems. The ITU-R originally defined eight KPIs under the IMT-2020 framework. However, as mobile networks continue to evolve, these KPIs are no longer adequate for addressing the advanced and disruptive applications expected by 2030 and beyond. Although the original eight KPIs (ITU-R, 2015) remain applicable to 6G, their target values must be revised to align with ongoing technological progress and the emergence of new use cases. Moreover, additional KPIs will be

required to assess new functionalities in 6G, including positioning accuracy, sensing capabilities, enhanced security, and system intelligence.

Table 2.1 A comparison between 5G and 6G KPIs.

KPI	5G	6G
Area Traffic Capacity [Mb/s/m^2]	10	1000 - 10000
Downlink Peak data rate [Gb/s]	20	1000
Uplink Peak data rate [Gb/s]	10	1000
Latency (radio interference) [ms]	1	0.1
Reliability [%]	99.999	99.9999999
Maximum Mobility [km/h]	500	1000
Localization precision	10 cm in 2D	1 cm in 3D
Visible Light Communication	No	Yes
Artificial Intelligence integration	Partially	Fully

To address this gap, several quantitative and qualitative KPIs were proposed by C. Wang et al. (2023). Figure 2.1 displays the 17 KPIs proposed for 6G, with those highlighted in red to being considered in 5G standardization. These are compared with 5G indicators.

The 6G vision is encapsulated by the concept of "strong security, global coverage, full applications, all digital, all spectra, and all senses," as illustrated in Figure 2.2 (C. Wang et al., 2023). To realize global coverage, 6G aims to unify terrestrial, aerial, maritime, and space-based communication networks into a single integrated system. Addressing the increasing demand for traffic and connectivity, 6G will operate across the entire spectrum—ranging from sub-6 gigahertz (GHz) to mmWave, terahertz, and optical frequencies. In support of various vertical sectors, 6G will tightly couple communication with computing, storage, control, sensing, positioning, AI, and big data, facilitating advanced use

cases such as integrated sensing and communication (ISAC). It will also deliver rich user experiences through technologies like holographic communication, extended reality (XR), and the tactile internet. In other words, 6G will bridge the digital and physical realms to enable intelligent interconnection among humans, machines, environments, and devices. Robust security will be built into the system via network endogenous mechanisms (J. Wu, 2022), covering both physical and network layers, while AI-driven features will further strengthen intelligent, adaptive security capabilities.

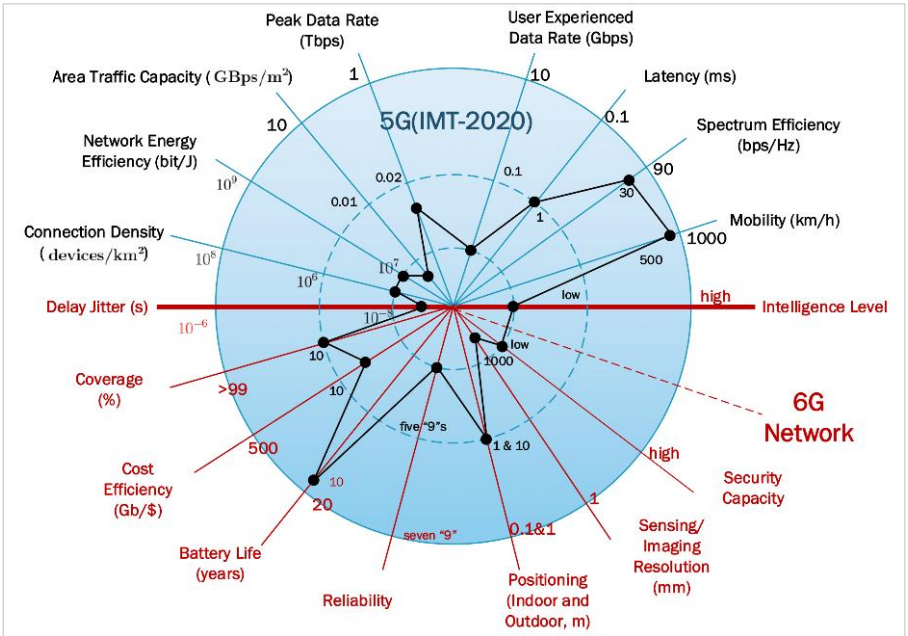

Figure 2.1 6G KPIs.

The grand vision of 6G outlines a transformative direction for next-generation communication systems. With full-spectrum utilization and worldwide coverage, 6G aims to broaden the capabilities of networks by enabling intelligent services that tightly integrate communication, sensing, and computation, all while maintaining strong security. Within this framework, the technological foundations of 5G are no longer sufficient to meet the elevated demands and complexity of the envisioned 6G landscape.

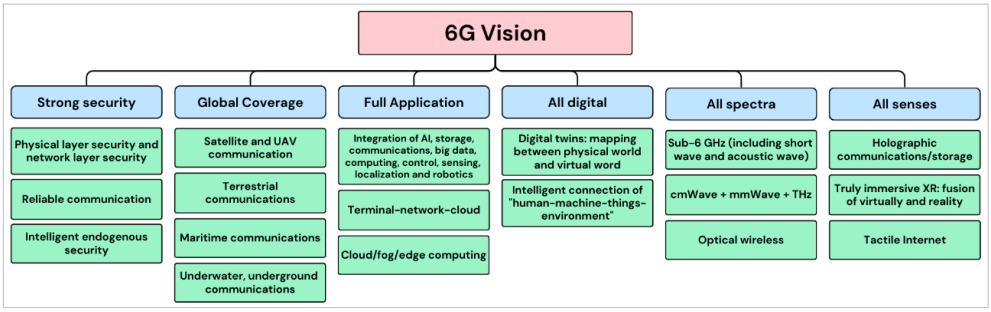

Figure 2.2 Global coverage, all spectra, full applications, all senses, all digital, and strong security.

Numerous studies have investigated potential core technologies for 6G. However, works such as (Chowdhury et al., 2020; Bariah et al., 2020; Saad et al., 2019; You et al., 2020) presented various techniques without clear categorization, which may lead to ambiguity and limit readers' understanding of the overall technological landscape. Other studies narrowed their focus to only a subset of technologies (Zong et al., 2019; Bhat & Alqahtani, 2021) or lacked sufficient detail on the proposed methods (Z. Zhang et al., 2019). Although the ITU-R outlined technology trends for 2030 and beyond (International Telecommunication Union, 2022), its draft did not include a supporting literature review. Moreover, certain emerging technologies—such as nanoscale or molecular communication—though promising, are constrained in scope and are less likely to serve as foundational pillars for 6G (Khan et al., 2020; Saad et al., 2019). Based on prior research and recent advancements, 16 candidate technologies for 6G have been identified and organized into four key evolutionary directions, as illustrated in Figure 2.3 (C. Wang et al., 2023; Pillai, 2024).

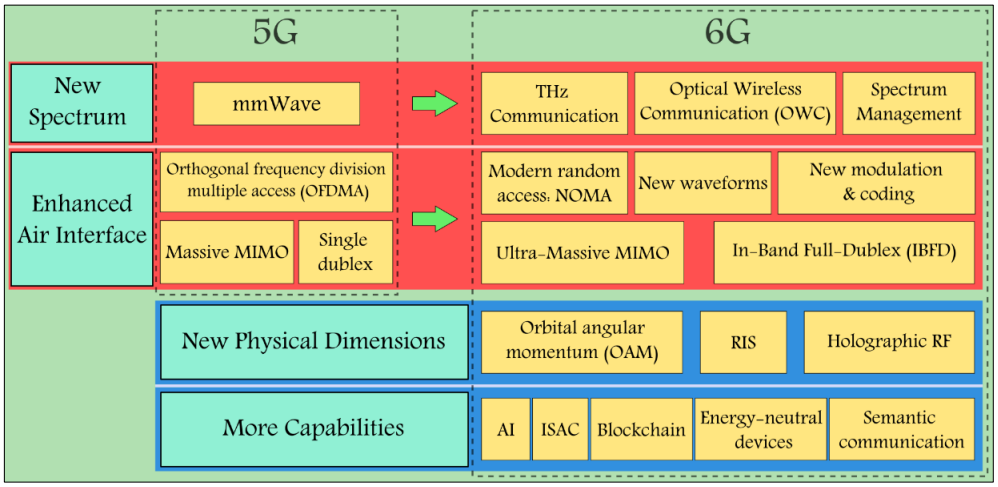

Figure 2.3 Potential 6G key technologies.

Nowadays, healthcare applications extend beyond patient care and play a vital role in enhancing overall quality of life. They include a broad range of services such as emergency response, ambulance coordination, Intelligent Wearable Devices (IWDs), and Hospital-to-Home (H2H) solutions. Among these, IWDs are particularly impactful, offering significant support to patients (Lu & Zheng, 2020). These devices connect remotely to transmit critical health data via the Internet, which is then processed in specialized monitoring and diagnostic centers. The transmitted data typically covers metrics like heart rate, medical conditions, blood analysis results, body weight, and dietary habits. By enabling more effective health monitoring, IWDs reduce the need for frequent clinical visits or long-term hospitalization. To further support their operation, Wireless Body Area Networks (WBANs) are employed, enabling efficient data acquisition from wearable devices across diverse environments (Mucchi et al., 2020).

In addition, connecting the numerous sensors and actuators within a WBAN demands substantial network capacity. One of the most latency-sensitive applications is remote robotic surgery, which requires end-to-end delays of less than 1 millisecond (Nidhi et al., 2021). Such procedures depend on highly

reliable networks capable of transmitting accurate data at high speeds between distant medical facilities. To fulfill stringent Quality of Service (QoS) requirements, healthcare communication infrastructures must go beyond conventional wireless network architectures. These networks must support mobility, deliver high capacity, achieve ultra-low latency, enable energy-efficient (green) communication to protect patient health, and maintain uninterrupted connectivity with at least 99.99% reliability. Considering these critical needs, 6G emerges as a promising solution, offering the performance characteristics essential for advancing modern healthcare systems (Hussein & El-Kader, 2017).

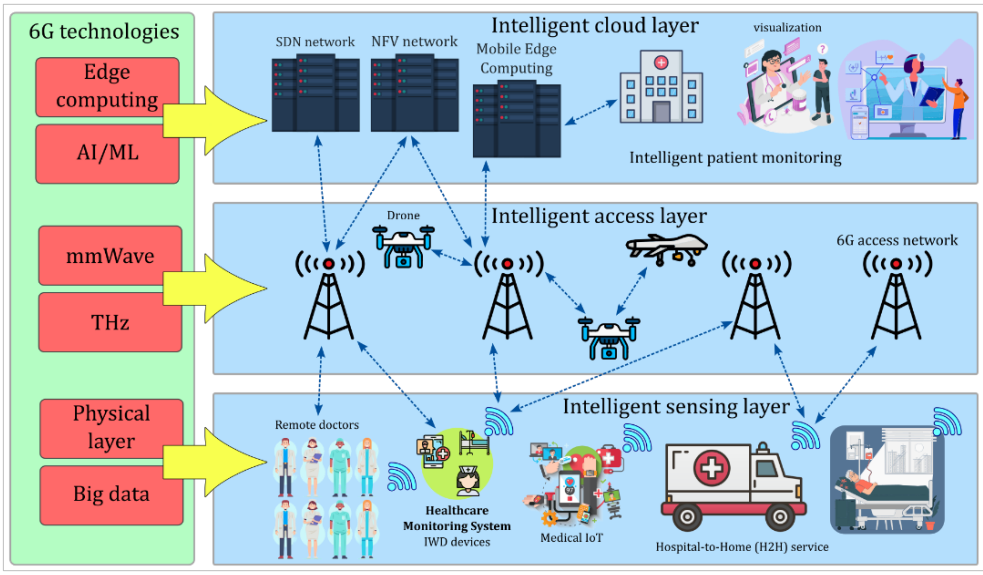

Figure 2.4 The architecture of AI-enabled 6G in healthcare industry.

6G is also expected to be instrumental in enabling affordable remote healthcare services. Its advanced capabilities will support more practical and scalable at-home patient care, while efficiently managing large populations of users simultaneously. 6G is envisioned to transform healthcare networks by incorporating the human body into the broader communication ecosystem. The architectural framework of a 6G-enabled healthcare network, shown in Figure

2.4, features core deployment layers including intelligent sensing, intelligent access, and intelligent cloud services (Hakeem et al., 2022).

The study by the World Economic Forum (2019) emphasized the rising significance of intelligent healthcare in contemporary life, predicting that future healthcare systems will be entirely driven by AI. It recognized 6G as a key enabler of this transformation, offering the communication backbone necessary for intelligent healthcare solutions. The report reviewed several 6G-supported applications poised for integration, including holographic communication, haptic interfaces, AI, augmented reality (AR), and virtual reality (VR). Moreover, it presented a number of innovative services to elevate healthcare system performance, such as blood sample analyzers, H2H platforms, precision medicine, and an advanced insurance model tailored for hospital environments.

In recent decades, wireless communication technologies have advanced rapidly, propelled by sectors such as voice and data transmission, the IoT, smart manufacturing, and the development of smart homes and cities (Noor-A-Rahim et al., 2022; Giordani et al., 2020). Today, the term "wireless" is largely synonymous with RF technologies, which dominate the global market. RF occupies a range from 30 kilohertz (kHz) to 300 GHz within the electromagnetic spectrum and is firmly regulated by national and international authorities. Specific RF bands are typically allocated to licensed users, including mobile network operators, TV broadcasters, and fixed microwave links. However, the rapid growth of high-data-demand wireless services is pushing RF spectrum capacity to its limits, leading to increasing congestion (Uysal et al., 2016).

To overcome the limitations of the congested RF spectrum, higher-frequency electromagnetic waves—specifically in the millimeter-wave and terahertz bands—have been explored as candidates for high-speed wireless communication. These frequency ranges have already demonstrated the capability to support gigabit-per-second (Gbps) data rates (Buzzi et al., 2019; X. Wang et al., 2018; Song, 2021). However, the optical frequency spectrum surpasses both in terms of available unlicensed bandwidth, offering the potential

for ultra-high-speed wireless data transmission even when employing relatively simple modulation techniques (Hong et al., 2020).

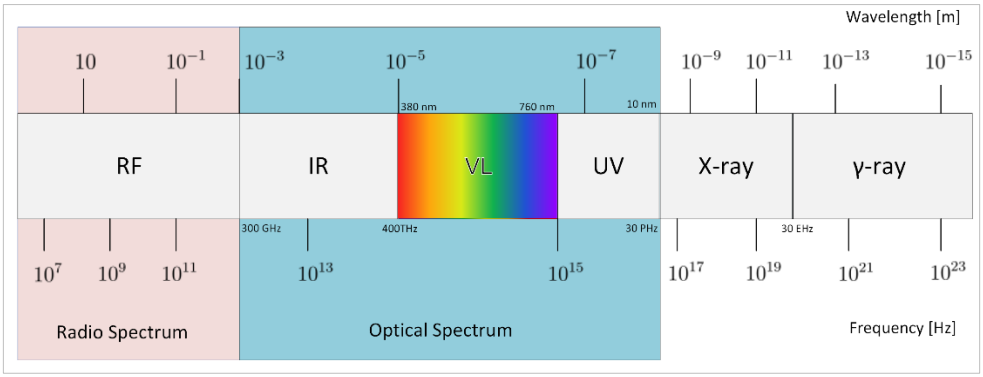

Figure 2.5 Electromagnetic spectrum.

Optical Wireless Communication (OWC) refers to the transmission of optical signals through unguided media, with its specific applications determined by the operating frequency. It spans the entire optical spectrum, including IR, visible light (VL), and ultraviolet (UV) bands, as shown in Figure 2.5. In recent years, OWC has gained significant attention as a promising approach for delivering high-speed wireless connectivity and as an effective alternative to conventional RF systems, which are becoming increasingly congested (Khalighi & Uysal, 2014; Hamza et al., 2018; Nirmalathas et al., 2020; Alsulami et al., 2018).

Optical Wireless Communication systems that function within the visible light range of 390–750 nm are commonly known as VLC systems. These systems utilize LEDs, which can be modulated at high speeds while maintaining their primary function of illumination without noticeable impact on visual perception. This dual functionality—serving both as a light source and a data transmitter—makes VLC a sustainable and energy-efficient technology, with strong potential to transform the way lighting is used within communication systems.

Free-Space Optical (FSO) systems operate mainly in the near-infrared spectrum, ranging from 750 to 1600 nm. These systems commonly utilize laser transmitters to achieve high data transmission rates, reaching up to 10 Gbps per wavelength. Offering both cost efficiency and compatibility with existing communication protocols, FSO systems serve as a practical solution for alleviating backhaul constraints in contemporary network infrastructures.

Interest in ultraviolet communication (UVC) has grown steadily, driven by latest advancement in solid-state optical sources and detectors working within the UV range of 200–280 nm. At ground level, this segment of the spectrum experiences minimal solar interference, allowing for the deployment of photon-counting detectors paired with wide field-of-view receivers. These features improve signal reception while suppressing background noise, making UVC particularly effective for outdoor non-line-of-sight (NLoS) scenarios. As a result, such systems are ideal for low-power, short-range applications like wireless sensor networks (WSNs) and ad-hoc communication setups (Uysal et al., 2016).

To contextualize OWC within the broader communications landscape, Figure 2.6 illustrates the coverage areas and data rates associated with both traditional RF and OWC systems (Nirmalathas et al., 2020). OWC is regarded as a promising and transformative technology, offering advantages such as high data throughput, improved energy efficiency, and a sustainable alternative to increasingly crowded RF bands. Nevertheless, its deployment comes with certain limitations. In outdoor FSO systems, environmental conditions like fog, rain, and airborne particles can severely degrade both data rates and coverage. On the other hand, indoor OWC systems often face constraints from multipath effects, receiver noise, and interference, all of which can hinder overall system capacity.

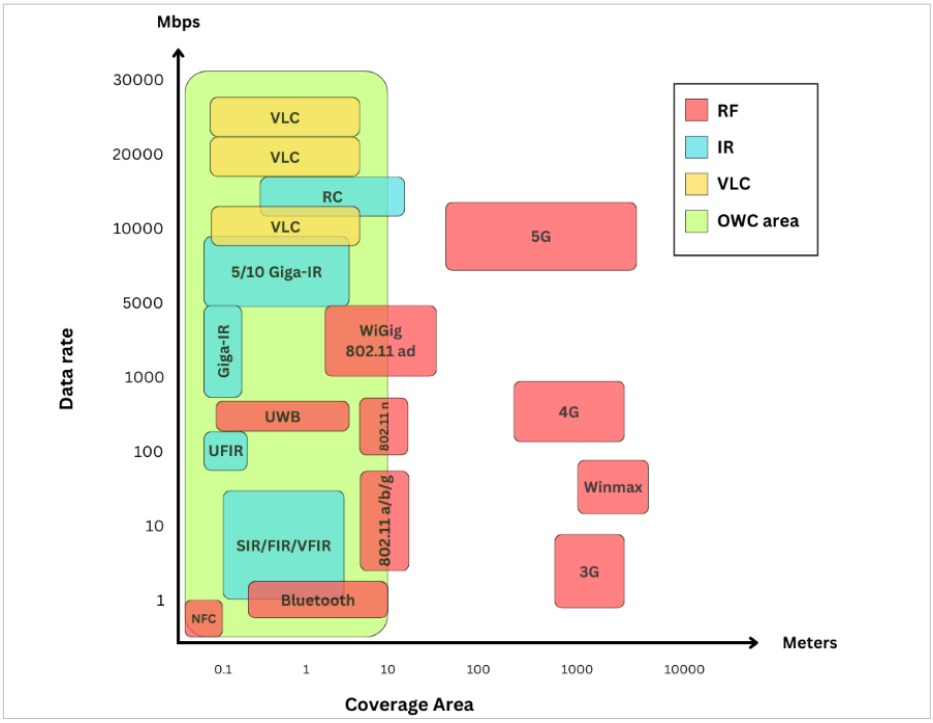

Figure 2.6 Data rates and coverage area of different wireless technologies.

Indoor environments are responsible for an estimated 70–80% of mobile data traffic (Uysal, 2019), highlighting the urgent need for wireless access solutions that are not only high-speed but also cost-effective and energy-efficient. As RF bands become increasingly congested, VLC has gained attention as a viable complementary or alternative technology (Chi, 2018; Dimitrov & Haas, 2015; Uysal et al., 2016). VLC operates by modulating LEDs at very high speeds, which remain invisible to the human eye, enabling these luminaires to support data transmission while still fulfilling their lighting function. With access to the broad bandwidth of the optical spectrum, VLC can help offload traffic from cellular and Wi-Fi networks. Additionally, it serves as a suitable solution in RF-restricted or sensitive environments such as hospitals, aircraft, petrochemical plants, and mining operations (Miramirkhani & Uysal, 2020).

VLC has garnered significant attention in recent years from both academic and industrial sectors, resulting in a wide range of studies and comprehensive

review papers (O'Brien et al., 2008; O'Brien, 2011; Jovicic et al., 2013; Pathak et al., 2015; Qiu et al., 2016; Luo et al., 2017; Al-Kinani et al., 2018; Karunatilaka et al., 2015). Early research in VLC focused primarily on establishing point-to-point connections and enhancing the physical layer. These systems predominantly rely on IM/DD, wherein data is conveyed by varying the brightness of LEDs and captured by photodetectors (PDs) at the receiver end. Due to the inherent requirement of IM/DD that transmitted signals must be real and non-negative, initial studies concentrated on simple modulation schemes, including on–off keying (OOK), pulse position modulation (PPM), and pulse width modulation (PWM) (Rajagopal et al., 2012; Komine & Nakagawa, 2004).

Due to the multipath characteristics of VLC channels and the inherent low-pass behavior of LEDs and receiver circuitry, the effective electrical bandwidth is significantly constrained. To address intersymbol interference (ISI) in these frequency-selective channels, multicarrier transmission methods—especially orthogonal frequency division multiplexing (OFDM)—have become a prevalent solution in contemporary research (Fernando et al., 2012; Dissanayake & Armstrong, 2013; Mossaad et al., 2015; Bian et al., 2019). Numerous optical OFDM variants have been presented to meet the requirement that the LED driving signals must remain real-valued and non-negative. In addition, advanced strategies like adaptive transmission (L. Wu et al., 2014; Hong et al., 2016; Narmanlioglu et al., 2017), relay-assisted communication (Kizilirmak et al., 2015; Feng et al., 2018; Na et al., 2018), and multiple-input multiple-output (MIMO) schemes (Fath & Haas, 2013; Zhu et al., 2015; Wei et al., 2016) have been explored to further enhance system performance. More recently, research focus has expanded to higher-layer solutions aimed at evolving VLC into a scalable, multi-user, and fully integrated wireless network. These developments address critical issues such as medium access control (H. Li et al., 2019; Ling et al., 2018), interference management (S. Ma et al., 2018), handover protocols (N. Y. Wang & Haas, 2015), and resource allocation (Dastgheib et al., 2018).

Similar to other wireless communication technologies, a VLC system's physical layer performance is largely influenced by the characteristics of the propagation channel and the hardware limitations of both transmitter and receiver front-ends. As a result, accurate propagation channel modeling is essential for effective system design and performance analysis. Although early work often relied on simplified LOS models, recent studies have increasingly focused on constructing more realistic VLC channel representations to capture the complexity of practical environments (Al-Kinani et al., 2018; Qiu et al., 2016; Uysal et al., 2017; Donmez & Miramirkhani, 2021).

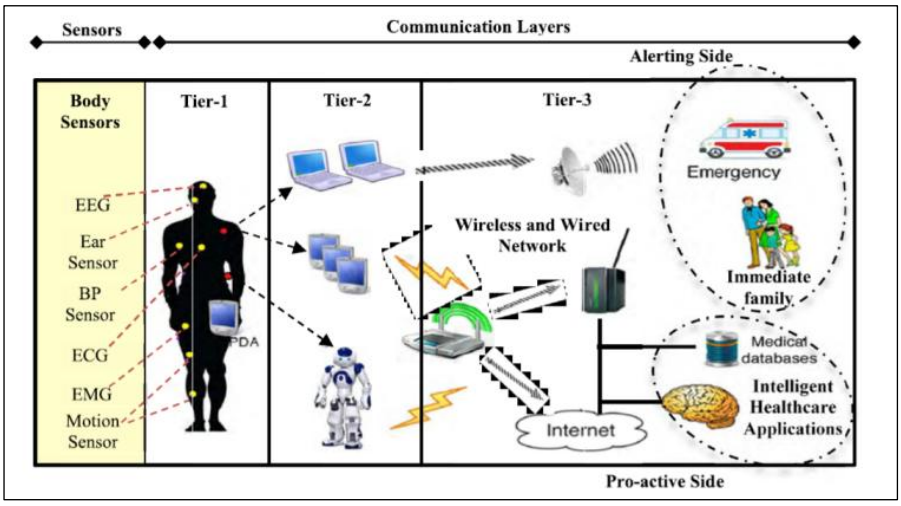

Figure 2.7 The architecture of a remote health monitoring system (Dalloul et al., 2023).

Probabilistic remote health monitoring, also known as remote patient monitoring or telehealth monitoring, utilizes technology to observe patients' health conditions from a distance. This process involves gathering, transmitting, and analyzing health-related data, enabling medical professionals to make informed clinical decisions, monitor patients, and deliver interventions on timely manner without requiring in-person visits (Yakovlev et al., 2012). Numerous technologies support this model, including wearable devices, sensors, mobile

apps, and modern communication infrastructures (Marzencki et al., 2011; Ramesh et al., 2012; Mia et al., 2021). The adoption of such systems has shown notable benefits in improving health outcomes, enhancing medication compliance, and boosting patient involvement and satisfaction. In addition, these systems promote individualized care, facilitate remote consultations, and empower patients to manage their own health more effectively (Hassan et al., 2013). Figure 2.7 presents an overview of the system architecture.

Remote health monitoring systems face several significant challenges, particularly concerning data security, system reliability, and energy consumption (Sagahyroon, 2017; Boric-Lubecke et al., 2014; Petkovic, 2009). The transmission of sensitive medical data over wireless networks raises serious privacy concerns, as it can expose patient information to potential cyber threats. Reliability is equally vital, as any malfunction or disruption in the system may lead to delayed responses or misdiagnoses, posing risks to patient safety. Moreover, the energy demands of wearable devices used in these systems represent another key issue; frequent recharging can be burdensome for users who depend on battery-powered equipment.

Integrating VLC into MBSNs within the framework of 6G technology offers effective solutions to the aforementioned challenges. MBSNs are composed of wearable or implantable technologies designed to track essential physiological parameters, including body temperature, heart rate, and blood pressure. VLC is especially advantageous for indoor passive health monitoring, as it utilizes existing lighting systems to facilitate both illumination and data transmission. This approach allows for precise, energy-efficient, and secure health data communication without relying on invasive sensors or requiring patients to remain in fixed positions (J. Li et al., 2024). Table 2.2 categorizes various medical body sensors according to their clinical applications, placement on the body, and specific use cases. For instance, subcutaneous sensors used to track glucose levels are commonly applied in glucose home monitoring (Donmez et al., 2021).

Table 2.2 Applications of MBSNs .

Clinical Applications	Sensor Location	Sensor Types
Glucose home monitoring	Eye	Glucose
	Subcutaneous	Glucose
	Arm	Multi-Variable
Cardiopulmonary and vascular monitoring	Wrist	Ultrasound
		Multi-Variable
		Photoplethysmograph (PPG) Electrocardiograph (ECG)
	Finger (ring sensor)	Optical (heart rate)
	Phone adapter	Single-channel ECG
	Arm or thigh	Microwave reflectometric cardiopulmonary
Neuro	Clothes	Inertial sensors Accelerometers
	Wrist or ankle	Accelerometer Motion
Physiotherapeutic care and recovery support.	Ankle	Pedometers Accelerometer

VLC technology's immunity to EMI is particularly valuable in healthcare settings, as it prevents communication systems from disrupting the operation of sensitive medical equipment—an essential factor for maintaining patient safety. Additionally, concerns about the long-term effects of RF exposure further highlight the need for alternative communication methods like VLC. Its inherent security advantages, such as the use of directional light and LoS transmission, make VLC especially well-suited for handling sensitive medical data, such as medical records and live health data, by minimizing the likelihood of interception or unauthorized access at the physical transmission level (Zhao et al., 2018). While features like high data throughput and low latency are central to applications such as internet access and gaming, healthcare places greater emphasis on reliability, security, and minimal EMI. As such, VLC presents a strong candidate for medical communication systems, offering secure and dependable performance without compromising the safety or function of surrounding medical devices (Uysal et al., 2016; Caputo et al., 2023).

Although VLC offers several advantages, its application in healthcare also presents certain challenges, such as the need for LoS communication, susceptibility to signal interference, and the financial burden of infrastructure deployment (Caputo et al., 2023; Priyadharsini & Kunthavai, 2022). Overcoming these obstacles is essential for broader adoption of the technology. Nevertheless, ongoing advancements in VLC research are progressively enhancing communication reliability, latency performance, and system robustness, positioning VLC as a key enabler in the future of healthcare (Kurunathan et al., 2023). In support of safe deployment, the IEC 60601-1-2 standard for VLC-based MBSNs outlines the minimum separation required between medical devices and RF transceivers to ensure that electromagnetic disturbances do not compromise QoS ("MEDICAL ELECTRICAL EQUIPMENT — Part 1-2: General Requirements for Basic Safety and Essential Performance — Collateral Standard: Electromagnetic Disturbances — Requirements and Tests," 2014).

Consequently, VLC stands out as a promising alternative to RF for remote health monitoring within 6G-enabled systems. Combining VLC with 6G in MBSNs represents a significant advancement in contemporary healthcare, enabling reliable and secure wireless data exchange between medical sensors and external systems. Modern medical environments, including hospitals and clinics, are progressively implementing cutting-edge solutions such as Wireless Sensor Networks, the Internet of Medical Things (IoMT), telehealth services, and biomedical signal analysis. These systems rely on real-time monitoring of physiological parameters to support early detection of health issues and ensure timely medical intervention.

Recent studies have shown growing interest in OWC-enabled MBSNs, with IR communication already adopted in clinical settings to support wireless data exchange between wearable sensors and monitoring equipment. Within this framework, standardized protocols have been defined for mobile IR devices functioning under fixed LoS conditions in close proximity to patients.

(ISO/IEEE International Standard Health Informatics-Point-of-Care Medical Device Communication-Transport Profile-Infrared, 2004). In addition, the use of IR transmitters and non-coherent light sources like LEDs in OWC systems is subject to compliance with established eye safety standards (Photo-biological Safety of Lamps and Lamp Systems (Identical With CIE S009), 2006; Safety of Laser Products Part 1: Equipment Classification and Requirement, 2007). Hadjidj et al. (2012) highlighted several key challenges associated with wireless MBSNs, particularly emphasizing energy efficiency as a critical concern due to the high power demands of wireless communication. Another significant challenge lies in the influence of the human body on signal propagation, which degrades channel performance and complicates accurate modeling—especially when accounting for anatomical complexity and motion. Notably, Hadjidj et al. (2012) offered a broad overview rather than in-depth analysis of channel behavior. Additionally, most existing MBSN systems in current literature are still built upon RF, acoustic, or long-wave magnetic communication technologies, as outlined by the IEEE 1902.1 standard (Donmez et al., 2021).

In the existing body of work on OWC channel modeling, there is a noticeable scarcity of studies addressing mobile downlink scenarios in VLC-based MBSNs. This gap is partly due to the emerging nature of VLC technology, but more critically, it stems from the complexities associated with modeling NLoS channels involving polychromatic light sources. Unlike IR transmitters that emit at a single optical wavelength, typical VL sources generate polychromatic signals. Since material reflectance varies with wavelength, VLC systems must consider this spectral dependency to accurately estimate the received signal power at the PD. Neglecting these wavelength-specific reflectance properties can lead to significant uncertainties in channel modeling. This complexity sets VLC apart from IR-based systems, where reflectance is more consistent due to the monochromatic nature of the source. As a result, IR models cannot be directly applied to VLC scenarios, which require specialized modeling techniques that account for the interactions between polychromatic

light and varying surface characteristics (Donmez et al., 2021; Donmez & Miramirkhani, 2021).

Moreover, channel modeling in VLC-based MBSNs becomes significantly more complex when the sensor nodes are attached to a moving human body rather than remaining stationary. Movement can introduce shadowing effects or cause complete signal blockage, with obstacles—including the body itself—intermittently obstructing the light path as the person moves unpredictably within a room. Accurately simulating such behavior requires realistic modeling of human mobility, as people do not follow fixed stride lengths, restrict movement to the four main directions, or always initiate their paths from predefined points like doorways. To effectively characterize practical and dynamic VLC-based MBSN channels, both realistic movement trajectories and wavelength-dependent surface interactions must be taken into account.

Despite increasing interest in OWC-based MBSNs, there is still a clear shortage of channel models specifically designed for these systems. This presents a significant limitation, as accurate channel modeling is fundamental to the development of efficient, reliable, and resilient communication links. Presently, existing models tend to draw from established IR modeling approaches: deterministic models (Gfeller & Bapst, 1979; Barry et al., 1993; López-HernáNdez & Betancor, 1997; Abtahi & Hashemi, 1995; Carruthers & Kahn, 1997; Carruthers & Kannan, 2002; Jungnickel et al., 2002; Hayasaka & Ito, 2007) and stochastic models (López-HernáNdez et al., 1998a; López-HernáNdez et al., 1998b; M. I. S. Chowdhury et al., 2014; Dimitrov et al., 2009) are commonly employed for uplink IR channels. Meanwhile, downlink modeling in VLC-based systems relies on deterministic (Nguyen et al., 2010; Long et al., 2014; K. Lee et al., 2011; Ding et al., 2015; Schulze, 2016; Chen et al., 2016; Al-Kinani et al., 2016a; Al-Kinani et al., 2016b) and stochastic (J. Lee & Lee, 2008; Rodríguez et al., 2013; Rufo et al., 2017; Uysal et al., 2017; Miramirkhani & Uysal, 2015; Miramirkhani et al., 2017; Miramirkhani & Uysal, 2020) VLC models. These models are typically categorized into four types based

on the deployment environment: indoor, outdoor, underground, and underwater, as shown in Figure 2.8 (Yahia et al., 2021).

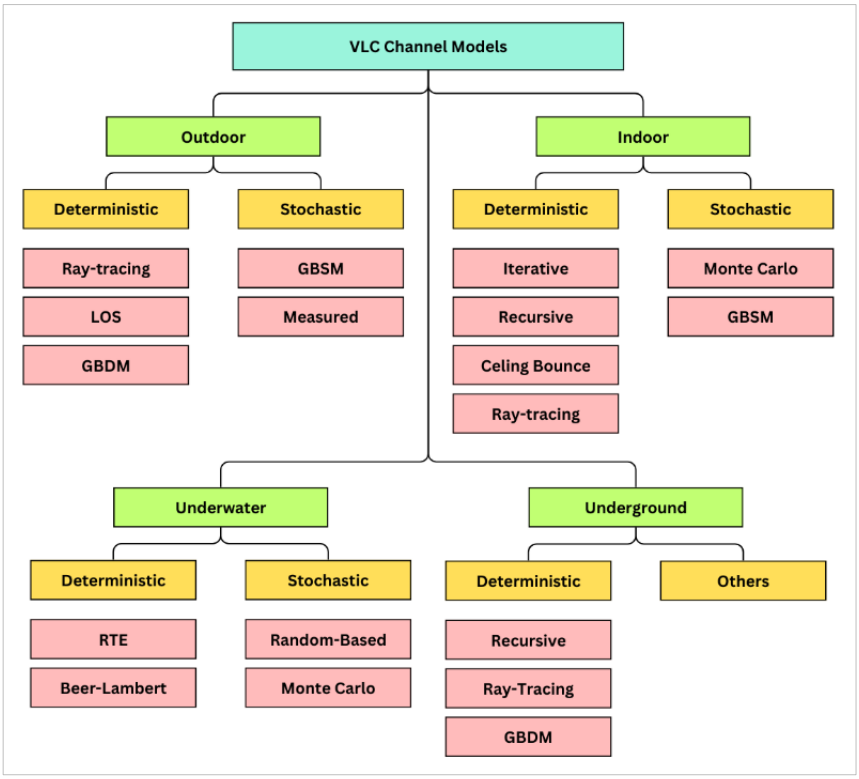

Figure 2.8 Classification of VLC channel approaches.

This proposal implements the site-specific channel modeling method employing non-sequential ray tracing, which accurately characterizes the optical propagation behavior within a defined indoor environment, as presented in (Miramirkhani & Uysal, 2020; Donmez & Miramirkhani, 2021). In (Miramirkhani & Uysal, 2020), four distinct healthcare scenarios are evaluated: clinic, Intensive Care Unit (ICU) ward, family-centered patient room, and semi-private patient room. These scenarios, illustrated in Figure 2.9 , incorporate considerations such as wavelength dependency, the influence of human presence, and the effect of furniture on signal propagation. Table 2.3 outlines the

surface coating materials used in each setting, while Table 2.4 details the physical dimensions and specifications for the modeled environments.

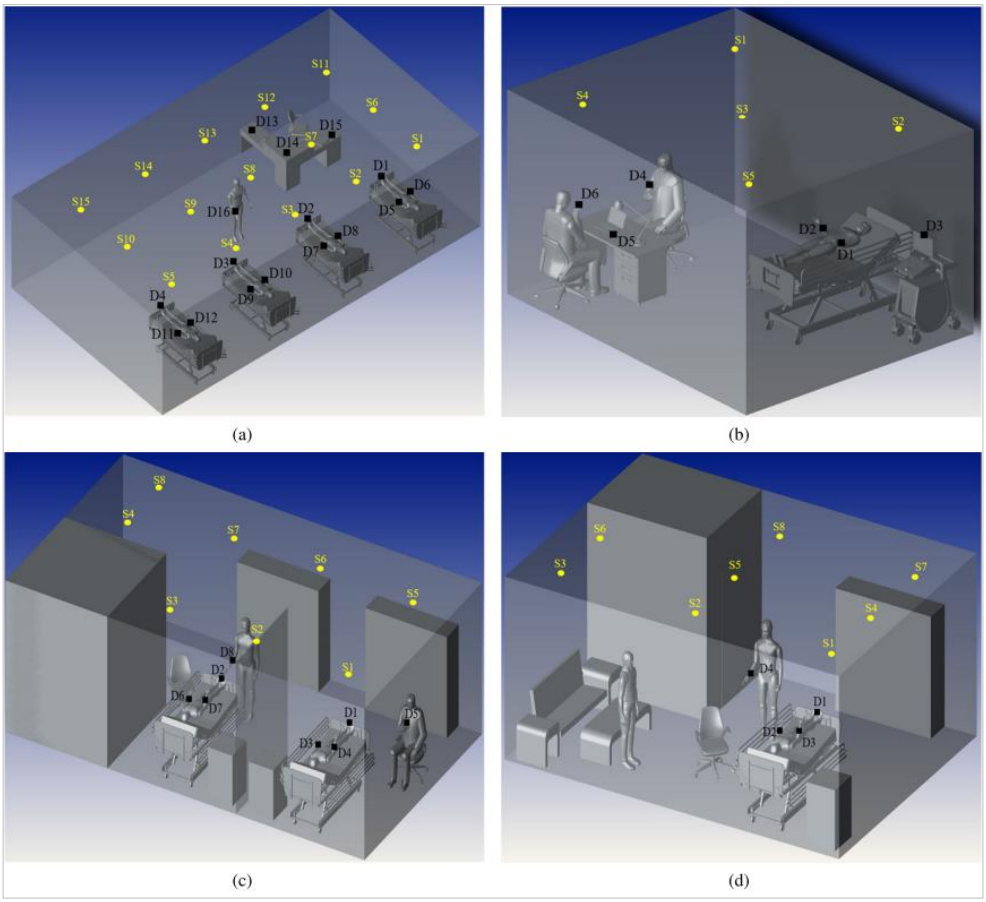

Figure 2.9 Scenarios under consideration: (a) ICU ward, (b) clinic, (c) semi-private patient room, and (d) family centered.

Table 2.3 Coating materials for the scenarios under consideration.

	Scenario 1 ICU ward	**Scenario 2 Clinic**	**Scenario 3 Semi-private patient**	**Scenario 4 Family-centered patient room**
Walls	Plaster	Plaster	Plaster	Plaster
Ceiling	Plaster	Plaster	Plaster	Plaster
Floor	Pinewood	Pinewood	Pinewood	Pinewood
Hospital bed	Aluminum	Aluminum	Aluminum	Aluminum
ICU desk	Pinewood	-	-	-
Chair	Black gloss paint	Black gloss paint	Black gloss paint	Black gloss paint
Medical ultrasound machine	-	Aluminum	-	-
Desk	-	Pinewood	-	-
Laptop	-	Black gloss paint	-	-
WC door	-	-	Pinewood	Pinewood
Curtain	-	-	Cotton	
Drawer	-	-	Pinewood	-
Wardrobe	-	-	Pinewood	-
Sofa cover	-	-	-	Cotton
Side tables	-	-	-	Pinewood
Coffee tables	-	-	-	Pinewood

Table 2.4 Specifications of scenarios under consideration.

Features	Clinic	ICU ward	Semi-private patient room	Family-centered patient room
Dimensions (L × W × H) [m]	5 × 4 × 3	11.5 × 6.5 × 3	8.8 × 5 × 3	7 × 5 × 3
Number of beds	1	4	2	1
Number PDs	6	16	4	4
Number of sources	5	15	8	8
Number of bodies	3	5	4	3
Clear floor area per bed [m^2]	14	13.69	14.13	23.66
Side clearance on non-transfer side of bed [m]	≈ 1	≈ 1	≈ 1	≈ 1
Clearance at the foot of each bed [m]	1.7	2.3	2.3	2.3
Side clearance on transfer side of bed [m]	≫ 1.22	1.5	2	≫ 1.22

2.2. MOBILE VLC-BASED MBSNS CHANNEL MODELS

A site-specific channel modeling approach based on non-sequential ray tracing is employed, allowing rays to propagate randomly through the environment, with absorption, reflection, and scattering occurring each time they encounter an object. The software Zemax® is utilized, which supports more than 10 reflections in non-sequential ray tracing mode to obtain a site-specific CIR (Donmez & Miramirkhani, 2021). The key steps of the proposed site-specific channel modeling for VLC-based Mobile Body Sensor Networks are illustrated in Figure 3.1.

Two reference MBSN scenarios are selected from Figure 2.9: an ICU ward and a family-type patient room (FTPR), as depicted in Figure 2.10 , in accordance with hospital room specifications outlined in the Interim Amendment for the 2018 Residential Guidelines (2020). Within the Zemax®

simulation environment, the reflective properties of all 3D CAD elements—including room surfaces, luminaires, and PDs—are carefully defined. For lighting, Cree® 14-40 LHE luminaires are chosen, featuring a half viewing angle of 55 degrees and a luminous efficacy of 125 lumens per watt. These luminaires are installed on the ceilings of each scenario to satisfy both the required minimum average illumination levels (Lighting for Hospitals and Healthcare Facilities, 2016) and the minimum uniformity illuminance ratio of 0.7.

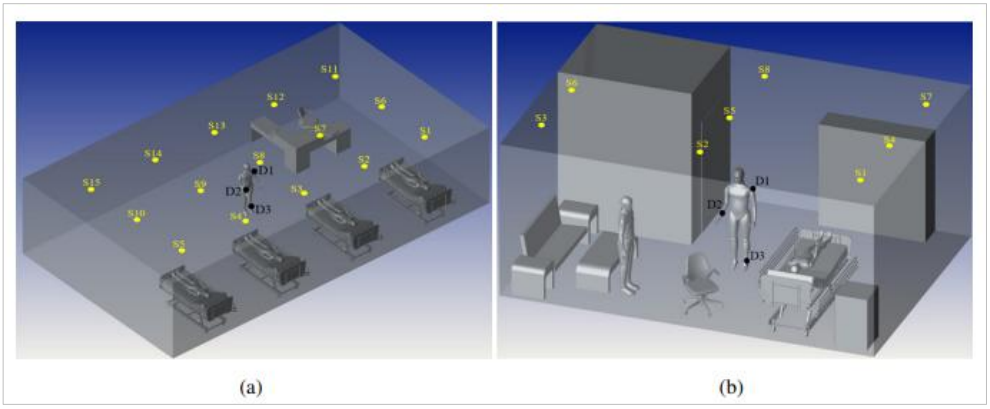

Figure 2.10 Hospital scenarios (a) ICU ward and (b) FTPR

The ICU ward scenario measures 11.5 m × 6.5 m × 3 m and includes 15 luminaires mounted on the ceiling. This environment accommodates four patients in hospital beds and features a desk and chair for medical personnel, who move unpredictably within the space. In comparison, the FTPR, sized at 7 m × 5 m × 3 m, includes a restroom and is illuminated by 8 ceiling-mounted luminaires. It contains one patient in bed, various furnishings for patient use, a sofa bed for a companion, and medical staff who also exhibit random movement. In both scenarios, three MBSN nodes are placed on the mobile human body—specifically on the shoulder (D1), wrist (D2), and ankle (D3)—reflecting typical MBSN deployment practices.

2.3. ML-BASED VLC SYSTEM

Machine Learning, a subset of Artificial Intelligence, operates on the concept that machines can independently learn to address specific tasks when provided with appropriate data. Through the application of sophisticated mathematical and statistical methods, ML enables machines to undertake cognitive tasks typically reserved for human intelligence (Musumeci et al., 2018). It proves especially useful for tackling complex challenges that either require numerous iterations under traditional approaches or lack conventional solutions. Reinforcement learning addresses sequential decision-making as an optimization of long-term reward (policy learning), whereas supervised ML in our setting addresses estimation of unknown channel/position variables from data.

In recent years, ML has matured to a level where wireless systems can leverage it to analyze data and derive actionable insights through direct interaction. Nevertheless, despite their synergistic capabilities, ML and wireless communication have often been explored in isolation within academic research (Saxena et al., 2023). Conventional wireless communication channel modeling generally employs probabilistic and signal processing-based algorithms; however, these methods frequently fall short in real-world conditions, potentially leading to inaccurate system evaluations. ML techniques, in contrast, can detect and rectify system deficiencies without the need for highly intricate algorithmic structures. This advantage is particularly relevant in scenarios where data availability is limited, as is often the case with wireless—especially optical—signals (Pachpande et al., 2018).

In machine learning, the performance of a model is critically dependent on its configuration, which is determined by a set of hyperparameters. Unlike model parameters that are learned during training, hyperparameters are set prior to the learning process and govern its behavior, such as the learning rate in an optimizer or the number of trees in a Random Forest (RF). The process of identifying the

optimal combination of these values is known as hyperparameter optimization (HPO). Given that the search space of possible hyperparameter configurations can be vast, efficient and effective search strategies are essential for maximizing model performance (Hutter et al., 2019). The choice of strategy involves a fundamental trade-off between computational expense and the quality of the resulting solution.

Grid Search is an exhaustive hyperparameter tuning method that evaluates all specified combinations of hyperparameter values. A grid is defined where each axis represents a hyperparameter and the points on the axis represent the values to be tested. The algorithm then trains and evaluates a model for every single point on this grid. The primary advantage of this method is its completeness; if the optimal set of parameters exists within the discrete grid, Grid Search is guaranteed to find it. However, its principal disadvantage is the curse of dimensionality. The number of required model evaluations grows exponentially with the addition of new hyperparameters, rendering the method computationally intractable for problems with a large parameter space.

Random Search offers a more efficient alternative by sampling a fixed number of parameter combinations from specified statistical distributions. Instead of systematically checking every combination like Grid Search, it randomly selects points within the search space. Research has demonstrated that for most datasets, only a few hyperparameters significantly impact final model performance, and Random Search is more likely to discover good values for these important parameters by exploring a wider range of values more quickly (Bergstra & Bengio, 2012). Its main limitation is that it does not leverage information from past evaluations to guide future sampling, meaning each trial is independent and there is no guarantee of converging on the optimal solution.

Bayesian Optimization is a sequential model-based optimization (SMBO) technique that intelligently selects the next set of hyperparameters to evaluate based on prior results. It works by building a probabilistic surrogate model of the objective function, typically using a Gaussian Process, which maps

hyperparameter values to their performance metric (Rasmussen & Williams, 2006). An acquisition function is then used to balance exploration (sampling in regions of high uncertainty) and exploitation (sampling in regions likely to yield high performance). This informed approach makes Bayesian Optimization significantly more sample-efficient than Grid or Random Search, often finding a superior set of hyperparameters with far fewer model evaluations (Snoek et al., 2012). Its primary drawbacks are its increased implementation complexity and its inherently sequential nature, which can make parallelization less straightforward.

A typical VLC system tailored for hospital environments includes three core components: an LED-based transmitter, an optical photodetector receiver, and the VLC channel, as illustrated in Figure 2.11. This diagram also identifies potential integration points for ML techniques throughout the system. On the transmission side, a binary data stream modulates an RF carrier, followed by pre-equalization and upconversion processes. The resulting electrical signal modulates the LED's light intensity. The transmission occurs through free space, common in indoor or occasionally underwater settings. At the receiver, the optical signal undergoes downconversion, post-equalization, demodulation, and decryption to recover the original binary data. The bit error rate (BER) of the decoded signal serves as a primary performance metric for the system (Saxena et al., 2023).

To improve overall system performance, ML techniques are incorporated into both the transmitter and receiver architectures. These integrations target critical functions such as compensating for transceiver nonlinearity, performing accurate channel estimation, mitigating jitter, enabling location tracking, detecting modulation schemes, estimating phase, and strengthening security. Through the application of ML, VLC systems can become more resilient, adaptive, and efficient—capable of meeting the demands of dynamic and sensitive healthcare environments.

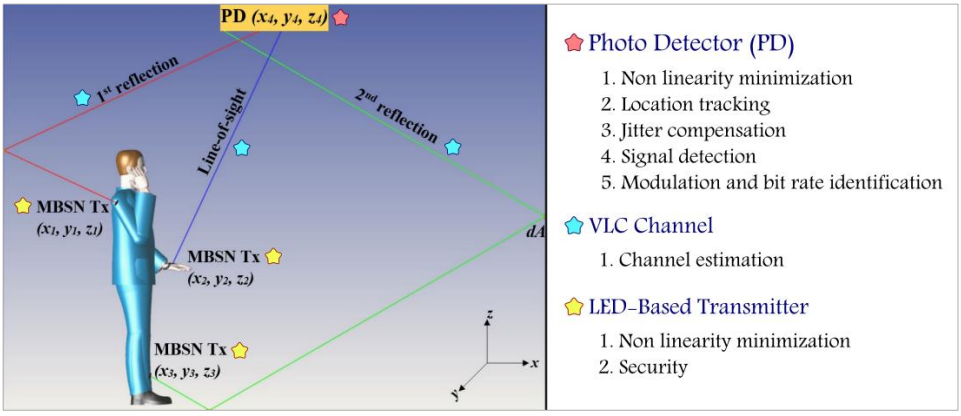

Figure 2.11 ML applications in a VLC-Based MBSNs system.

In VLC-Based MBSNs, ongoing challenges stem from the highly dynamic nature of environments influenced by human body movement. One major issue is the variability in channel DC gain, which can change substantially due to factors such as patient motion, varying distances between the transmitter and receiver, obstructions, and shadowing. These conditions result in fluctuating received signal strength (RSS), which in turn increases the likelihood of data transmission errors (Pathak et al., 2015; Arnon et al., 2012; Ghassemlooy et al., 2017).

To overcome these challenges, adaptive modulation presents a viable solution by dynamically modifying the modulation order based on current channel conditions. This approach enhances spectral efficiency (SE) while preserving the necessary reliability for communication within MBSNs. By continuously adapting the modulation scheme, the system can strike an effective balance between maintaining high data rates and ensuring robust, error-resilient communication.

Our dataset supports three task families: (i) QL-based adaptive modulation, (ii) LSTM-based channel-parameter estimation with LSTM, and (iii) MLP-based localization. There is currently no widely accepted hospital-VLC benchmark for any of these tasks. To approximate benchmark status, we utilize the CIRs results from the simulation in (Donmez et al., 2021). For

adaptive modulation, evaluation is conducted by reward definitions plus SER/QoS constraints. Meanwhile, channel estimation by RMSE on PL and RMS delay spread. Finally, position estimation is evaluated by Euclidean RMSE. We include different model to set as a reference baselines. This package yields a benchmark baseline for future research in this field.

2.4. ML-BASED ADAPTIVE MODULATION

Previous research applying ML to link adaptation has primarily focused on non-VLC communication systems, such as RF technologies (Elwekeil et al., 2018; Mashhadi et al., 2021; D. Lee et al., 2020; Bobrov et al., 2021; Saxena et al., 2021) and underwater acoustic communications (Fu & Song, 2018; Su et al., 2019; Byun et al., 2021; Y. Zhang et al., 2022). While some work has explored ML techniques in VLC, only Bayat Rizi et al. (2024) specifically addressed adaptive modulation in VLC-based MBSNs. However, their approach did not integrate channel parameter estimation into the learning model.

Research on ML-based link adaptation in RF systems has explored several methodologies. For instance, Elwekeil et al. (2018) employed a deep convolutional neural network that uses per-subcarrier Signal-to-Noise Ratio (SNR) and noise variance to predict the modulation and coding scheme (MCS) without requiring data preprocessing. However, the model's high input dimensionality—due to hundreds of subcarriers—and dependency on large offline datasets limits its suitability for real-time, resource-constrained body sensors. Mashhadi et al. (2021) introduced deep Q-learning, defining states with a fixed window of recent RSS values and actions as Quadrature Amplitude Modulation (QAM) orders. Nonetheless, their use of offline training methods makes real-time implementation impractical. In D. Lee et al. (2020), the SNR range is segmented into fixed regions for M-ary Phase Shift Keying (MPSK) selection using a Deep Q-Network (DQN) framework. Yet, this static partitioning and episodic trial design may struggle to adapt under non-stationary

channel conditions. Mashhadi et al. (2021) later refined their work by incorporating outdated channel state information (CSI) to mitigate delay effects in indoor RF scenarios using deep Q-learning. Bobrov et al. (2021) introduced an online deep learning method for massive MIMO systems, pretrained on Outer Loop Link Adaptation (OLLA) outputs and fine-tuned using Acknowledgement / Negative Acknowledgement (ACK/NACK) feedback. The model leverages features such as sub-band SINR, Channel Quality Indicator (CQI), Reference Signal Received Power (RSRP), and time-since-sounding. However, it carries biases from offline training, assumes full-buffer traffic, and does not capture complex feature dependencies. Saxena et al. (2021) proposed a tuning-free Thompson sampling bandit model that uses a latent SINR distribution and defines MCS as the action space. However, its reliance on Gaussian-innovation assumptions and empirically tuned Doppler smoothing may be unsuitable for VLC scenarios characterized by LoS dominance and noise from ambient lighting.

In acoustic underwater communication (AUWC) systems, one of the primary challenges is the long propagation delay, which often renders real-time access to current CSI impractical. To address this, Fu and Song (2018) proposed a Dyna-Q algorithm capable of predicting the channel state and estimating throughput. Su et al. (2019) extended this work by introducing a Q-learning algorithm that incorporates multiple transmission parameters for decision-making. Furthermore, Byun et al. (2021) demonstrated that in underwater environments, the relationship between SNR and BER is relatively weak, complicating the task of accurate link adaptation. In response, Y. Zhang et al. (2022) presented a deep Q-learning approach specifically designed to handle link adaptation in AUWC systems. A detailed overview of ML-based link adaptation techniques in both RF and AUWC systems can be found in Tables 2.5 and 2.6, respectively (Bayat Rizi et al., 2024).

Table 2.5 Comparison Table of Existing Machine Learning-based Link Adaptation Studies in RF systems

Ref.	Method	System Model	Proposed ML Model
(Elwekeil et al., 2018)	Deep convolutional neural network	Convolutionally codded MIMO-OFDM wireless system	Maps feature sets to MCS using large datasets; feature space: per-subcarrier SNR and noise variance; high-dimensional input; no preprocessing required.
(Mashhadi et al., 2021)	Deep Q-learning	Indoor single-input single-output (SISO) wireless system	Predicts current CSI and adapts links using past RSS; state space: RSS from last τ frames; action space: QAM orders; no environment knowledge or quantization error.
(D. Lee et al., 2020)	Deep Q-learning	Wireless system over Rayleigh-faded channel model	DQN-based adaptive modulation with trial policy; state: fixed SNR regions; actions: Gray-coded MPSK; no channel knowledge or quantization error assumed.
(Bobrov et al., 2021)	Online Deep Learning	Massive MIMO-OFDM wireless system	Pretrained fully connected NN, fine-tuned online via ACK/NACK to adapt MCS; features: sub-band SINR, CQI, time-since-sounding, RSRP, current MCS; boosts throughput vs. OLLA; no channel knowledge needed.
(Saxena et al., 2021)	Latent Thompson Sampling	Fading wireless channels as a multi-armed bandit	Treats MCS options as bandit arms, capturing inter-scheme dependencies; state space: latent SINR distribution based on ACK/NACK history; action space: discrete MCS selections; autonomously adapts to channel dynamics; surpasses traditional methods; no prior environmental knowledge necessary.

Table 2.6 Comparison Table of Existing Machine Learning-based Link Adaptation Studies in AUWC Systems

Ref.	Method	System Model	Proposed ML Model
(Fu & Song, 2018)	Dyna-q algorithm	Autonomous underwater vehicle	Predicts current CSI for adaptive modulation; states: effective SNR; actions: QPSK, BPSK, 8PSK.
(Su et al., 2019)	Hot-booting Q-learning algorithm	Underwater acoustic	Optimizes QoS through adaptive modulation and coding; employs offline learning for quicker convergence; states: transmission factors from current and past packets; actions: MFSK and coherent single-carrier schemes.
(Byun et al., 2021)	MLP network	Acoustic Internet of underwater things	Highlights severe propagation loss and channel variability; traditional AMC depends on SNR-BER mapping, which is unreliable underwater. key link quality metrics include delay spread, BER, SNR, and frequency shift.
(Y. Zhang et al., 2022)	LSTM-enhanced DQN-based adaptive modulation	Underwater acoustic	Tackles partial channel observation using RL with LSTM; Link adapts via delayed CSI; states: effective SNR over last τ slots; actions: {BPSK, QPSK, 8PSK, 16QAM}; no channel knowledge needed; no quantization error.

Recent studies have examined the integration of VLC in MBSNs and hospital environments. Lebas et al. (2018) explored patient monitoring systems using VLC and IR transmission. Fernández et al. (2024) evaluated VLC system performance for smart patient monitoring, while Candia (2024) investigated VLC-based indoor localization in hospitals. Guaña-Moya et al. (2024) reviewed advancements in channel coding and modulation, emphasizing the importance of adaptive technologies for enhancing reliability and efficiency in dynamic healthcare settings.

Building on prior research, Bayat Rizi et al. (2024) introduced an ML-driven adaptive modulation framework tailored for VLC-enabled MBSNs,

focusing on the complexities posed by dynamic hospital environments and patient movement. Their methodology employed detailed ray tracing to generate CIRs across diverse scenarios. To assess SE gains, the study compared both adaptive and fixed modulation techniques. A Q-learning approach was implemented due to its capacity to adapt to varying environmental conditions without requiring explicit CSI. However, the study was confined to modulation optimization and did not address the estimation of channel parameters.

2.5. ML-BASED CHANNEL PARAMETER ESTIMATION

Equally vital to system performance are VLC channel parameters, particularly the channel DC gain and RMS delay spread. The DC gain indicates signal attenuation and directly affects the RSS, and as a result, the SNR, which is a crucial metric for system performance evaluation. In parallel, the RMS delay spread captures multipath propagation effects, providing insight into the signal's temporal dispersion within the channel.

Within the VLC domain, various strategies have been introduced to develop reliable and efficient communication systems. A fundamental requirement in this process is the precise estimation of key channel parameters. One widely used method is channel sounding, which involves transmitting training sequences or pilot signals to characterize the channel at the receiver end. Another approach is estimating the CIR, typically achieved by sending known impulses through the channel to understand its behavior. Additionally, statistical models based on Rayleigh or Rician distributions, as well as analyses in the time and frequency domains, are often utilized to extract parameters such as SNR, delay spread, and multipath effects.

Recently, ML techniques have emerged as a powerful tool for estimating channel characteristics by learning complex patterns between transmitted and received signals. These data-driven methods offer a promising alternative to conventional techniques, providing more accurate and adaptable estimations

under varying channel conditions. Incorporating ML into channel estimation processes has been shown to improve the robustness and performance of VLC systems, making them more resilient to the dynamic nature of real-world environments.

The use of ML techniques for estimating channel parameters in emerging technologies like VLC has become increasingly vital due to their ability to significantly improve communication system performance. These methods can process large datasets and uncover complex dependencies among variables that affect signal propagation. This subsection presents several prominent ML-based approaches that have shown effectiveness in wireless channel estimation. These range from basic models such as Linear Regression (LR) to more advanced techniques like K-Nearest Neighbors (KNN) and Support Vector Regression (SVR), feedforward neural networks (FNNs) like the Multi-Layer Perceptron (MLP), as well as more complex architectures like Recurrent Neural Networks (RNNs) and their variants—vanilla RNNs, Gated Recurrent Units (GRUs), and Long Short-Term Memory (LSTM) networks. Each technique brings unique strengths, from ease of interpretation to the ability to learn and represent temporal patterns, making them well-suited for optimizing performance in VLC systems.

Linear Regression (LR) is a foundational supervised learning method commonly employed to model the relationship between independent input features and a dependent output variable. It operates under the assumption of linearity between these variables, making it particularly effective for identifying trends and generating initial predictions. LR often serves as a baseline model, providing valuable insights that can guide the development or selection of more advanced ML techniques for deeper analysis (Maulud & Abdulazeez, 2020). However, it suffers from linear bias and underfitting of nonlinear VLC channels and sensitive to scaling.

K-Nearest Neighbors (KNN) is a supervised, non-parametric ML algorithm widely used for both regression and classification tasks. It functions

by assessing the similarity between input data points and their nearest neighbors in the feature space, commonly employing distance measures such as Euclidean, Manhattan, Minkowski, or Hamming distances (Rahman et al., 2024). In regression applications, the output is predicted by averaging the values of the k nearest neighbors, whereas in classification, the label most frequently occurring among those neighbors is assigned to the input (S. Zhang, 2021). The method is non-parametric and simple, but memory-heavy and suffers in high-dimensional/noisy features with latency at inference.

Support Vector Regression (SVR) is a supervised learning method that adapts Support Vector Machines (SVM) for use in both linear and nonlinear regression tasks (Zhou et al., 2021). SVR aims to minimize prediction error by introducing an epsilon-tube around the true output values, within which small deviations are ignored. This approach allows the model to concentrate on larger, more impactful errors rather than attempting to fit every data point precisely. By mapping inputs into higher-dimensional feature spaces, SVR identifies optimal hyperplanes that enable accurate and robust predictions (Yu et al., 2020). However, the performance hinges on kernel and hyper parameters and is prone to high training cost and limited extrapolation.

Multi-Layer Perceptron (MLP) is a feedforward artificial neural network (ANN) model comprising multiple layers of fully connected neurons with nonlinear activation functions—typically including one or more hidden layers between the input and output layers. MLPs excel at learning complex, nonlinear relationships in data, making them highly suitable for modeling intricate channel behaviors in wireless systems. In the context of VLC, particularly for indoor environments, MLP-based models have been shown to estimate signal propagation and REMs with increased accuracy, reduced training sample requirements, and faster inference—making them highly appropriate for real-time channel estimation tasks (Serpi & Politi, 2023). The model is generally strong with understanding complex nonlinearities but is data-hungry, overfits with small datasets, and sensitive for hyperparameter selection.

Recurrent Neural Networks (RNNs) are deep learning models specifically designed to handle sequential data, making them ideal for applications such as language modeling, text generation, speech recognition, time-series forecasting, and video analysis. Their key feature is a built-in memory mechanism that allows previous inputs to influence current outputs, enabling the network to capture temporal patterns and dependencies across sequences (Gizzini & Chafii, 2023). The most basic variant, known as the vanilla RNN (Mao & Sejdić, 2022), performs reasonably well on short sequences where recent inputs primarily determine the output. However, vanilla RNNs are limited in handling long-term dependencies due to the vanishing gradient problem, which hinders the network's ability to preserve and transmit information over longer input sequences.

Another effective RNN variant is the Gated Recurrent Unit (GRU), which employs a streamlined gating mechanism to enhance performance and computational efficiency (Zengeya & Fonou-Dombeu, 2024). GRUs utilize two primary gates: the update gate (z_t) and the reset gate (r_t). These gates control the retention and discarding of information across time steps—where the update gate decides the extent of past information to carry forward, and the reset gate determines how much of the previous state to forget (Lent et al., 2022). This structure allows GRUs to model sequential data efficiently while addressing the limitations of traditional RNNs. This model contains fewer parameters and faster than LSTM but can underperform on tasks needing very long memory, remains susceptible to overfitting and gating saturation, and results are sensitive to sequence length and optimization settings.

To explore channel estimation in ML-driven VLC systems, Jativa et al. (2021) proposed the use of an Extreme Learning Machine (ELM) for both channel estimation and equalization in underground mining VLC deployments. Their ELM-based method, which utilizes single-layer feedforward networks (SLFNs), showed improvements in BER performance. Similarly, Alkandari et al. (2023) investigated the error performance of VLP systems by combining

VLC and indoor positioning techniques for 3D drone localization, using ANN-based ML. Their findings revealed marked improvements in localization accuracy. Du et al. (2021) introduced an ML-based VLP system designed for rapid deployment in Industrial Internet-of-Things (IIoT) environments, employing an XGBoost-based estimator for position prediction. In another study, Razaz et al. (2024) leveraged LSTM to enhance indoor channel estimation in VLC systems. The LSTM-based estimator demonstrated superior performance over the traditional Kalman Filter (KF), achieving more accurate channel estimation and reduced BER. Furthermore, Sharma et al. (2023) proposed an LSTM-driven approach to estimate channels in optical Intelligent Reflecting Surface (IRS) VLC systems with non-linear characteristics. Their results showed that the LSTM-based solution provided better signal detection and system reliability, effectively compensating for distortions in practical VLC scenarios.

Z. Ma et al. (2022) conducted a comparative analysis of three ML algorithms for channel estimation in multi-wavelength VLC systems, with results indicating that Sparse Autoencoders (SAEs) deliver superior performance. Building on this, Ullah et al. (2023) proposed a hybrid Deep Neural Network (DNN) model that integrates an MLP, bidirectional LSTM, and GRU to estimate PL and detect jamming in Vehicular Visible Light Communication (V-VLC) environments. Their hybrid model demonstrated greater accuracy and lower error rates than existing approaches. Similarly, Salama et al. (2022) focused on enhancing channel estimation in indoor VLC systems by reducing the BER. They compared the effectiveness of DNN, YOLO v3, and the KF across three modulation schemes. The results revealed that DNN surpassed KF in performance, and incorporating YOLO v3 further optimized channel estimation compared to conventional techniques. Furthermore, Mitra and Kaddoum (2022) propose the use of Random Fourier Features (RFF)-based ML to address the nonlinearity inherent in VLC channels. Their approach achieves reduced training error and improved classification accuracy, particularly under

conditions with limited data availability. In parallel, Naser et al. (2022) investigates the application of Federated Learning (FL) in VLC systems as a decentralized alternative to traditional centralized ML models. This method effectively tackles issues related to data privacy and system communication overhead, while also emphasizing critical design considerations to bolster robustness and operational efficiency. A comprehensive overview of current ML-driven VLC channel estimation methods is presented in the table below.

Table 2.7 Existing channel estimation machine learning-based VLC comparison.

Ref.	Method	System Model	Machine Learning Improvements
(Jativa et al., 2021)	ELM	VLC-based Underground mining system	Enhances BER in challenging conditions, approaching the performance of perfect CSI and surpassing traditional methods.
(Alkandari et al., 2023)	ANN	3D VLP under industrial channel conditions	Minimizes positioning errors and improves accuracy in smoke-obstructed channels.
(Du et al., 2021)	XGBoost	Indoor VLP for smart trolley localization	Speeds up deployment by reducing training time without compromising positioning accuracy.
(Razaz et al., 2024)	LSTM	Indoor VLC channel	Surpasses Kalman Filter in BER, improving accuracy and system robustness.
(Sharma et al., 2023)	LSTM	IRS-aided non-linear VLC system	LSTM surpasses conventional methods in overall system efficiency.
(Z. Ma et al., 2022)	LSTM, GRU, and Sparse Autoencoders	Multi-wavelength VLC using tricolor LEDs	SAEs outperform other ML algorithms in channel modeling accuracy.
(Ullah et al., 2023)	Hybrid DNN	V-VLC and IEEE 802.11p systems	Surpasses traditional models with improved detection accuracy and lower error rates.

Table 2.7 (Next) Existing channel estimation machine learning-based VLC comparison.

Ref.	Method	System Model	Machine Learning Improvements
(Salama et al., 2022)	DNN, YOLO v3, and Kalman Filter	Indoor VLC with various modulation schemes	DNN substantially lowers BER across all proposed modulation schemes, outperforming the Kalman Filter.
(Mitra & Kaddoum, 2022)	RFF	Nonlinear VLC systems	Reduces training complexity while enhancing accuracy.
(Naser et al., 2022)	FL	VLC network overview by application type	Cuts data transfer costs, enhances privacy, and improves performance.

2.6. ML-BASED POSITION ESTIMATION

Localization has been a crucial concept throughout technological and human history, starting from early techniques like Polynesian navigation, which allowed long-distance voyages across the vast Pacific Ocean for thousands of years. Today, modern localization mainly relies on electronic systems that determine positions through receivers collecting data from satellites or base stations. Recently, location-based services (LBS) have played a significant role in enhancing daily life (Schiller & Voisard, 2004). These technologies, such as the Global Positioning System (GPS), are now ubiquitous, helping with tasks like navigation, object tracking, personal movement monitoring, and creating real-time maps (Bo et al., 2016; H. Chen et al., 2017; Y. Zhang et al., 2009). The use of these technologies spans across multiple sectors, including transportation, portable devices, mining, aviation, and the military, with new applications emerging daily.

While GPS remains the dominant localization technology worldwide, it is well known that GPS has limitations, particularly in indoor environments. The primary issue is that satellite signals are obstructed by building structures like walls and ceilings. This challenge has led to the development of various indoor

positioning systems (IPSs), including WiFi (Zou et al., 2017), ZigBee (Konings et al., 2017), Bluetooth (Huang et al., 2019), ultra-wideband (UWB) (Tiemann et al., 2015), ultrasound (Hazas & Hopper, 2006), and infrared (Santo et al., 2017). These technologies can provide positioning accuracy ranging from centimeters to meters. However, they encounter several challenges. Firstly, wireless positioning technologies are vulnerable to EMI. The complex indoor wireless environment can cause frequency band overlap, leading to interference between technologies like WiFi and UWB. Secondly, there is a trade-off between positioning accuracy and cost. For instance, infrared and ultrasonic technologies can achieve centimeter-level accuracy, but the need for numerous specialized transmitters and receivers results in high deployment costs. These issues hinder the widespread adoption of the aforementioned indoor positioning technologies (Liu et al., 2021).

The emerging visible light positioning (VLP) technology holds significant potential in the positioning field, prompting both academia and industry to pursue further research (Luo et al., 2017; Gu et al., 2016).

VLP systems can generally be classified based on the type of optical receiver used: camera-based or PD-based, as shown in Figure 2.12. Camera-based VLP systems identify luminaires by taking images and decoding the signals they transmit. This approach encompasses several sub-techniques, including image transformation with a single camera, using an additional accelerometer for transformation, employing two lenses and two image sensors, and utilizing a database for image transformation.

Table 2.8 provides a comparison of various indoor positioning technologies (Liu et al., 2021). From the table, it is evident that VLP and radio frequency positioning are similar in terms of cost and power consumption, yet VLP offers positioning accuracy that is 2-20 times higher than RF technology. Moreover, while the accuracy of VLP is comparable to that of ultrasonic and ultra-wideband technologies, its cost is lower. Overall, VLP stands out due to its high accuracy, low deployment cost, and broad applicability. LED-based VLP

technology strikes a balance between positioning accuracy and deployment cost, making it an attractive solution.

Due to the low inter-cell interference in VLC-based systems like VLP (Dowhuszko & Pérez-Neira, 2017), the stability of the communication link improves, making it possible to detect subtle changes in the received optical signal. This results in better activity recognition accuracy compared to RF-based solutions. Additionally, the same infrastructure used for illumination can be repurposed for VLC-based monitoring. VLC technology is also advantageous in environments such as hospitals, where RF systems are prohibited due to electromagnetic compatibility issues.

VLP systems can generally be classified based on the type of optical receiver used: camera-based or PD-based, as shown in Figure 2.12. Camera-based VLP systems identify luminaires by taking images and decoding the signals they transmit. This approach encompasses several sub-techniques, including image transformation with a single camera, using an additional accelerometer for transformation, employing two lenses and two image sensors, and utilizing a database for image transformation.

Table 2.8 Comparison of Indoor positioning technologies (H: High; M: Medium; and L: Low).

Technology	Accuracy (m)	Energy Consumption	Deployment	Cost
Wi-Fi	1 ~ 5	H	M	M
Infra-red	0.1 ~ 2	L	L	M
UWB	0.01 ~ 1	L	L	M
Ultrasound	0.03 ~ 1	L	L	M
Bluetooth	1 ~ 5	L	H	L
ZigBee	1 ~ 10	L	L	M
Visible Light	0.05 ~ 1	L	L	L

Photodetector-based VLP systems, in contrast, detect optical power intensity and convert the RSS into current. Localization in these systems relies on the intensity of the received light signal, with key positioning parameters like RSS. Techniques related to RSS include the use of LEDs with PWM, trilateration, and the fusion of RSS with Inertial Measurement Units (IMU), as well as methods involving spatial beams, light polarization, light splitting properties of convex lenses, encoded projection, shadow and reflection, and ambient light sensors. Another critical parameter is the Angle of Arrival (AOA), which determines the localization by identifying the angle at which the light signal reaches the receiver. AOA is linked with techniques such as light polarization, light splitting properties of convex lenses, encoded projection, shadow and reflection, and ambient light sensors. Finally, Time Difference of Arrival (TDOA) localizes by measuring the time differences of signals arriving from various transmitters, with associated techniques including encoded projection, shadow and reflection, and ambient light sensors.

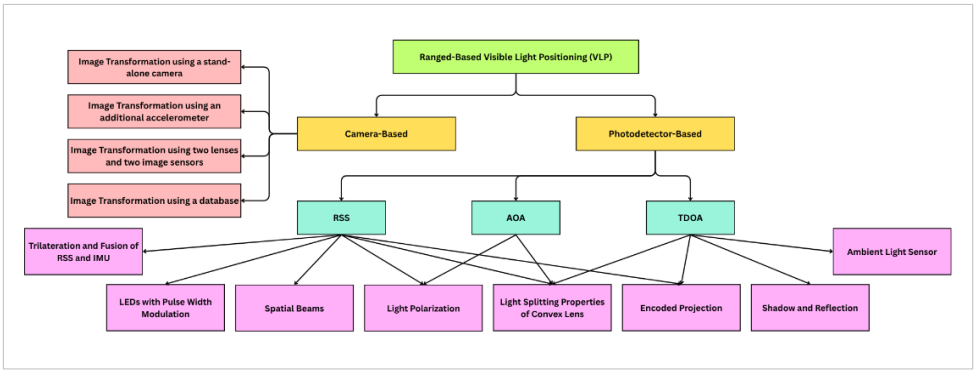

Figure 2.12 Types of LED-Based VLP technologies.

Popular positioning algorithms in VLP include Triangulation, which involves Trilateration and Angulation, Fingerprinting, and Proximity. Triangulation is a localization method based on the geometric properties of triangles. It comprises trilateration and angulation: the former infers ranges from

TOA, TDOA, AOA, or RSS measurements, while the latter estimates position from intersecting direction lines (Lashkari et al., 2018; Zafari et al., 2019). With TOA, the measured transmit–receive time defines a circle centered at each transmitter; in 2D, three or more transmitters are typically required to intersect the corresponding circles. TOA is constrained by short indoor path lengths, roughly 3 meters, which demand fast hardware response and tight time synchronization between transmitter and receiver, making real-time implementation difficult (Khalaf-Allah, 2015). TDOA removes the need for receiver–transmitter synchronization by requiring only inter-transmitter synchronization—feasible when a single controller drives the transmitters—but still relies on resolving small arrival-time differences, which imposes high processing speed on receivers and microcontrollers (Jung et al., 2011; Trong-Hop et al., 2013). As an angulation solution, AOA computes the direction of each transmitter at the receiver and finds the intersection point; it depends on signal features such as RSS or TOA, so it inherits the limitations of the underlying measurement method (Eroglu et al., 2015; Yang et al., 2014). RSS in particular can be unreliable over time due to environmental sensitivity, which complicates accurate localization (Tran & Ha, 2021).

Fingerprint-based scene analysis estimates the receiver's location by matching an online measurement to an offline database of fingerprints; performance scales with the density of the fingerprint map, and more reference points typically yield lower error (Zafari et al., 2019). Common estimators include KNN, SVM, ANN, and probabilistic methods. This approach is widely adopted in LED-based indoor systems because implementation is straightforward and moderate processing capability suffices. However, accuracy depends on receiver/filter quality and environmental stability, since RSS is sensitive to sunlight, artificial lighting, and multipath from surfaces and building structure. A main limitation is the need to collect many reference points—often thousands in large areas—which is labor-intensive and time-consuming. Although recent studies reduce the required survey load, their robustness still

needs validation across hardware platforms and diverse environments (Tran & Ha, 2019, 2021).

Proximity is a positioning method suited to deployments with a dense grid of transmitters at known coordinates. The receiver's location is inferred from which transmitters detect it: with a single detection, the estimate defaults to that transmitter's coordinates; with multiple detections, the estimate is often assigned to the transmitter reporting the strongest signal. Achieving high accuracy therefore requires many transmitters, which may conflict with lighting design and aesthetic constraints in existing buildings (Luo et al., 2017). Proximity methods still rely on signal measurements and thus share several practical limitations with trilateration (e.g., measurement sensitivity and hardware constraints), especially when RSS is used for detection.

Using DIALux to build the simulation, the authors in (S. Song et al., 2021) design an indoor VLP system and apply LR in both simulated and experimental settings to estimate the PD's 2D coordinates. The mean errors—11.1 cm in simulation and 10.5 cm in experiment—are close, showing good agreement. Because the model is posed as a least-squares problem, it is non-iterative, which lowers training time and complexity. When room dimensions and LED luminaire specifications are provided, DIALux produces data suitable for training, thereby reducing data-collection effort.

To locate a PD in 2D, the study (Yuan et al., 2020) fuses Wi-Fi, Bluetooth, and magnetic-field fingerprints through multitask learning (MTL) and then refines the estimate with weighted-coefficients k-nearest neighbors (WCkNN). MTL captures correlations among fingerprint features, while WCkNN adjusts the position within the selected class. A weighted average of candidate locations—using positioning errors as weights—yields an average error of 195 cm. In the same line, DNN-based error-prediction models compute the discrepancy between each projected coordinate and the ground truth. Extending this direction, Tran and Ha (2019) first expand RSS features via kNN and then pass the most informative ones to a RF to cut complexity and computation,

reaching ≈2 cm average accuracy—about five times better than common kNN variants. Notably, high accuracy is maintained even away from the room center, where multipath is strongest, and the method accounts for ambient light, thermal noise, shot noise, and high reflection rates.

X. Li et al. (2018) proposed a three-layer ANN that predicts the PD's 2D coordinates using TDOA features from multiple LEDs. TDOA is used to construct the input features, which are then mapped by the ANN, achieving an average positioning error of 1.66 cm. The approach improves robustness by learning a stable mapping between delay estimates and spatial coordinates. In (Du et al., 2019), an ANN is employed to simplify the otherwise complex trilateration in a 3D VLP setup with LED transmitters and a PD receiver. Compared with conventional trilateration, the ANN-assisted approach reaches 11.93 cm accuracy and is about 50× faster computationally. By framing trilateration as a near-linear mapping, the method reduces problem complexity and speeds up position estimation substantially. Cao et al. (2021) introduce a Memory-augmented ANN (M-ANN) to correct deviations and estimate a PD's 3D position from LED RSS values. A memory module is added to a two-layer ANN to form a recurrent cell, enabling feature extraction over discrete testing moments and limiting large errors during abrupt changes. A Genetic-Algorithm (GA) component imputes missing RSS values when LEDs are blocked. Even in a worst case with two blocked LEDs, the method reports 3.53 cm accuracy. With receiver tilt and angle fixed and known, T. Yuan et al. (2018) present an FNN that extracts features to infer relative distances between a camera-based receiver and the LEDs. Triangulation, together with MPL-based distance mapping, then produces the 2D position, achieving a mean error of 1.9 cm.

In (X. Wang et al., 2019), a deep-learning LSTM model performs indoor localization using smartphone magnetic and light sensors. The model ingests preprocessed bimodal image-like data derived from the sensors to estimate the camera receiver's 2D position. It achieves an average error of 120 cm with computation time under 0.1 s, making it suitable for real-time services. Hsu et

al. (2022) Compare LSTM with LR and a standard ANN for a system using only LED transmitters and a silicon-based solar-cell receiver. The authors find that LSTM gives the highest accuracy. The reported mean percentage error corresponds to 2.9 cm, attributed to better noise suppression and handling of time-varying effects.

Table 2.9 Existing machine learning-based VLP approaches comparison

Ref.	ML Model	VLP Method	Position Error (cm)	Setup/size	Sensor	LED Number
(S. Song et al., 2021)	LR	Fingerprints	11.1	Experiment 2 x 1.5 x 2.7 (m)	PD	4
(Tran & Ha, 2019)	kNN	Fingerprints	2	Simulation 5 x 5 x 3 (m)	PD	4
(Yuan et al., 2020)	WCkNN	Fingerprints	195	Experiment 1.5 x 4.4 x 7.6 (m)	PD	4
(X. Li et al., 2018)	ANN	Trilateration	1.66	Experiment 5 x 5 x 3 (m)	PD	4
(Du et al., 2019)	ANN	Trilateration	11.93	Experiment 1.2 x 1.2 x 2 (m)	PD	3
(Cao et al., 2021)	Memory ANN	Triangulation	3.53	Experiment 0.6 x 0.6 x 0.1 (m)	PD	3
(T. Yuan et al., 2018)	MLP	Proximity	1.9	Simulation 1.3 x 1.3 x 2 (m)	Camera	5
(X. Wang et al., 2019)	DL LSTM	Fingerprints	120	Experiment 8 x 20 (m)	Camera	10
(Hsu et al., 2022)	LSTM	Triangulation	2.9	Experiment 1.3 x 1.3 x 2 (m)	Solar cell	1

Diversity in wireless communication is the utilization of independently faded replicas of the same information over time, frequency, space, or polarization to lower error probability and outage and to stabilize link quality in multipath fading channels. Time diversity interleaves or codes across intervals longer than the channel coherence time; frequency diversity spreads

transmission across subbands wider than the coherence bandwidth (e.g., multicarrier/OFDM); spatial diversity uses multiple antennas at the transmitter and/or receiver; and polarization/angle diversity leverages differently polarized or directed propagation modes, with the received branches combined to maximize reliability. These mechanisms are formalized through combining rules such as selection combining, equal-gain combining, and maximal-ratio combining, which yield quantifiable diversity orders and performance gains against Rayleigh/Rician fading. Their primary applications are reliability enhancement, coverage extension, and throughput gains via reduced retransmissions or adaptive coding, and they underpin modern cellular and local-area systems (Simon & Alouini, 2002).

Spatial diversity employs multiple antennas to create independently faded branches at the transmitter, receiver, or both, and then combines or codes across them to achieve a higher diversity order. In the context of VLC-based MBSNs, spatial diversity is particularly valuable due to the deterministic and directionally constrained nature of optical propagation. In practical healthcare scenarios, where patients exhibit random movement and orientation changes, leveraging spatial diversity ensures that communication is maintained even if one or more links experience blockage or severe attenuation.

Against this background, the main contributions of this paper are briefly outlined below:

- We employ an advanced ray tracing technique, as proposed in (Donmez et al., 2021), to generate CIRs specific to realistic hospital environments. The model integrates user-specific parameters and artificial structures while complying with indoor illumination standards. It also incorporates wavelength-dependent surface reflectance, diffuse and specular reflection components, real light source measurements, and up to 10 orders of reflection.
- We present a Q-learning–based link adaptation scheme tailored for DC-biased Optical Orthogonal Frequency Division Multiplexing

(DCO-OFDM) with Intensity Modulation and Direct Detection (IM/DD) as proposed in (Bayat Rizi et al., 2024). This scheme addresses the dynamic QoS requirements inherent in 6G VLC-enabled healthcare monitoring systems.

- We introduce a robust machine learning algorithm for accurate estimation of PL and RMS delay spread in VLC-based MBSNs. This enhances channel reliability for robust operation in 6G-enabled healthcare applications.
- We propose a robust ML-based algorithm for estimating position in VLC-based MBSNs using Bayesian hyperparameter optimization by focusing on spatial diversity to enhance connection reliability in 6G health monitoring networks in case of blocking the signal of one or more sensors.

CHAPTER 3

3. METHODOLOGY

3.1. CHANNEL MODEL FOR VLC-BASED MBSNS

The proposed approach adopts a site-specific channel modeling technique based on non-sequential ray tracing, where rays propagate freely throughout the environment and interact with objects through absorption, reflection, and scattering at each encounter. Zemax® software is utilized for this purpose, as it enables simulation of more than 10 reflections in non-sequential mode to accurately generate the CIR tailored to the specific environment. The core steps involved in this VLC-based MBSNs channel modeling process are depicted in Figure 3.1.

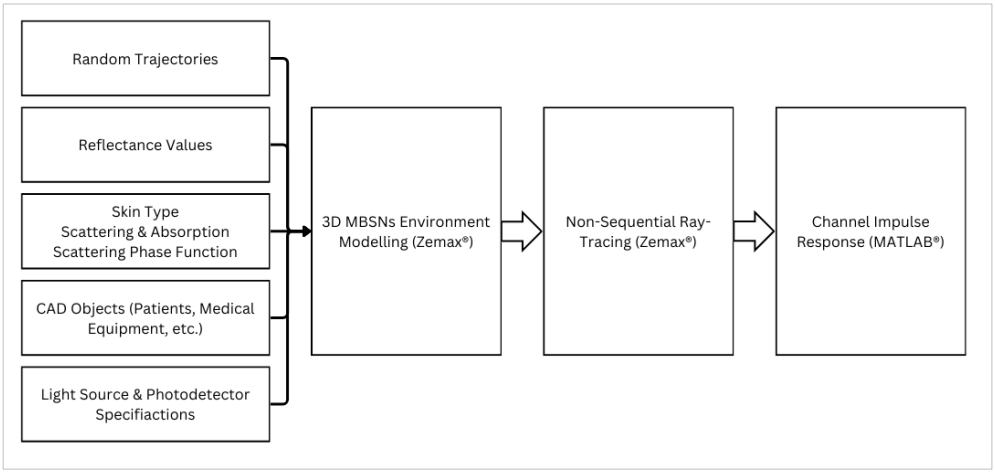

Figure 3.1 Main steps of site-specific channel modeling for VLC-based MBSNs.

In MBSN systems, on-body sensor nodes are constrained by limited power and compact form factors, necessitating low-complexity designs. As a result, the system model—depicted in Figure 3.2 —assigns the task of modulation order selection to the transmitter side to reduce the computational burden on the sensor nodes.

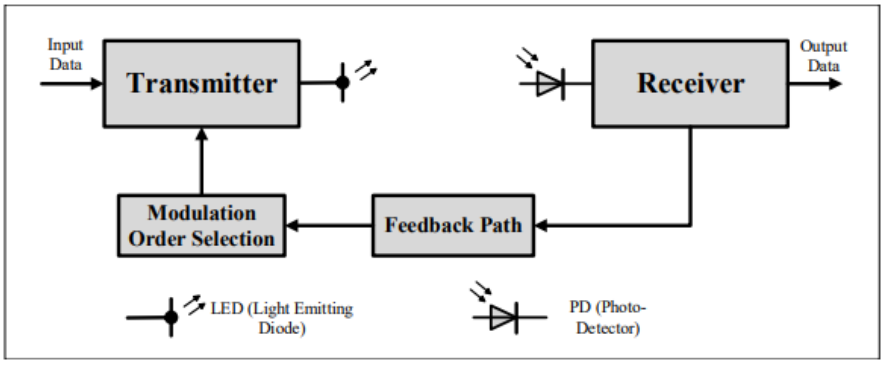

Figure 3.2 VLC-based Adaptive Modulation MBSNs system model.

M-ary Pulse Amplitude Modulation (PAM) is employed in this VLC system, using a realistic CIR expressed as (Ghassemlooy et al., 2017).

$$s(t) = 2P_{avg} \sum_{i} m_i p(t - iT) \tag{3.1}$$

where $s(t)$ is the modulated signal, P_{avg} denotes the average optical power, $m_i \in \{m/(M-1) | m = 0, 1, \ldots, M-1\}$ is the amplitude of the i_{th} symbol, $p(t)$ is the pulse shape with $T^{-1} \int p(t)dt = 1$ and $p(t) = 0$ for $t \notin [0, T]$, and T is the symbol duration.

The modulated optical signal, denoted by $s(t)$, is transmitted through the VLC channel. The corresponding received signal at the PD can be represented as follows:

$$r(t) = s(t) * h(t) + n(t) \tag{3.2}$$

where $n(t)$ accounts for noise contributions, including background interference and shot noise, assumed to follow a white Gaussian distribution. The CIR is represented by $h(t)$, and is modeled as:

$$h(t) = \sum_{k=1}^{M} P_k \delta(t - t_k) \tag{3.3}$$

where P_k represents the gain of the k^{th} ray, t_k represents the travel duration of the k^{th} ray, and M represents the total number of collected rays. The received photocurrent at the output of the PD is obtained as follows.

$$I(t) = \sum_{k=1}^{K} P_k s(t - t_k) + n(t) \tag{3.4}$$

$$= \sum_{i} 2RP_{avg} m_i \sum_{k=1}^{K} P_k p(t - iT - \tau_k) + n(t) \tag{3.5}$$

In this context, R represents the responsivity of the PDs. Since no universal analytical model exists for accurately describing indoor VLC channels, simulating the channel under specific environmental conditions becomes necessary. To address this, Donmez and Miramirkhani (2021) employed a site-specific, non-sequential ray tracing method to simulate two distinct hospital scenarios.

As illustrated in Figure 2.10 , three PDs are positioned on the patient's shoulder, wrist, and ankle in both the ICU ward and FTPR scenarios. The patient's movement follows random trajectories, and the corresponding CIR for each PD is simulated based on these paths. The goal is to maximize throughput while ensuring that the symbol error rate (SER) remains within a predefined threshold throughout the movement. To achieve this, the order of PAM is adaptively selected. Consequently, the adaptive modulation optimization problem is formulated as follows.

$$\arg\max \mu \in I \{R\mu : SER\mu \leq SER_{tar}\} \tag{3.6}$$

Here, R_μ denotes the throughput corresponding to a given modulation order μ. The set I represents all available modulation orders under consideration. SER_μ is the instantaneous SER associated with modulation order, and SER_{tar} defines the target or maximum permissible SER.

The key challenge in solving the optimization problem described in equation (3.6) lies in the discrete nature of the modulation order μ, which can only assume specific values from the finite set $I = \{2, 4, \ldots, 64\}$. This constraint transforms the optimization task into a combinatorial problem, necessitating a search within a discrete action space. Although the action set is finite, conducting a full exhaustive search is impractical for on-body sensor nodes, which are subject to strict limitations in both computational power and energy resources.

Furthermore, the SER_μ is a complex, nonlinear function of both the instantaneous CIR $h(t)$ and the received SNR ρ, both of which are subject to continuous variation due to patient movement, body shadowing, and multipath propagation in indoor medical settings. Since closed-form analytical expressions for BER or throughput under the ray-traced VLC channel model in (Donmez & Miramirkhani, 2021) do not exist, the feasible set $\{\mu : SER_\mu \leq SER_{tar}\}$ becomes non-convex and must be computed numerically.

These characteristics render traditional convex optimization and gradient-based methods ineffective. Therefore, a model-free, lightweight decision-making strategy is required—one that can adapt in real time while meeting stringent power and latency constraints of MBSN devices.

A VLC-based MBSNs channel is typically described by its DC channel gain, which quantifies the steady-state component of the received optical power. This DC gain is defined as:

$$H_0 = \int_0^{+\infty} h(t)dt \tag{3.7}$$

Then, the PL is then computed by

$$PL = -10 \log_{10} H_0 \tag{3.8}$$

Another key characteristic of the VLC-based MBSNs channel is the RMS delay spread, which quantifies the temporal dispersion of the received signal due to multipath propagation. It is defined as the standard deviation of the delays and is given by:

$$\tau_{RMS} = \sqrt{\frac{\int_0^{+\infty} (t - \tau_0)^2 h(t) dt}{\int_0^{+\infty} h(t) dt}} \tag{3.9}$$

where τ_0 is the mean delay spread.

$$\tau_0 = \frac{\int_0^{+\infty} t\, h(t) dt}{\int_0^{+\infty} h(t) dt} \tag{3.10}$$

In each scenario, a set of 20 unique random trajectories is produced, where every trajectory comprises 10 sequential spatial locations. Each path begins from a randomly chosen starting point, and subsequent positions are determined using randomly selected step lengths and direction angles ϕ, drawn from a uniform distribution. The user follows this path step by step, as outlined by Donmez and Miramirkhani (2021). The simulation space is defined by its width A and length B, along with a constraint matrix $\mathrm{C}_{2\times2}$ that delineates the boundaries of permissible movement within the hospital environment. The full set of coordinates for the 10 points in each trajectory is stored in a matrix $\mathrm{D}_{10\times2}$. A validation step is conducted for each coordinate to ensure it remains within the designated movement zone. Once all valid trajectories are established, the CIR is calculated at each location for the three PD placements: D1 on the shoulder, D2 on the wrist, and D3 on the ankle.

From the obtained CIRs, the corresponding PL and RMS delay spread values are derived. These results are then illustrated using histograms and best-fit distributions for all three PD placements across both ICU ward and FTPR scenarios. The random trajectory generation process is formally outlined in the algorithm below. FTPR. The random trajectory generator algorithm is outlined below.

Algorithm 1: Random Trajectory Generator

Initiate:
A, B, $\mathbf{C}$, $0.3 \leq s \leq 0.6$, $0 \leq \phi \leq 2\pi$, and $\mathbf{D}$;
Generation of the starting point:
x_1 =rand($[0, A], 1$); y_1 =rand($[0, B], 1$);
$\mathbf{D}(1, :) = [x_1, y_1]$;
Generation of the remaining points:
for m=2← 10 **do**
s =rand($[0.3, 0.6], 1$);
ϕ =rand($[0, 2\pi], 1$);
$\mathbf{D}(m, :) =$
$[\mathbf{D}(m-1, 1) + s \cdot cos(\phi), \mathbf{D}(m-1, 2) + s \cdot sin(\phi)]$;
Check overlapping with objects:
for n=1← 10 **do**
if $\mathbf{C}(1, 1) \leq \mathbf{D}(n, 1) \leq \mathbf{C}(1, 2)$ & $\mathbf{C}(2, 1) \leq \mathbf{D}(n, 2) \leq \mathbf{C}(2, 2)$ **then**
print Successfully done.
else
print Regenerate.
return $\mathbf{D}$

3.2. DYNAMIC OPTICAL COMMUNICATION STRATEGIES FOR ADAPTIVE MODULATION IN VLC-BASED MEDICAL BODY SENSOR NETWORKS

Given the highly variable and unpredictable nature of VLC-based MBSNs, adaptive modulation becomes a complex task that aligns well with the principles of reinforcement learning (RL). This section begins with a concise overview of RL, then delves into the proposed adaptive modulation strategy utilizing a Q-learning framework.

3.2.1. Reinforcement Learning-based Adaptive Modulation

Reinforcement Learning (RL) is a machine learning paradigm focused on the dynamic interaction between an agent and its environment. The agent aims to discover an optimal policy by taking sequential actions that maximize its long-term cumulative reward. Unlike supervised learning, which relies on a complete set of labeled data, RL allows the agent to learn through experiential trial and error, without requiring prior knowledge or labeled examples of the environment's behavior.

Q-learning is a prominent RL algorithm developed to address Markov Decision Processes (MDPs). To fully understand Q-learning, it's essential to define its core elements. The state space, S, includes all possible states s that the agent can observe within the environment. The action space, A, consists of the set of all possible actions a that the agent may take in each state. The immediate reward function, $r(s,a)$, specifies the reward the agent receives directly after executing action a in state s. The policy, $\pi(s)$, governs the decision-making process by determining which action the agent selects for a given state. The Q-function, $Q(s,a)$, estimates the expected cumulative discounted reward when taking action a in state s, following a given policy. In Q-learning, the values of $Q(s,a)$ are iteratively updated using the following mechanism.

$$Q(s,a) \leftarrow Q(s,a) + \alpha \left[r(s,a) + \gamma \max_{a' \in A, s' \in S} Q(s',a') - Q(s,a) \right] \quad (3.11)$$

Where $\alpha \in [0,1]$, $\gamma \in [0,1]$, s', a' denote the learning rate, discount factor, next state, and possible actions, respectively. Q-learning is utilized to derive an optimal policy that maximizes the expected total reward over time as follows.

$$\pi^*(s) = \arg\max_{a \in A} Q(s,a) \quad (3.12)$$

A commonly used method to balance exploration and exploitation is the ϵ-greedy strategy (Sutton & Barto, 2018).

3.2.2. Q-Learning-based Adaptive Modulation

In the adaptive modulation optimization problem, the state space is initially defined by the tuple (H_0, ρ), where ρ denotes the quantized received SNR The action space comprises the set of selectable modulation orders. When the agent chooses a modulation order corresponding to a specific channel state, it triggers a transition to a new state within this predefined state space.

This scenario can be modeled as an MDP and addressed using the Q-learning algorithm. As illustrated in Figure 3.3, changes in state occur due to both patient movement and the agent's actions.

In the proposed model, state transitions within the MDP for Q-learning-based adaptive modulation are driven solely by the agent's actions at the current CIR, without accounting for changes induced by human movement. Since patient motion is relatively slow, the agent has adequate time to explore each state. Once training is complete, the agent selects the appropriate modulation order based on initial channel observations.

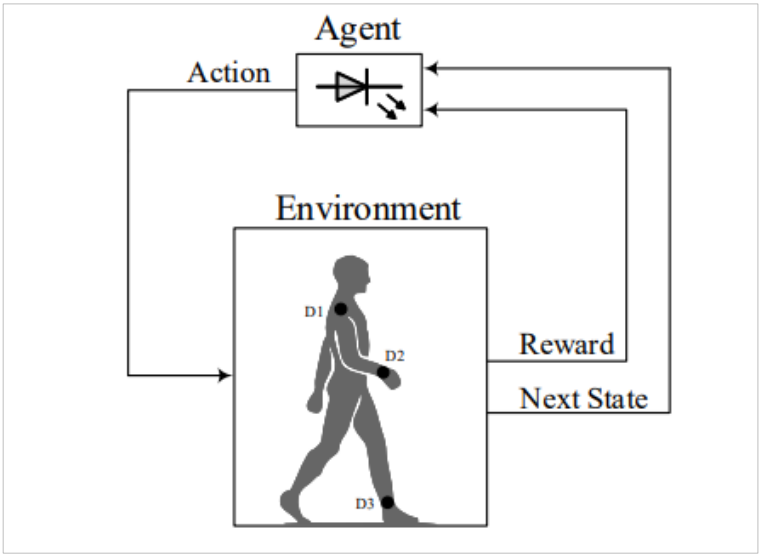

Figure 3.3 Reinforcement learning model of VLC-based MBSNs adaptive modulation.

The received SNR is defined as follows.

$$\rho = \frac{P}{\sigma_n^2} |H_0|^2 \tag{3.13}$$

where P is the transmitted optical power, σ^2 is the noise power, and H_0 is the channel DC-gain given by

$$H_0 = \int_0^{+\infty} h(t)dt = \sum_{k=1}^{M} P_k \tag{3.14}$$

where P_k and M are defined in equation ((3.3).

The reward function, denoted by $r(s,a)$, is defined as the achieved throughput when performing action a in state s within the environment and is expressed by.

$$r(s,a) = \begin{cases} \log_2(\mu)\big(1 - SER_\mu\big), & \text{if } SER_\mu \leq SER_{tar} \\ -SER_\mu, & \text{if } SER_\mu > SER_{tar} \end{cases} \tag{3.15}$$

where SER_{tar} denotes the target SER that must be met. To support exploration, the ϵ-greedy strategy is applied by initially assigning a relatively high value to ϵ. This allows the agent to take random actions early in the learning process, helping it better understand the environment. As learning advances, the value of ϵ is gradually reduced, guiding the agent to increasingly depend on the learned policy. A summary of the proposed Q-learning-based adaptive modulation approach is provided in Algorithm 2.

Algorithm 2: Q-learning-based Adaptive Modulation for VLC-based MBSN

Data: Indicate $[h_n, \rho_t]$ as s_t and PAM modulation orders as a_t

Input : Environment and Q-learning parameters (α, γ,S,A, min ϵ as le, n)

Output: Optimal Q-values $Q(s_t, a_t)$

Initialize $Q(s_t, a_t)$ with random values or with 0 $\forall s \in S, a \in A$;

while *true* **do**

- Observe the MBSNs channel and calculate and quantize DC-gain as h_n;
- calculate s_t;
- **while** *n is constant* **do**
  - **if** *t is a multiple of 10* **then**
    - Reduce ϵ with coefficient n;
    - $\epsilon = \max(\epsilon, \text{le})$;
  - **if** *rand(0,1)* $< \epsilon$ **then**
    - Choose $a_t \in A$ randomly;
  - **else**
    - $a_t = \text{argmax}_a\ Q(s_t, a)$;
  - The transmitter sends the modulated signal to the receiver;
  - Receive feedback ρ_{t+1} and quantized $\text{SNR}_{r_{t+1}}$;
  - $s_{t+1} = [h_n, \rho_{t+1}]$;
  - Calculate reward as $r(s_t, a_t)$ based on Eq. 9
  - $Q(s_t, a_t) = (1 - \alpha)Q(s_t, a_t) + \alpha[r(s_t, a_t) + \gamma \max_{a'}\ Q(s_{t+1}, a')]$;
  - Update s_t with s_{t+1};

End

3.3. ROBUST PATH LOSS AND RMS DELAY SPREAD ESTIMATION ALGORITHMS FOR RELIABLE VLC COMMUNICATION IN 6G HEALTH MONITORING NETWORKS

Comprehensive simulation results reported in (Donmez & Miramirkhani, 2022) indicate that the log-normal distribution closely matches the PL histograms, as illustrated by

$$f(PL) = \frac{1}{PL\sigma\sqrt{2\pi}} \exp\left(-\frac{(\ln(PL) - \mu)^2}{2\sigma^2}\right) \tag{3.16}$$

Here, μ and σ represent the location and scale parameters of the log-normal distribution, respectively. Likewise, extensive simulations in (Donmez & Miramirkhani, 2022) confirmed that the log-normal distribution effectively fits the RMS delay spread histograms, as shown below.

$$f(\tau_{RMS}) = \frac{1}{\tau_{RMS}\sigma\sqrt{2\pi}} \exp\left(-\frac{(\ln(\tau_{RMS}) - \mu)^2}{2\sigma^2}\right) \tag{3.17}$$

where μ and σ denote location and scale parameters, respectively.

Long Short-Term Memory is a specialized form of Recurrent Neural Network that includes an input gate $i^{(t)}$, forget gate $f^{(t)}$, cell gate $c^{(t)}$, and output gate $o^{(t)}$ (Guo et al., 2019). This architecture enables the prediction of user mobility along random paths without requiring prior knowledge of the sample points. The overall structure is depicted in Figure 3.4. Additionally, unlike conventional techniques, LSTM can effectively manage complex and dynamic propagation environments, offering improved accuracy, adaptability, and performance (Van Houdt et al., 2020). The algorithm begins by updating the block input based on the current input $x^{(t)}$ and the previous LSTM output $y^{(t-1)}$, as follows.

$$z^{(t)} = g\left(W_z x^{(t)} + R_z y^{(t-1)} + b_z\right) \tag{3.18}$$

where W_z, R_z, and b_z are the weights with the input, output, and the bias weight vector, respectively. The predicted output is obtained by combining the current cell state with the output gate, as expressed below.

$$y^{(t)} = g\left(c^{(t)}\right) \odot o^{(t)} \tag{3.19}$$

where $\odot$ is the point-wise multiplication of two vectors along with $g(x) = \tanh(x)$. The detailed procedure is presented in Algorithm 3, which computes the gradients required to update the weights associated with each gate.

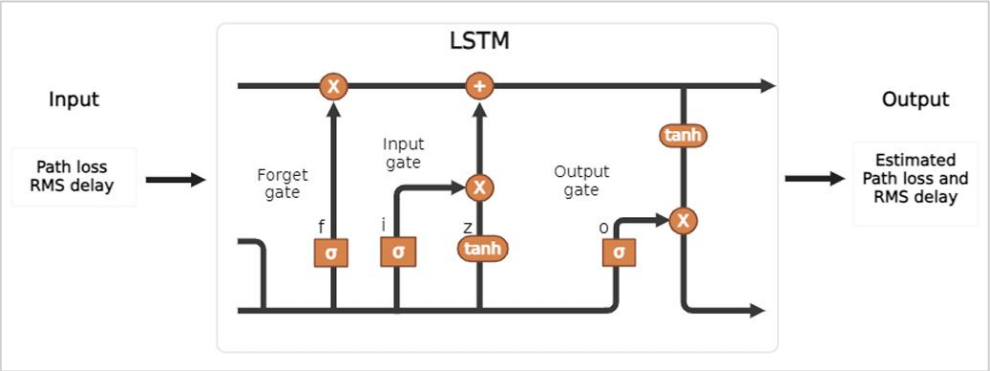

Figure 3.4 LSTM architecture to estimate PL and τ_{RMS} of VLC-based MBSNs.

Root Mean Squared Error (RMSE) was utilized as the loss function to evaluate the performance of the ML-based system. RMSE is commonly used in VLC-based MBSNs due to its effectiveness in measuring the accuracy of estimated channel parameters like PL and RMS delay spread. By emphasizing deviations in the predicted values, RMSE offers valuable feedback on how accurately the system reflects real-world behavior. The RMSE is defined mathematically as follows:

$$\text{RMSE} = \left(\frac{1}{n} \sum_{j=1}^{n} \left(y_j - \hat{y}_j \right)^2 \right)^{1/2} \tag{3.20}$$

where y_j, $\hat{y}_j$, and n represent the actual data, estimated data, and number of data points, respectively.

Moreover, PL and RMS delay spread were utilized as input features for training the LSTM model. The dataset was partitioned into 80% for training and 20% for validation purposes. To enhance the model's training consistency and overall performance, data normalization was applied during the preprocessing stage. The LSTM network architecture featured a hidden layer with 55 neurons, selected to provide an effective trade-off between computational complexity and the capacity to learn temporal patterns. To mitigate the risk of overfitting, a dropout layer with a dropout rate of 0.4 was incorporated, followed by a fully

connected layer and a regression output layer designed to generate continuous-valued predictions. The training process employed the Adam optimizer, which offers advantages in convergence speed, training efficiency, and model generalization. A total of 400 training epochs were conducted to ensure adequate model learning. These settings were guided by established ML practices in VLC applications, reflecting their suitability for realistic deployment scenarios as illustrated by Shu et al. (2024). Additional LSTM design details are provided in Table 3.1.

Table 3.1 LSTM Architecture Parameters.

Parameter	Specification
Optimizer	ADAM
Number of iterations	800
Learning Rate	0.01
Number of Epochs	400
Number of Hidden units for LSTM layer	55

To evaluate the time complexity of the proposed LSTM model, let B denote the effective batch size, H the number of hidden units, and F the number of input features. The overall computational cost per iteration can be approximated as $O(BH(F + H))$.

Algorithm 3: ML-based Path Loss and RMS Delay Spread Estimation for VLC-based MBSNs

Data: Path loss (PL), and RMS delay spread (τ_{RMS})
Input : PL and τ_{RMS}
Output: Obtain the estimated $\hat{PL}$, and $\tau_{\hat{RMS}}$
while *true* **do**
    Pass PL and τ_{RMS} through ML gates
    while *In block input* $z^{(t)}$ **do**
        Update the block input based on the current information $x^{(t)}$ and previous output $y^{(t-1)}$
    while *In the input gate* $i^{(t)}$ **do**
        Revise $x^{(t)}$,$y^{(t-1)}$ and the previous cell value $c^{(t-1)}$
    while *In forget gate* $f^{(t)}$ **do**
        Decide which information should be removed using $x^{(t)}$,$y^{(t-1)}$ and $c^{(t-1)}$
    while *In the cell gate* $c^{(t)}$ **do**
        Compute $c^{(t)}$ based on $z^{(t)}$,$i^{(t)}$, $c^{(t-1)}$, and $f^{(t)}$
    while *In the output gate* $o^{(t)}$ **do**
        Calculate $o^{(t)}$ by $x^{(t)}$,$y^{(t-1)}$ and $c^{(t)}$
    while *In the block output* $y^{(t)}$ **do**
        Predict $y^{(t)}$ based on, g($c^{(t)}$), along with $o^{(t)}$
Modify each gate weights and estimate $\hat{PL}$, and $\tau_{\hat{RMS}}$
End

3.4. RELIABLE POSITION ESTIMATION ALGORITHM FOR ENHANCED 6G HEALTH MONITORING APPLICATIONS

The position estimation framework for VLC-based MBSNs employs a comprehensive machine learning pipeline designed to predict spatial coordinates from channel impulse response features. The methodology encompasses data preprocessing, model development, hyperparameter optimization, and performance evaluation stages to ensure robust and accurate position estimation in dynamic healthcare environments.

The dataset comprises position coordinates and corresponding channel features extracted from the VLC CIRs obtained from the extensive simulations conducted by Donmez et al. (2022). Position data consists of two-dimensional coordinates (x, y) representing the spatial location of body-mounted sensors within the hospital environment, while the feature vector includes two, four, or six channel parameters, namely PL and RMS delay spread, derived from the CIR measurements. Further details about the dataset are shown in the table below.

Table 3.2 Dataset statistics

Scenario	Type	Variable	Unit	Number of data points	Min	Max	Mean	Std
FTPR	Feature	PL_D1	dB	200	61.3	66.2	63.07	0.78
		PL_D2			61.6	65.1	63.23	0.75
		PL_D3			64	70	67	1.12
		RMS_D1	ns		6.96	10.61	8.65	0.57
		RMS_D2			7.03	10.17	8.57	0.64
		RMS_D3			6.21	10.04	7.96	0.77
	Target	X	mm		-2780	527	-1098.01	661.18
		Y			-1534	-464	-1015.39	265.33
ICU	Feature	PL_D1	dB	200	63.1	71.59	66.95	1.76
		PL_D2			64	70	66.64	1.17
		PL_D3			66	71.8	69.09	1.17
		RMS_D1	ns		9.06	14.22	11.9	1.14
		RMS_D2			9.02	14.11	11.85	1
		RMS_D3			8.94	14.09	11.31	0.89
	Target	X	mm		-1707	4906	1710.215	1625.97
		Y			-2803	218	-1236.97	659.54

Let $X_t \in \mathbb{R}^F$ denote the feature vector at discrete time index t with F features per observation (e.g., PL and RMS delay spread from one, two, or three PDs), and let $\boldsymbol{y}_t = [x_t, y_t]^\top \in \mathbb{R}^2$ be the corresponding position in millimeters. To exploit short-term dynamics, a sliding window of length L is applied to form supervised pairs

$$\left(\boldsymbol{X}_i^{(L)}, \boldsymbol{y_i}\right), \text{ with } \boldsymbol{X}_i^{(L)} = [X_i, X_{i+1}, \dots, X_{i+L-1}], \boldsymbol{y_i} = \boldsymbol{y_{i+L-1}} \quad (3.21)$$

Where i is the starting index of the window and L is the sequence length. $\boldsymbol{y_i} = \boldsymbol{y_{i+L-1}}$ indicates that the sequence predicts the position at the final time step. The learning algorithm is model-agnostic and maps each $(L \times F)$ window to a 2D position estimate via a parametric function g_θ, so that $\widehat{\boldsymbol{y}}_i = g_\theta\left(\boldsymbol{X}_i^{(L)}\right)$, where θ collects all trainable or tunable parameters of the chosen estimator (e.g., weights of a neural network or kernel and margin parameters of a support vector regressor)

Pre-processing is performed within each training fold to preclude Normalization bleed. For each feature dimension $f \in \{1, \dots, F\}$, the training-fold mean μ_f and standard deviation σ_f are computed, and both training and out-of-sample set windows are standardized by

$$\tilde{X}^{(f)} = \frac{X^{(f)} - \mu_f}{\sigma_f} \quad (3.22)$$

Where $X^{(f)}$ and $\tilde{X}^{(f)}$ are the raw and standardized values of feature f, respectively, and μ_f, σ_f are estimated only from the training portion. The targets are also standardized per fold via $\tilde{\boldsymbol{y}} = \left(\boldsymbol{y} - \boldsymbol{\mu}_y\right) \oslash \boldsymbol{\sigma}_y$, where $\mu_y \in \mathbb{R}^2$ and $\sigma_y \in \mathbb{R}^2$ are the training-fold mean and standard deviation of the $[x, y]$ coordinates and $\oslash$ denotes elementwise division. At inference time, $\tilde{\boldsymbol{y}}$ is mapped back to the original scale using the same $\boldsymbol{\mu}_y$ and $\boldsymbol{\sigma}_y$. The split is chosen to be train/validation/test as 64/16/20. Since for each scenario there is only 200 data points, validation test was slightly reduced to let model train on more data.

Evaluation follows a blocked K-fold cross-validation approach. Let N be the number of time steps in the original stream; the index set $\{1, \dots, N\}$ is

partitioned into K contiguous blocks of comparable size, and at fold k one block is used for testing while the remaining past data form the pool for training and validation. Within each training fold, a contiguous validation slice comprising a proportion $\alpha \in (0, 1)$ of the available training windows is reserved to monitor generalization and to enable early stopping with a patience of P epochs; her α is the validation proportion and P is the maximum number of epochs without improvement before training is halted.

A single objective selects hyperparameters by minimizing, over K-fold cross-validation, the average loss computed per fold as RMSE plus a variance penalty that quantifies the mismatch between the prediction spread and the data spread. To measure the Euclidean RMSE, per axis RMSE is normalized and computed as

$$\mathrm{NMRSE}_x = \frac{\sqrt{\frac{1}{M}\sum_{j=1}^{M}\left(x_j - \hat{x}_j\right)^2}}{\sigma_x} \tag{3.23}$$

$$\mathrm{NMRSE}_y = \frac{\sqrt{\frac{1}{M}\sum_{j=1}^{M}\left(y_j - \hat{y}_j\right)^2}}{\sigma_y} \tag{3.24}$$

Here $M$is the number of test samples in the fold; x_j and y_j are the true coordinates at sample j; $\hat{x}_j$ and $\hat{y}_j$ are the corresponding predictions; and σ_x and σ_y are the empirical standard deviations of $\{x_j\}_{j=1}^{M}$ and $\{y_j\}_{j=1}^{M}$, respectively. The aggregate normalized error is then

$$\mathrm{NMRSE} = \sqrt{\frac{(\mathrm{NMRSE}_x)^2 + \left(\mathrm{NMRSE}_y\right)^2}{2}} \tag{3.25}$$

Calibration is encouraged via a variance-matching penalty that compares the prediction spread with the empirical spread on the same fold. Denote by $\hat{\sigma}_x = \mathrm{std}\left(\{x_j\}_{j=1}^{M}\right)$ and $\hat{\sigma}_y = \mathrm{std}\left(\{y_j\}_{j=1}^{M}\right)$ the prediction standard deviations. The penalty is defined as

$$\mathcal{V} = \frac{1}{2}\left[\left(1 - \frac{\hat{\sigma}_x}{\sigma_x}\right)^2 + \left(1 - \frac{\hat{\sigma}_y}{\sigma_y}\right)^2\right] \tag{3.26}$$

and the objective used by Bayesian optimization is

$$\mathcal{L} = \mathrm{NMRSE} \cdot (1 + \omega_{var}\, \mathcal{V}) \tag{3.27}$$

Where $\omega_{var} \geq 0$ is the weighting assigned to calibration. Each candidate configuration is trained within the fold, and the fold objectives are averaged for selection. Hyperparameter search uses a surrogate-based acquisition strategy; the specific ranges for sequence length, depth, width, regularization and optimization settings are summarized in Table 3.3.

Table 3.3 Search Space of Sensor configuration-dependent parameters.

ML model	Hyperparameter	Search Space
LSTM	Number of LSTM Layers	[1, 3]
	Number of Hidden Units	[32, 128]
	Dropout Rate	[0.3, 0.7]
	Learning Rate	[10^{-4}, 10^{-1}]
	L2 Regularization	[10^{-5}, 10^{-1}]
	Batch Size	[8, 32]
	Sequence Length	[2, 10]
GRU	Number of GRU Layers	[1, 3]
	Number of Hidden Units	[32, 128]
	Dropout Rate	[0.3, 0.7]
	Learning Rate	[10^{-4}, 10^{-1}]
	L2 Regularization	[10^{-5}, 10^{-1}]
	Batch Size	[8, 32]
	Sequence Length	[2, 10]
RNN	Number of RNN Layers	[1, 3]
	Number of Hidden Units	[32, 128]
	Dropout Rate	[0.3, 0.7]
	Learning Rate	[10^{-4}, 10^{-1}]
	L2 Regularization	[10^{-5}, 10^{-1}]
	Batch Size	[8, 32]
	Sequence Length	[2, 10]
MLP	Number of MLP Layers	[1, 3]
	Number of Hidden Units	[32, 128]
	Dropout Rate	[0.3, 0.7]
	Learning Rate	[10^{-4}, 10^{-1}]
	L2 Regularization	[10^{-5}, 10^{-1}]
	Batch Size	[8, 32]
	Sequence Length	[2, 10]

Table 3.3 (Next) Search Space of Sensor configuration-dependent parameters.

ML model	Hyperparameter	Search Space
KNN	Number of Neighbors	[2, 5]
	Distance Metric	[Euclidean, City block, Cosine, Correlation]
	Distance Weight	[Equal, Inverse, Squared inverse]
	Local Regression Regularization	$[10^{-6}, 1]$
LR	Alpha	[0.1, 0.9]
	Lambda	$[10^{-5}, 10^{-1}]$
SVR	Kernel Function	[Linear, Gaussian, RBF, Polynomial]
	Box Constraint	$[10^{-1}, 10^{4}]$
	Epsilon	$[10^{-4}, 1]$

Because the selected estimator is a multilayer perceptron acting on flattened windows, the mapping $\hat{\boldsymbol{y}} = g_\theta\left(\boldsymbol{X}^{(L)}\right)$ specializes to a composition of affine maps and pointwise nonlinearities. If the hidden width of the first layer is h_{base} and the network has d hidden layers, a pyramidal topology is adopted whereby the width of hidden layer $i \in \{1, \ldots, d\}$ is

$$h_i = \max\left(8, \left\lfloor \frac{h_{base}}{2^{i-1}} \right\rfloor\right) \tag{3.28}$$

So that the representation gradually contracts toward the regression head.

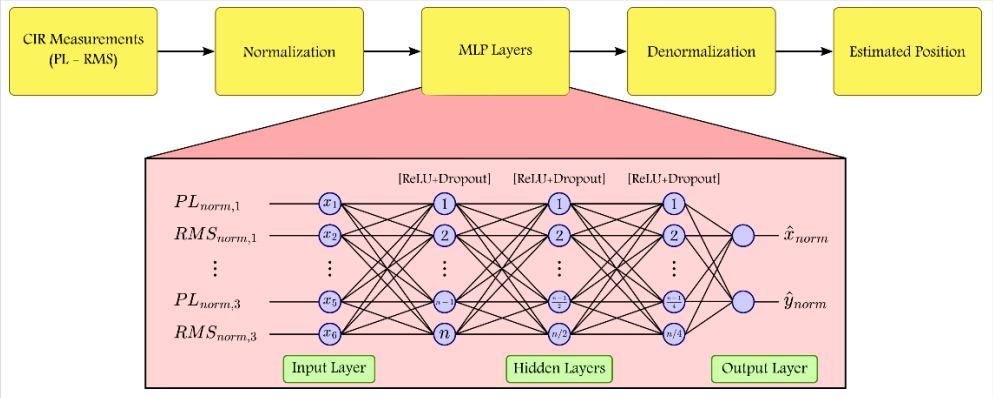

Figure 3.5 System Architecture for MLP-Based Position estimation in VLC-Based MBSNs.

With ReLU activations $\Phi(z) = \max\{z, 0\}$ at each hidden layer, the model takes the form

$$f_1 = \Phi(W_1 \boldsymbol{z} + b_1) \tag{3.29}$$

$$f_i = \Phi(W_i f_{i-1} + b_i) \tag{3.30}$$

$$\hat{\boldsymbol{y}} = W_{d+1} f_d + b_{d+1} \tag{3.31}$$

Where $\boldsymbol{z} \in \mathbb{R}^{LF}$ is the vectorized $L \times F$ window, W_i and b_i are the weight matrices and bias vectors with $i = 2, \ldots, d$, and $\hat{\boldsymbol{y}} \in \mathbb{R}^2$ is the predicted position. Dropout with rate $\delta \in [0,1]$ is applied after each hidden layer during training to regularize the estimator, and ℓ_2 weight decay with coefficient $\beta \geq 0$ is included in the optimization objective. Adam with initial step size $\eta > 0$ and a piecewise decay schedule is used to minimize the training loss on standardized inputs and standardized targets, and early stopping with patience P is triggered based on a contiguous validation slice from the training fold. The cross-validation method remains blocked in time to avoid overlap between training and test windows; all standardization statistics are computed on the training portion and then applied to validation and test data to prevent leakage. Figure 3.5 demonstrates the proposed system architecture using MLP for position estimation in VLC-Based MBSNs. The hyperparameter optimization approach is illustrated in Algorithm 4. Also, Algorithm 5 shows the methodology of the optimized models.

Algorithm 4 Bayesian Hyperparameter Optimization for MLP-Driven VLC-Based MBSNs Position Estimation

Input: Features $\{PL_i, RMS_i\}$ where $i \in \mathcal{F}$
$\mathcal{F} \in \{\{1\},\{2\},\{3\},\{1,2\},\{1,3\},\{2,3\},\{1,2,3\}\}$
Positions $\mathbf{Y} \in \mathbb{R}^{n\times 2}$, folds $K = 5$
Variance weight $w_{var} = 1.0$, seed $s = 100$
Output: Optimal hyperparameters θ^*

Initialize search space Θ:
$L \in [2, 10]$, $N_l \in [1, 3]$, $H \in [32, 128]$
$\alpha \in [10^{-4}, 10^{-1}]$, $\lambda \in [10^{-5}, 10^{-1}]$
$B \in [8, 32]$, $p_d \in [0.3, 0.7]$
Set $T_{max} = 20$ evaluations or $T_{limit} = 600$ seconds
Initialize Gaussian Process surrogate $\mathcal{GP}$

while evaluations $< T_{max}$ **and** time $< T_{limit}$ **do**
Sample θ_t using Expected Improvement
Initialize: $\mathcal{L}_t \leftarrow 0$, $\mathcal{V}_t \leftarrow 0$
for fold $k = 1$ to K **do**
Set random seed: rng$(s + k \times 100)$
$b_{size} \leftarrow \lfloor n/K \rfloor$
$idx_{test} \leftarrow [(k-1)\cdot b_{size} + 1 : k \cdot b_{size}]$
$idx_{train} \leftarrow [1:n] \setminus idx_{test}$

$m \leftarrow |idx_{train}| - L + 1$
for $i = 1$ to m **do**
$\mathbf{X}_{tr}[i,:] \leftarrow$ Flatten$(\{PL_j, RMS_j\}_{j\in\mathcal{F}}[i : i + L - 1])$
$\mathbf{Y}_{tr}[i,:] \leftarrow \mathbf{Y}[idx_{train}[i + L - 1],:]$
end for

$n_{val} \leftarrow \lfloor 0.2 \cdot m \rfloor$
$v_{start} \leftarrow$ randi$([1, m - n_{val} + 1])$
$idx_{val} \leftarrow [v_{start} : v_{start} + n_{val} - 1]$
$idx_{tr} \leftarrow [1:m] \setminus idx_{val}$

$\mu_X, \sigma_X \leftarrow$ mean$(\mathbf{X}_{tr}[idx_{tr},:])$, std$(\mathbf{X}_{tr}[idx_{tr},:])$
$\mu_Y, \sigma_Y \leftarrow$ mean$(\mathbf{Y}_{tr}[idx_{tr},:])$, std$(\mathbf{Y}_{tr}[idx_{tr},:])$

$\mathcal{M}_k \leftarrow$ ConstructMLP(L, N_l, H, p_d)
Train $\mathcal{M}_k$ with Adam(α), L2(λ), batch B
on $(\mathbf{X}_{tr}[idx_{tr},:], \mathbf{Y}_{tr}[idx_{tr},:])$
validate on $(\mathbf{X}_{tr}[idx_{val},:], \mathbf{Y}_{tr}[idx_{val},:])$
with early stopping patience = 10

Create test sequences from idx_{test}
$\hat{\mathbf{Y}}^k_{te} \leftarrow$ Predict$(\mathcal{M}_k, \mathbf{X}^k_{te})$
$e_k \leftarrow$ RMSE$(\mathbf{Y}^k_{te}, \hat{\mathbf{Y}}^k_{te})$
$v_k \leftarrow \max(0, 1 - \frac{\text{std}(\hat{\mathbf{Y}}^k_{te})}{\text{std}(\mathbf{Y}^k_{te})})^2$
$\mathcal{L}_t \leftarrow \mathcal{L}_t + e_k/K$
$\mathcal{V}_t \leftarrow \mathcal{V}_t + v_k/K$
end for
$J(\theta_t) \leftarrow \mathcal{L}_t \cdot (1 + w_{var} \cdot \mathcal{V}_t)$
Update $\mathcal{GP}$ with $(\theta_t, J(\theta_t))$
end while
return $\theta^* = \arg\min_\theta J(\theta)$

Algorithm 5 MLP-Based VLC-MBSNs Position Estimation

Input: Features $\{PL_i, RMS_i\}$ where $i \in \mathcal{F}$
$\mathcal{F} \in \{\{1\},\{2\},\{3\},\{1,2\},\{1,3\},\{2,3\},\{1,2,3\}\}$
Positions $\mathbf{Y} \in \mathbb{R}^{n\times 2}$, folds $K = 5$
Optimal parameters $\theta^* = (L^*, N_l^*, H^*, p_d^*, \alpha^*, \lambda^*, B^*)$ from Algorithm 4
Output: Trained model $\mathcal{M}^*$, predictions $\hat{\mathbf{Y}}$

Initialize $\mathbf{X}_{\mathcal{F}} \leftarrow []$
for each sensor $i \in \mathcal{F}$ **do**
  $\mathbf{X}_{\mathcal{F}} \leftarrow \mathbf{X}_{\mathcal{F}} \cup [PL_i, RMS_i]$
end for

Initialize $\hat{\mathbf{Y}}_{all} \leftarrow []$, $\mathbf{Y}_{all} \leftarrow []$
for fold $k = 1$ to K **do**
  Set random seed: rng$(100 + k \times 100)$
  $b_{size} \leftarrow \lfloor n/K \rfloor$
  $idx_{test} \leftarrow [(k-1)\cdot b_{size} + 1 : k \cdot b_{size}]$
  $idx_{train} \leftarrow [1:n] \setminus idx_{test}$

  $m \leftarrow |idx_{train}| - L^* + 1$
  for $i = 1$ to m **do**
    $\mathbf{X}_{tr}[i,:] \leftarrow$ Flatten$(\{\mathbf{X}_{\mathcal{F}}[j], RMS_j\}_{j\in\mathcal{F}}[i : i + L^* - 1])$
    $\mathbf{Y}_{tr}[i,:] \leftarrow \mathbf{Y}[idx_{train}[i + L^* - 1], :]$
  end for

  Create test sequences from idx_{test}
  $\mathbf{X}_{te}, \mathbf{Y}_{te} \leftarrow$ Similar sequence creation for test data

  $n_{val} \leftarrow \lfloor 0.2 \cdot m \rfloor$
  $v_{start} \leftarrow$ randi$([1, m - n_{val} + 1])$
  $idx_{val} \leftarrow [v_{start} : v_{start} + n_{val} - 1]$
  $idx_{tr} \leftarrow [1:m] \setminus idx_{val}$

  $\mu_X, \sigma_X \leftarrow$ mean$(\mathbf{X}_{tr}[idx_{tr},:])$, std$(\mathbf{X}_{tr}[idx_{tr},:])$
  $\mu_Y, \sigma_Y \leftarrow$ mean$(\mathbf{Y}_{tr}[idx_{tr},:])$, std$(\mathbf{Y}_{tr}[idx_{tr},:])$

  $\mathcal{M}_k \leftarrow$ ConstructMLP(L^*, N_l^*, H^*, p_d^*)
  Train $\mathcal{M}_k$ with Adam(α^*), L2(λ^*), batch B^*
    on $(\mathbf{X}_{tr}[idx_{tr},:], \mathbf{Y}_{tr}[idx_{tr},:])$
    validate on $(\mathbf{X}_{tr}[idx_{val},:], \mathbf{Y}_{tr}[idx_{val},:])$
    with early stopping patience = 10

  Create test sequences from idx_{test}
  $\hat{\mathbf{Y}}_k^{te} \leftarrow$ Predict$(\mathcal{M}_k, \mathbf{X}_k^{te})$
  $\hat{\mathbf{Y}}_{all} \leftarrow \hat{\mathbf{Y}}_{all} \cup \hat{\mathbf{Y}}_k^{te}$
  $\mathbf{Y}_{all} \leftarrow \mathbf{Y}_{all} \cup \mathbf{Y}_k^{te}$
end for

$RMSE_x \leftarrow \sqrt{\text{mean}((\mathbf{Y}_{all}[:,1] - \hat{\mathbf{Y}}_{all}[:,1])^2)}$
$RMSE_y \leftarrow \sqrt{\text{mean}((\mathbf{Y}_{all}[:,2] - \hat{\mathbf{Y}}_{all}[:,2])^2)}$
$RMSE_{total} \leftarrow \sqrt{RMSE_x^2 + RMSE_y^2}$

return $\mathcal{M}^*$, $\hat{\mathbf{Y}}_{all}$, $(RMSE_x, RMSE_y, RMSE_{total})$

CHAPTER 4

4. RESULTS AND DISCUSSION

A site-specific, non-sequential ray tracing technique, as described by Donmez et al. (2021), is employed to derive the CIRs for both the ICU ward and FTPR hospital scenarios. In each case, CAD models are used to determine wavelength-dependent reflectance values and to define the spatial arrangement of ceiling-mounted luminaires and body-mounted PDs. The luminaires are strategically positioned to meet minimum average illumination requirements as well as lighting uniformity criteria. The MBSN setup includes three sensor nodes: D1 located on the shoulder, D2 on the wrist, and D3 on the ankle of a mobile subject (Donmez et al., 2021). The ICU environment features four patients in beds, a mobile healthcare worker, a desk, and a chair. In contrast, the FTPR scenario includes a single patient in bed, a walking caregiver, assorted furniture, a sofa, and a restroom. The ICU room measures 11.5 m × 6.5 m × 3 m and contains 15 ceiling-mounted luminaires, while the FTPR spans 7 m × 5 m × 3 m and includes 8 luminaires. For each setup, 20 random walking paths are generated, with each trajectory consisting of 10 sequential positions determined by uniformly distributed step lengths and movement directions. Using these trajectories, PL and RMS delay spread are extracted from the CIR, representing realistic deployment scenarios and serving as inputs for ML models aimed at estimating these channel characteristics.

4.1. Q-LEARNING-BASED ADAPTIVE MODULATION

This study utilizes the CIRs derived from earlier work (Donmez et al., 2021). The performance evaluation centers on SE across various schemes: Q-learning-based adaptive modulation, KNN-based adaptive modulation, a non-

adaptive approach, and the theoretical optimal SE. A flat fading channel model is adopted for all channels, as it aligns well with the low data rate requirements conventional of MBSN applications and has proven valuable for the purposes of this study. The parameters used in the adaptive modulation algorithm, along with an overview of the system model, are detailed in Table 4.1.

Table 4.1 System model and Q-Learning model parameters.

Parameter	Value
μ	$\{2, 4, 8, 16, 32, 64\}$
σ	0.5
Modulation Scheme	M-PAM
P_{elec}	10 dBm
Min ϵ	0.001
γ	0.5
N_0	6.464×10^{-23}
SER_{tar}	10^{-3}
Max Episodes	500
Responsivity of PDs	1

The Q-learning-based modulation strategy operates without requiring CSI during training, instead relying on continuous interaction with the environment to guide its learning process. Although the exploration rate is progressively reduced, the algorithm maintains an active level of exploration, allowing it to adjust in real time to variations in both the system model and external conditions. These adaptive and exploratory traits are central to the algorithm's design. As Bayat Rizi et al. (2024) illustrated, the initial training phase is dominated by exploration, resulting in a high SER that surpasses the target threshold. Over time, the SER declines as the Q-table becomes sufficiently populated with experience. At this point, the agent increasingly opts for deterministic actions using a greedy policy. Interestingly, once greedy behavior is adopted, the SER

does not drop drastically but stabilizes slightly below the target SERtar. This outcome is beneficial, as excessively low SER values do not contribute to optimal SE.

In (Bayat Rizi et al., 2024), Figure 5 illustrates the SE outcomes for various methods, using the optimal SE—defined as the maximum SE achievable while maintaining the target SERtar—as the baseline for evaluation. In this configuration, the KNN approach utilizes 60% of the CIRs, corresponding to 12 trajectory samples, and estimates outcomes based on the three closest neighbors. While the non-adaptive method employs binary PAM to ensure compliance with SERtar, both KNN and Q-learning approaches offer notable improvements in SE. However subfigures a, b, and e show that there are instances where the KNN method surpasses the optimal SE, suggesting that it does not satisfy the SERtar constraint in those particular cases.

Additionally, the Q-learning-based adaptive modulation scheme yields notable enhancements in SE compared to the non-adaptive method. In the ICU ward, the SE increases observed are 151% for D1, 178% for D2, and 81% for D3. In the FTPR scenario, the model demonstrates even greater SE enhancements, reaching 304%, 303%, and 151% for D1, D2, and D3, respectively. The higher SE gains observed in the FTPR setting, compared to the ICU ward, indicate a broader variation in channel DC gain within the FTPR environment, consistent with the findings in (Donmez & Miramirkhani, 2021).

Additionally, PDs positioned on the shoulder (D1) and wrist (D2) demonstrate greater SE improvements using the learning-based adaptive modulation method compared to those placed on the ankle (D3) in both scenarios. This difference arises from the sinusoidal nature of the DC gain observed in D1 and D2, which is primarily influenced by LOS rays. In contrast, D3 is predominantly affected by NLOS rays, resulting in a more uniform DC gain profile. The limited variation in DC gain for D3 leads to reduced SE performance relative to the other sensor nodes.

In highly dynamic healthcare environments like emergency wards, Q-learning-based adaptive modulation encounters specific difficulties. As the algorithm depends on adequate exploration to identify optimal actions, rapidly changing channel conditions can prevent the Q-table from converging to an effective policy. To address this issue, the system can promptly switch to the most robust, lowest-order modulation scheme (e.g., 2-PAM). While this approach lowers throughput, it ensures that the target SER is maintained, even in the absence of fully trained models.

To handle the challenges of dynamic and unpredictable environments, various studies have introduced fallback strategies to enhance system robustness. Lecerf et al. (2022) proposed a fallback mechanism based on pseudo-rewards, where several "pseudo-agents" are trained in parallel with the main policy. These agents are guided by a modified reward that includes a distance-related pseudo-reward component. During operation, the system can switch to the fallback agent whose behavior best matches the current state distribution, enabling more conservative choices when the primary policy becomes unreliable. For systems with limited resources, Xiang et al. (2023) introduced an exploration-guided method that strongly penalizes Q-values tied to actions with repeated failures. This method also employs bootstrapped initialization of the Q-table, where Q-values are set using heuristic estimates based on their inverse distance from performance targets. Additionally, it includes a dynamic ε-greedy strategy that increases exploration following errors and decreases it when performance stabilizes. These combined techniques promote faster convergence, guide early decisions toward safer actions, and adaptively manage the trade-off between exploration and exploitation in fluctuating channel conditions.

4.2. LSTM-BASED PATH LOSS AND RMS DELAY SPREAD ESTIMATION

Following extensive simulations using different ML techniques, the estimated PL and RMS delay spread for nodes D1–D3 across both the ICU ward and FTPR scenarios were obtained. The corresponding RMSE values for each case are provided in Tables 4.2 and 4.3. Among the evaluated models, the LSTM algorithm consistently delivers the best performance in both environments, recording the lowest RMSE for both PL and RMS delay spread (Antaki et al., 2025). These results confirm the effectiveness of LSTM in reducing prediction errors.

Table 4.2 Estimated path loss and RMS delay within an ICU Ward through different techniques.

Method	ICU Ward					
	RMSE of τ_{RMS} (ns)			RMSE of PL (dB)		
	D1	D2	D3	D1	D2	D3
KNN	1.8088	1.5987	1.4401	2.3142	1.8848	1.7834
SVR	1.1774	0.9769	0.9107	1.847	1.3671	1.2654
GRU	1.0794	0.9593	0.884	1.706	1.1808	1.1774
RNN	1.0904	0.9734	0.9039	1.7398	1.2647	1.1785
LSTM	1.0567	0.9348	0.8784	1.6797	1.1679	1.1464

Table 4.3 Estimated path loss and RMS delay within FTPR through different techniques.

Method	FTPR					
	RMSE of τ_{RMS} (ns)			RMSE of PL (dB)		
	D1	D2	D3	D1	D2	D3
KNN	0.8199	0.9602	1.2166	0.9110	0.9770	1.7908
SVR	0.6277	0.6753	0.8834	0.7829	0.8184	1.1762
GRU	0.6183	0.6352	0.8555	0.7359	0.7832	1.1480
RNN	0.6237	0.6509	0.8509	0.7663	0.7929	1.1886
LSTM	0.5830	0.6230	0.7657	0.7210	0.7327	1.0652

As presented in Table 4.2, the LSTM model consistently delivers the lowest RMSE values for both PL and RMS delay spread across all detector locations (D1–D3) in the ICU ward, outperforming other models such as GRU, vanilla RNN, SVR, and KNN, all of which exhibit comparatively higher error levels. In the context of PL estimation within the ICU, LSTM achieves RMSEs of 1.6797, 1.1679, and 1.1464 for D1, D2, and D3, respectively. In comparison, GRU, the second-best performing model, produces slightly higher RMSE values of 1.7060, 1.1808, and 1.1774. A similar trend is evident in Table 4.3, where LSTM again yields the lowest RMSEs for PL estimation in the FTPR scenario—0.7210 at D1, 0.7327 at D2, and 1.0652 at D3—outperforming GRU, which registers RMSEs of 0.7359, 0.7832, and 1.1480 at the corresponding detectors. For RMS delay spread in the ICU scenario, LSTM again leads with RMSEs of 1.0567, 0.9348, and 0.8784 at D1, D2, and D3, outperforming GRU's respective scores of 1.0794, 0.9593, and 0.8840. Likewise, in the FTPR scenario, Table 4.3 shows that LSTM attains the best results for RMS delay spread with RMSEs of 0.5830, 0.6230, and 0.7657 at D1, D2, and D3, respectively, while GRU follows closely with slightly higher values of 0.6183, 0.6352, and 0.8555. All remaining models under comparison consistently produce higher RMSEs across both channel parameters and deployment environments.

Table 4.2 also shows that, in the ICU ward scenario, D1 experiences the highest RMSE in PL estimation among the three detectors. This observation is in agreement with the findings of Donmez et al. (2022), which report that D1 has the largest variance in its log-normal distribution at 0.0262, compared to 0.0176 for D2 and 0.0169 for D3—supporting the established link between greater variance and increased estimation error. Likewise, Table 4.3 demonstrates that in the FTPR scenario, D3 registers the highest RMSE compared to D1 and D2. This is consistent with Donmez et al. (2022), where D3 was found to have the highest variance at 0.0168, while D1 and D2 recorded lower values of 0.0123 and 0.0119, respectively. These results

further validate the positive correlation between detector variance and RMSE in PL estimation.

Table 4.2 reveals that, within the ICU ward scenario, D1 yields the largest RMSE in estimating RMS delay spread among the three detector positions. This outcome corresponds with the analysis by Donmez et al. (2022), which identified D1 as having the highest variance in its log-normal distribution—0.0975—compared to 0.0847 for D2 and 0.0780 for D3. The greater variance observed at D1 accounts for the increased estimation error. On the other hand, Table 4.3 shows that D3 produces the highest RMSE for RMS delay spread in the FTPR environment. This is consistent with Donmez et al. (2022), where D3 was reported to have the most significant variance, measured at 0.0967, while D1 and D2 exhibited lower values of 0.0659 and 0.0747, respectively. These findings reinforce the direct correlation between higher statistical variance and elevated RMSE in delay spread estimation.

A practical complexity evaluation was carried out to support the selection of LSTM by comparing its training and inference durations against GRU and RNN in both the ICU ward and FTPR scenarios, as detailed in Tables 4.4 and 4.5. This analysis centers on LSTM, GRU, and RNN due to their demonstrated effectiveness and prevalent use in MBSN applications. As discussed earlier, these architectures are inherently designed for sequential data regression tasks and excel at modeling temporal relationships, making them particularly suitable for time-series prediction and real-time health monitoring use cases.

Table 4.4 Time complexity of an ICU ward.

Method	ICU Ward					
	Execution Time of τ_{RMS} (s)			Execution Time of PL (s)		
	D1	D2	D3	D1	D2	D3
GRU	72.711	69.671	73.468	70.197	72.19	68.958
RNN	73.018	72.917	73.787	70.368	72.578	73.488
LSTM	69.946	68.786	68.948	68.051	65.854	66.229

Table 4.5 Time complexity of FTPR.

Method	FTPR					
	Execution Time of τ_{RMS} (s)			Execution Time of PL (s)		
	D1	D2	D3	D1	D2	D3
GRU	70.491	71.846	70.65	72.531	71.791	70.652
RNN	71.625	73.173	75.559	73.353	72.299	71.616
LSTM	69.74	70.22	69.65	69.112	70.484	69.919

As shown in Table 4.4, LSTM expresses greater performance over GRU and RNN in terms of execution time for both PL and RMS delay spread across all three nodes (D1–D3) within the ICU ward, validating the selection of LSTM for this task. The execution times for PL estimation at D1, D2, and D3 were 68.051 s, 65.854 s, and 66.229 s, respectively, while the corresponding times for RMS delay spread estimation were 69.946 s, 68.786 s, and 68.948 s. Likewise, Table 4.5 indicates that LSTM also yields the most efficient execution times for D1–D3 within the FTPR, further supporting its suitability. Specifically, the PL execution times were 69.112 s, 70.484 s, and 69.919 s, and for RMS delay spread, the times were 69.740 s, 70.220 s, and 69.650 s, respectively.

The results align with expectations, as the LSTM model—built with memory cells and gating mechanisms—handles long-term dependencies effectively, making it well-suited for the time-varying nature of PL and RMS

delay spread in VLC-based MBSNs. While its RMSE was similar to other models like GRU, the LSTM approach stood out for its lower computational load, minimal need for hyperparameter adjustment, and shorter training time, all within standard modeling practices. Its strength in capturing complex sequences confirms LSTM as the most reliable and efficient choice for this task.

When deployed in real hospital environments, LSTM models encounter several practical challenges, including energy efficiency, system integration hurdles, computational demands, and the unpredictability of healthcare settings. To address these issues, (Saxena et al., 2022) applied LSTM to enhance Hospital Management System performance by analyzing both historical and real-time data under two resource allocation scenarios. Their results revealed a close match between predicted and actual outcomes, with residuals tightly clustered around zero. Similarly, (Karsanti et al., 2019) used LSTM to forecast patient visits at a community health center using 43 months of historical data. LSTM outperformed alternative models, achieving a Mean Absolute Percentage Error (MAPE) of 4.714, a Mean Absolute Error (MAE) of 154.796, and a RMSE of 167.631. These outcomes demonstrate LSTM's capacity for high accuracy and resilience in dynamic healthcare settings. Additionally, its efficiency in learning temporal patterns helps alleviate concerns related to computational complexity. Overall, these studies underscore the potential of LSTM models to address core operational challenges in hospitals, such as minimizing patient wait times, optimizing staff deployment, and improving patient care outcomes.

4.3. MLP-BASED POSITION ESTIMATION

The position estimation experiments were conducted on an Intel Core i5-11400H CPU operating at 2.70 GHz, evaluating six ML models across multiple sensor configurations in both FTPR and ICU scenarios. The comprehensive study encompassed LR, SVR, KNN, MLP, LSTM, and GRU, with performance evaluated through RMSE metrics for both individual coordinates and Euclidean distance.

The position estimation performance across different sensor configurations in the FCPR scenario reveals clear trade-offs between model complexity, accuracy, and computational efficiency. The classical ML approaches—LR, SVR, and KNN—demonstrated the fastest training times but consistently yielded the highest position errors.

LR exhibited the poorest performance with Euclidean RMSE values ranging from 646.91 mm to 743.97 mm across different sensor configurations, , as shown in Table 4.6. The model required minimal training time of 0.0164 seconds for the D1-D2-D3 configuration, as illustrated in Table 4.10, yet this computational efficiency came at the cost of failing to capture the complex nature of realistic channel models in VLC-based indoor environments. Moreover, in Figure 4.2a , due to the model's low complexity, Predictions along y axis shows poor performance compared to others. Also, as illustrated in Figure 4.3a, the predictions defaulted to predicting values around the mean value with small variance even with the introduced variance penalty.

SVR showed marginal improvements over LR, achieving Euclidean RMSE values between 631.35 mm and 790.04 mm, with the D1-D2 configuration producing the best performance. Despite requiring longer training times than LR, SVR still struggled to model the nonlinear mappings of PL and RMS readings to estimated positions effectively. The model's performance degradation was particularly evident for individual sensor

configurations, where D2 alone resulted in an RMSE of 790.04 mm, indicating a 25.2% increase in error compared to the multi-sensor setup.

KNN produced the worst overall results among all models, with Euclidean RMSE values ranging from 669.85 mm to 884.87 mm. The D2 individual sensor configuration yielded particularly poor performance with a 32.1% degradation compared to the D1-D2-D3 configuration. While KNN maintained competitive training times of 0.0239 seconds, its inability to leverage temporal dependencies rendered it unsuitable for accurate position estimation in dynamic healthcare environments.

The sequential models demonstrated substantially superior performance, with LSTM achieving the lowest Euclidean RMSE across most configurations. For the combined D1-D2-D3 setup, LSTM recorded 573.01 mm, representing a 12.3% improvement over LR and 14.4% over KNN. The model maintained consistent performance across paired sensor configurations, achieving 603.28 mm for D1-D2 and 602.28 mm for D1-D3, demonstrating robust spatial tracking capabilities. In the X-coordinate prediction, LSTM achieved the best performance at 526.54 mm for D1-D2-D3, outperforming LR by 12.4% and KNN by 14.8%. Similarly, for Y-coordinate estimation, LSTM achieved 221.55 mm, showing an 8.2% improvement over LR and 12.8% over KNN.

GRU exhibited comparable performance to LSTM with marginally higher error rates, achieving 584.99 mm for D1-D2-D3, which represents only a 2.1% increase compared to LSTM. The model demonstrated competitive performance in specific configurations, particularly for D2-D3 where it achieved 670.35 mm, only 3.2% higher than LSTM's 692.63 mm. However, GRU's computational requirements proved significantly higher, with training times of 2.99 seconds for D1-D2-D3, representing a 41.6% increase over LSTM's 2.11 seconds.

The hyperparameter optimization phase revealed substantial computational disparities between model architectures. LSTM required 72.25 seconds for optimization in the D1-D2-D3 configuration, while GRU

demanded 120.12 seconds, a 66.2% increase. Classical methods demonstrated significantly faster optimization, with KNN requiring only 3.55 seconds and LR 5.38 seconds. However, these time savings became irrelevant given their inadequate positioning accuracy for practical healthcare applications, as illustrated in Table 4.9.

MLP emerged as a compelling compromise between accuracy and computational efficiency. With a Euclidean RMSE of 586.19 mm for D1-D2-D3, MLP achieved performance within 2.3% of LSTM while requiring only 1.49 seconds for training—a 29.4% reduction compared to LSTM. The model's X-coordinate RMSE of 541.06 mm represented only a 2.8% increase over LSTM's optimal performance, while maintaining training times 29.7% faster. For Y-coordinate prediction, MLP achieved 222.68 mm, virtually matching LSTM's performance with a negligible 0.5% difference. The computational efficiency advantages of MLP become more pronounced during HPO, requiring only 46.30 seconds compared to LSTM's 72.25 seconds—a 35.9% reduction. This efficiency gain proves particularly valuable in clinical settings where models may require frequent retraining to accommodate environmental changes or new patient populations. The model's simpler architecture with no recurrent connections also facilitates easier deployment on resource-constrained medical devices while maintaining interpretability for clinical validation. Analysis of individual sensor performance shows MLP's robustness across different configurations. For D1 alone, MLP achieved 635.09 mm compared to LSTM's 614.96 mm. The D2 configuration showed MLP at 750.14 mm versus LSTM's 723.53 mm. These marginal accuracy differences, coupled with the 35-40% reduction in training time, position MLP as the optimal choice for practical deployment. The optimized hyperparameters of the MLP model in each Configuration in FCPR are shown in Table 4.11.

The variance analysis across coordinate predictions further supports MLP's selection. While LSTM achieved the lowest X-coordinate RMSE for most configurations, the differences remained within 2-4% of MLP's

performance. For Y-coordinate predictions, where errors were generally lower across all models, MLP matched or exceeded LSTM's accuracy in several configurations, including D1-D3 where it achieved 215.63 mm compared to LSTM's 209.68 mm.

Considering the real-time requirements of healthcare monitoring systems, where position updates must occur frequently to track patient movement effectively, MLP's computational advantages become decisive. The model's ability to achieve near-optimal accuracy with significantly reduced training and inference times makes it the most practical choice for VLC-based positioning in medical environments. The 29-36% reduction in computational overhead translates directly to improved system responsiveness and reduced energy consumption in battery-powered medical sensors.

Table 4.6 Euclidean distance RMSE of Position estimation for Different situations in FCPR (mm).

FCPR							
Method	**Joint Euclidean RMSE with Sensors configuration (mm)**						
	D1-D2-D3	**D1-D2**	**D1-D3**	**D2-D3**	**D1**	**D2**	**D3**
LR	653.6971	646.9070	661.3409	735.1672	658.2554	717.9221	743.9666
SVR	645.3091	631.3502	688.9499	691.3956	650.6571	790.0423	754.7221
KNN	669.8505	708.6693	747.6969	751.1670	776.7315	884.8671	866.0046
MLP	586.1917	630.2000	609.7385	675.1041	635.0866	750.1430	730.6306
LSTM	573.0067	603.2765	602.2763	692.6320	614.9587	723.5338	671.9466
GRU	584.9990	633.6995	619.4119	670.3519	634.0701	753.1933	712.8267

Table 4.7 RMSE of X Position estimation for Different situations in FCPR (mm).

FCPR							
Method	**X Position RMSE with Sensors configuration (mm)**						
	D1-D2-D3	**D1-D2**	**D1-D3**	**D2-D3**	**D1**	**D2**	**D3**
LR	601.2125	592.9701	611.5364	680.7598	607.9904	661.4757	691.2109
SVR	605.6843	567.3881	646.0504	640.1391	599.4756	720.2108	716.5561
KNN	617.8920	657.4590	694.7918	700.3226	728.0367	817.2387	809.7161
MLP	541.0605	578.9749	567.1355	631.0536	571.6376	704.0889	684.0840
LSTM	526.5386	553.9666	562.8492	634.9335	553.6035	676.2108	621.4124
GRU	537.1560	584.8773	578.1800	617.3273	564.5858	699.3461	666.4300

Table 4.8 RMSE of Y Position estimation for Different situations in FCPR (mm).

FCPR							
Method	**Y Position RMSE with Sensors configuration (mm)**						
	D1-D2-D3	**D1-D2**	**D1-D3**	**D2-D3**	**D1**	**D2**	**D3**
LR	241.3281	242.4013	240.5519	271.6453	240.6726	271.9076	270.7079
SVR	214.6484	241.9328	230.0456	259.8907	240.4264	312.3228	234.5551
KNN	254.1327	258.5329	271.6060	270.5713	265.1667	338.5409	306.4653
MLP	222.6806	238.4754	215.6254	239.3491	265.2947	252.5863	254.3577
LSTM	221.5465	230.1366	209.6757	272.4571	257.1246	253.3595	252.8487
GRU	225.0912	238.5662	215.4012	256.8128	278.2646	274.7510	252.8005

Table 4.9 Hyperparameters Optimization Time of Position estimation error for Different situations in FCPR (s).

FCPR							
Method	**Hyperparameters Optimization Time with Sensors configuration (s)**						
	D1-D2-D3	**D1-D2**	**D1-D3**	**D2-D3**	**D1**	**D2**	**D3**
LR	5.3792	5.4993	5.3518	5.4370	5.1606	5.1254	5.3526
SVR	6.9208	5.9109	9.8973	13.4521	10.5150	9.8926	15.7778
KNN	3.5476	3.3097	3.4438	3.6364	3.1470	3.3276	3.2047
MLP	46.3017	45.3168	36.2355	42.4811	48.5547	45.1107	38.4175
LSTM	72.2464	79.8541	88.3947	70.2681	85.9614	74.9421	74.1675
GRU	120.1207	112.1014	72.9070	78.4832	81.0732	78.6157	90.4337

Table 4.10 Training time of the best model for Position estimation error for Different situations in FCPR (s).

FCPR							
ML Model	**Model Training Time with Sensors configuration (s)**						
	D1-D2-D3	**D1-D2**	**D1-D3**	**D2-D3**	**D1**	**D2**	**D3**
LR	0.0164	0.0265	0.0256	0.0259	0.0304	0.0246	0.0268
SVR	0.0650	0.0817	0.0719	0.0718	0.0726	0.1221	0.0837
KNN	0.0239	0.0374	0.0367	0.0404	0.0109	0.0374	0.0366
MLP	1.4898	1.9096	1.3052	1.3613	1.3934	2.0880	1.3463
LSTM	2.1113	2.6876	2.6523	2.5602	3.2577	3.2788	2.5864
GRU	2.9911	6.0286	2.8710	3.4143	4.2347	2.4984	4..3841

The ICU environment presented significantly different performance characteristics compared to the FCPR, with all models exhibiting substantially higher position errors due to the increased spatial complexity. Surprisingly,

classical ML approaches demonstrated lower RMSE values in several configurations, with LR achieving 1888.92 mm for the D1-D2-D3 configuration, outperforming LSTM's 2095.06 mm by 9.8%. However, examination of the prediction scatter plots reveals a critical limitation: these classical models achieve lower RMSE through clustering predictions around the mean position rather than capturing actual movement patterns.

The 2D position scatter plots, actual versus predicted, and error distribution graphs, from Figure 4.29 to Figure 4.56, clearly illustrate this fundamental failure of classical approaches. LR, SVR, and KNN predictions concentrate in a tight cluster near the center of the movement space, essentially predicting the same mean position regardless of actual patient location. While this strategy minimizes RMSE when patients frequently occupy central areas, it renders the models useless for tracking actual patient movement or detecting position changes.

Table 4.11 Optimized Hyperparameters of the selected model in each Configuration in FCPR.

Optimal Model	Configurations	Hyperparameter	Optimized Value
MLP	D1-D2-D3	Number of MLP Layers	1
		Number of Hidden Units	117
		Dropout Rate	0.44609
		Learning Rate	0.015352
		L2 Regularization	0.00045914
		Batch Size	22
		Sequence Length	2
	D1-D2	Number of MLP Layers	2
		Number of Hidden Units	125
		Dropout Rate	0.31786
		Learning Rate	0.014225
		L2 Regularization	0.012499
		Batch Size	23
		Sequence Length	2
	D1-D3	Number of MLP Layers	1
		Number of Hidden Units	79
		Dropout Rate	0.31756
		Learning Rate	0.021361
		L2 Regularization	0.0076469
		Batch Size	29
		Sequence Length	2

Table 4.11 (Next) Optimized Hyperparameters of the selected model in each Configuration in FCPR.

Optimal Model	Configurations	Hyperparameter	Optimized Value
MLP	D2-D3	Number of MLP Layers	1
		Number of Hidden Units	123
		Dropout Rate	0.30363
		Learning Rate	0.030801
		L2 Regularization	0.00001961
		Batch Size	19
		Sequence Length	2
	D1	Number of MLP Layers	1
		Number of Hidden Units	115
		Dropout Rate	0.4166
		Learning Rate	0.0097657
		L2 Regularization	0.0010206
		Batch Size	27
		Sequence Length	4
	D2	Number of MLP Layers	2
		Number of Hidden Units	112
		Dropout Rate	0.30341
		Learning Rate	0.011186
		L2 Regularization	0.00018761
		Batch Size	21
		Sequence Length	4
	D3	Number of MLP Layers	1
		Number of Hidden Units	126
		Dropout Rate	0.40184
		Learning Rate	0.065093
		L2 Regularization	0.00037371
		Batch Size	31
		Sequence Length	4

SVR demonstrated mixed performance with Euclidean RMSE values ranging from 1927.44 mm to 2123.11 mm across configurations. Despite achieving the second-best performance for D2 individual sensor at 1927.44 mm, the model's predictions exhibited the same mean predictions. The training time of 0.06 seconds for D1-D2-D3 remained competitive, yet this efficiency becomes meaningless when the model fails to provide actionable position information.

KNN produced particularly poor results with the highest RMSE in multiple configurations, reaching 2321.56 mm for D2 alone—a 22.3% degradation compared to LR's 1898.49 mm. Despite maintaining fast training

times of 0.0287 seconds, KNN's complete failure to model the complex ICU environment eliminates it from practical consideration.

Among sequential models, LSTM achieved more consistent performance with Euclidean RMSE values ranging from 1926.25 mm for D1-D2 to 2243.34 mm for D3 alone. While these values appear higher than classical methods, the prediction visualizations, for example Figure 4.29 and Figure 4.30, reveal LSTM's greater ability to maintain spatial variance and track actual movement trajectories. In Figure 4.29e, the model's predictions span the full range of actual positions, demonstrating genuine position discrimination rather than mean collapse. For the D1-D2 configuration, LSTM achieved the best performance among all models at 1926.25 mm, with predictions maintaining realistic spatial distribution as evidenced in the scatter plots.

GRU exhibited variable performance across configurations, with particularly poor results for D1 alone at 2600.18 mm—the highest error among all models. However, for other configurations such as D2, GRU achieved 2099.92 mm, representing only an 8.9% increase over SVR's artificially low RMSE. The model required substantially longer training times of 3.33 seconds for D1-D2-D3, a 36.8% increase over LSTM's 2.44 seconds, while failing to provide commensurate accuracy improvements.

MLP emerged as the optimal compromise between meaningful position estimation and computational efficiency. With Euclidean RMSE values ranging from 2021.19 mm for D1-D2 to 2275.16 mm for D2-D3, MLP maintained comparable performance to sequential models while avoiding the variance collapse of classical approaches. The scatter plots demonstrate MLP's ability to produce distributed predictions across the movement space, capturing the essential spatial variations necessary for patient tracking. Critically, MLP achieved this performance with training times of only 1.27 seconds for D1-D2-D3—a 48.0% reduction compared to LSTM's 2.44 seconds.

The HPO phase revealed even more pronounced computational advantages for MLP in the ICU setting. MLP required only 37.73 seconds for

optimization in D1-D2-D3, compared to LSTM's 60.02 seconds—a 37.1% reduction. This efficiency gain proves particularly valuable in the dynamic ICU environment where frequent model updates may be necessary to accommodate changes in equipment placement, patient population, or clinical protocols. GRU's optimization time of 71.38 seconds, representing a 89.2% increase over MLP, which further undermines its practical viability.

Analysis of coordinate-specific predictions reinforces MLP's selection. For X-coordinate estimation, MLP achieved 2000.78 mm in D1-D2-D3, within 5.0% of LSTM's 1907.30 mm, while maintaining prediction distributions that span the actual position range. Y-coordinate predictions showed MLP at 808.78 mm, comparable to LSTM's 789.42 mm with only a 2.5% difference. These marginal accuracy trade-offs are more than compensated by MLP's superior computational efficiency and architectural simplicity.

The ICU results particularly highlight the importance of examining prediction patterns beyond simple RMSE metrics. While classical models appear superior numerically, their complete failure to capture spatial variations—evident in the clustered scatter plots and flat prediction lines—disqualifies them from practical deployment. MLP's ability to maintain meaningful position discrimination while achieving 37-48% reductions in computational overhead positions it as the optimal choice for ICU environments. The model successfully balances the competing demands of accuracy, computational efficiency, and prediction reliability, essential requirements for real-time patient monitoring in complex clinical settings. T

The consistency of MLP's performance across both FCPR and ICU scenarios further supports its selection. Unlike classical models that catastrophically fail to generalize across environments, or sequential models that require extensive computational resources, MLP provides stable, interpretable position estimates suitable for diverse healthcare settings. This robustness, combined with its computational advantages, makes MLP the

recommended architecture for practical VLC-based positioning system deployment in medical facilities.

Overall, MLP method achieves sub-meter accuracy of 58.6 cm for combined D1-D2-D3 sensor configurations in FTPR, with individual sensors yielding 63.5 cm (D1), 75.0 cm (D2), and 73.1 cm (D3), while in the more larger ICU environment, MLP maintains acceptable precision of 217.1 cm for D1-D2-D3, with paired configurations achieving 202.1 cm (D1-D2) and 216.3 cm (D1-D3), all while offering 35-48% reduction in computational requirements and 37-89% faster hyperparameter optimization compared to sequential models, making it the most practical solution for real-time patient tracking in healthcare facilities.

Table 4.12 Euclidean distance RMSE of Position estimation for Different situations in ICU (mm).

ICU							
Method	**Joint Euclidean RMSE with Sensors configuration (mm)**						
	D1-D2-D3	**D1-D2**	**D1-D3**	**D2-D3**	**D1**	**D2**	**D3**
LR	1888.9228	1902.8660	1870.1559	1892.7260	1887.4432	1898.4934	1876.2171
SVR	2066.2197	2123.1068	2027.9824	1976.2746	2027.2571	1927.4428	2000.8634
KNN	2057.8808	2165.2033	1996.4697	2112.2239	2102.9335	2321.5601	2194.2436
MLP	2171.1606	2021.1912	2162.7357	2275.1586	2129.6959	2195.9938	2093.3592
LSTM	2095.0557	1926.2460	2108.1733	2083.4015	2045.9988	2171.8175	2243.3370
GRU	2106.4690	2202.3601	2187.6489	2318.5507	2600.1769	2099.9208	2270.0718

Table 4.13 RMSE of X Position estimation for Different situations in ICU (mm).

ICU							
Method	**X Position RMSE with Sensors configuration (mm)**						
	D1-D2-D3	**D1-D2**	**D1-D3**	**D2-D3**	**D1**	**D2**	**D3**
LR	1720.6043	1734.1434	1702.8501	1730.9038	1722.1300	1737.1084	1714.6764
SVR	1878.4338	1946.6425	1856.7690	1836.2992	1822.4620	1759.1365	1869.5753
KNN	1891.6005	1999.6188	1831.6946	1963.9549	1941.9092	2164.4818	2053.2921
MLP	2000.7767	1871.6404	2020.9762	2087.7916	1969.3802	2012.1792	1925.6872
LSTM	1907.3002	1744.5535	1916.7806	1919.1003	1870.5704	1992.3247	2081.5561
GRU	1938.0997	1988.2506	2010.7021	2144.5296	2459.4861	1928.8179	2097.0583

Table 4.14 RMSE of Y Position estimation for Different situations in ICU (mm).

ICU							
Method	**Y Position RMSE with Sensors configuration (mm)**						
	D1-D2-D3	**D1-D2**	**D1-D3**	**D2-D3**	**D1**	**D2**	**D3**
LR	736.6078	741.4656	732.4658	717.1166	733.5928	718.9199	714.2446
SVR	822.5362	800.7210	777.1896	692.0686	835.2029	729.6363	682.8871
KNN	784.0245	811.0558	761.7421	739.9574	781.0386	816.3415	746.8184
MLP	808.7794	717.7009	714.4718	875.9332	725.8333	849.9995	758.9184
LSTM	789.4158	783.8768	828.3158	776.0652	771.0930	827.6053	783.6557
GRU	788.9425	915.5541	783.3847	832.3260	817.5018	766.8258	813.7450

Table 4.15 Hyperparameters Optimization Time of Position estimation error for Different situations in ICU (s).

ICU							
Method	**Hyperparameters Optimization Time with Sensors configuration (s)**						
	D1-D2-D3	**D1-D2**	**D1-D3**	**D2-D3**	**D1**	**D2**	**D3**
LR	5.5479	5.1358	5.4068	5.7126	5.1529	5.6079	5.6332
SVR	12.0517	10.6436	21.5098	9.9552	12.2857	10.2469	7.9504
KNN	4.0631	3.2631	3.3842	3.7142	3.0574	3.1628	3.2984
MLP	37.7290	46.7037	41.1845	39.1760	34.2357	33.4818	35.3279
LSTM	60.0187	69.1248	68.8303	66.7884	87.5028	59.9227	60.3470
GRU	71.3829	81.7432	57.069	83.9208	64.2570	95.3565	66.0911

Table 4.16 Training time of the best model for Position estimation error for Different situations in ICU (s).

ICU							
ML Model	**Model Training Time with Sensors configuration (s)**						
	D1-D2-D3	**D1-D2**	**D1-D3**	**D2-D3**	**D1**	**D2**	**D3**
LR	0.0147	0.0291	0.0276	0.0281	0.0666	0.0292	0.0284
SVR	0.0600	0.1066	0.0886	0.0832	0.1724	0.2547	0.0896
KNN	0.0287	0.0417	0.0428	0.0511	0.0443	0.0424	0.0422
MLP	1.2694	2.1158	1.3514	1.8706	1.8074	1.3284	1.2932
LSTM	2.4357	3.7047	3.2051	2.7419	5.1576	3.3593	2.8615
GRU	3.3347	3.3720	3.1971	4.0852	2.0514	4.2860	2.3500

Table 4.17 Optimized Hyperparameters of the selected model in each Configuration in ICU.

Optimal Model	Configurations	Hyperparameter	Optimized Value
MLP	D1-D2-D3	Number of MLP Layers	1
		Number of Hidden Units	111
		Dropout Rate	0.30099
		Learning Rate	0.025215
		L2 Regularization	0.0030387
		Batch Size	20
		Sequence Length	2
	D1-D2	Number of MLP Layers	2
		Number of Hidden Units	67
		Dropout Rate	0.42299
		Learning Rate	0.00020586
		L2 Regularization	0.039889
		Batch Size	13
		Sequence Length	10
	D1-D3	Number of MLP Layers	1
		Number of Hidden Units	62
		Dropout Rate	0.48713
		Learning Rate	0.0001013
		L2 Regularization	0.003367
		Batch Size	23
		Sequence Length	3
	D2-D3	Number of MLP Layers	1
		Number of Hidden Units	65
		Dropout Rate	0.31056
		Learning Rate	0.00011121
		L2 Regularization	0.019077
		Batch Size	18
		Sequence Length	7
	D1	Number of MLP Layers	1
		Number of Hidden Units	52
		Dropout Rate	0.30144
		Learning Rate	0.00079108
		L2 Regularization	0.00062936
		Batch Size	11
		Sequence Length	10
	D2	Number of MLP Layers	1
		Number of Hidden Units	63
		Dropout Rate	0.30576
		Learning Rate	0.058787
		L2 Regularization	0.00047169
		Batch Size	29
		Sequence Length	8
	D3	Number of MLP Layers	1
		Number of Hidden Units	68
		Dropout Rate	0.30016
		Learning Rate	0.00036638
		L2 Regularization	0.000011235
		Batch Size	19
		Sequence Length	10

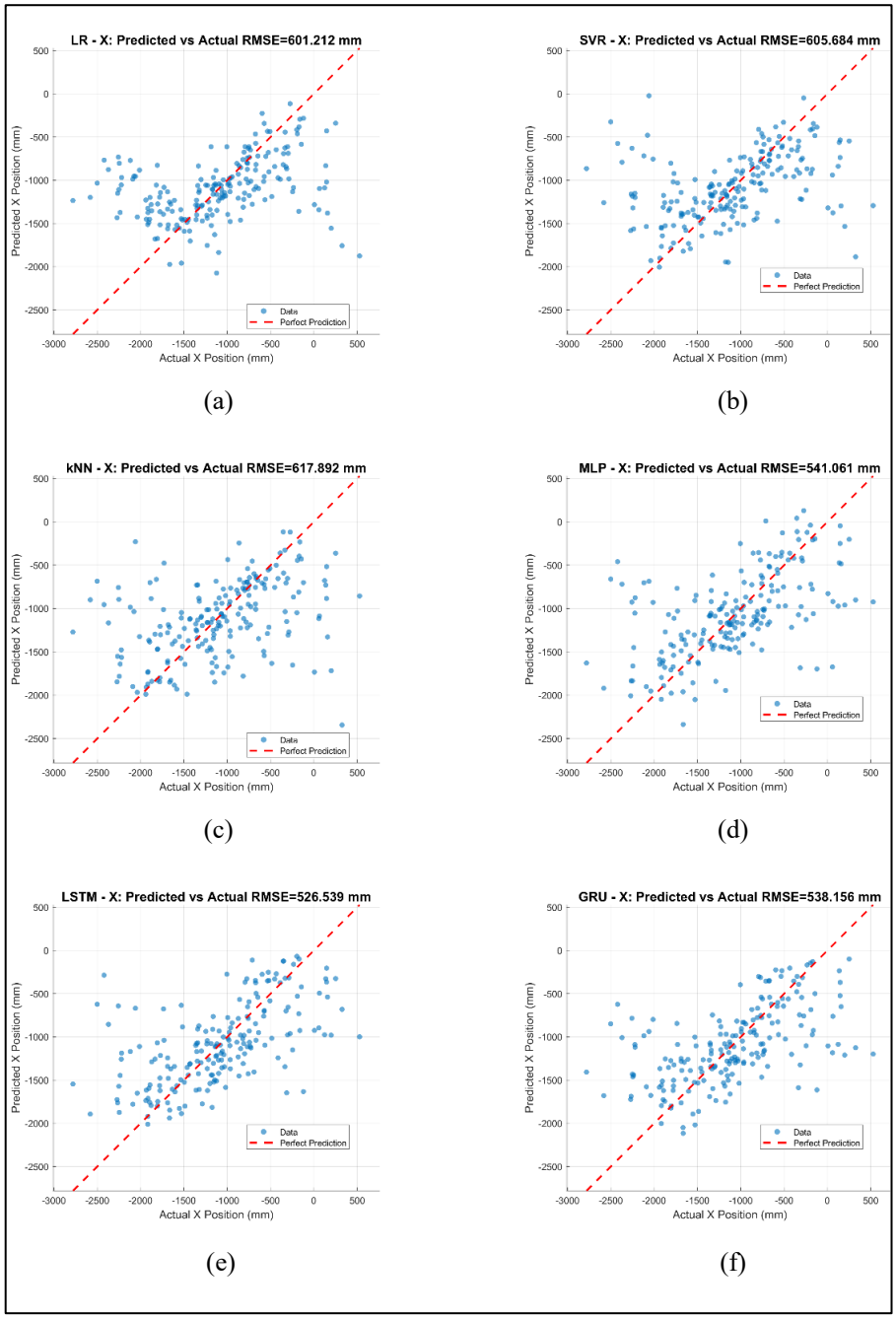

Figure 4.1 Actual versus Predicted X position for D1-D2-D3 situation in FCPR using (a) LR (b) SVR (c) kNN (d) MLP (e) LSTM (f) GRU.

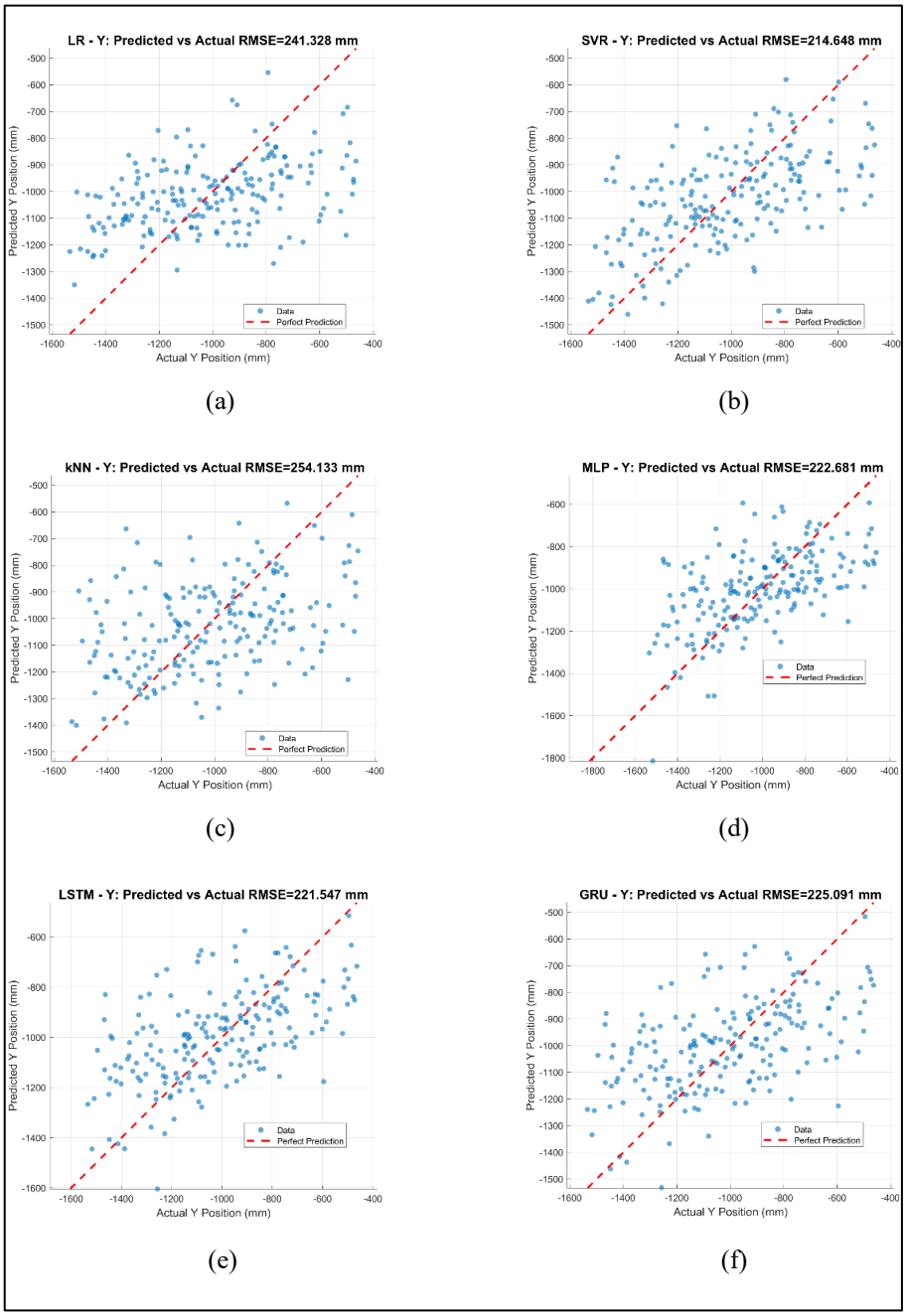

Figure 4.2 Actual versus Predicted Y position for D1-D2-D3 situation in FCPR using (a) LR (b) SVR (c) kNN (d) MLP (e) LSTM (f) GRU.

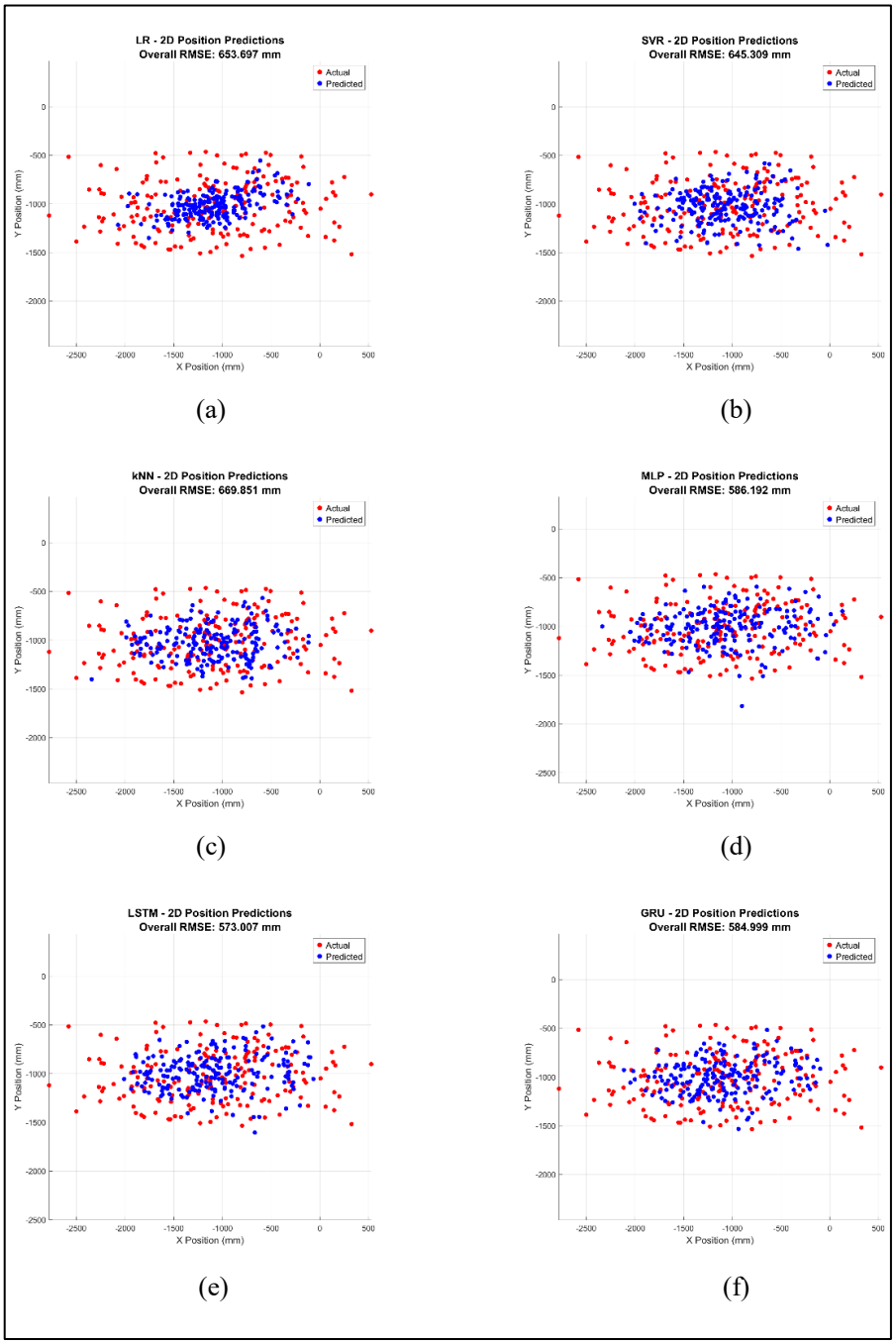

Figure 4.3 2D position predictions for D1-D2-D3 situation in FCPR using (a) LR (b) SVR (c) kNN (d) MLP (e) LSTM (f) GRU.

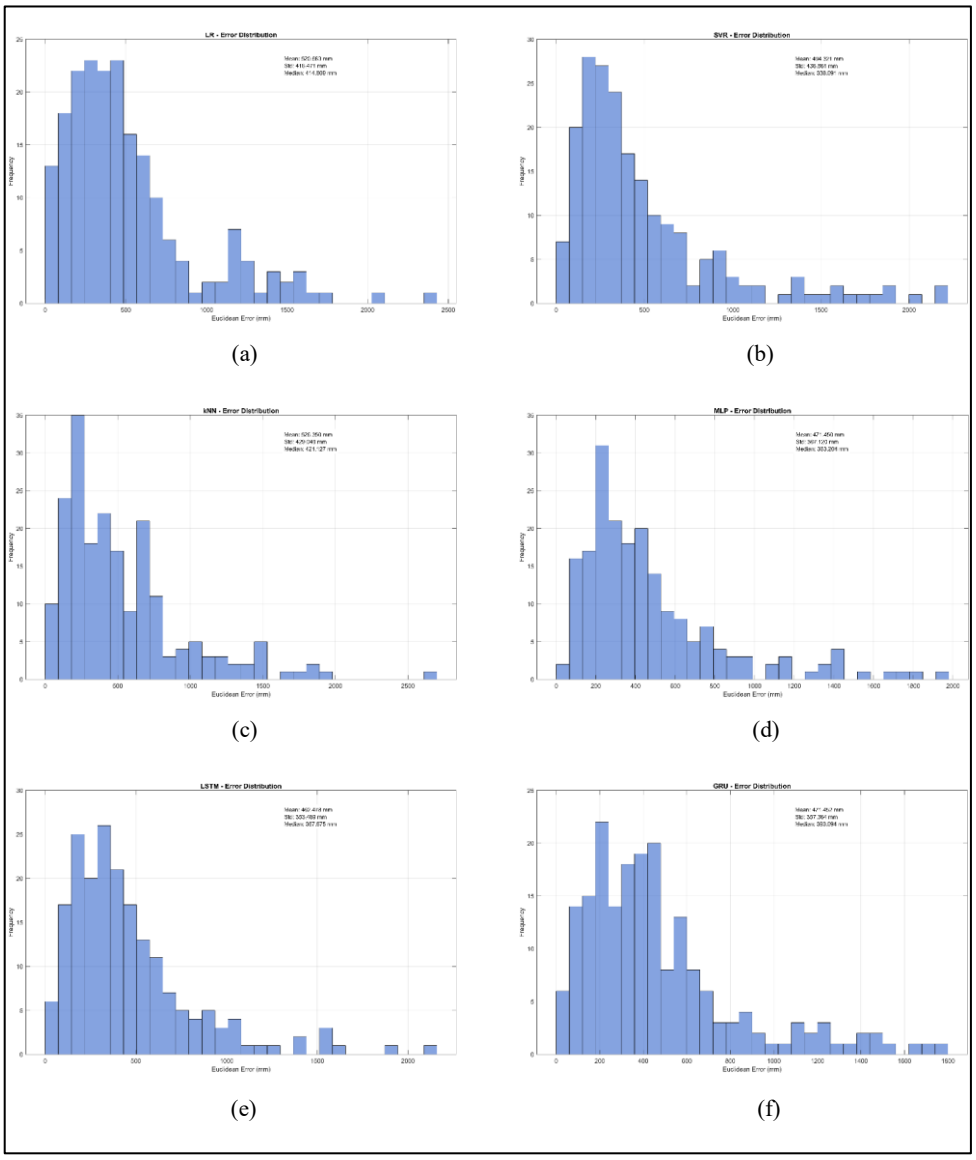

Figure 4.4 Error Distribution for D1-D2-D3 situation in FCPR using (a) LR (b) SVR (c) kNN (d) MLP (e) LSTM (f) GRU.

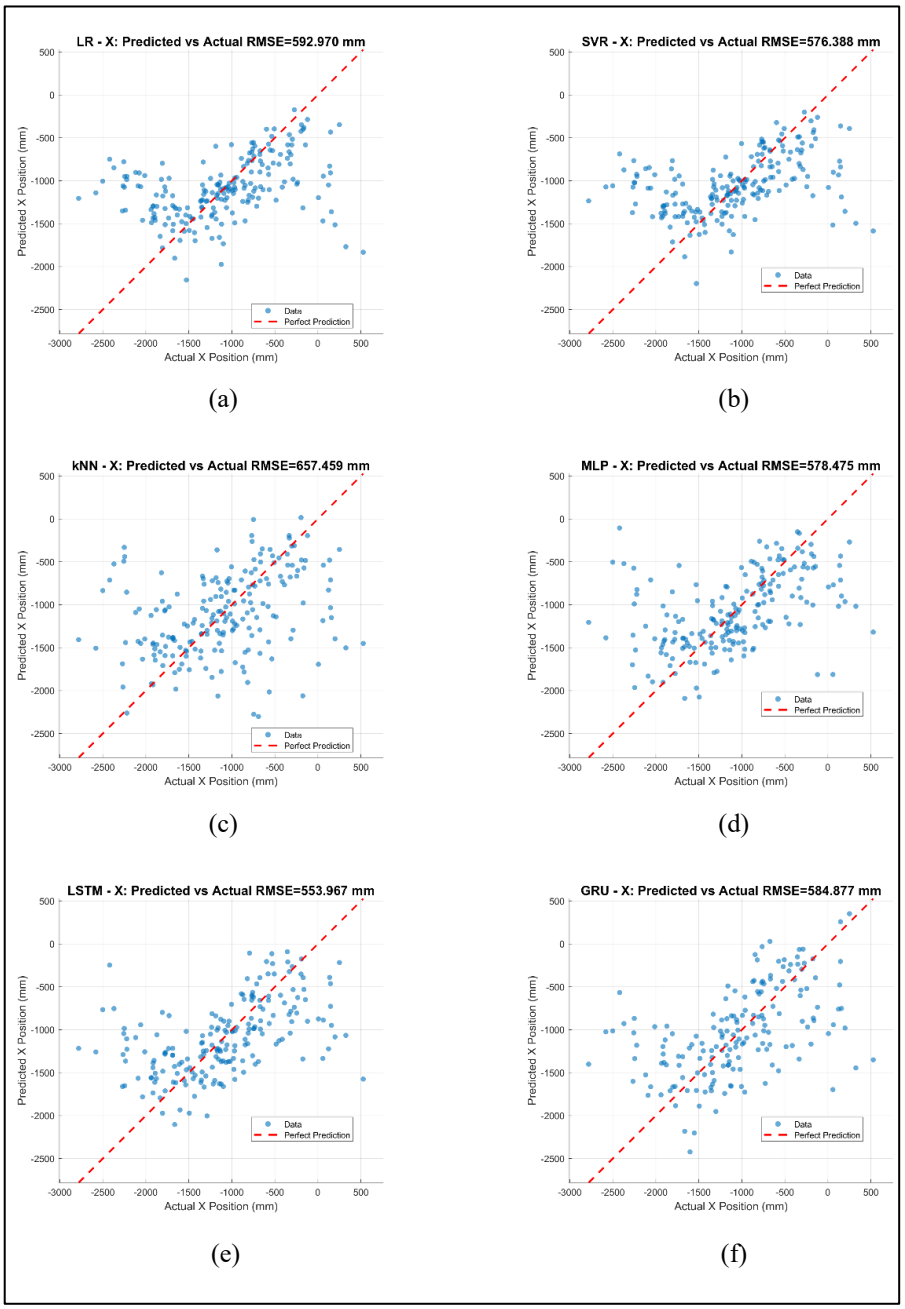

Figure 4.5 Actual versus Predicted X position for D1-D2 situation in FCPR using (a) LR (b) SVR (c) kNN (d) MLP (e) LSTM (f) GRU.

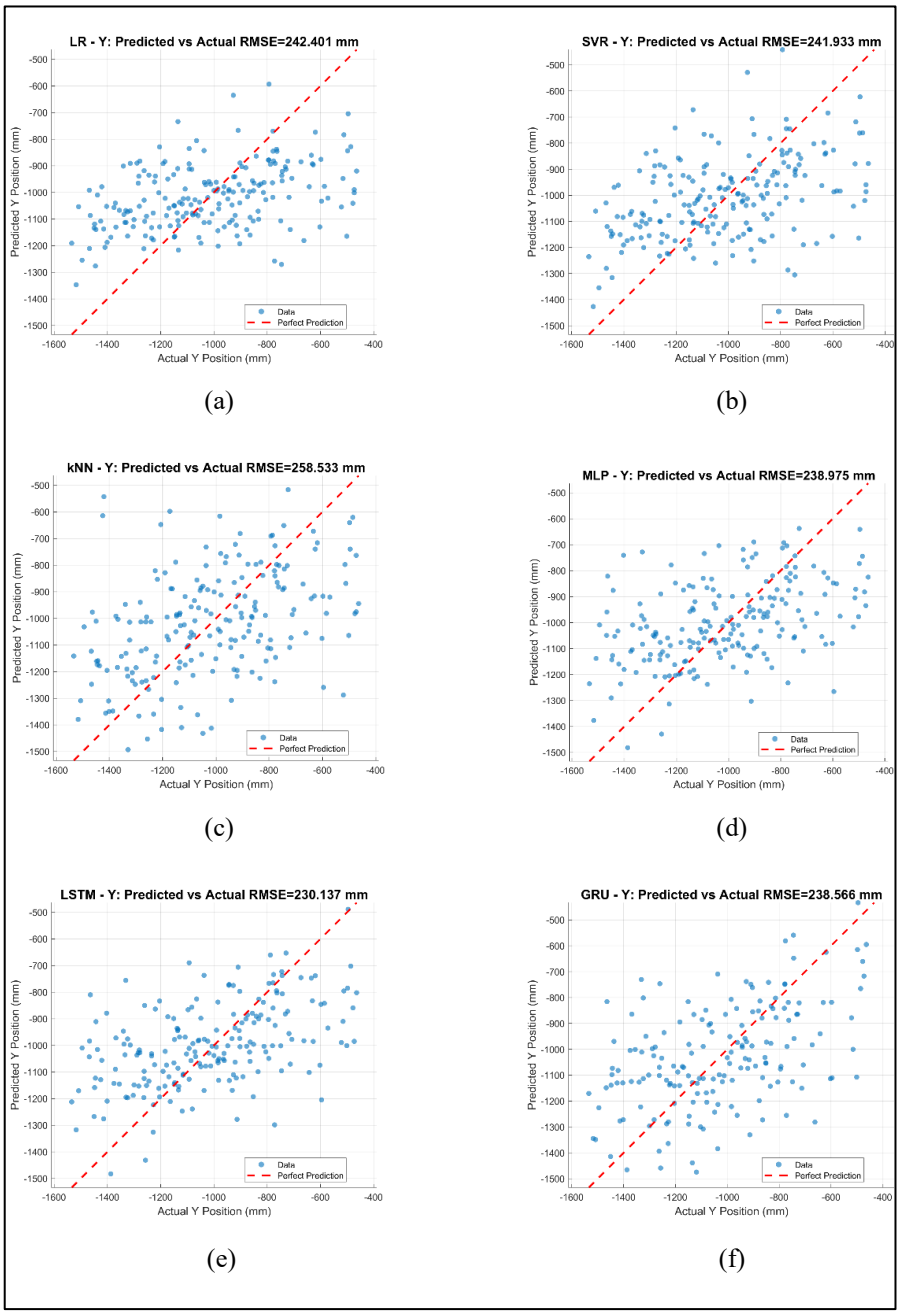

Figure 4.6 Actual versus Predicted Y position for D1-D2 situation in FCPR using (a) LR (b) SVR (c) kNN (d) MLP (e) LSTM (f) GRU.

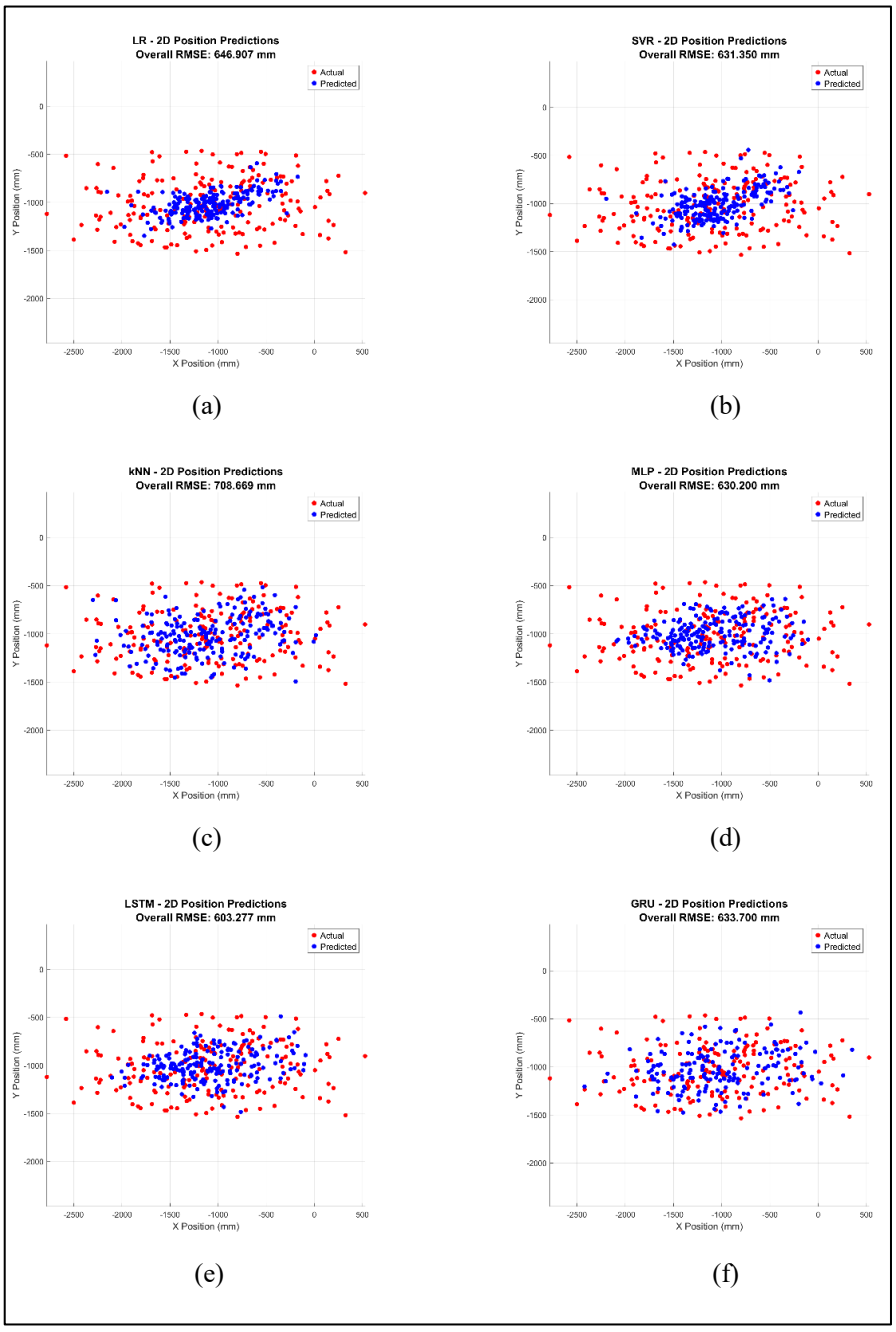

Figure 4.7 2D position predictions for D1-D2 situation in FCPR using (a) LR (b) SVR (c) kNN (d) MLP (e) LSTM (f) GRU.

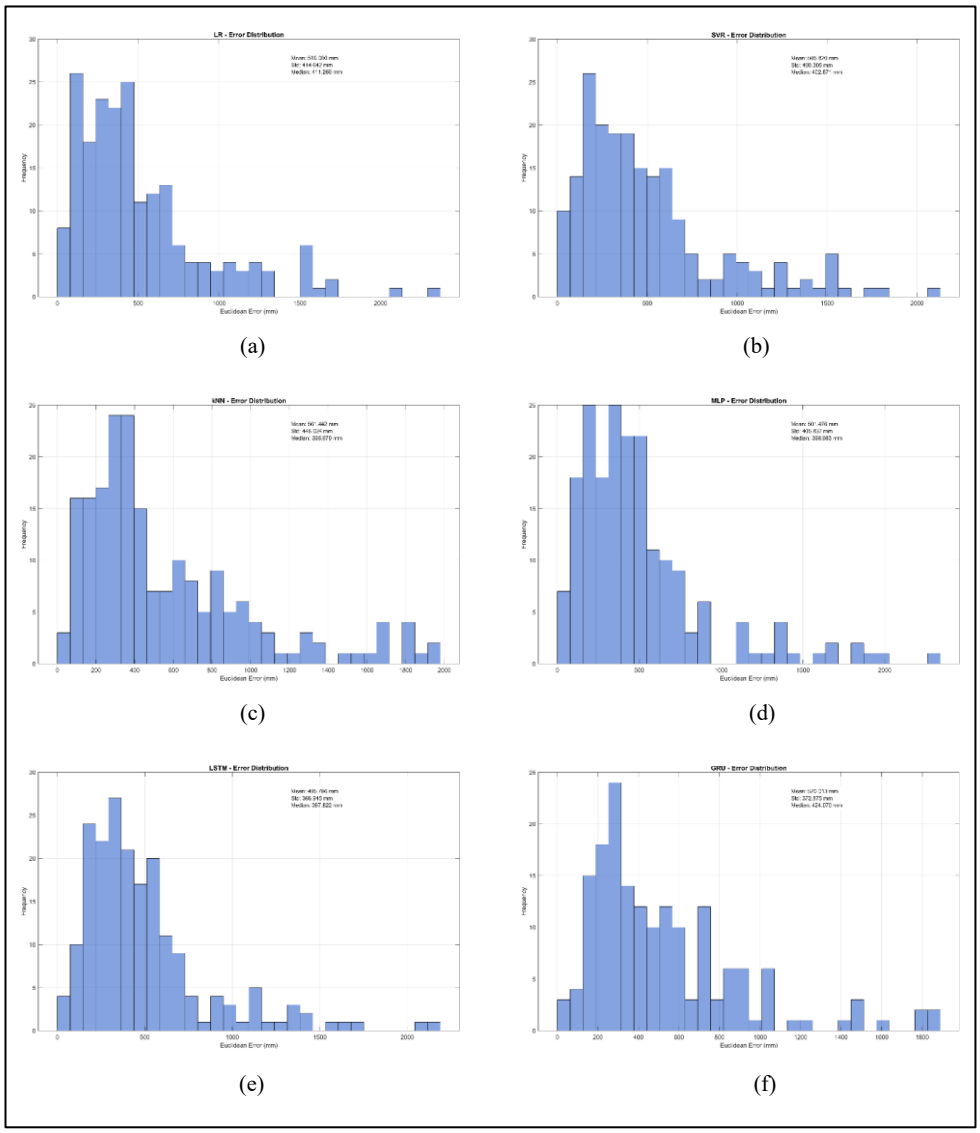

Figure 4.8 Error Distribution for D1-D2 situation in FCPR using (a) LR (b) SVR (c) kNN (d) MLP (e) LSTM (f) GRU.

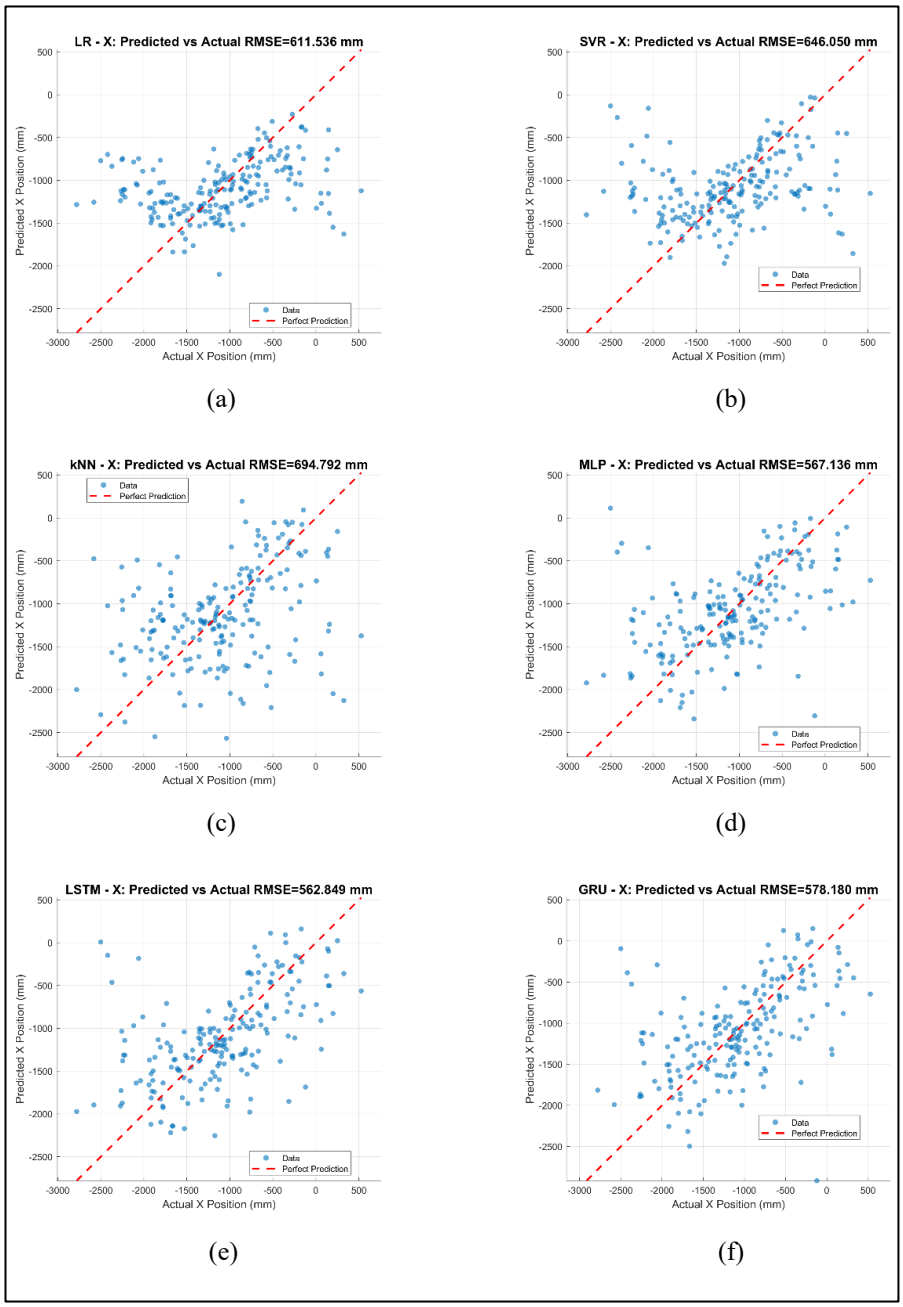

Figure 4.9 Actual versus Predicted X position for D1-D3 situation in FCPR using (a) LR (b) SVR (c) kNN (d) MLP (e) LSTM (f) GRU.

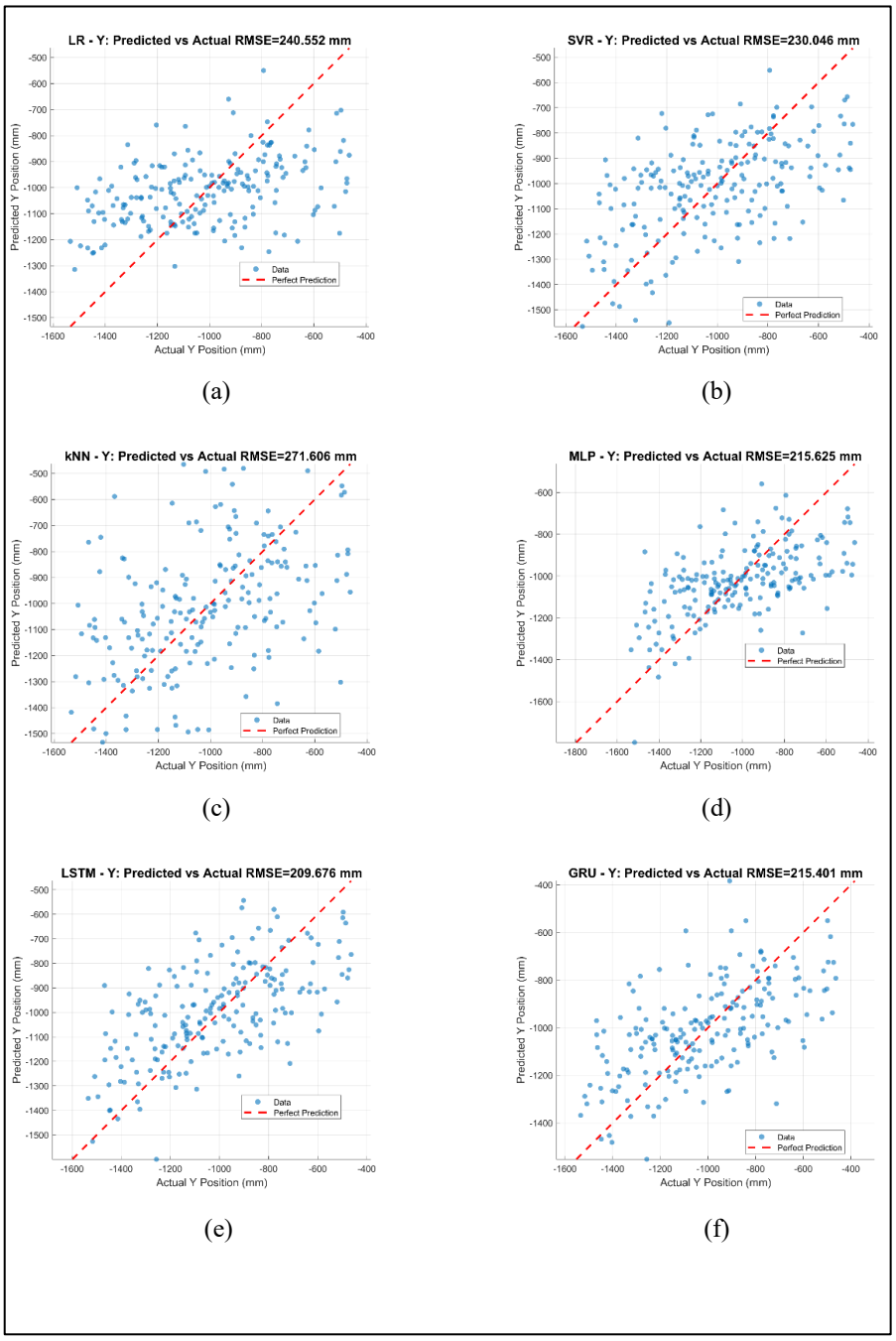

Figure 4.10 Actual versus Predicted Y position for D1-D3 situation in FCPR using (a) LR (b) SVR (c) kNN (d) MLP (e) LSTM (f) GRU.

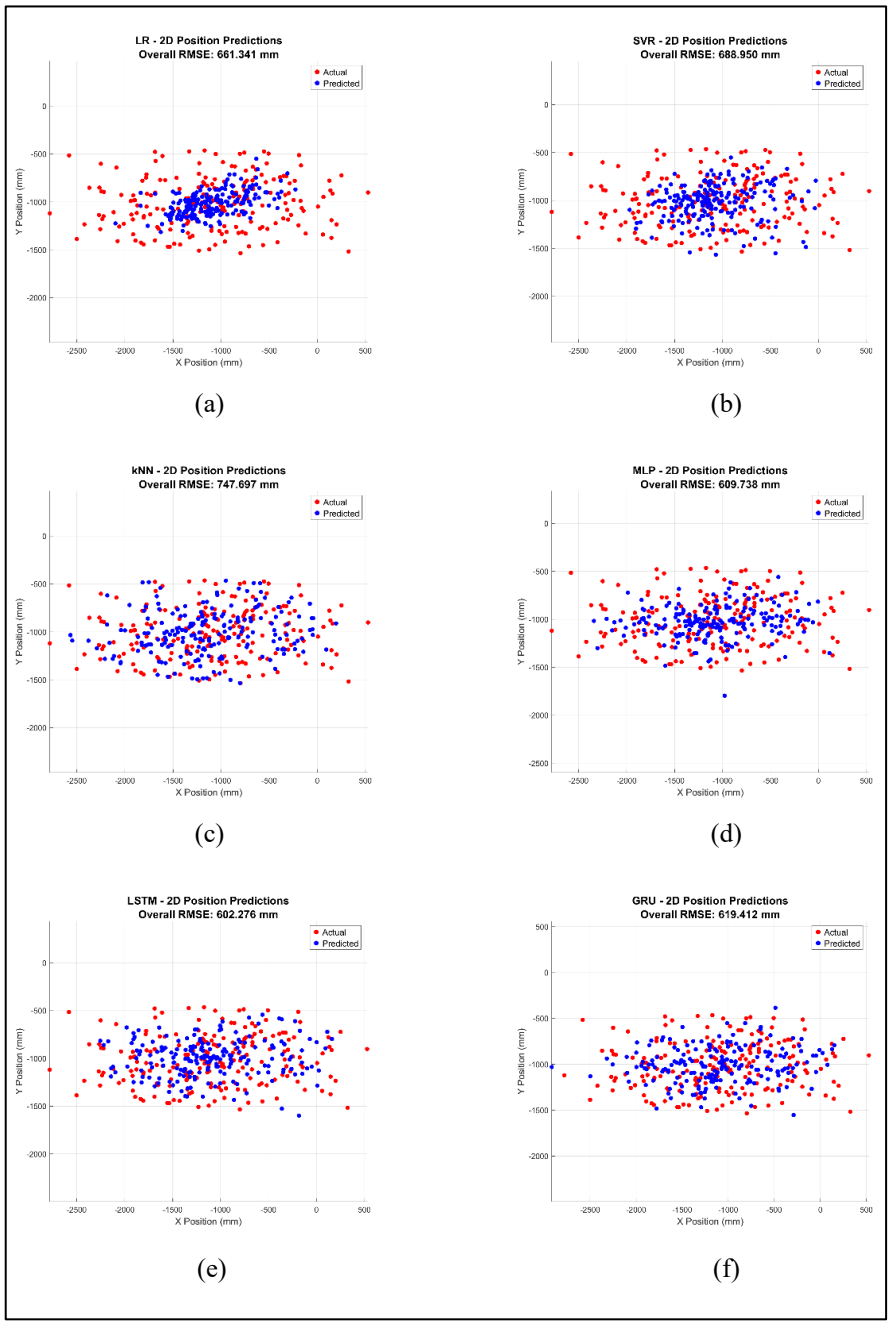

Figure 4.11 2D position predictions for D1-D3 situation in FCPR using (a) LR (b) SVR (c) kNN (d) MLP (e) LSTM (f) GRU.

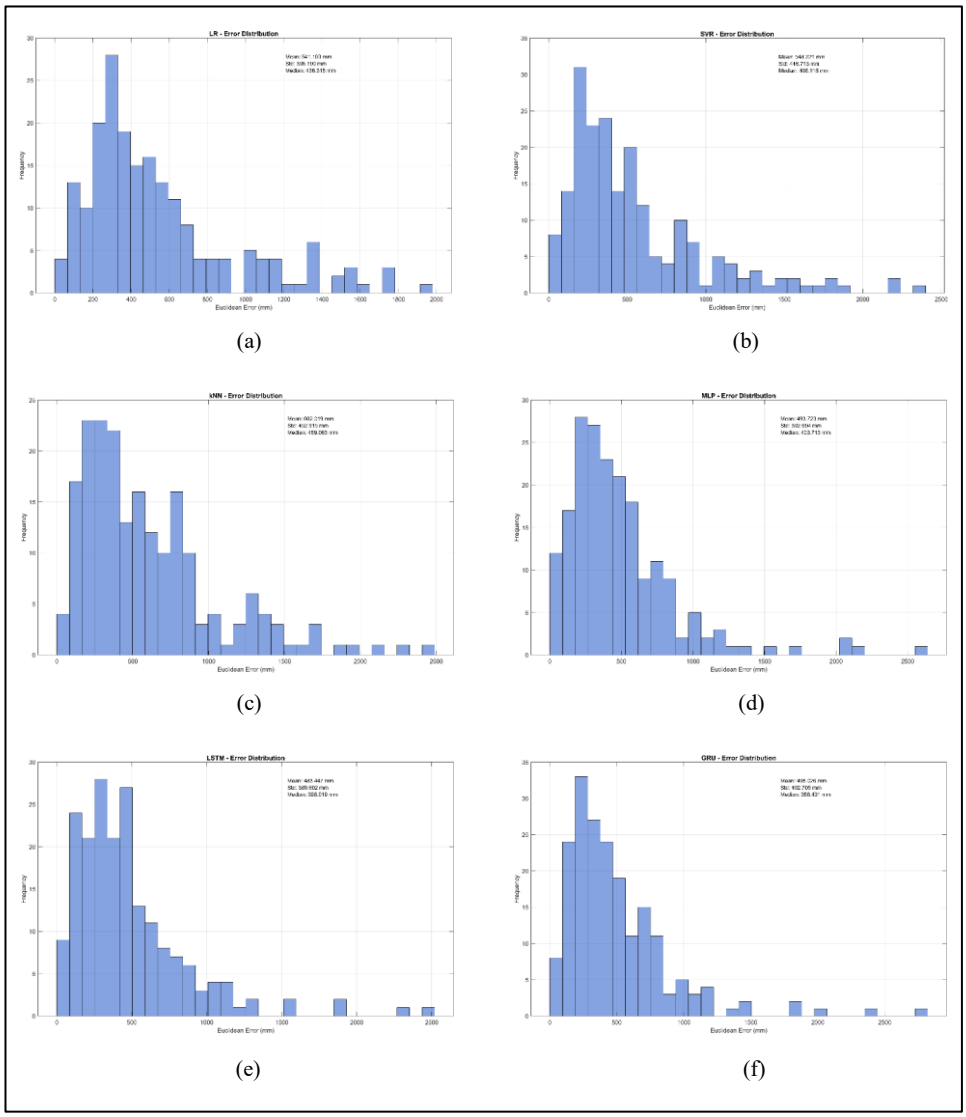

Figure 4.12 Error Distribution for D1-D3 situation in FCPR using (a) LR (b) SVR (c) kNN (d) MLP (e) LSTM (f) GRU.

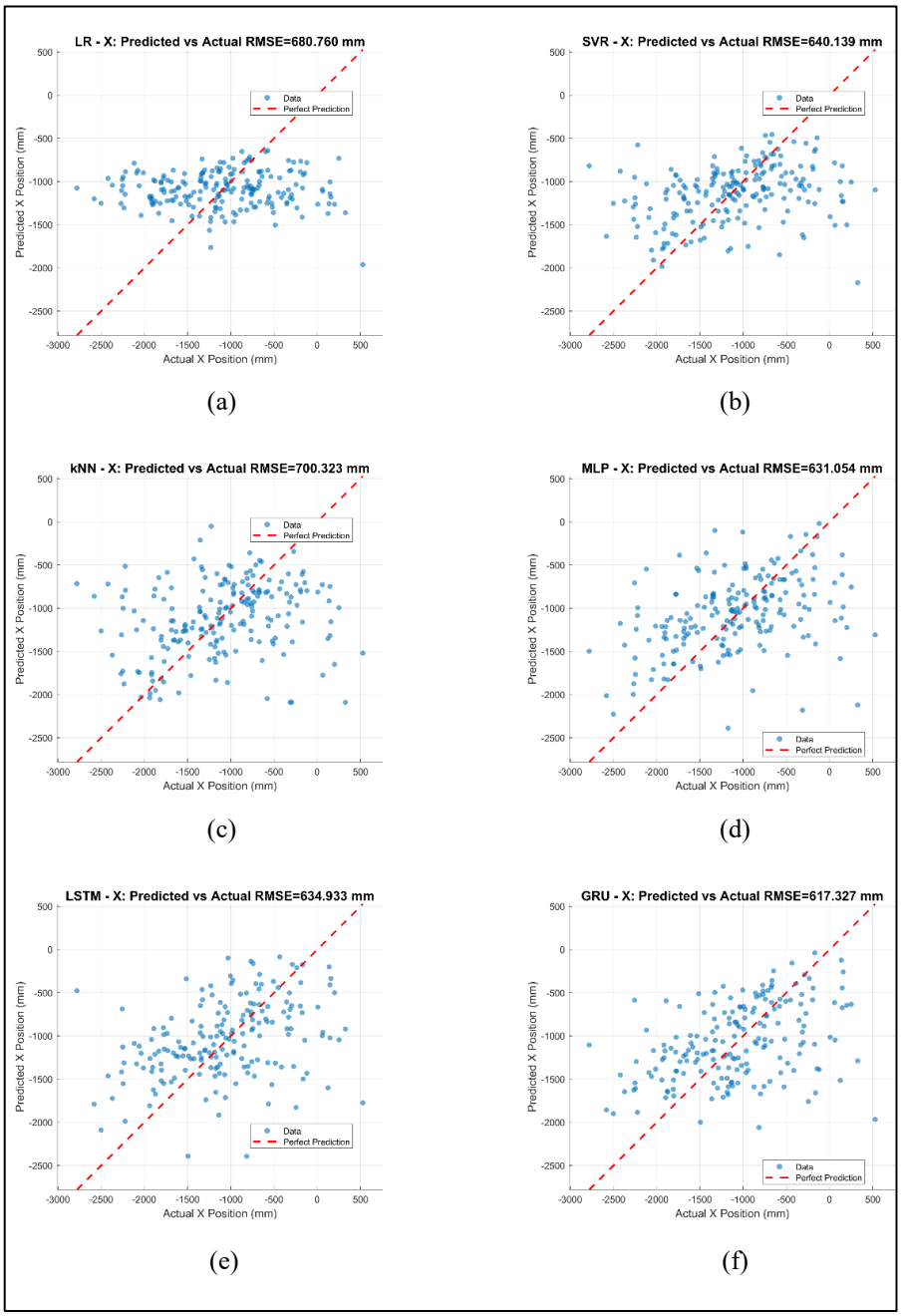

Figure 4.13 Actual versus Predicted X position for D2-D3 situation in FCPR using (a) LR (b) SVR (c) kNN (d) MLP (e) LSTM (f) GRU.

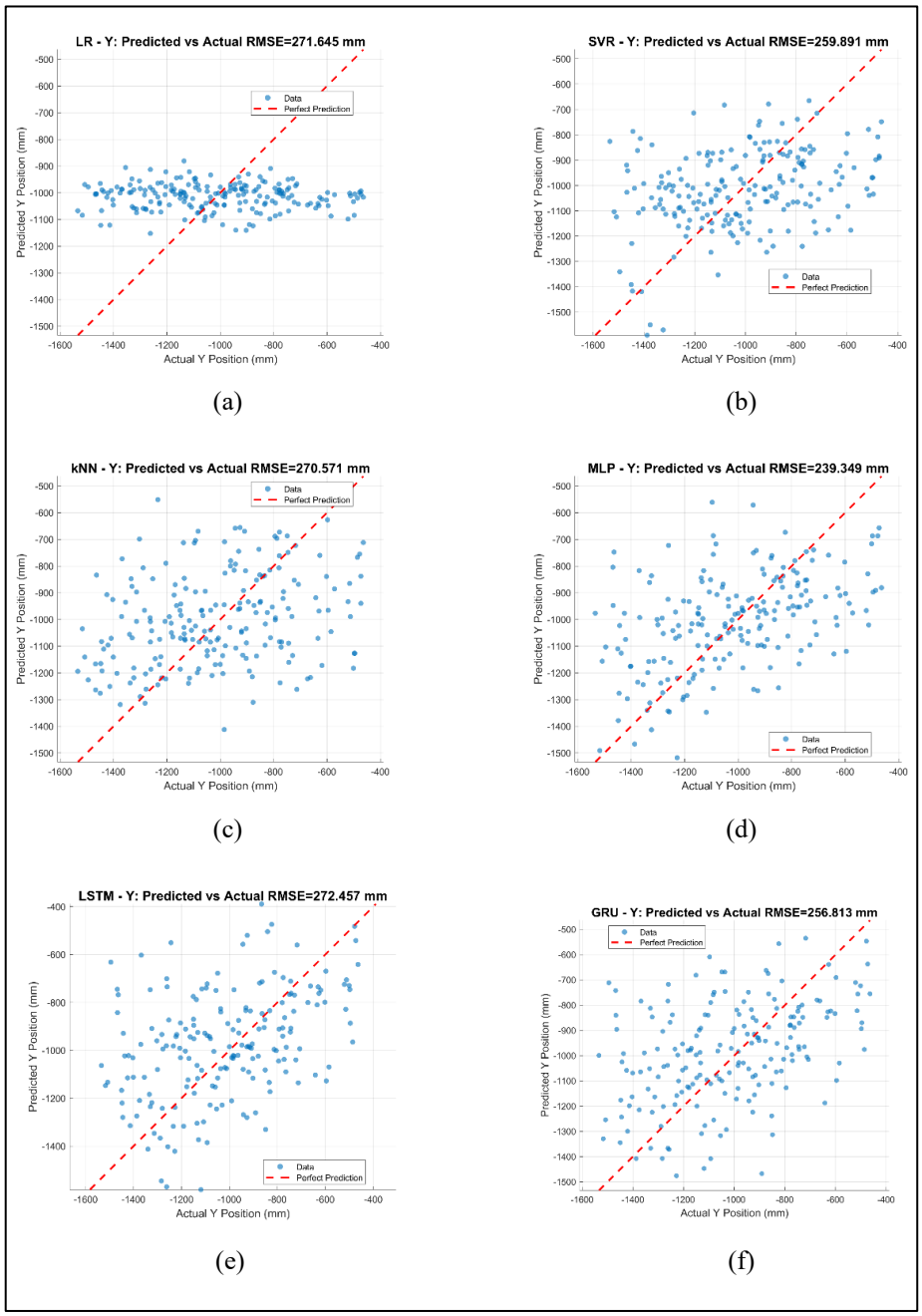

Figure 4.14 Actual versus Predicted Y position for D2-D3 situation in FCPR using (a) LR (b) SVR (c) kNN (d) MLP (e) LSTM (f) GRU.

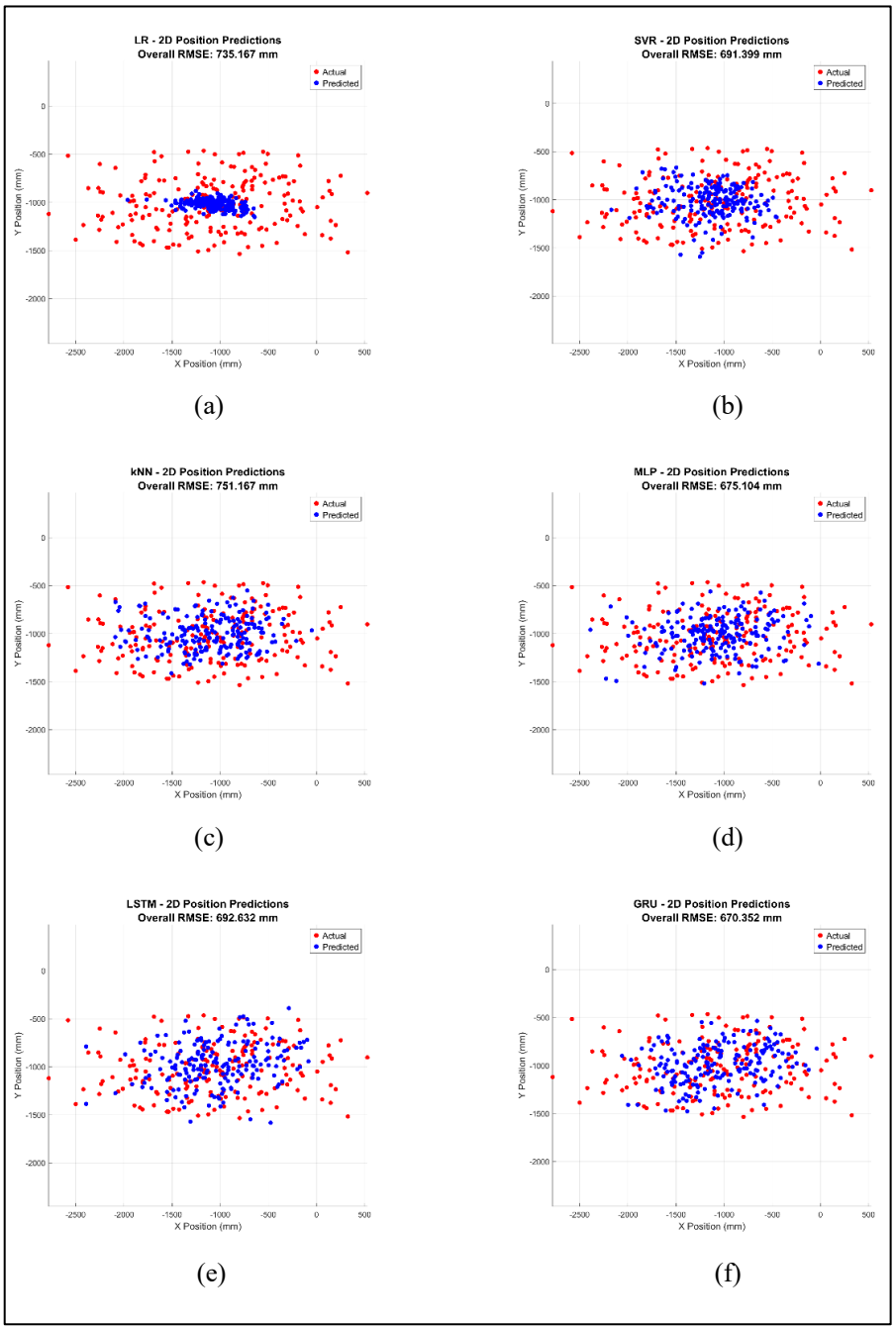

Figure 4.15 2D position predictions for D2-D3 situation in FCPR using (a) LR (b) SVR (c) kNN (d) MLP (e) LSTM (f) GRU.

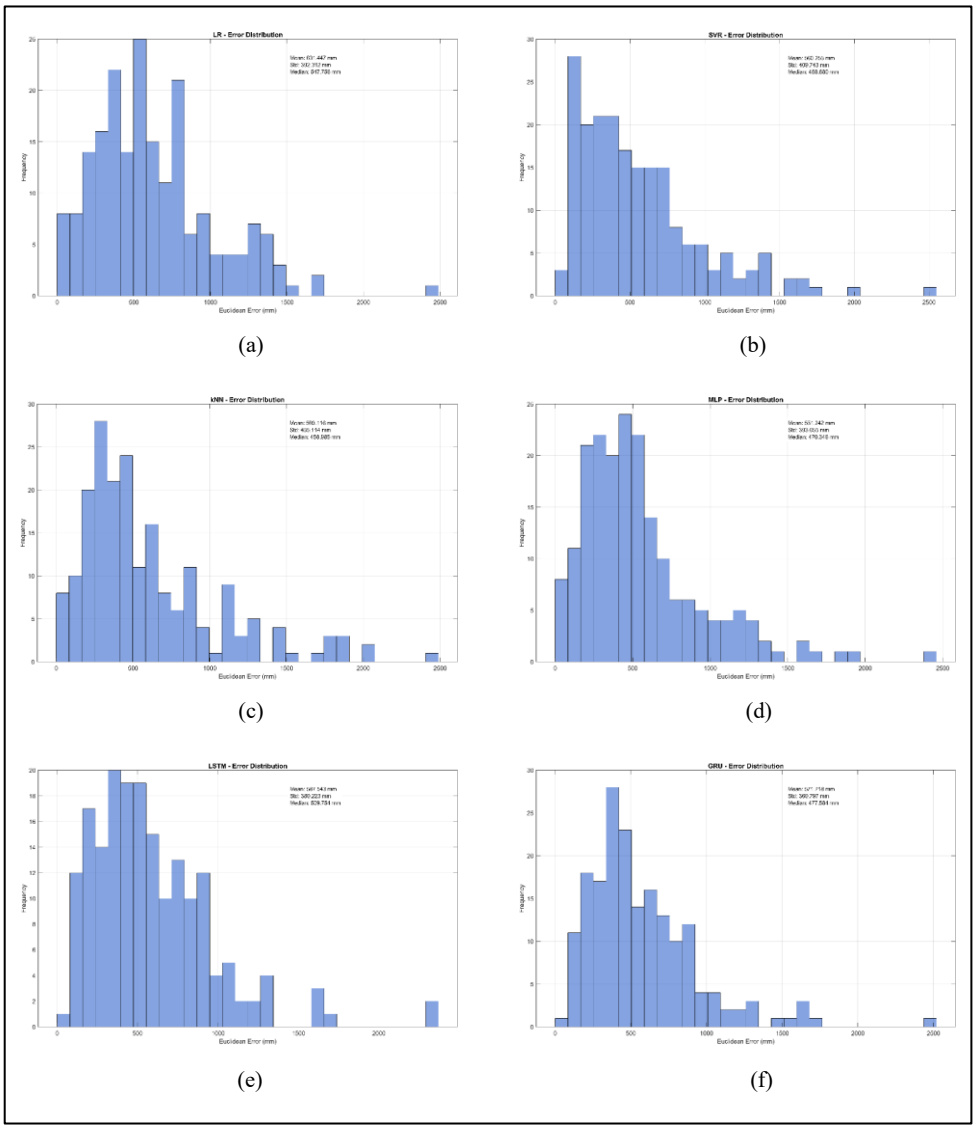

Figure 4.16 Error Distribution for D2-D3 situation in FCPR using (a) LR (b) SVR (c) kNN (d) MLP (e) LSTM (f) GRU.

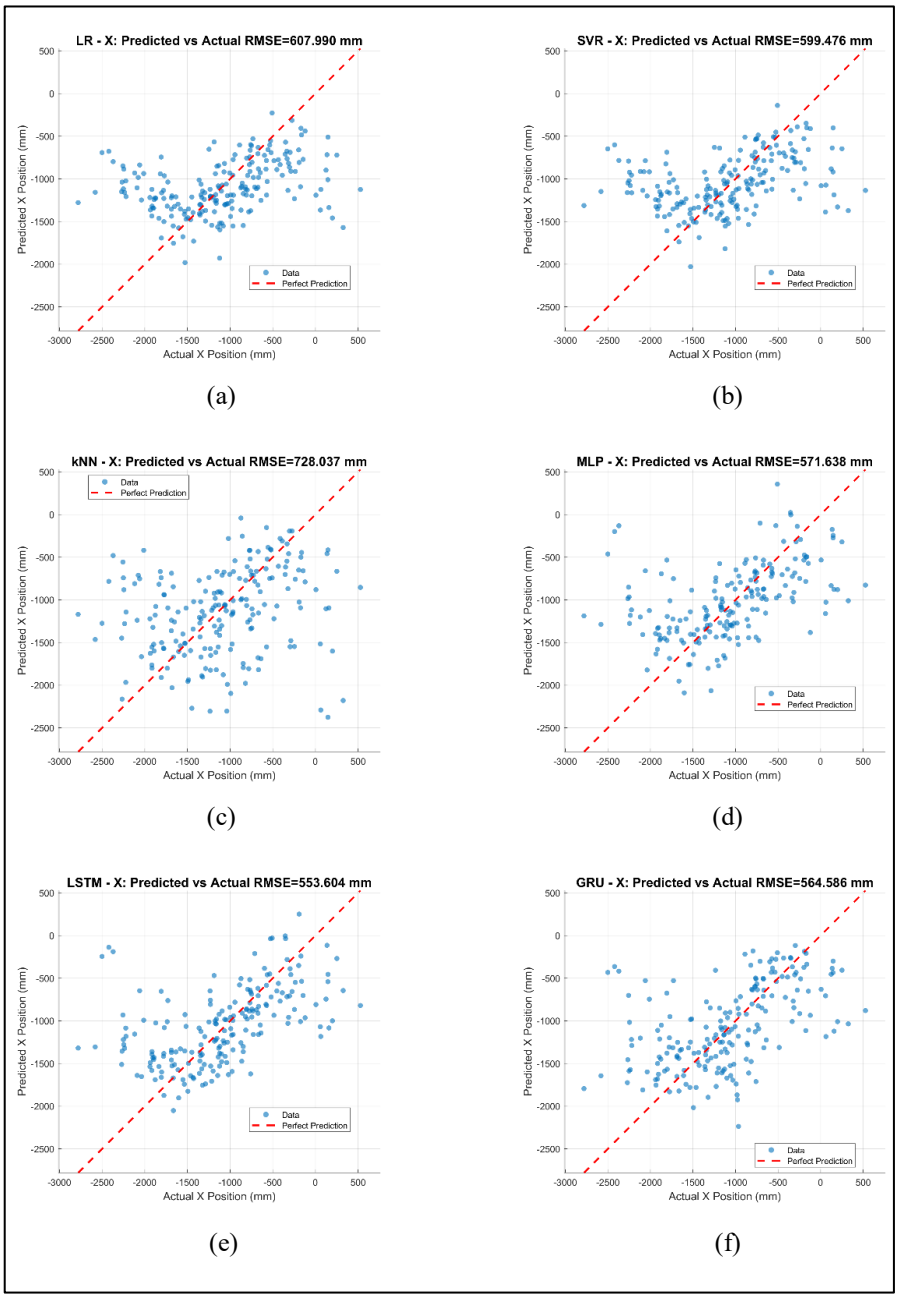

Figure 4.17 Actual versus Predicted X position for D1 situation in FCPR using (a) LR (b) SVR (c) kNN (d) MLP (e) LSTM (f) GRU.

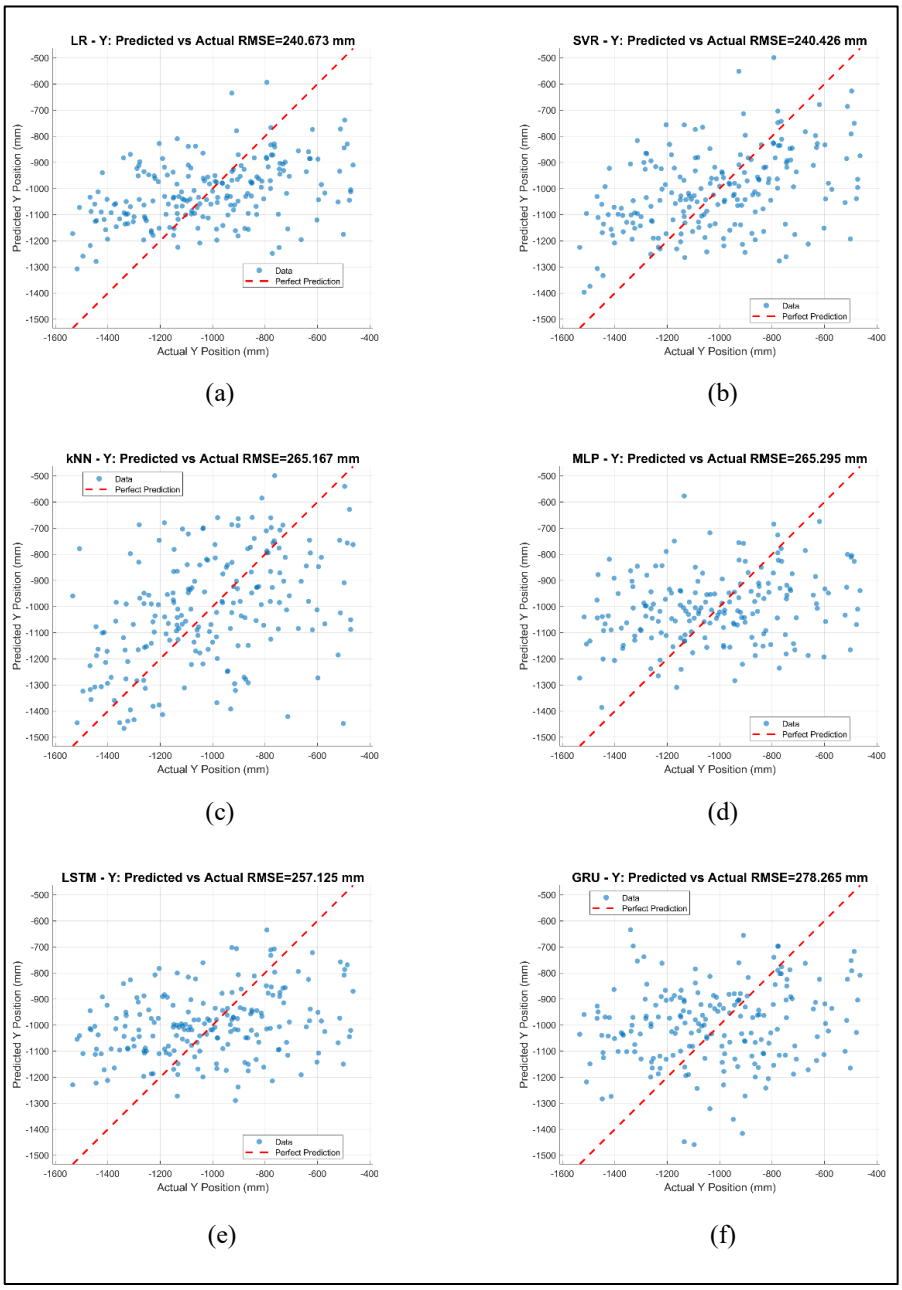

Figure 4.18 Actual versus Predicted Y position for D1 situation in FCPR using (a) LR (b) SVR (c) kNN (d) MLP (e) LSTM (f) GRU.

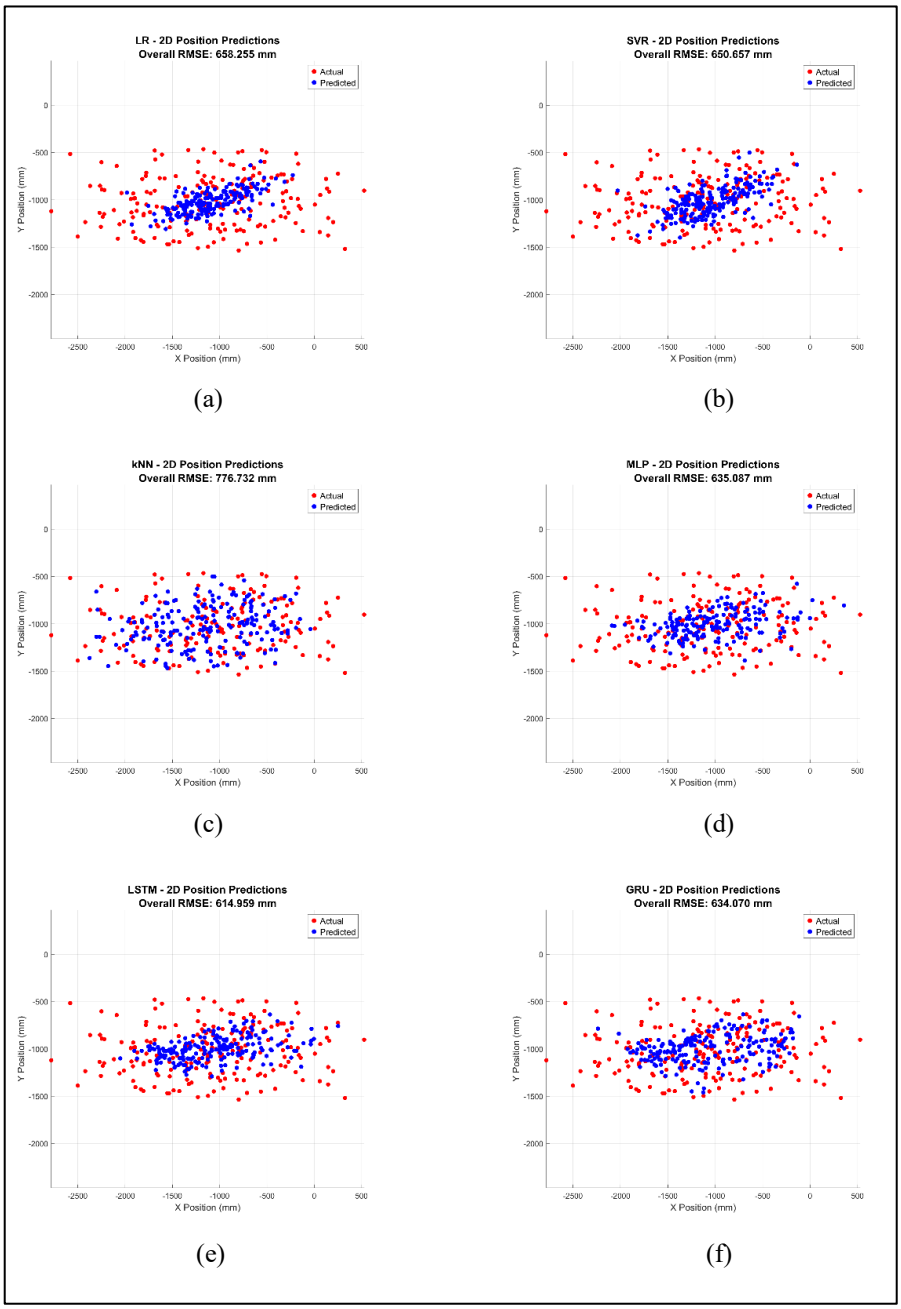

Figure 4.19 2D position predictions for D1 situation in FCPR using (a) LR (b) SVR (c) kNN (d) MLP (e) LSTM (f) GRU.

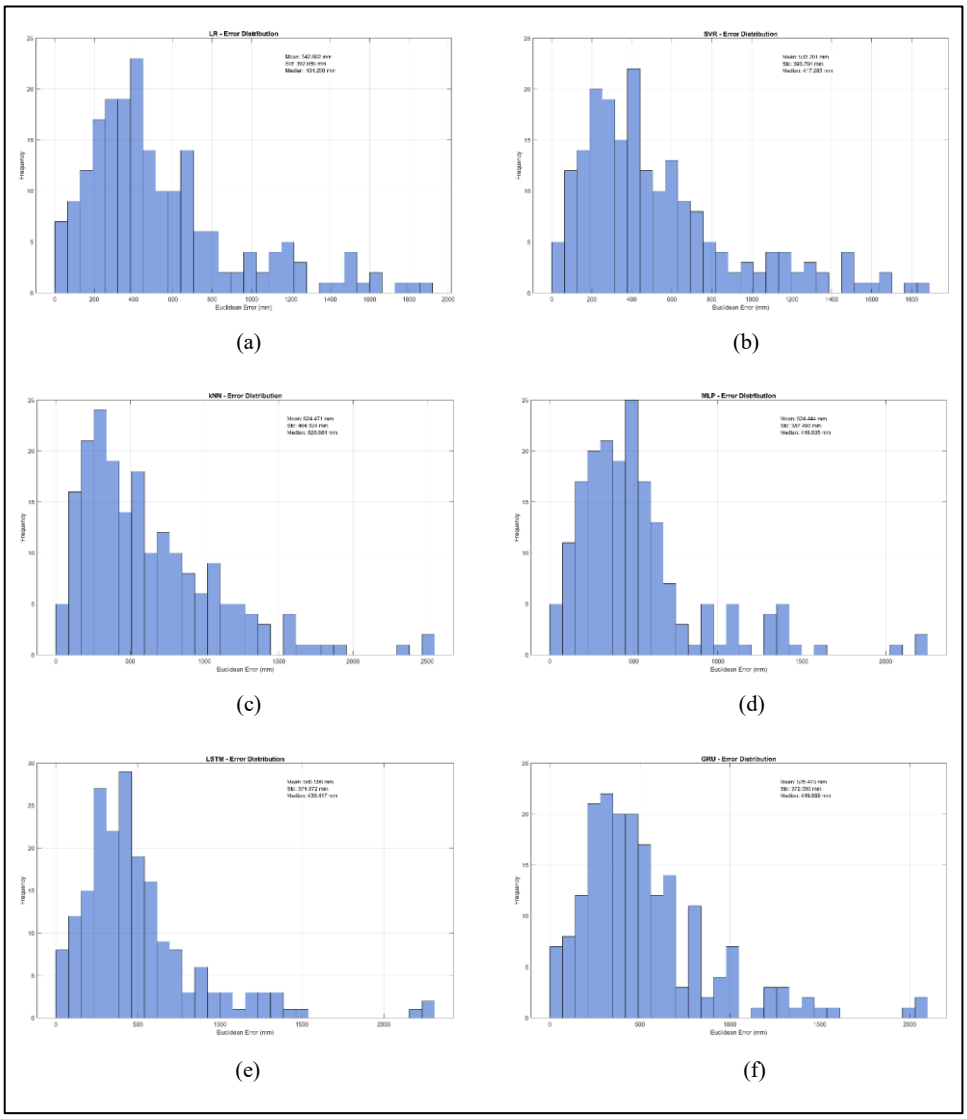

Figure 4.20 Error Distribution for D1 situation in FCPR using (a) LR (b) SVR (c) kNN (d) MLP (e) LSTM (f) GRU.

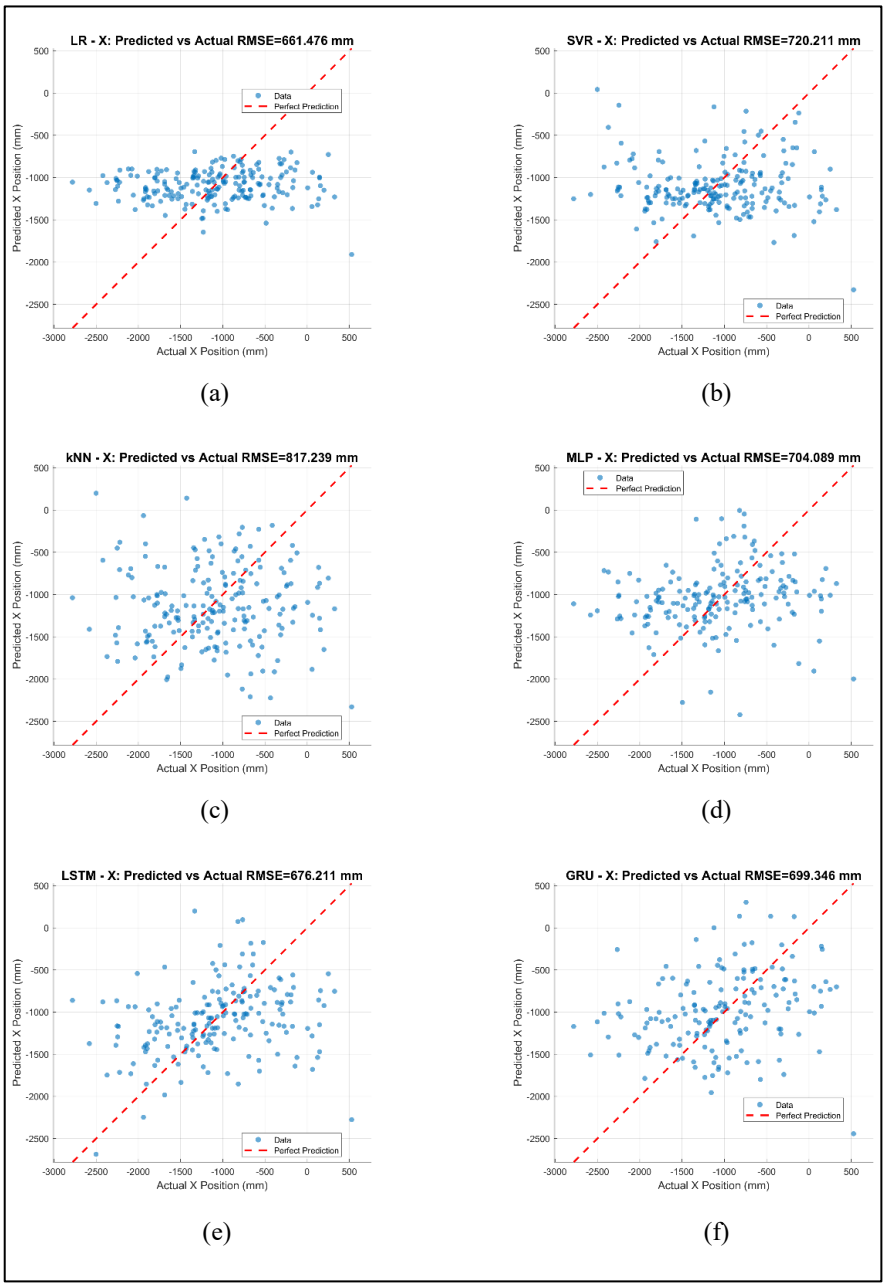

Figure 4.21 Actual versus Predicted X position for D2 situation in FCPR using (a) LR (b) SVR (c) kNN (d) MLP (e) LSTM (f) GRU.

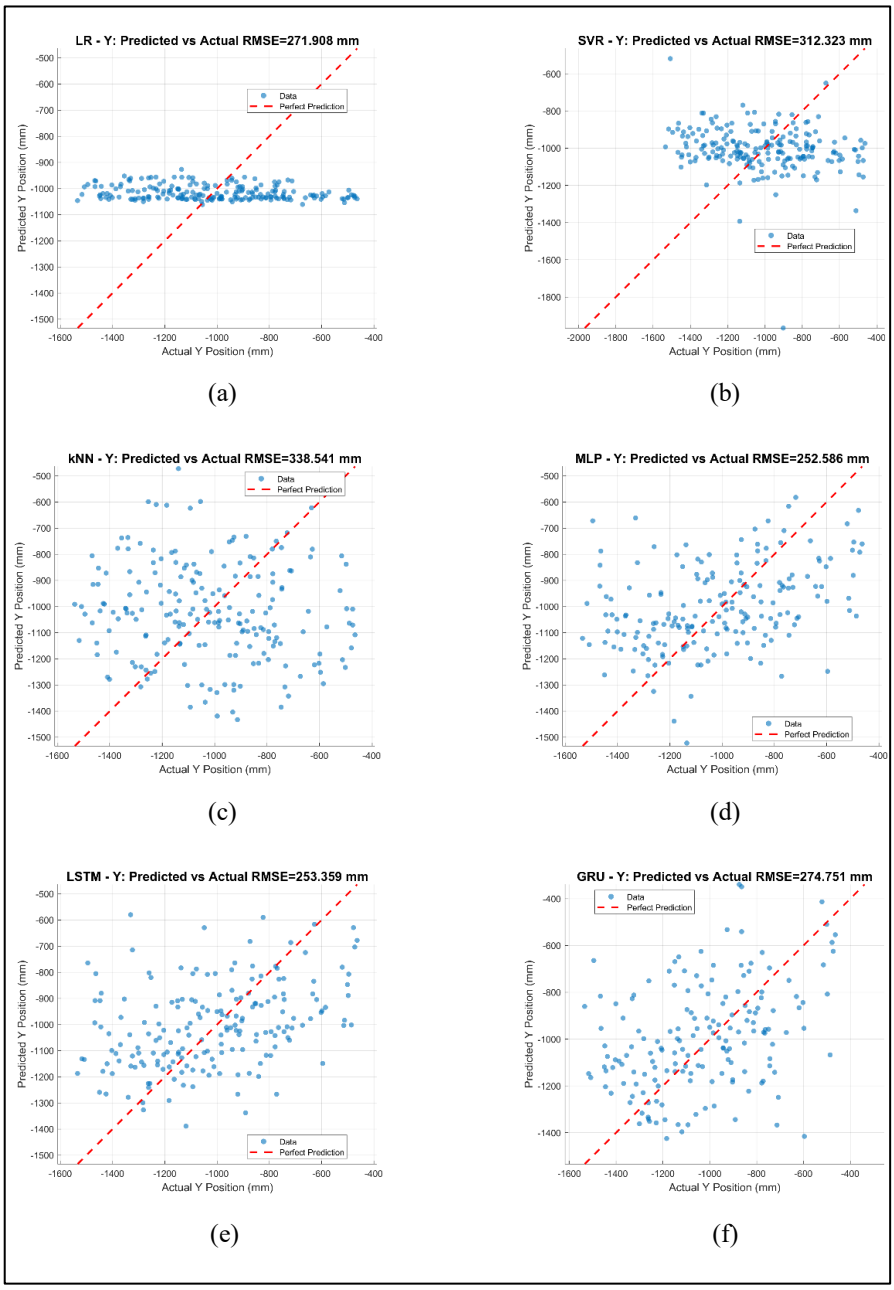

Figure 4.22 Actual versus Predicted Y position for D2 situation in FCPR using (a) LR (b) SVR (c) kNN (d) MLP (e) LSTM (f) GRU.

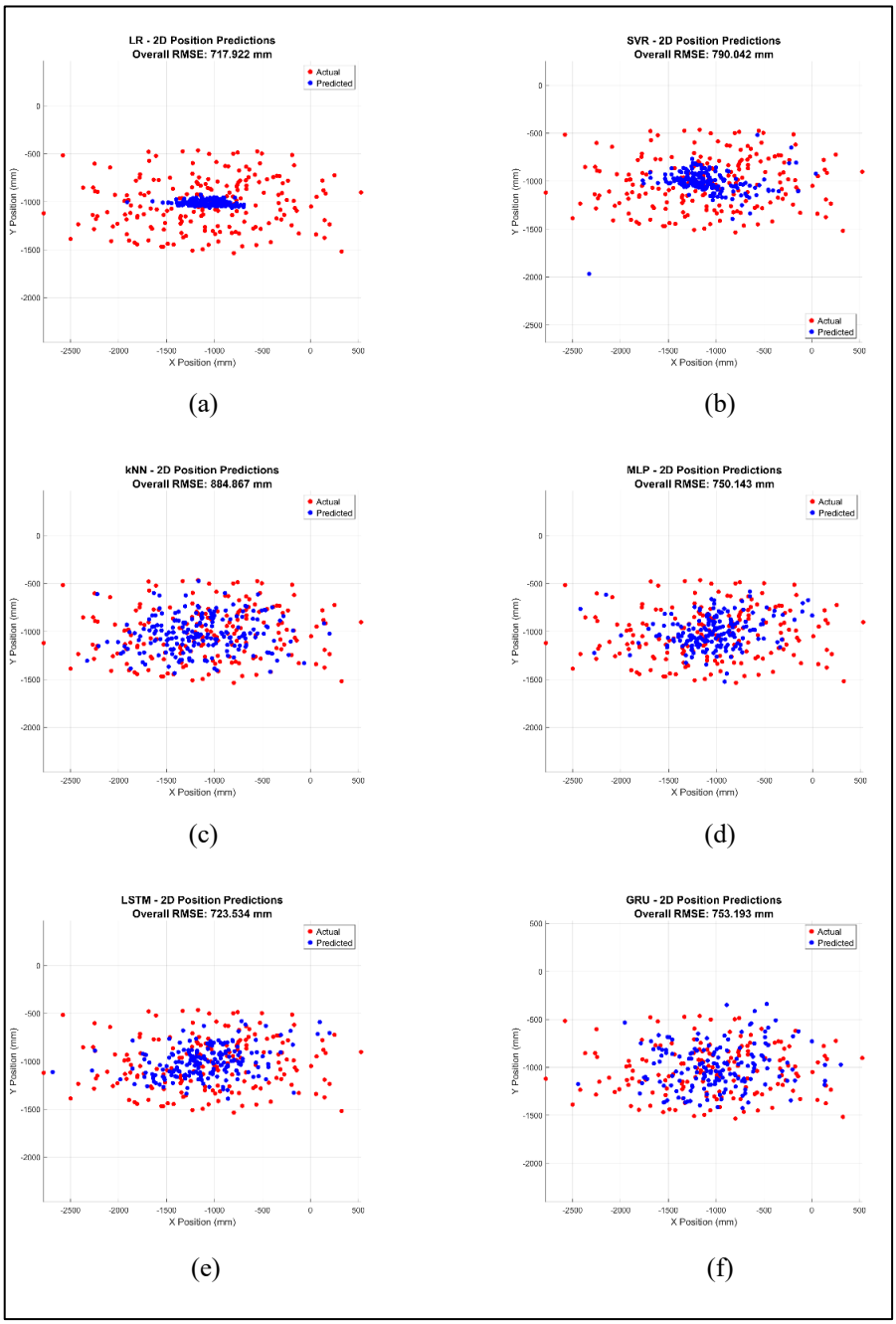

Figure 4.23 2D position predictions for D2 situation in FCPR using (a) LR (b) SVR (c) kNN (d) MLP (e) LSTM (f) GRU.

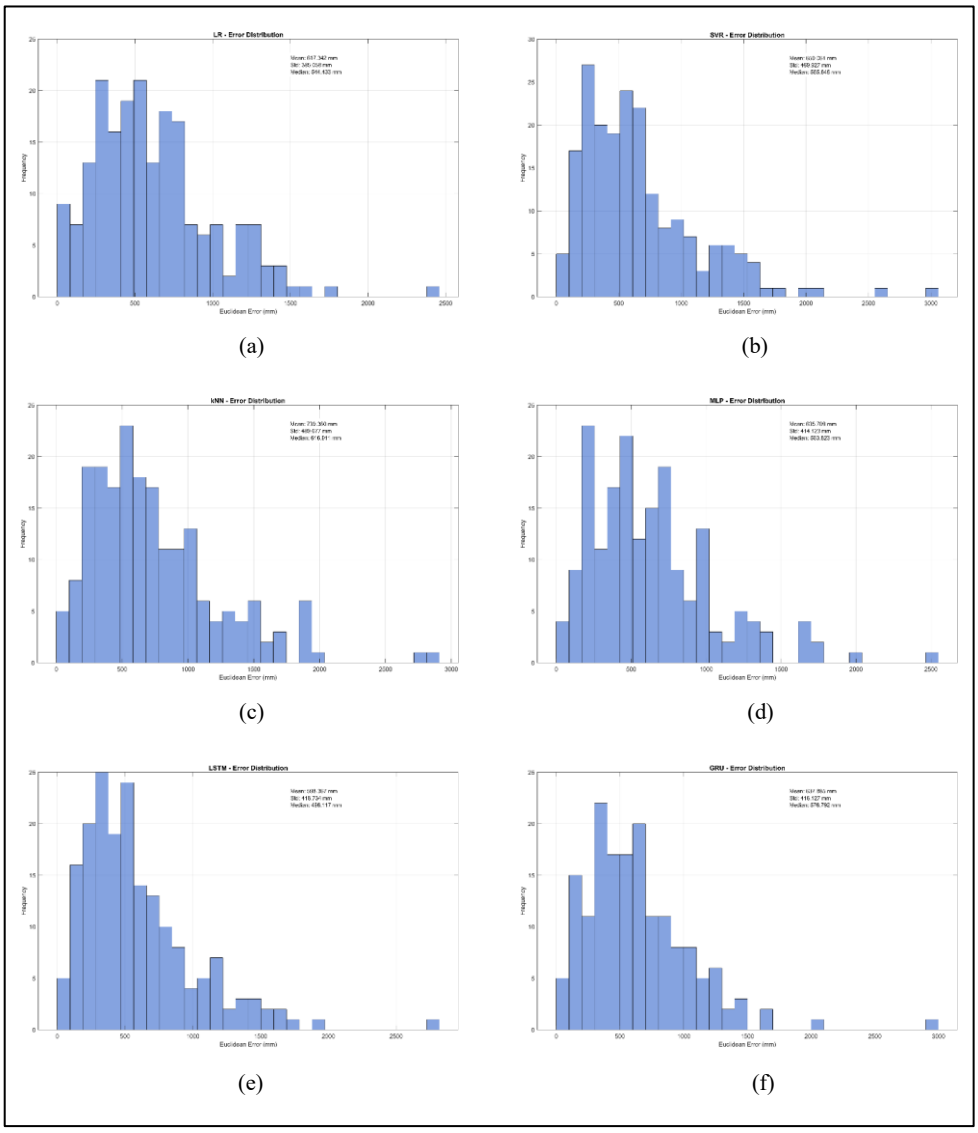

Figure 4.24 Error Distribution for D2 situation in FCPR using (a) LR (b) SVR (c) kNN (d) MLP (e) LSTM (f) GRU.

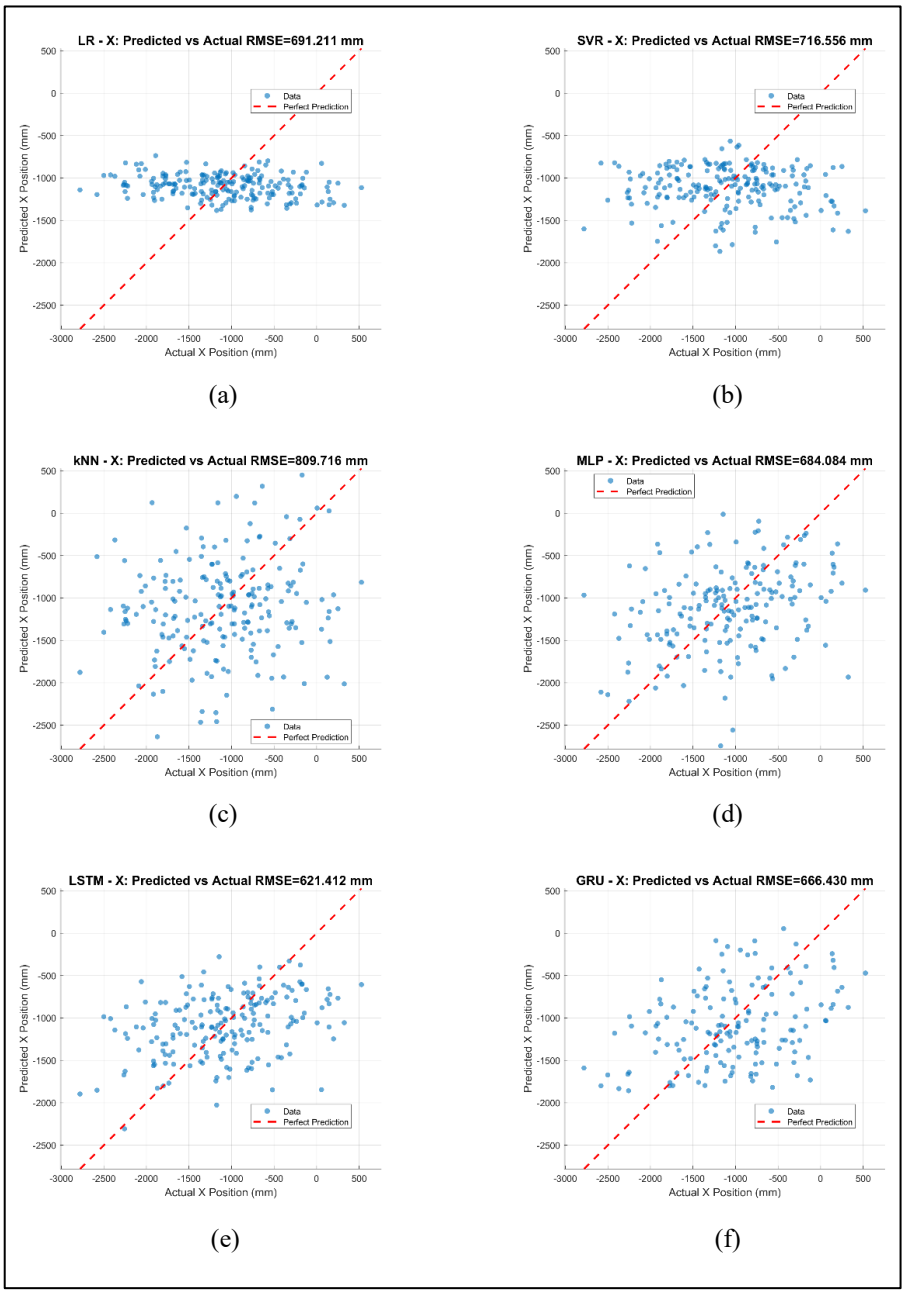

Figure 4.25 Actual versus Predicted X position for D3 situation in FCPR using (a) LR (b) SVR (c) kNN (d) MLP (e) LSTM (f) GRU.

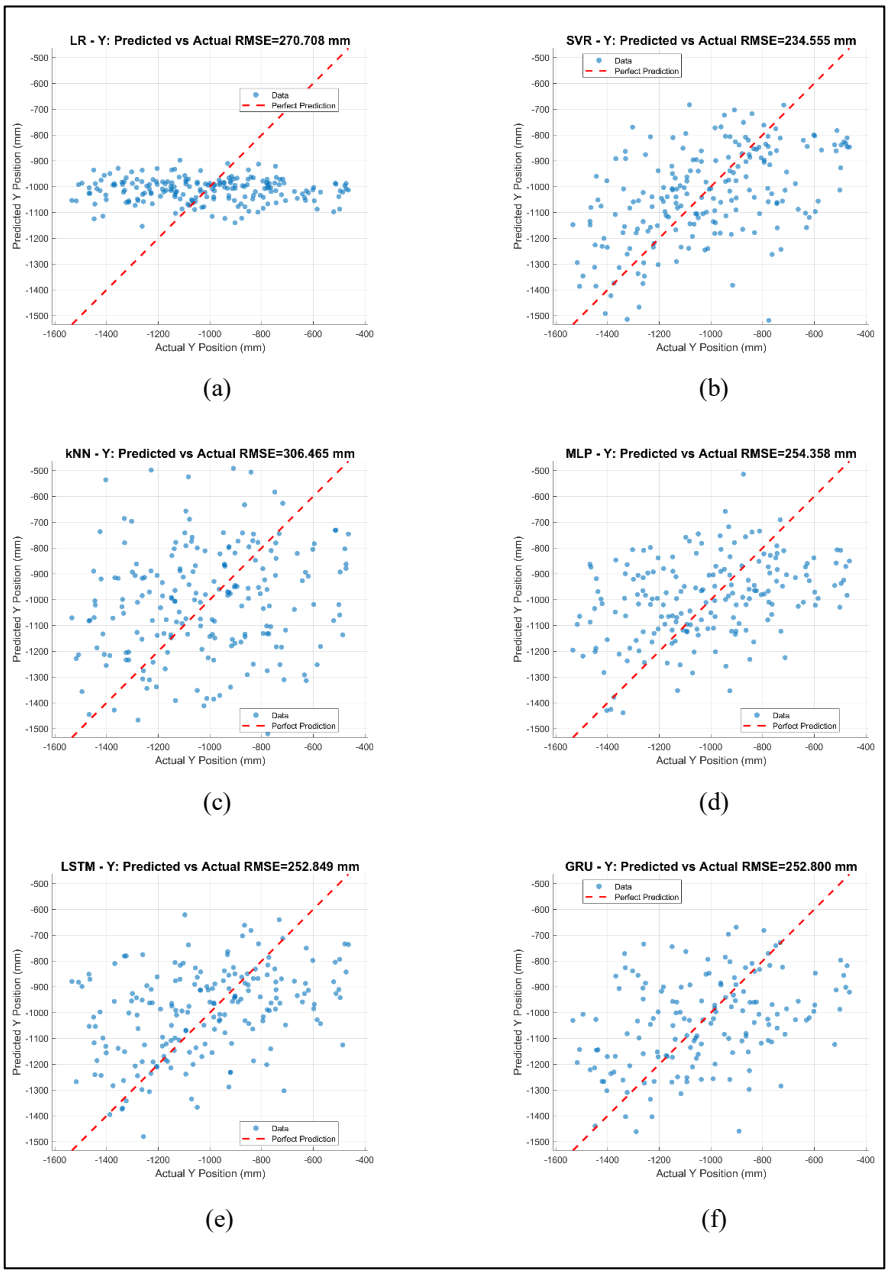

Figure 4.26 Actual versus Predicted Y position for D3 situation in FCPR using (a) LR (b) SVR (c) kNN (d) MLP (e) LSTM (f) GRU.

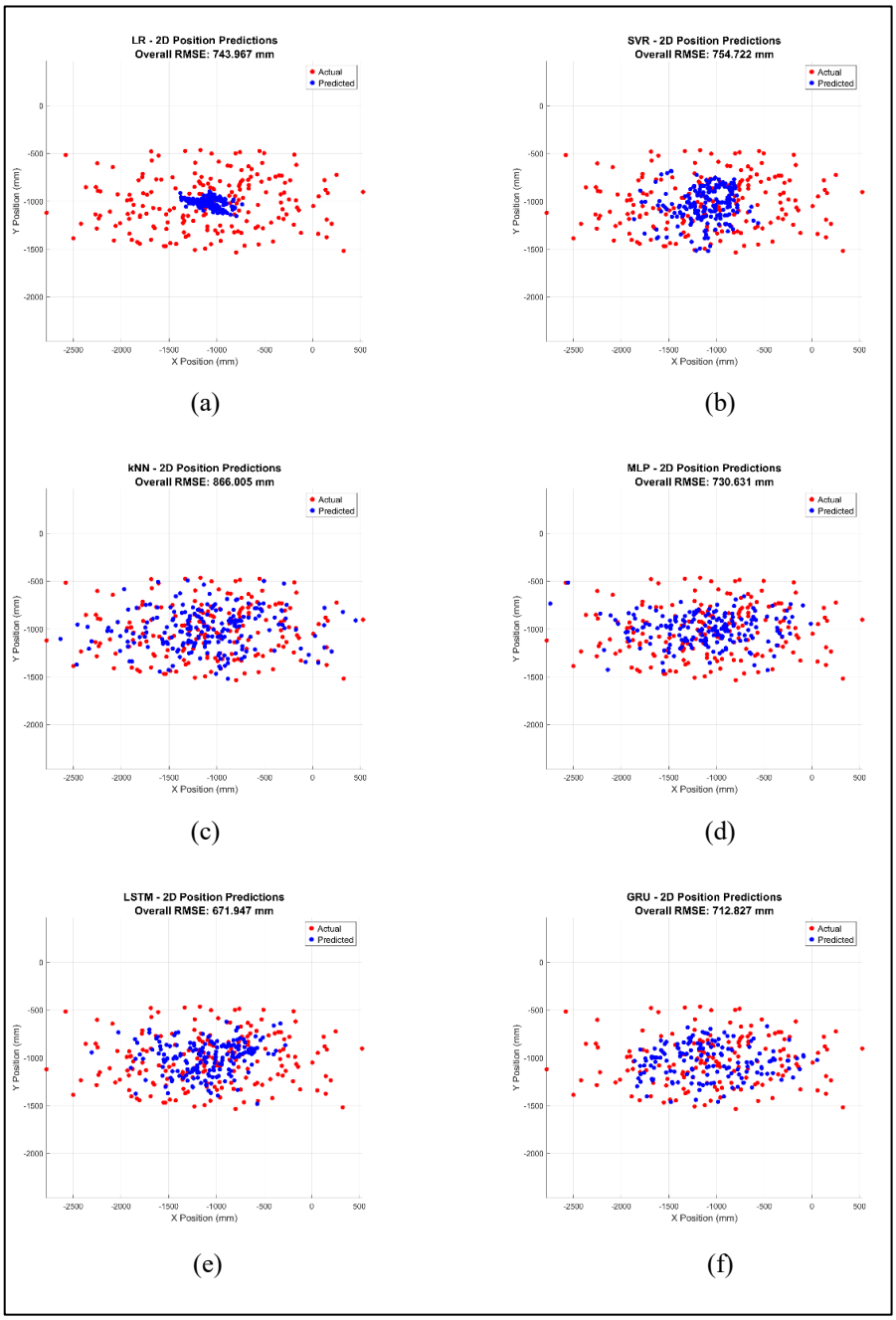

Figure 4.27 2D position predictions for D3 situation in FCPR using (a) LR (b) SVR (c) kNN (d) MLP (e) LSTM (f) GRU.

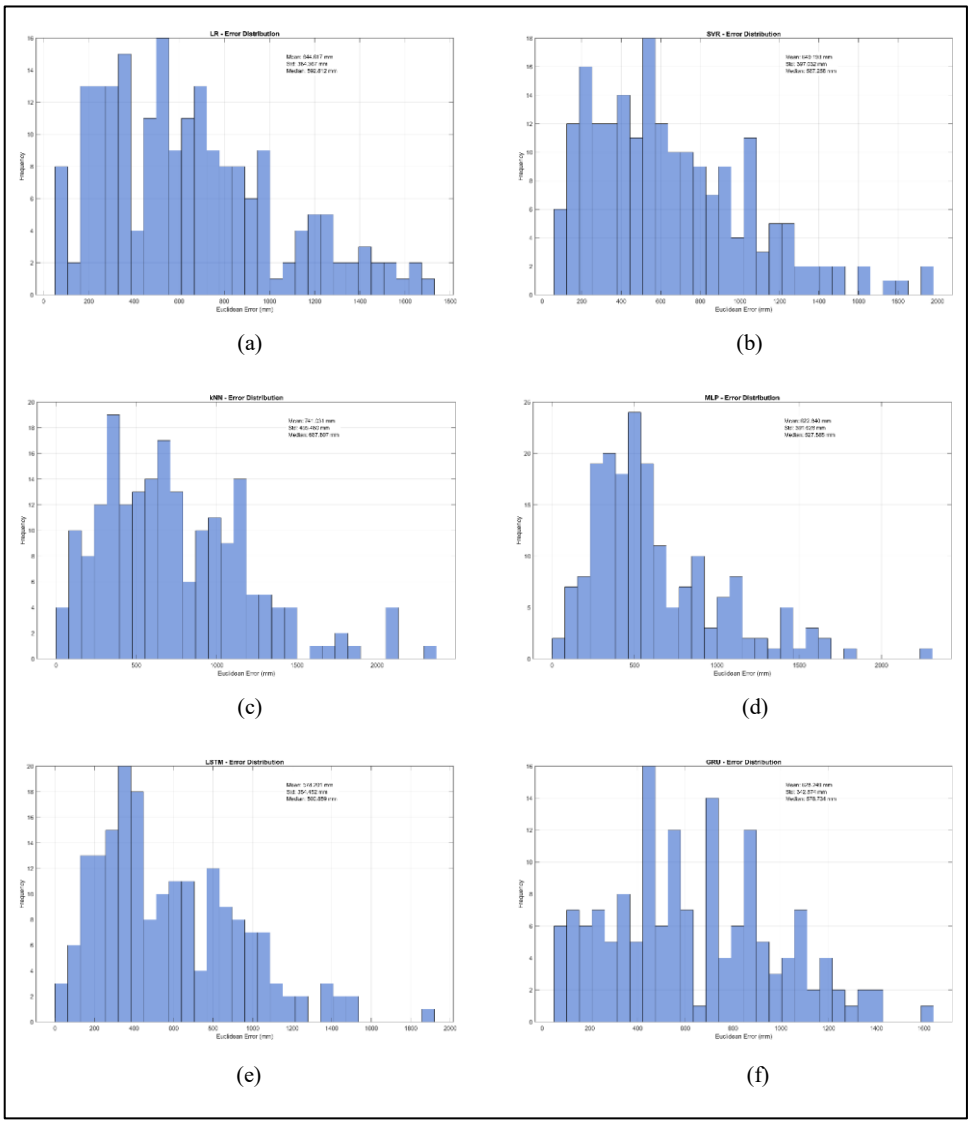

Figure 4.28 Error Distribution for D3 situation in FCPR using (a) LR (b) SVR (c) kNN (d) MLP (e) LSTM (f) GRU.

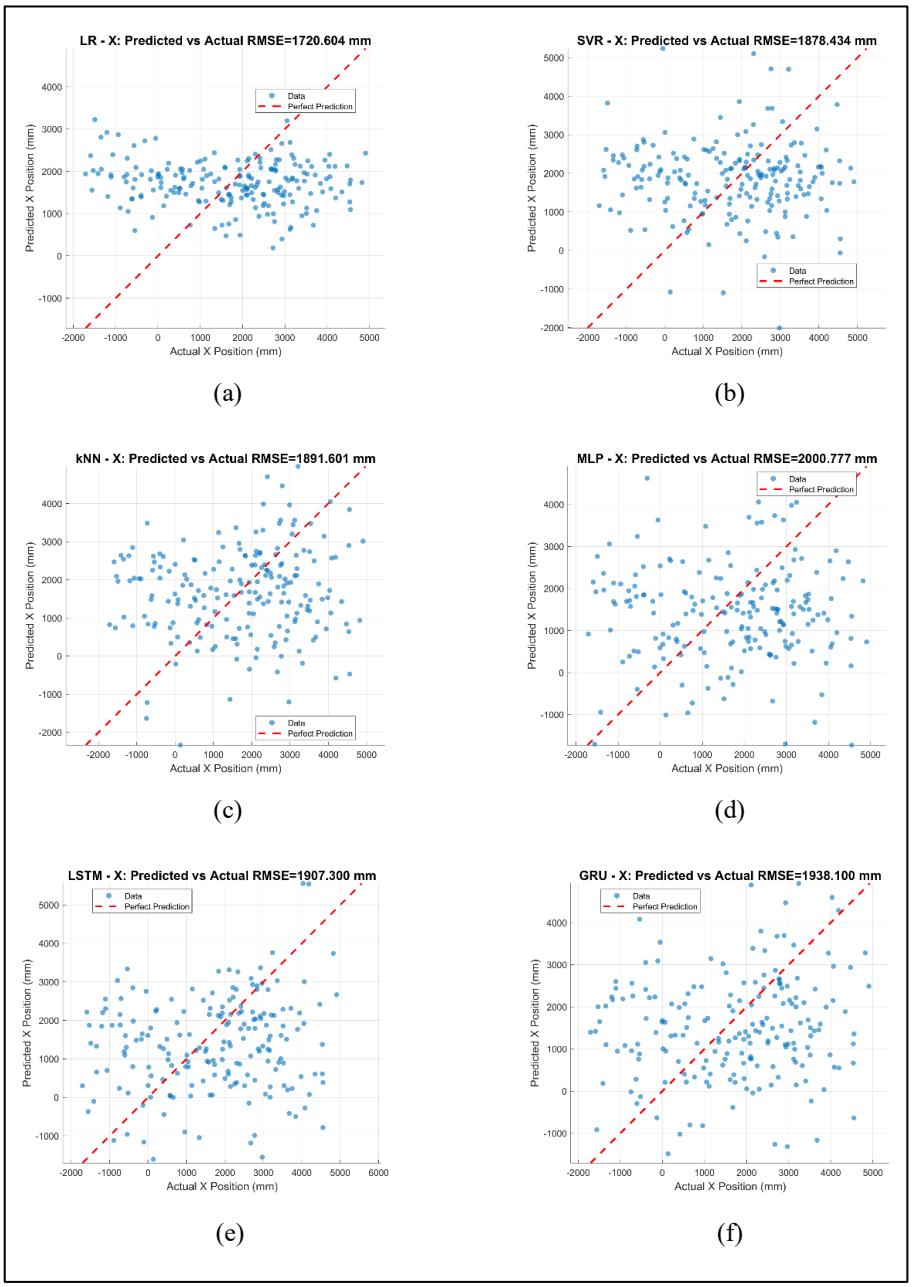

Figure 4.29 Actual versus Predicted X position for D1-D2-D3 situation in ICU using (a) LR (b) SVR (c) kNN (d) MLP (e) LSTM (f) GRU.

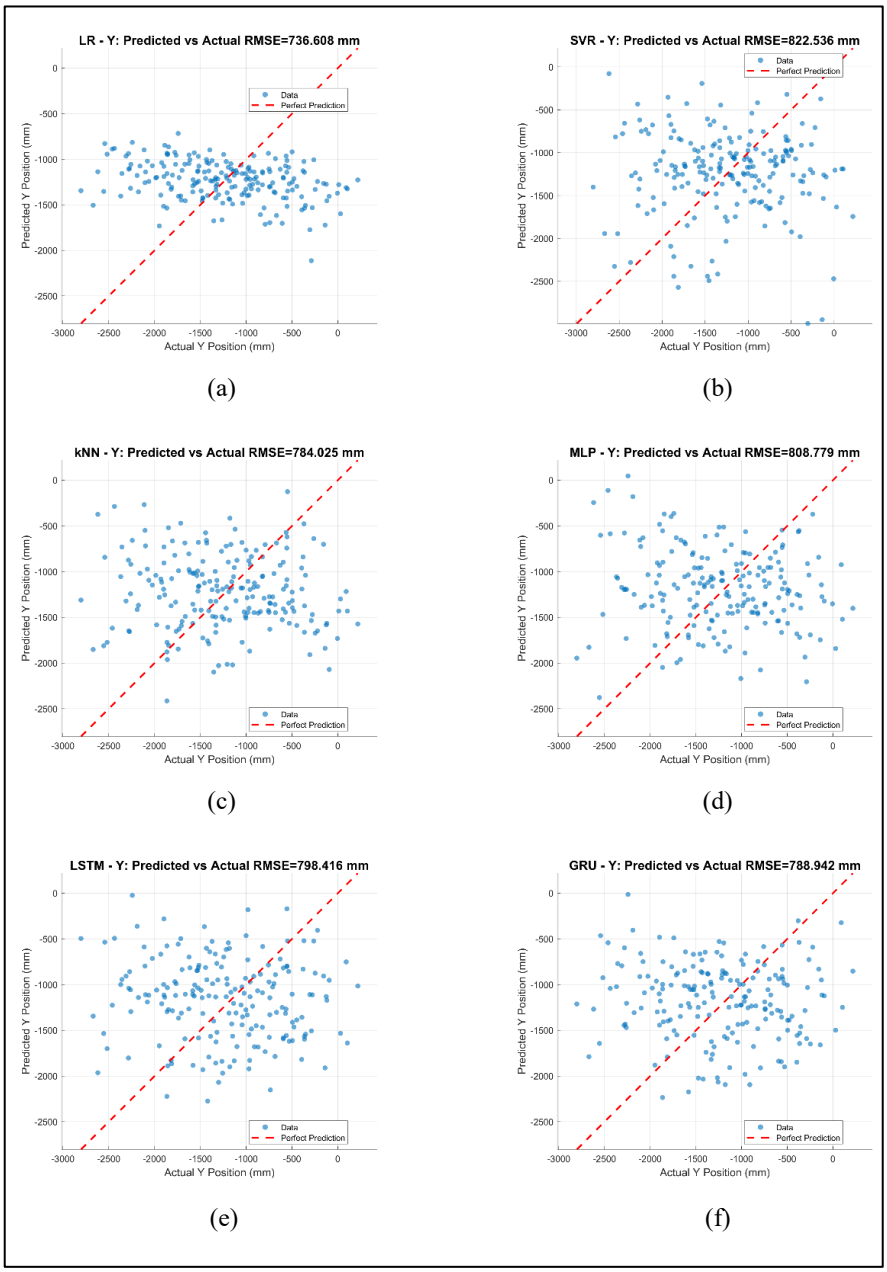

Figure 4.30 Actual versus Predicted Y position for D1-D2-D3 situation in ICU using (a) LR (b) SVR (c) kNN (d) MLP (e) LSTM (f) GRU.

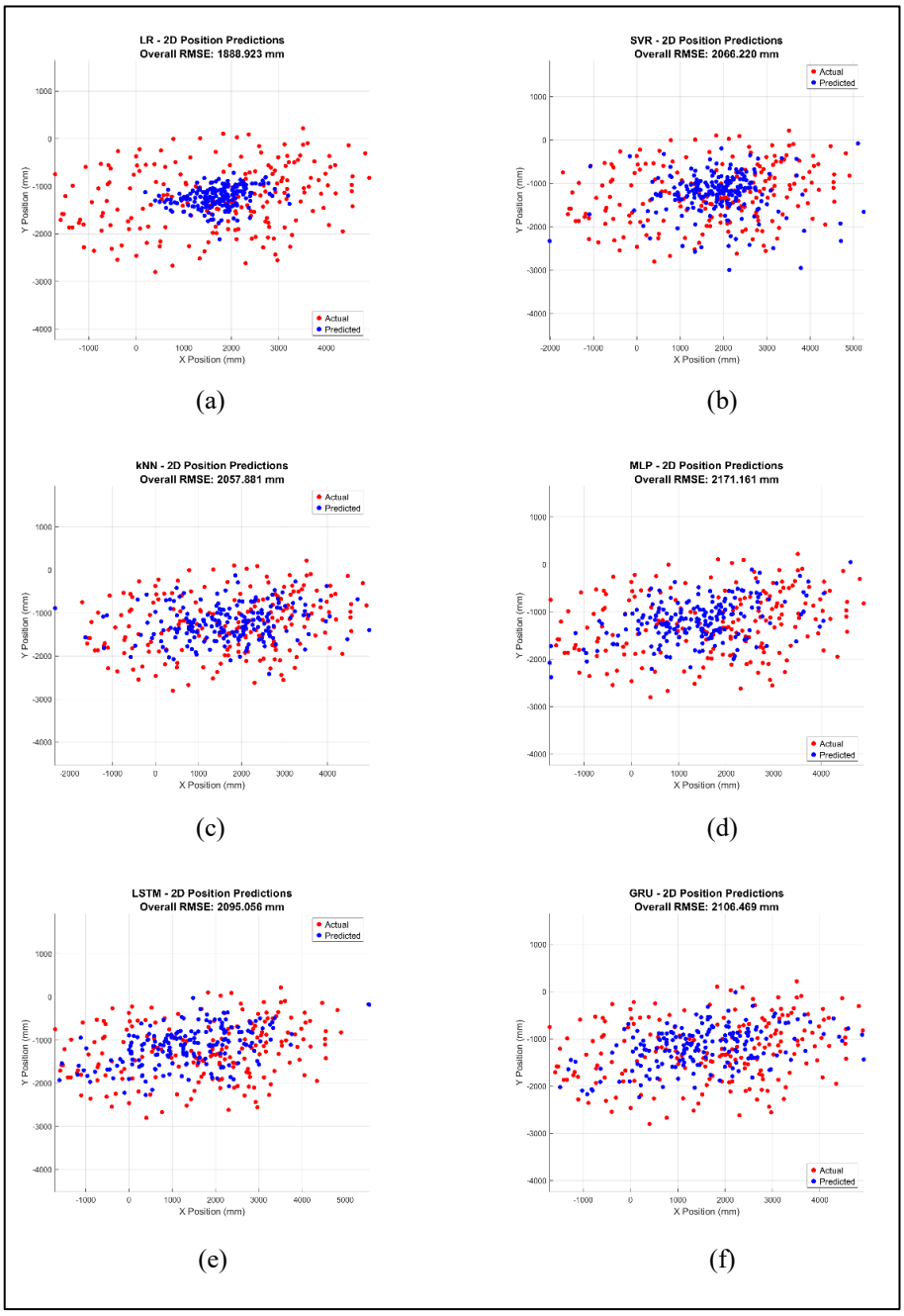

Figure 4.31 2D position predictions for D1-D2-D3 situation in ICU using (a) LR (b) SVR (c) kNN (d) MLP (e) LSTM (f) GRU.

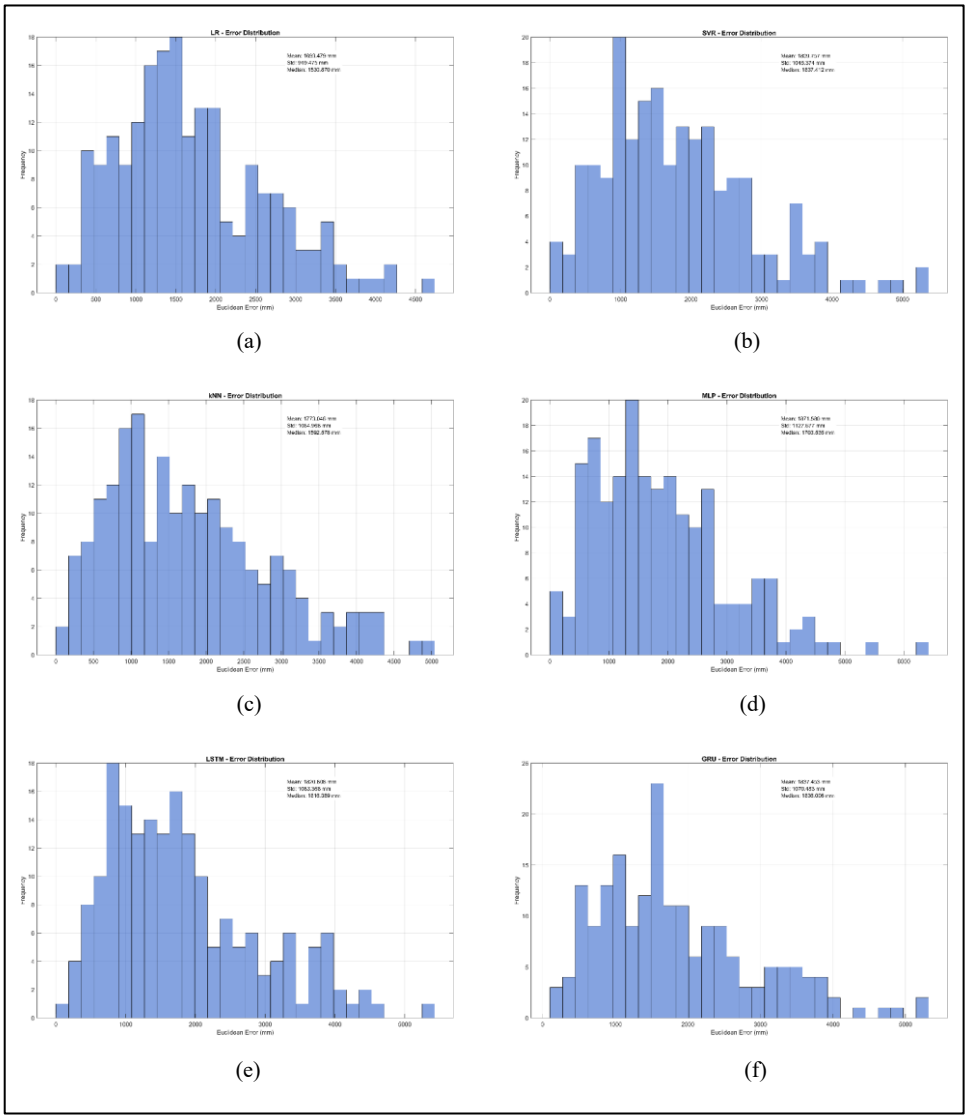

Figure 4.32 Error Distribution for D1-D2-D3 situation in ICU using (a) LR (b) SVR (c) kNN (d) MLP (e) LSTM (f) GRU.

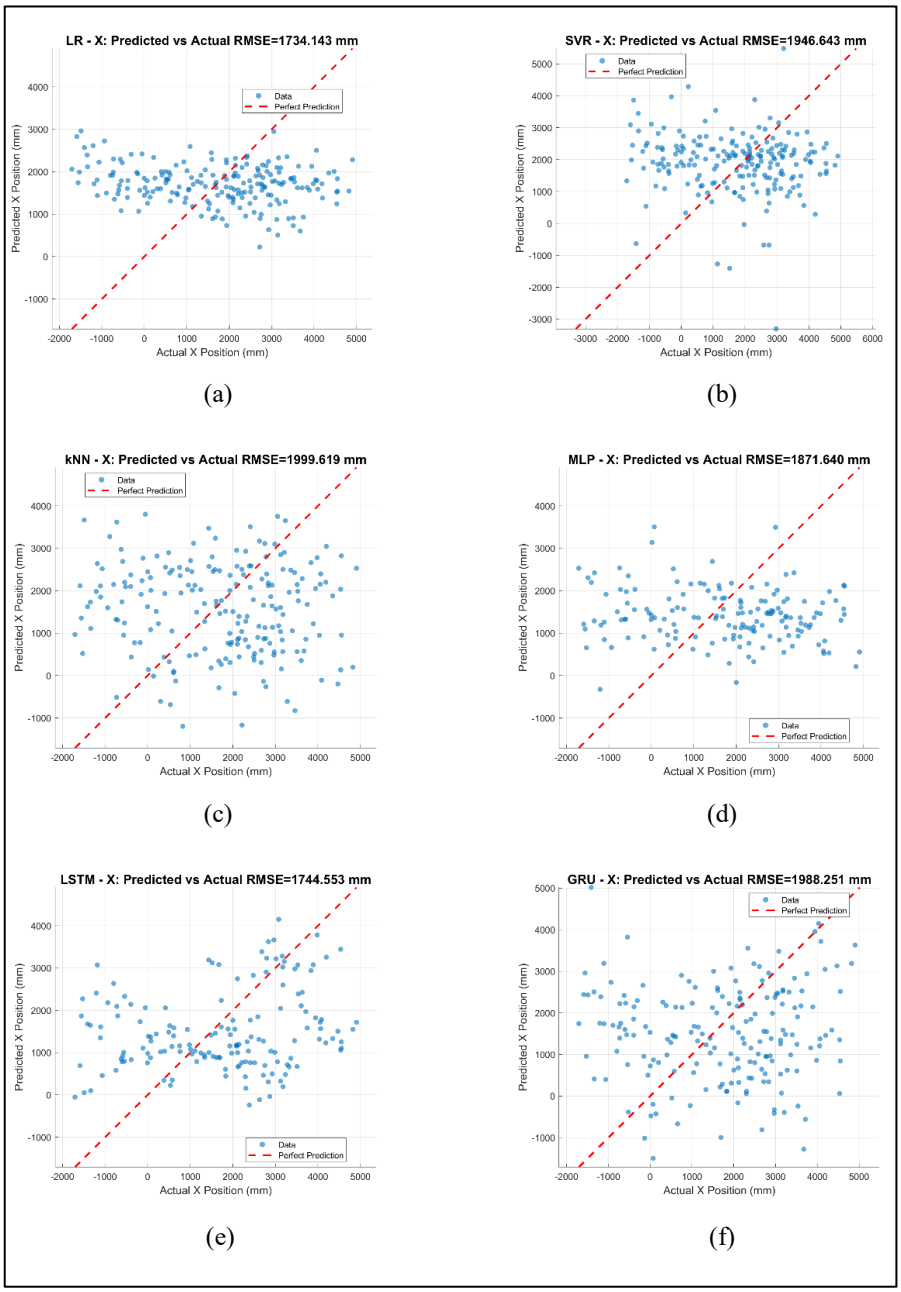

Figure 4.33 Actual versus Predicted X position for D1-D2 situation in ICU using (a) LR (b) SVR (c) kNN (d) MLP (e) LSTM (f) GRU.

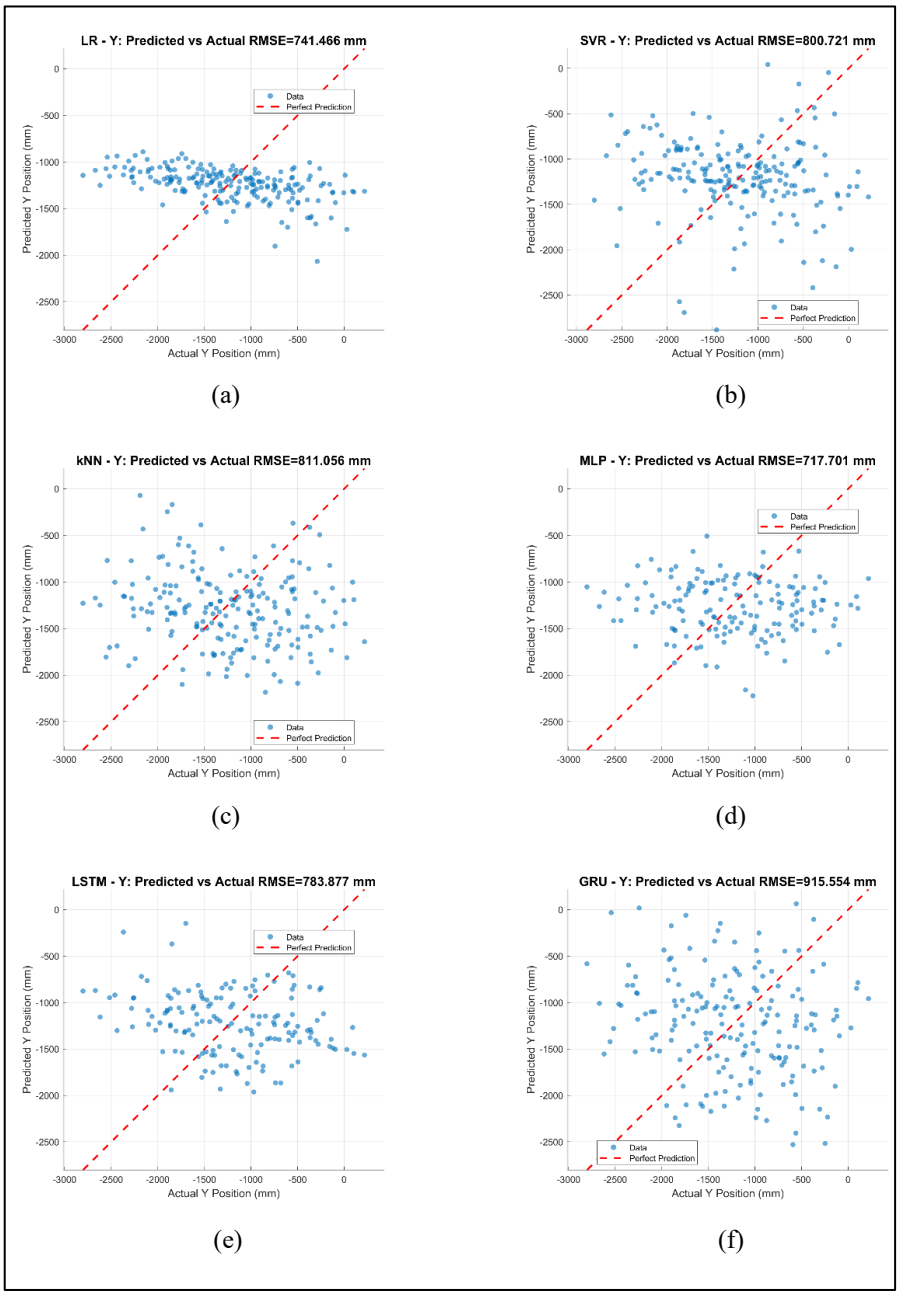

Figure 4.34 Actual versus Predicted Y position for D1-D2 situation in ICU using (a) LR (b) SVR (c) kNN (d) MLP (e) LSTM (f) GRU.

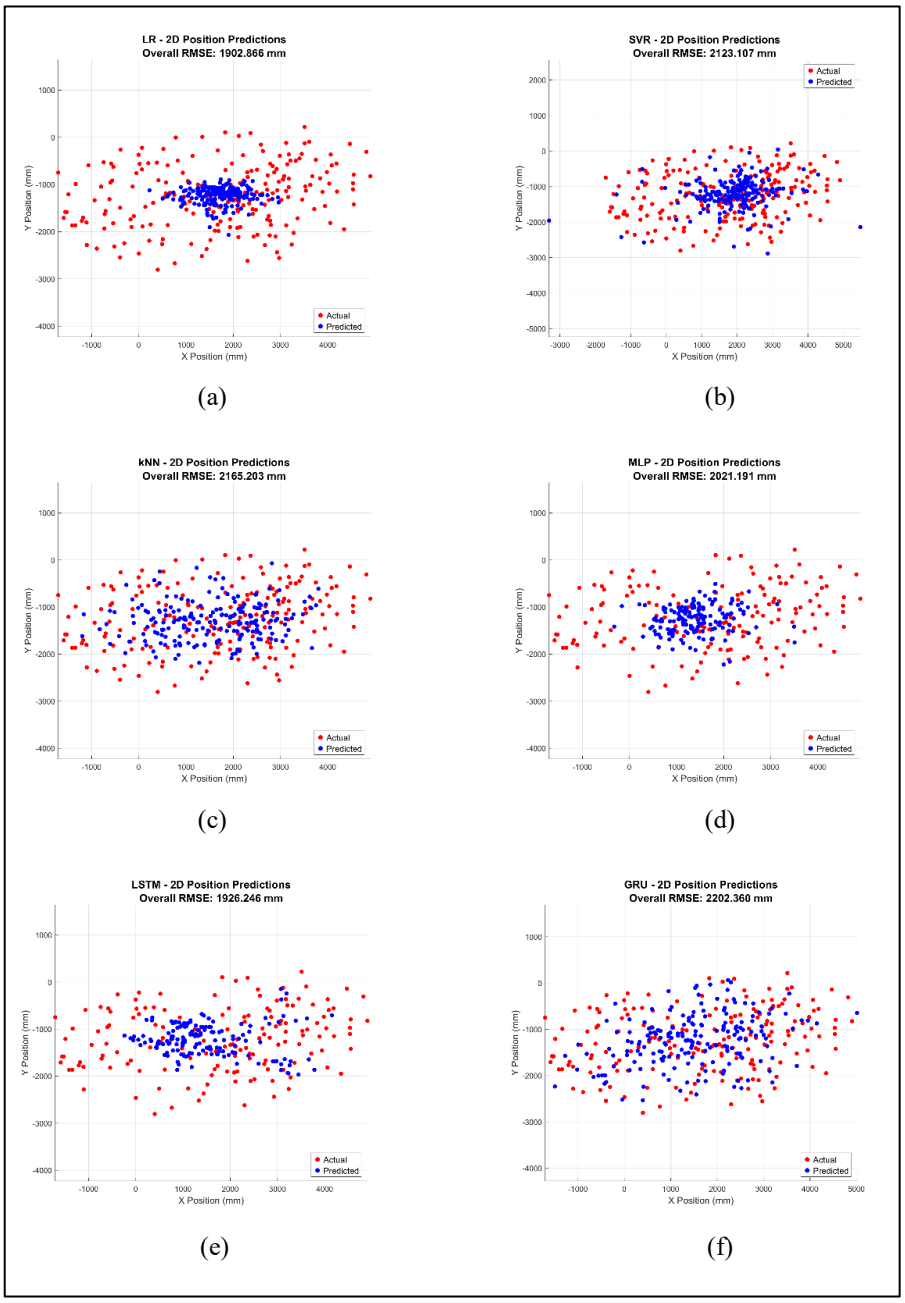

Figure 4.35 2D position predictions for D1-D2 situation in ICU using (a) LR (b) SVR (c) kNN (d) MLP (e) LSTM (f) GRU.

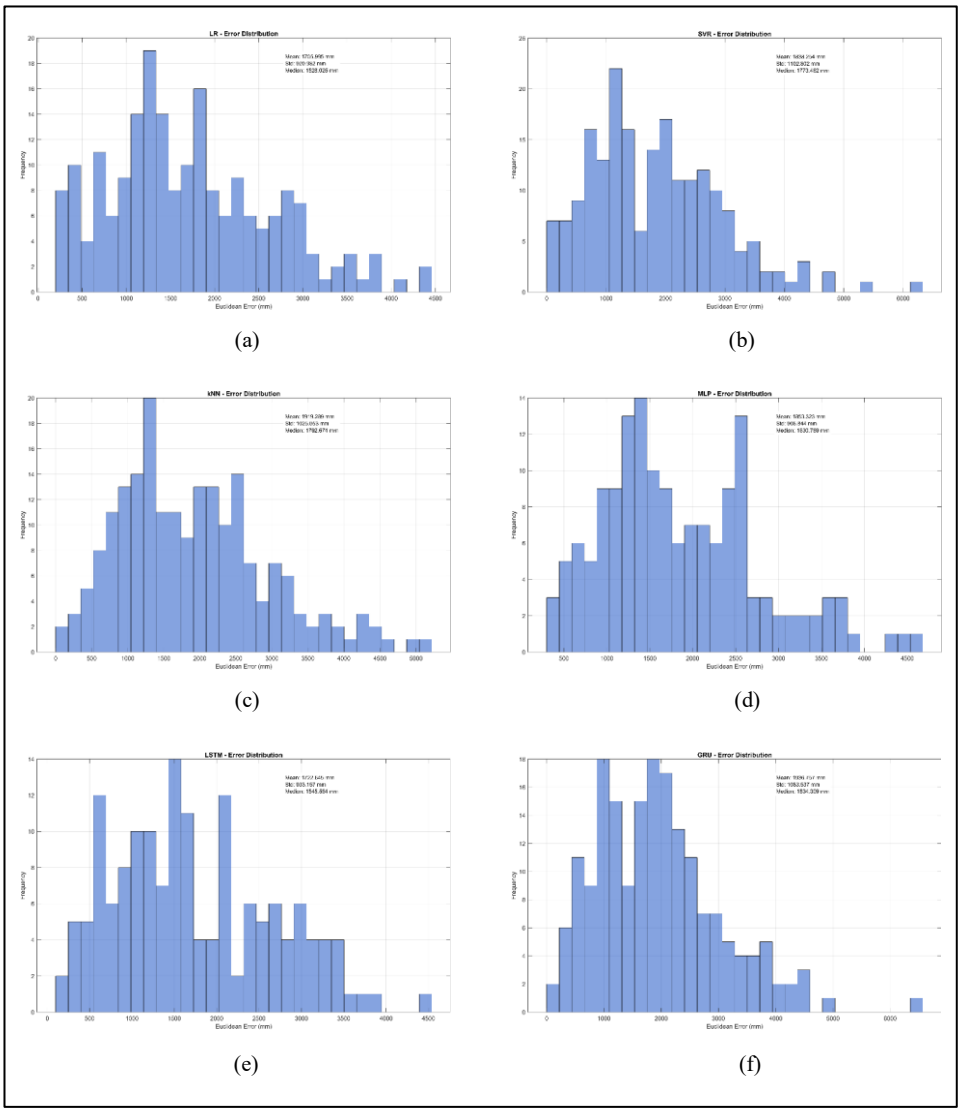

Figure 4.36 Error Distribution for D1-D2 situation in ICU using (a) LR (b) SVR (c) kNN (d) MLP (e) LSTM (f) GRU.

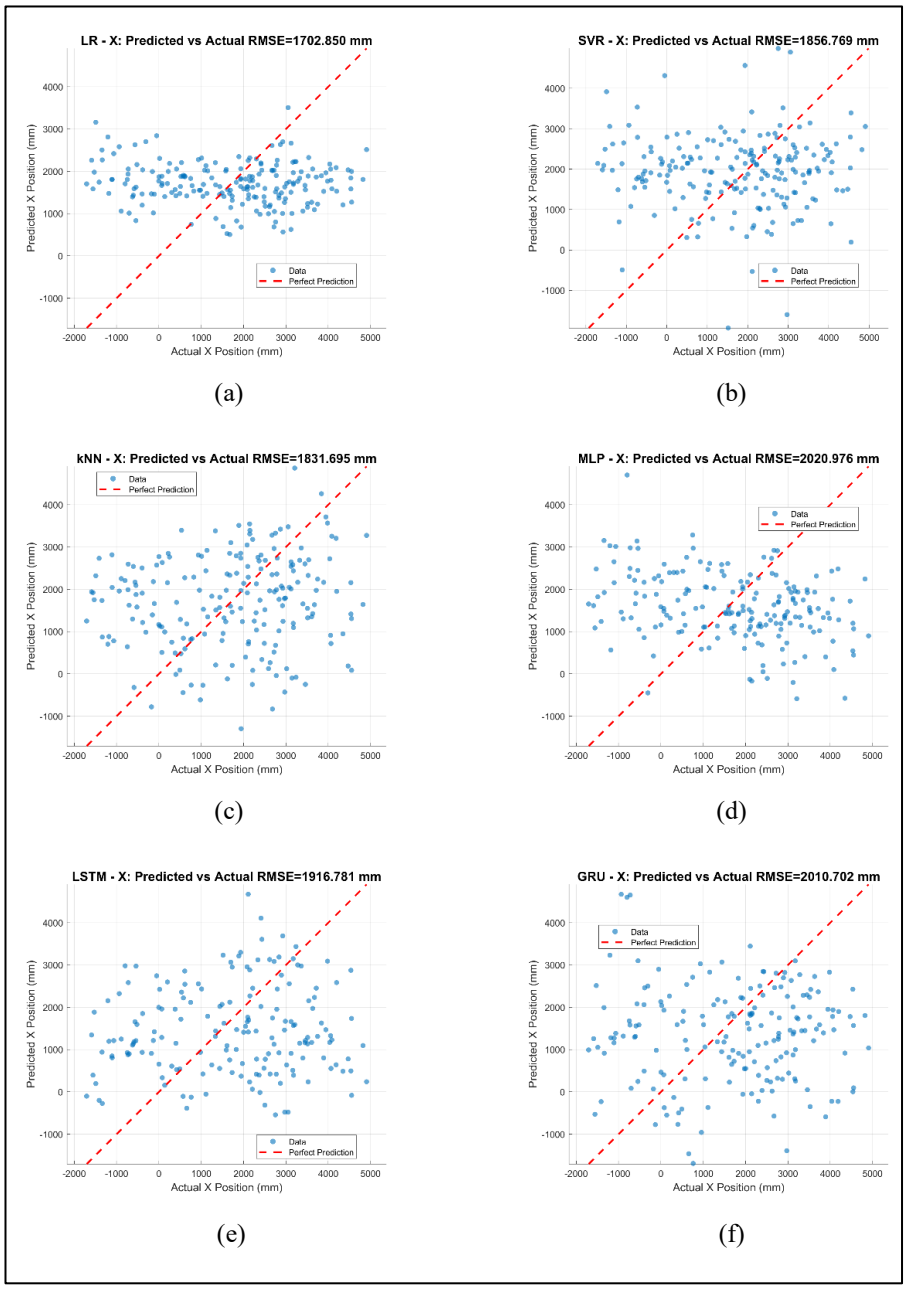

Figure 4.37 Actual versus Predicted X position for D1-D3 situation in ICU using (a) LR (b) SVR (c) kNN (d) MLP (e) LSTM (f) GRU.

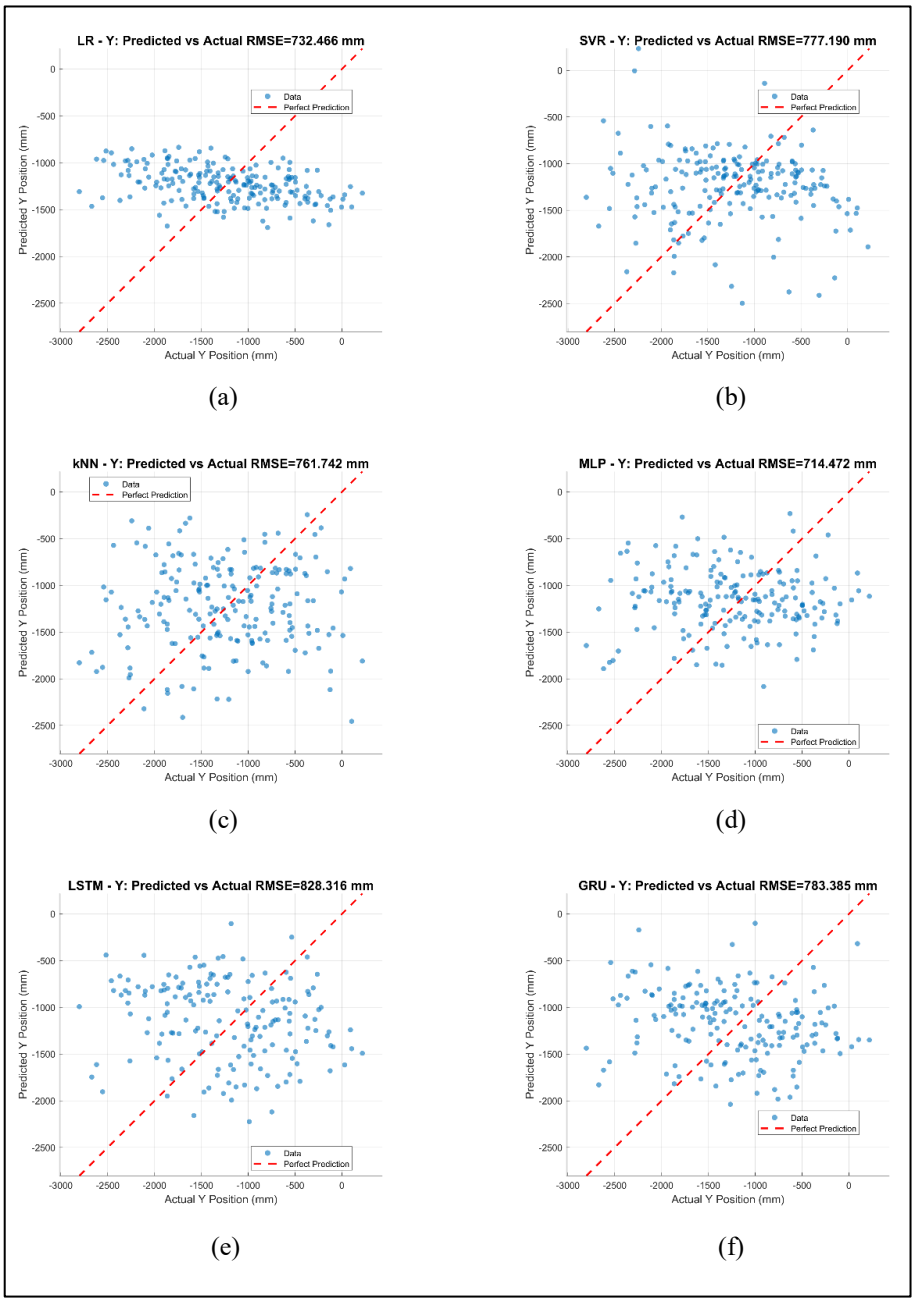

Figure 4.38 Actual versus Predicted Y position for D1-D3 situation in ICU using (a) LR (b) SVR (c) kNN (d) MLP (e) LSTM (f) GRU.

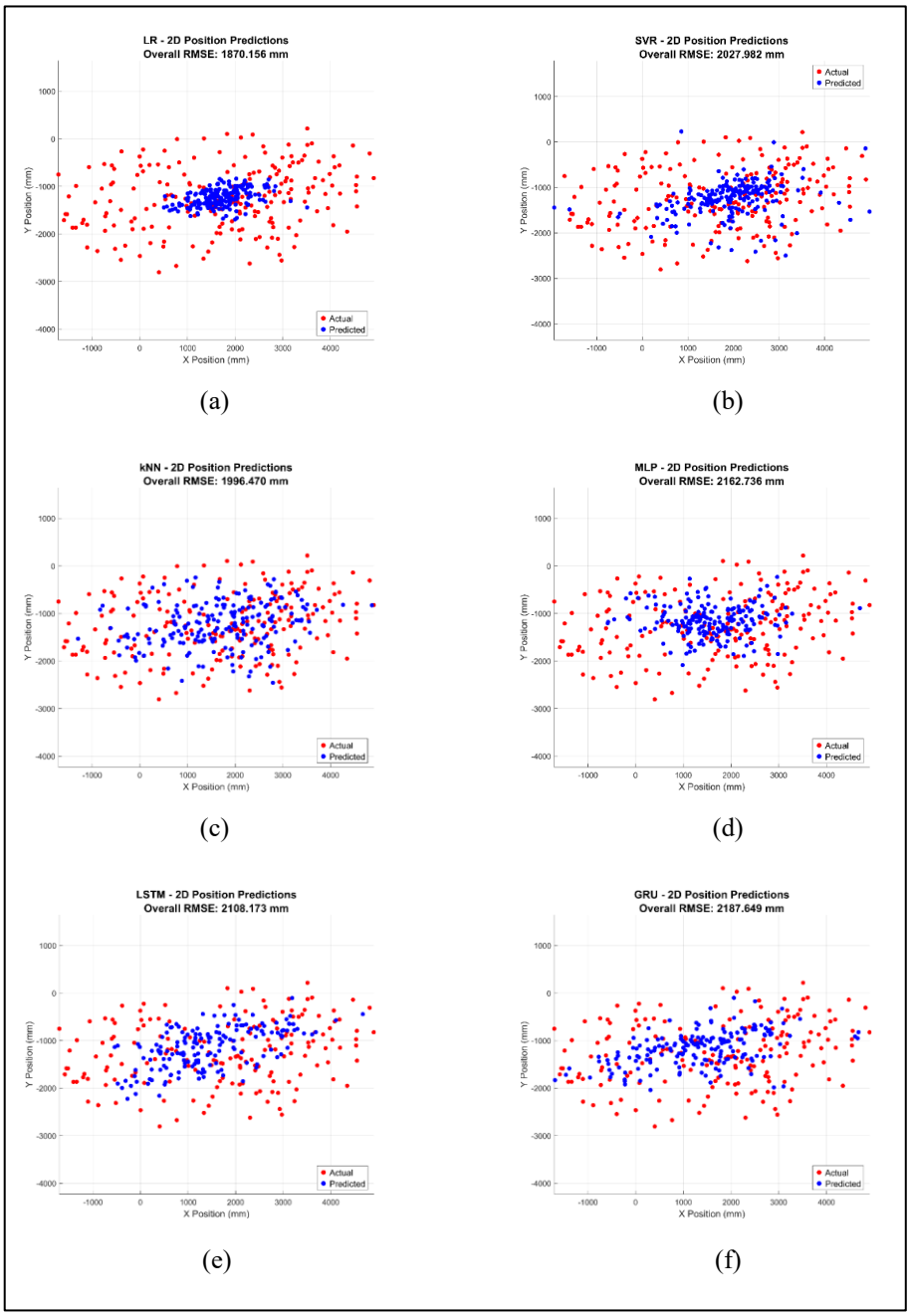

Figure 4.39 2D position predictions for D1-D3 situation in ICU using (a) LR (b) SVR (c) kNN (d) MLP (e) LSTM (f) GRU.

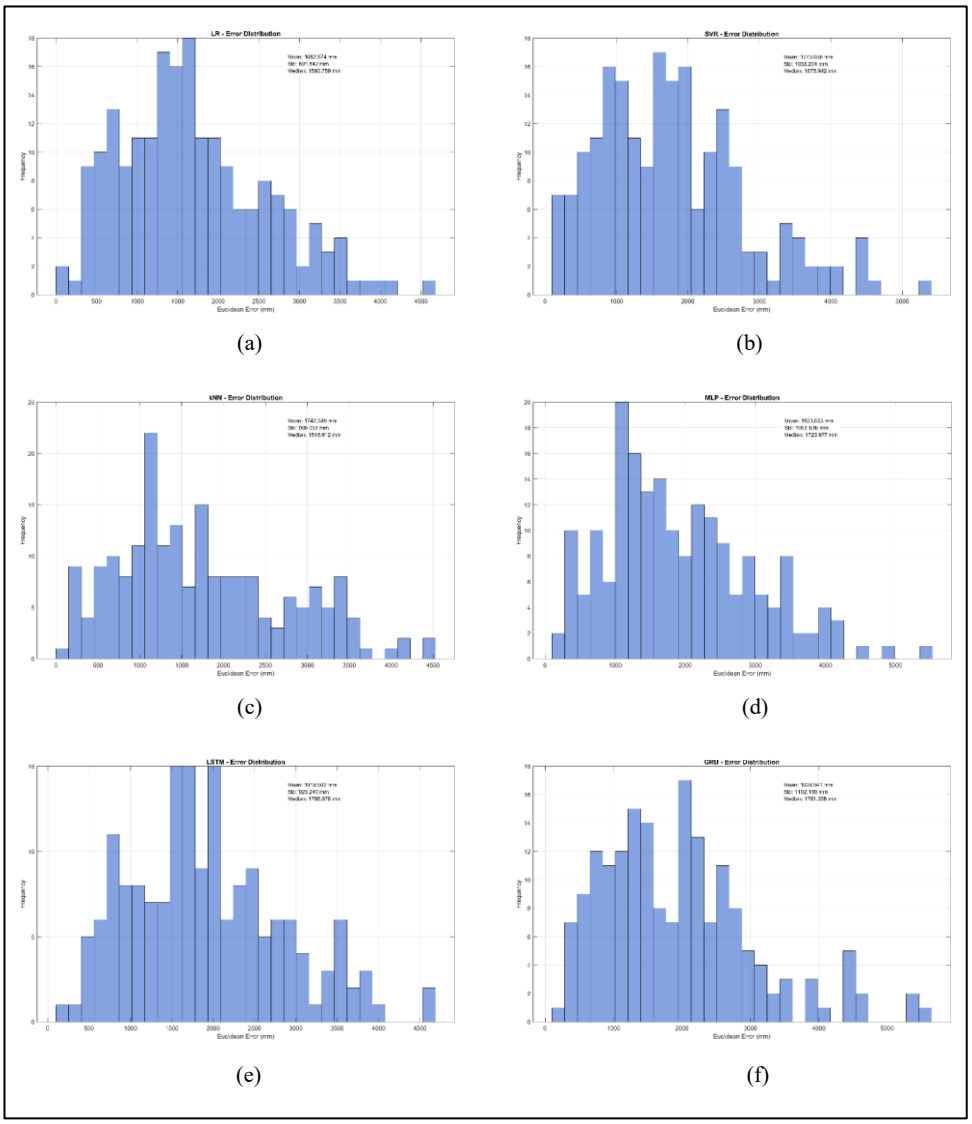

Figure 4.40 Error Distribution for D1-D3 situation in ICU using (a) LR (b) SVR (c) kNN (d) MLP (e) LSTM (f) GRU.

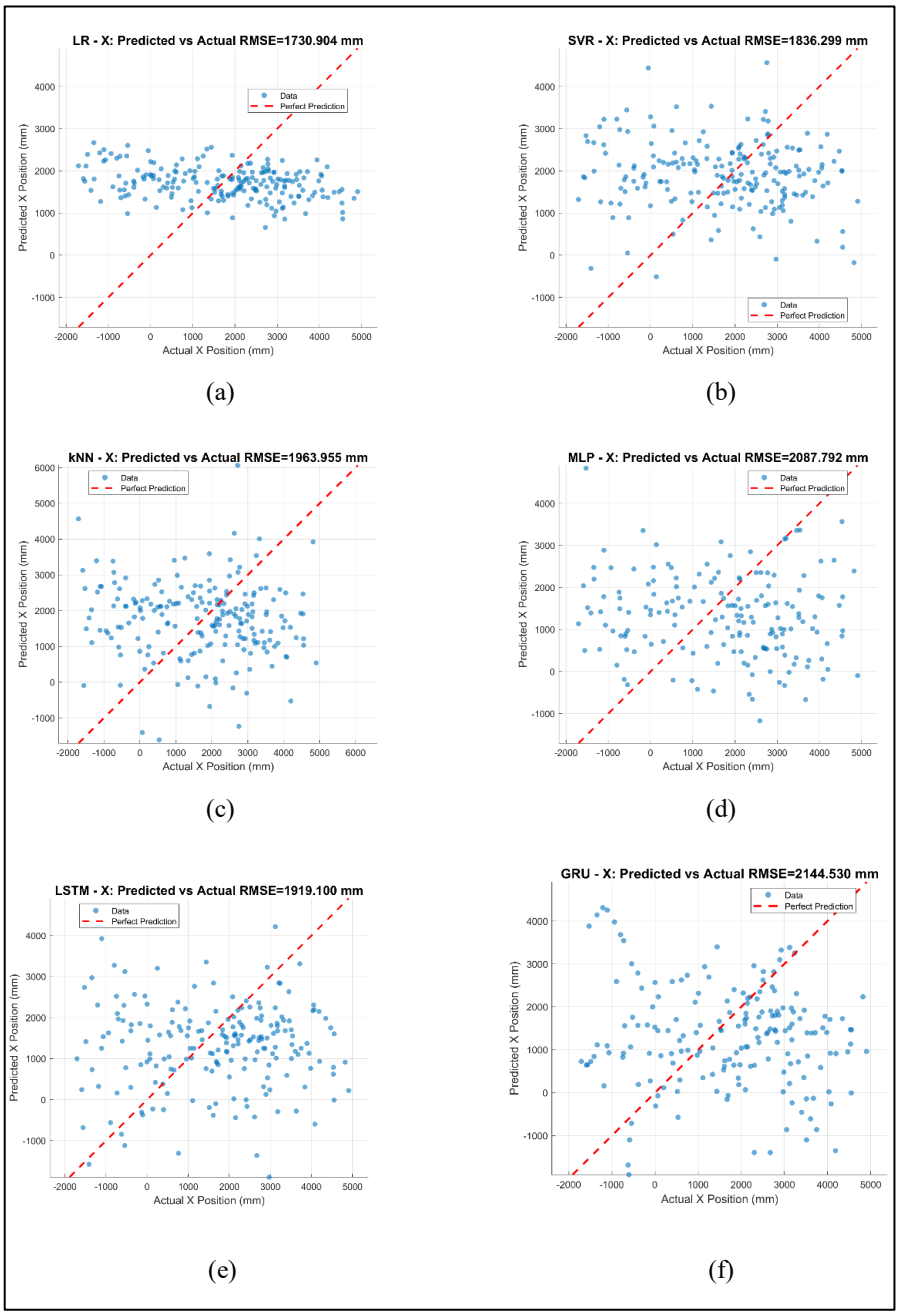

Figure 4.41 Actual versus Predicted X position for D2-D3 situation in ICU using (a) LR (b) SVR (c) kNN (d) MLP (e) LSTM (f) GRU.

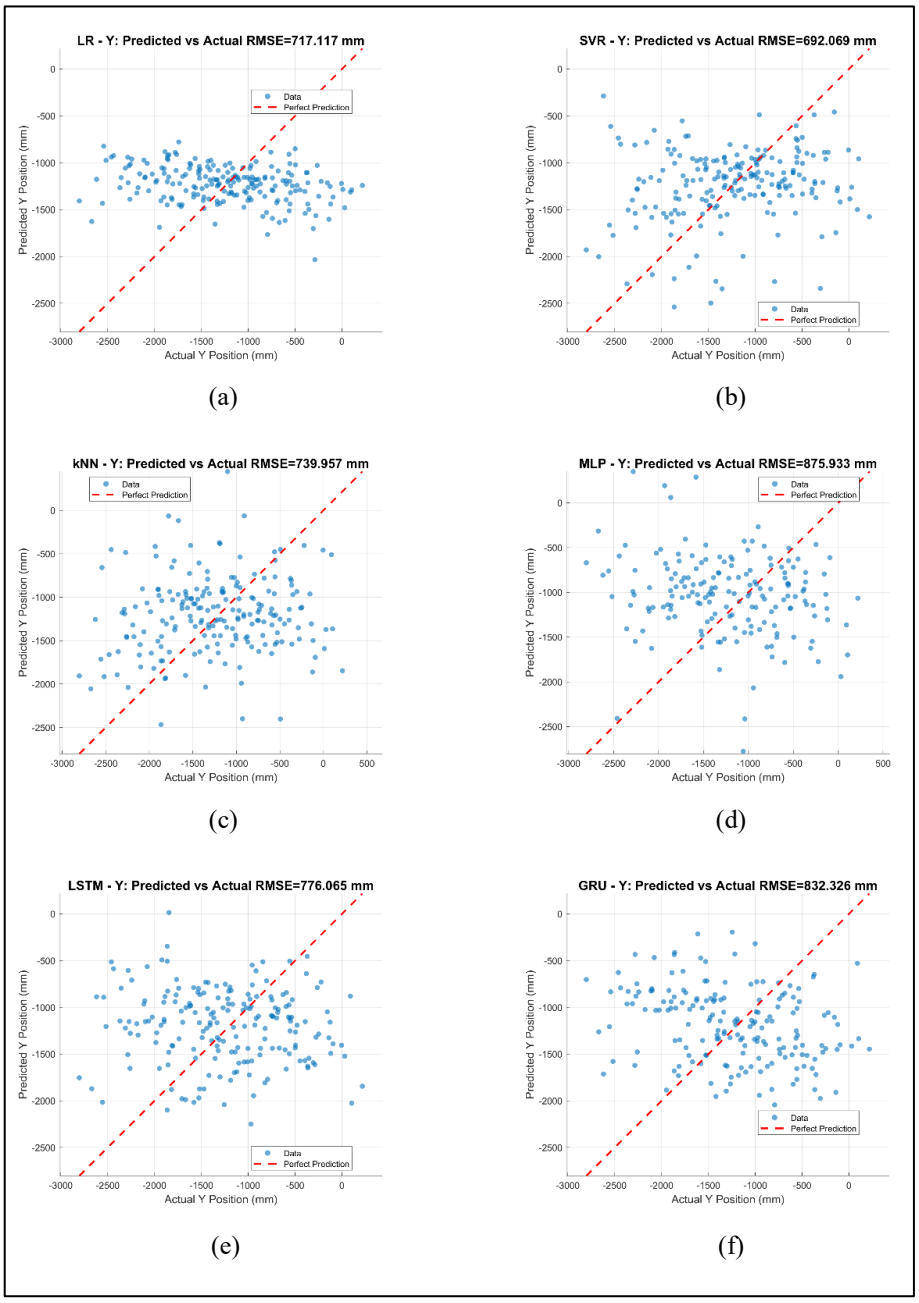

Figure 4.42 Actual versus Predicted Y position for D2-D3 situation in ICU using (a) LR (b) SVR (c) kNN (d) MLP (e) LSTM (f) GRU.

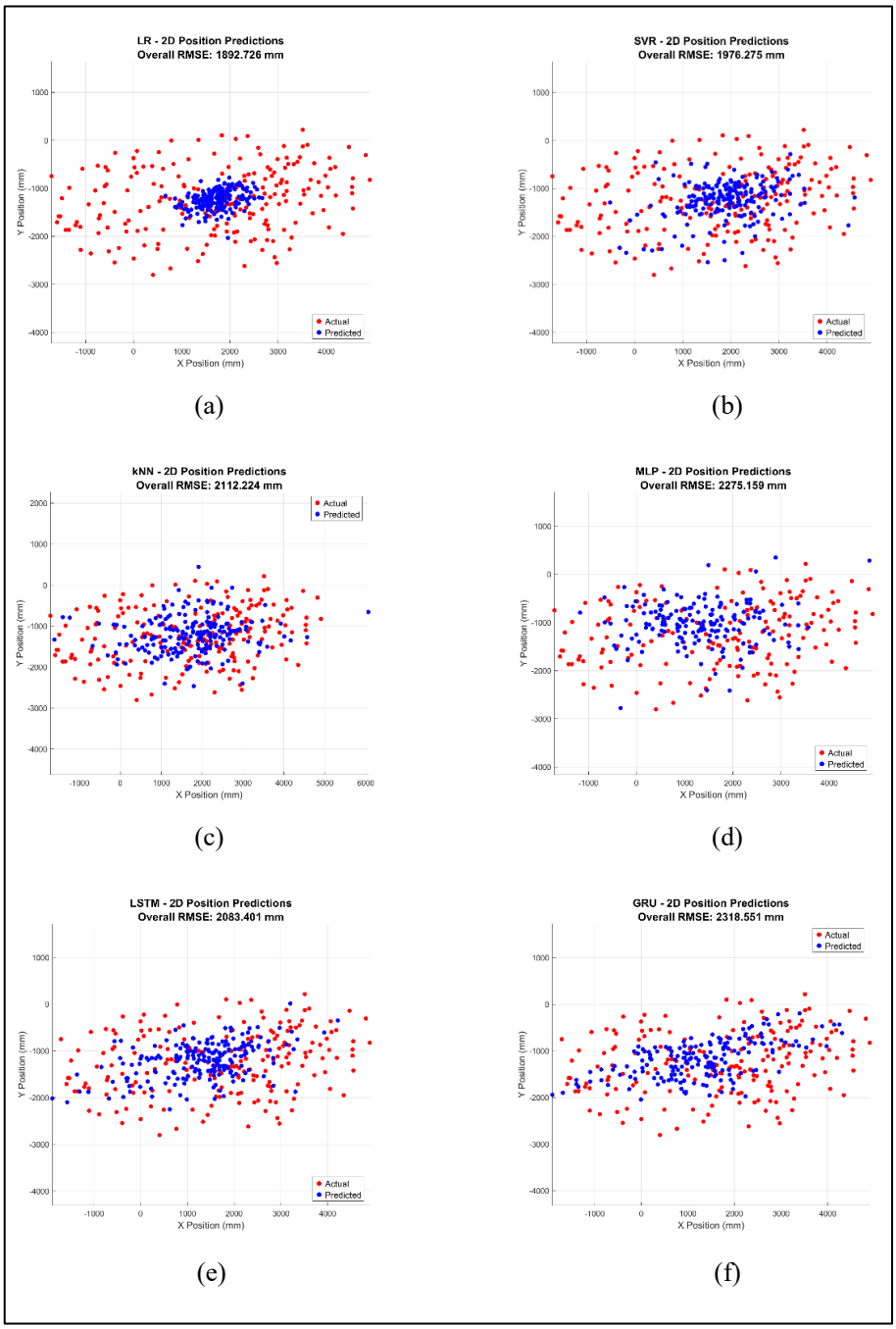

Figure 4.43 2D position predictions for D2-D3 situation in ICU using (a) LR (b) SVR (c) kNN (d) MLP (e) LSTM (f) GRU.

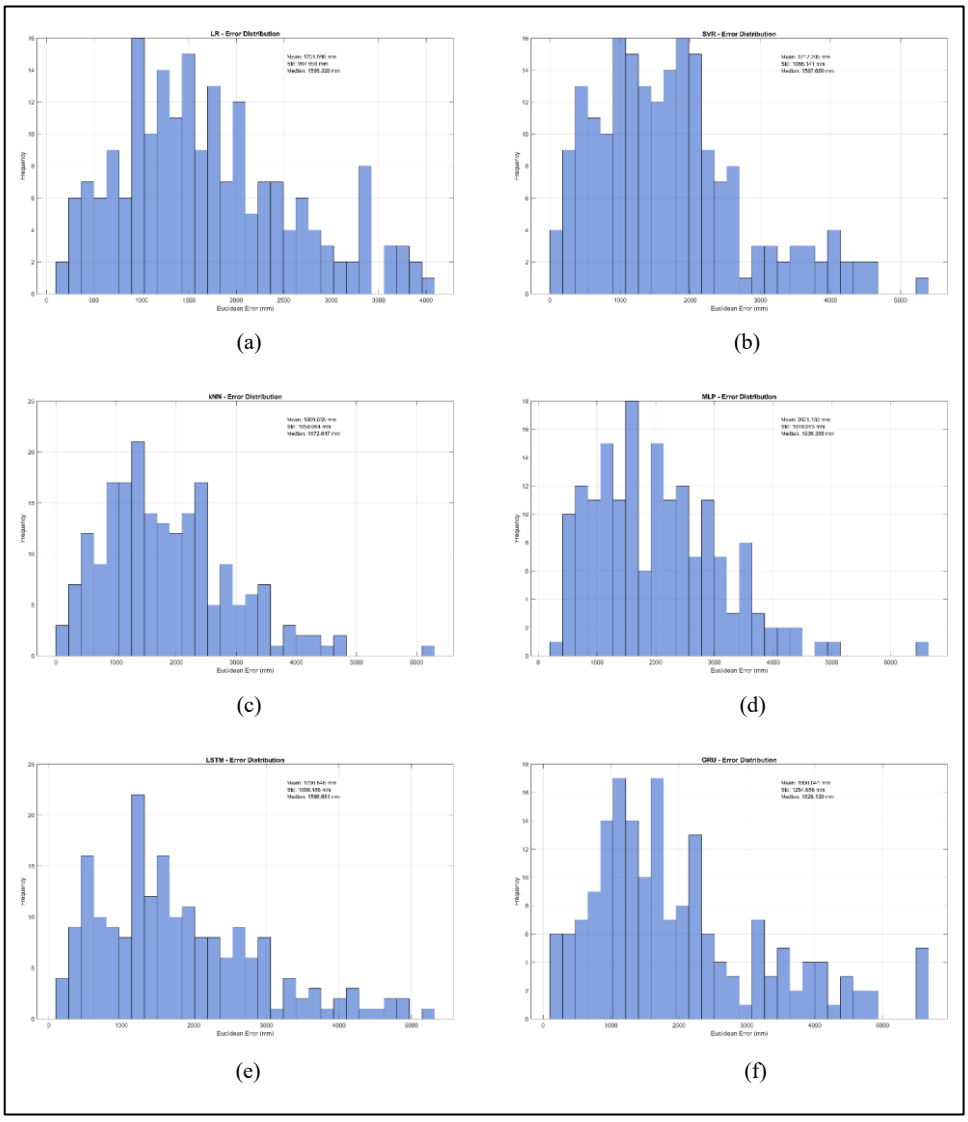

Figure 4.44 Error Distribution for D2-D3 situation in ICU using (a) LR (b) SVR (c) kNN (d) MLP (e) LSTM (f) GRU.

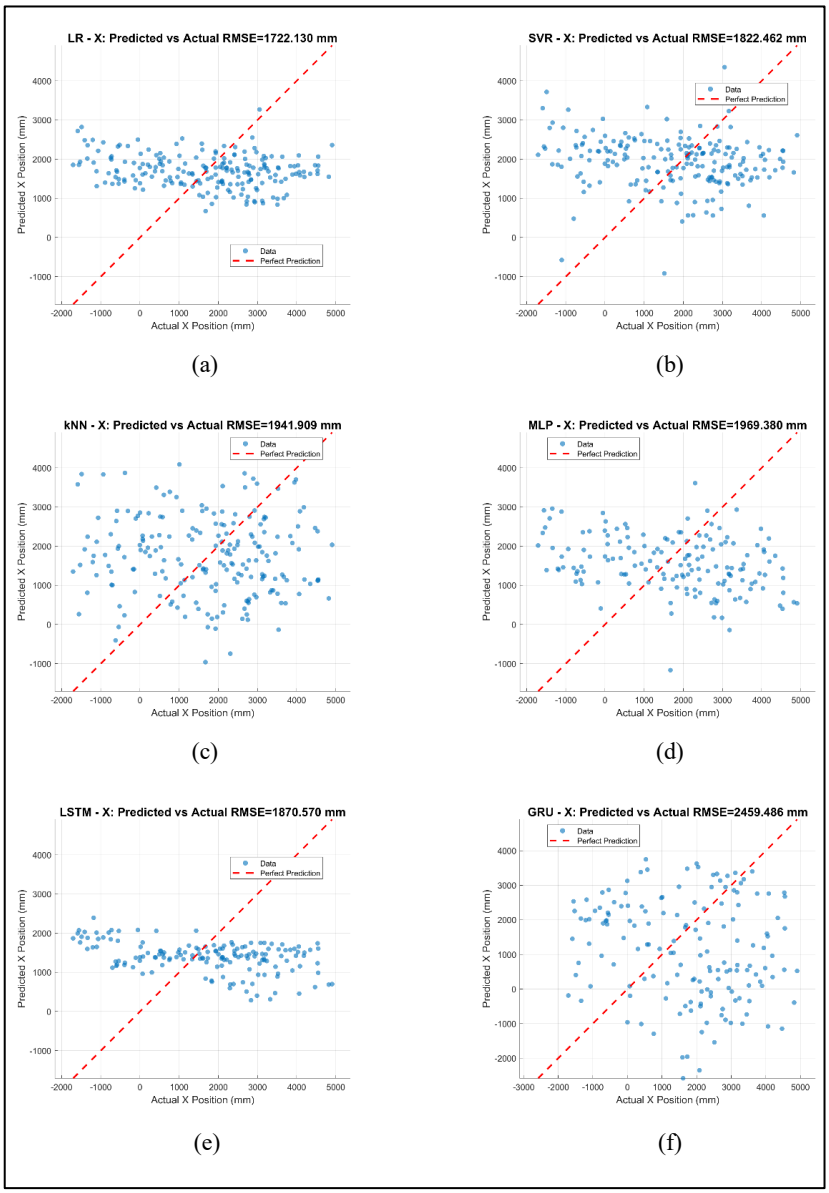

Figure 4.45 Actual versus Predicted X position for D1 situation in ICU using (a) LR (b) SVR (c) kNN (d) MLP (e) LSTM (f) GRU.

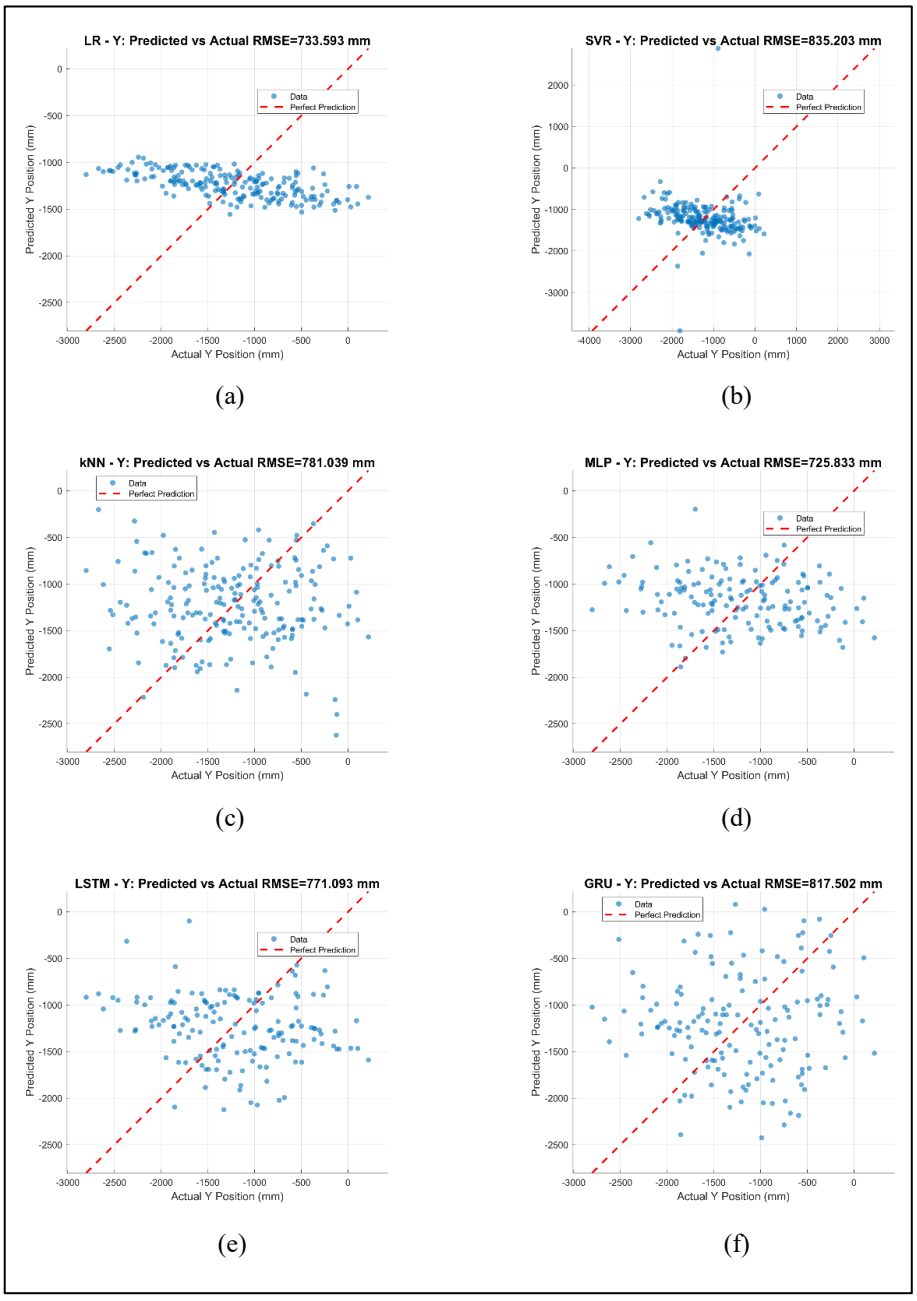

Figure 4.46 Actual versus Predicted Y position for D1 situation in ICU using (a) LR (b) SVR (c) kNN (d) MLP (e) LSTM (f) GRU.

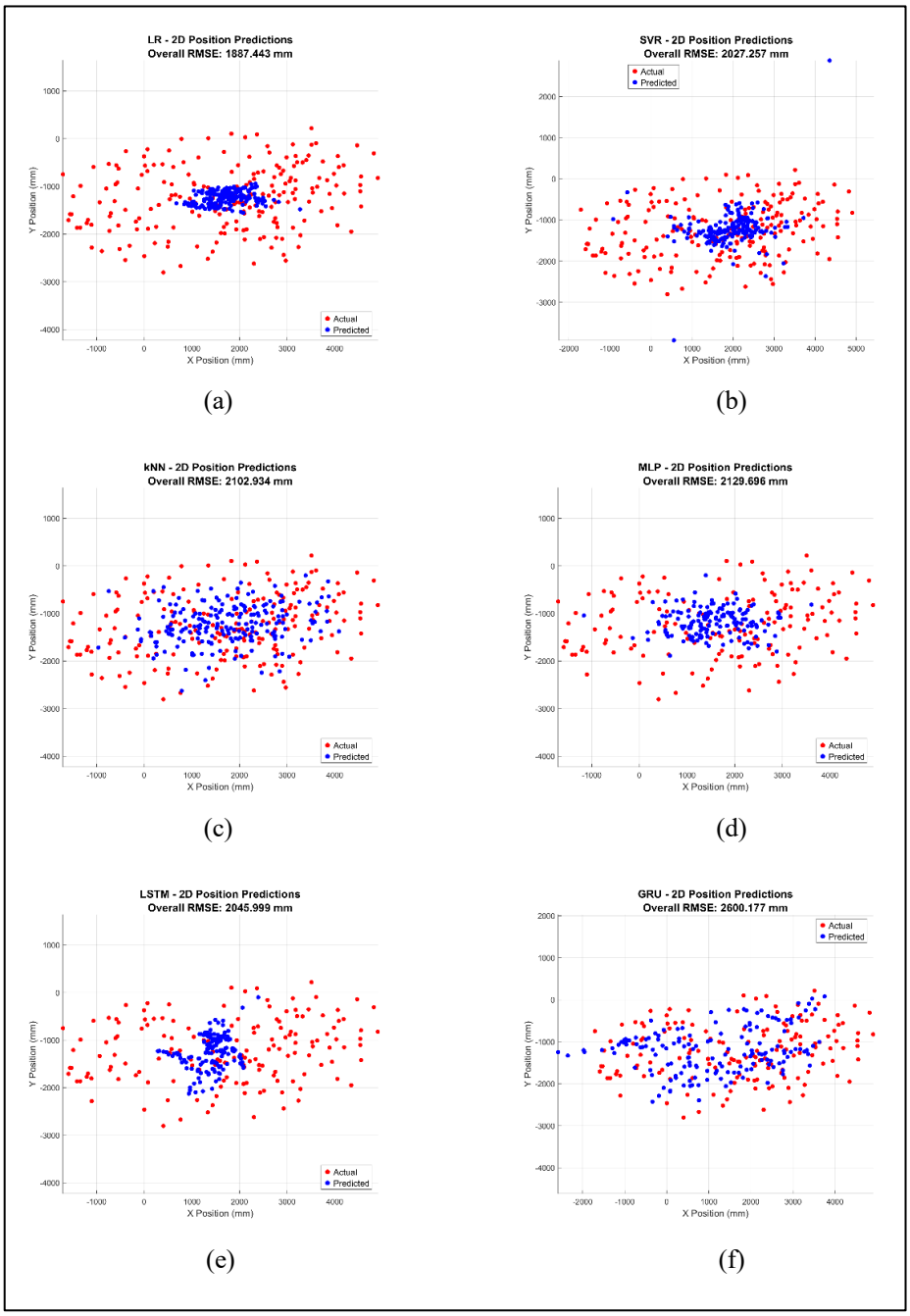

Figure 4.47 2D position predictions for D1 situation in ICU using (a) LR (b) SVR (c) kNN (d) MLP (e) LSTM (f) GRU.

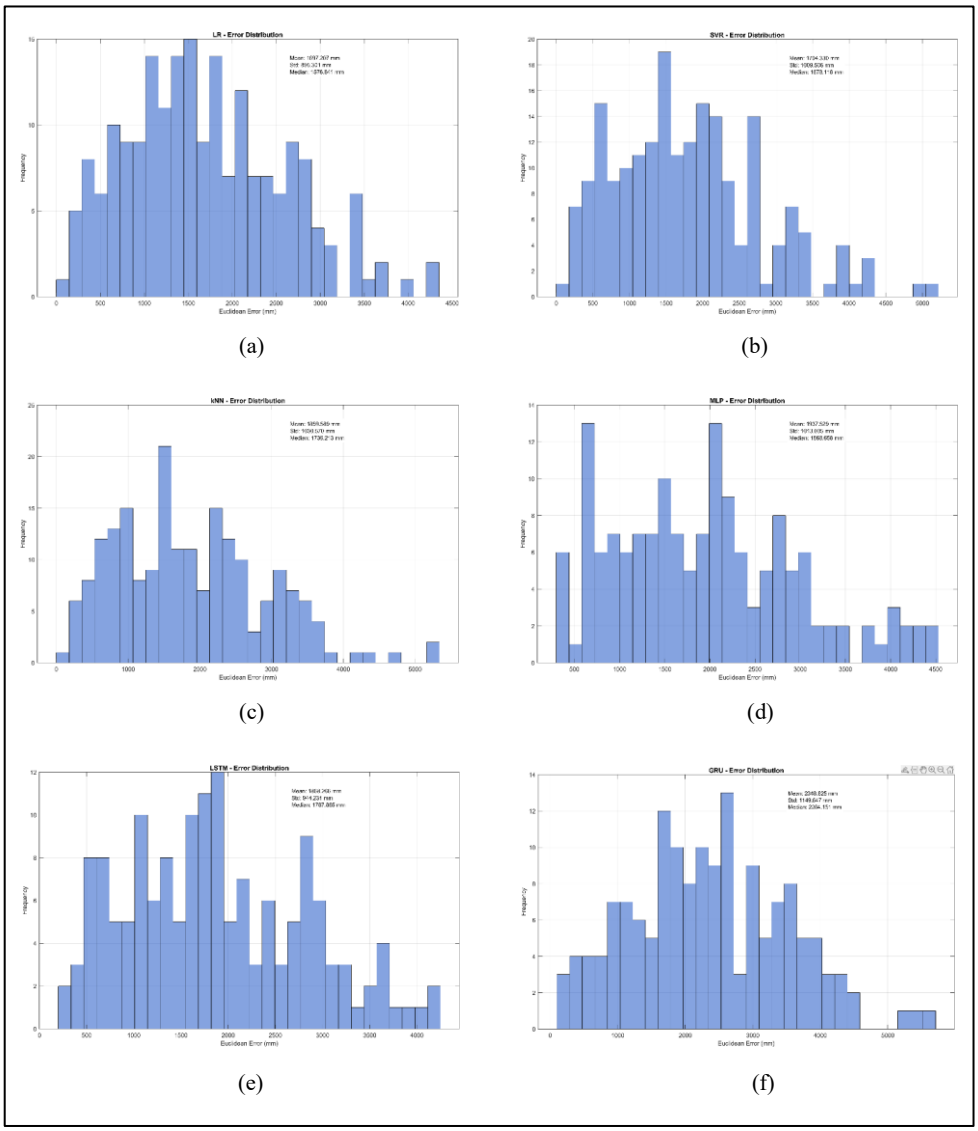

Figure 4.48 Error Distribution for D1 situation in ICU using (a) LR (b) SVR (c) kNN (d) MLP (e) LSTM (f) GRU.

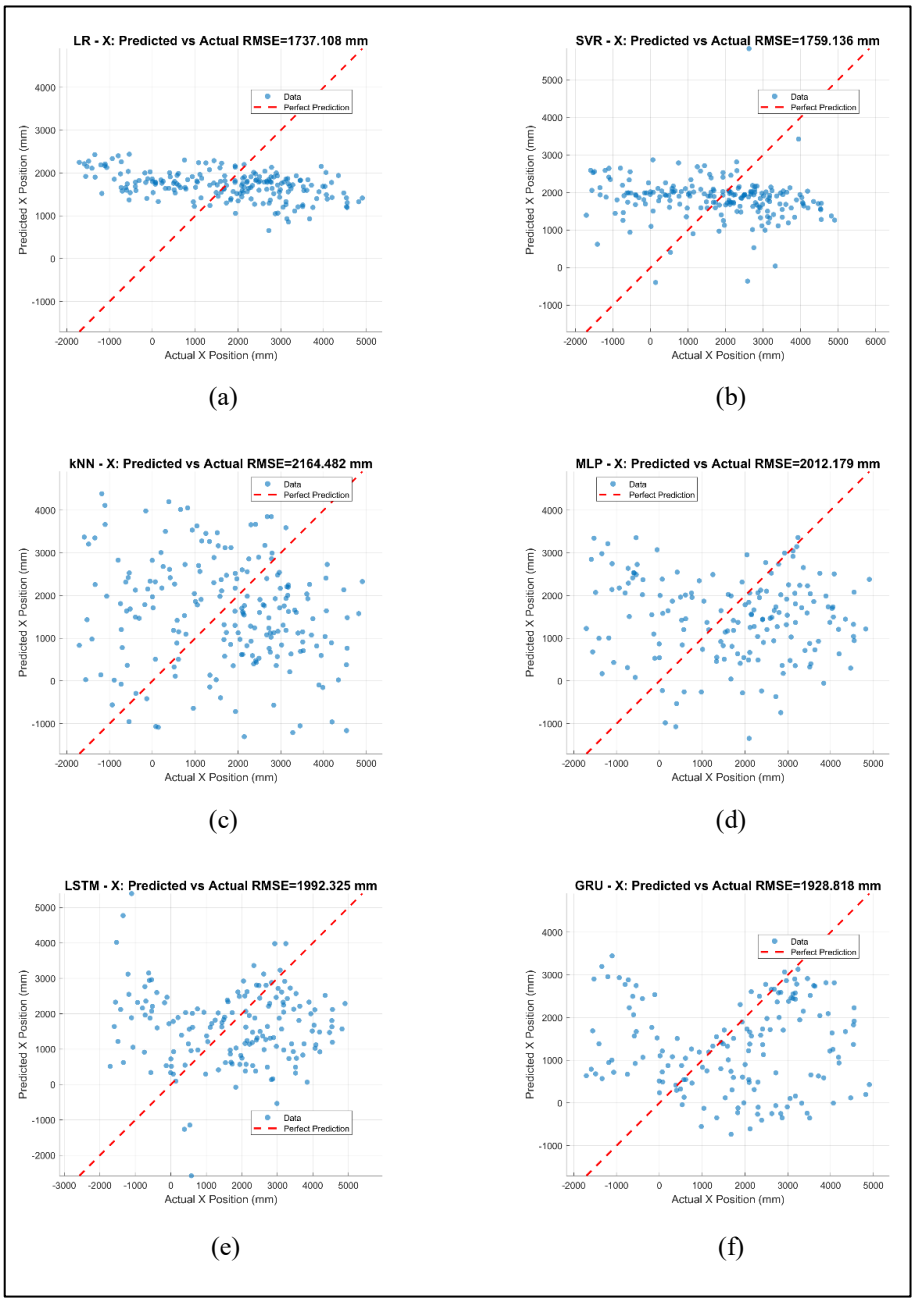

Figure 4.49 Actual versus Predicted X position for D2 situation in ICU using (a) LR (b) SVR (c) kNN (d) MLP (e) LSTM (f) GRU.

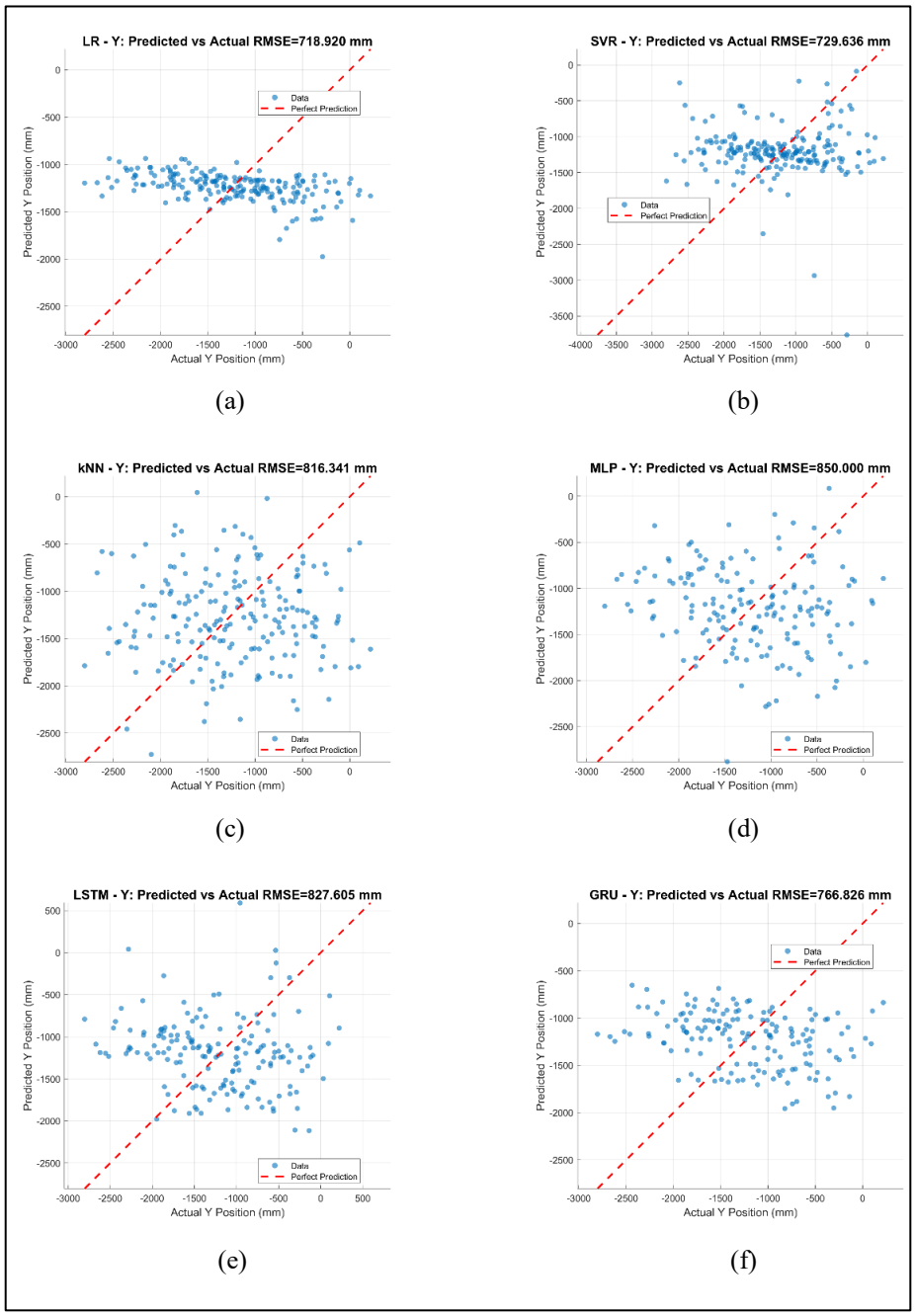

Figure 4.50 Actual versus Predicted Y position for D2 situation in ICU using (a) LR (b) SVR (c) kNN (d) MLP (e) LSTM (f) GRU.

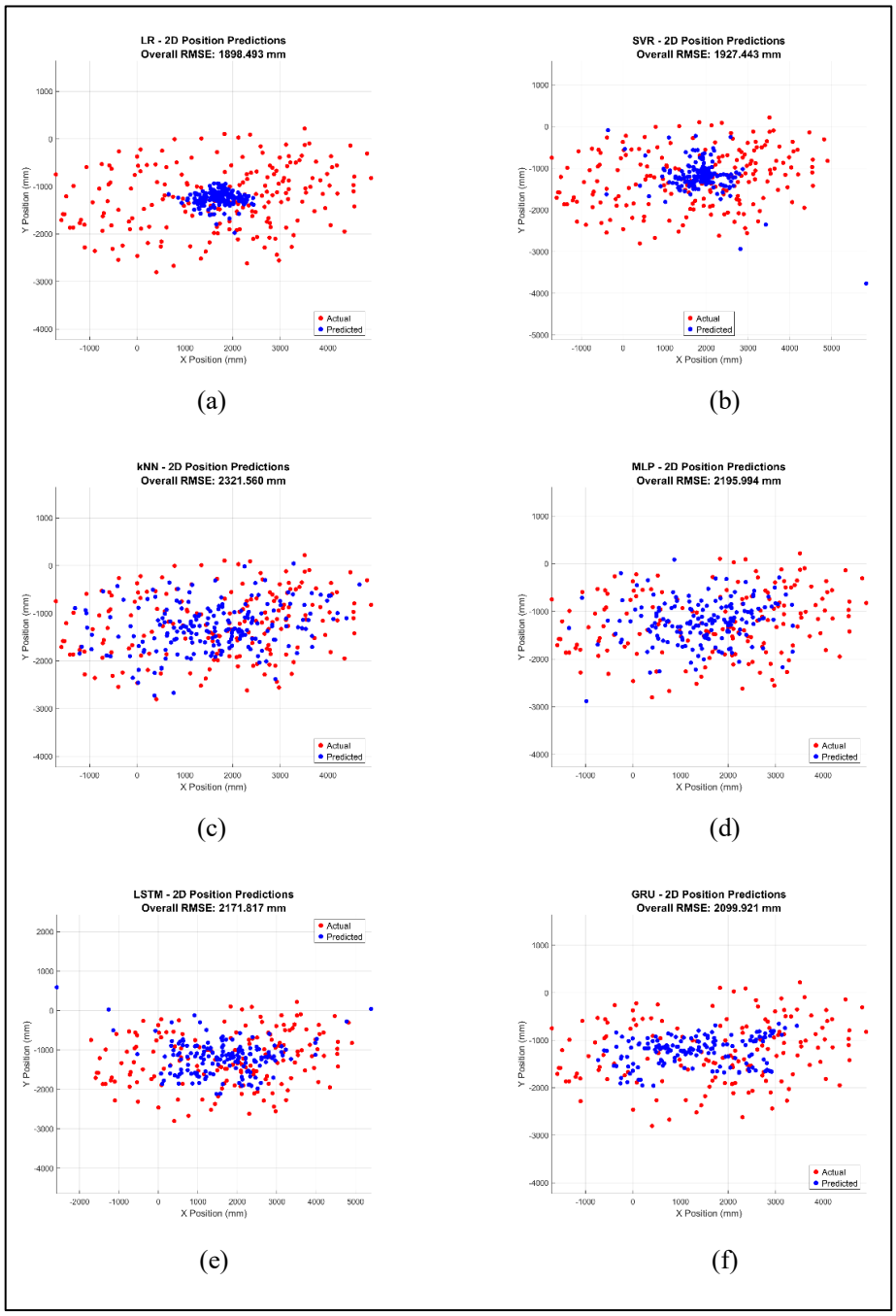

Figure 4.51 2D position predictions for D2 situation in ICU using (a) LR (b) SVR (c) kNN (d) MLP (e) LSTM (f) GRU.

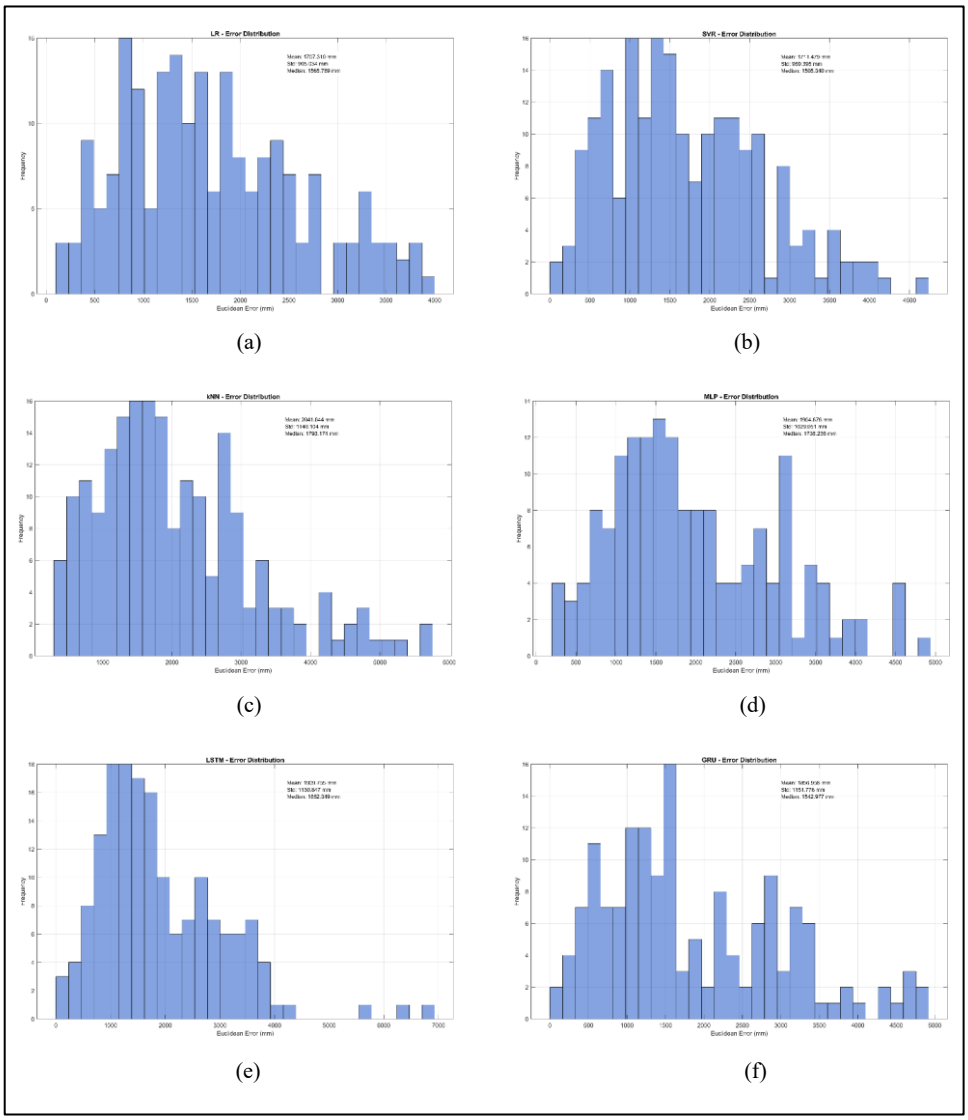

Figure 4.52 Error Distribution for D2 situation in ICU using (a) LR (b) SVR (c) kNN (d) MLP (e) LSTM (f) GRU.

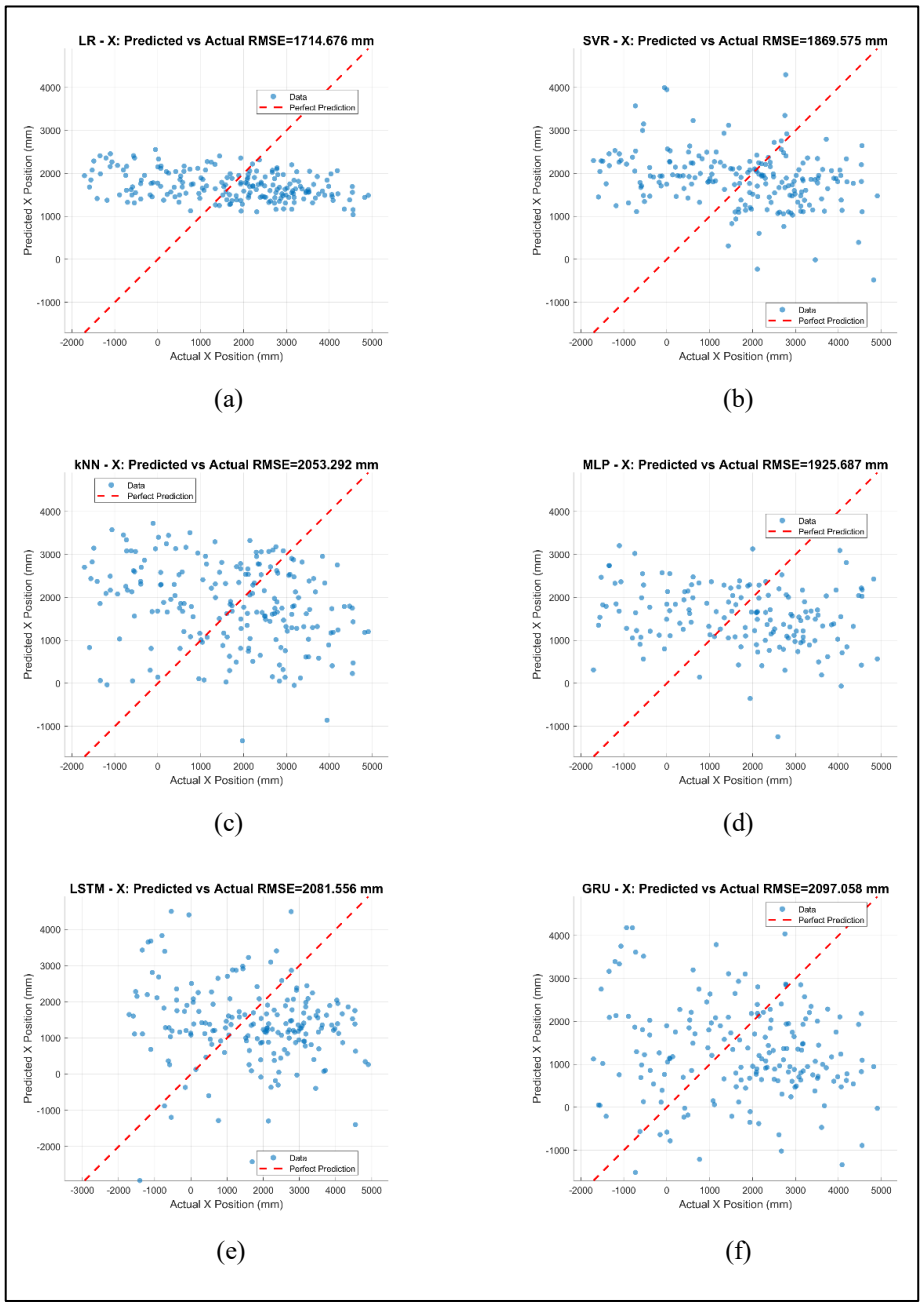

Figure 4.53 Actual versus Predicted X position for D3 situation in ICU using (a) LR (b) SVR (c) kNN (d) MLP (e) LSTM (f) GRU.

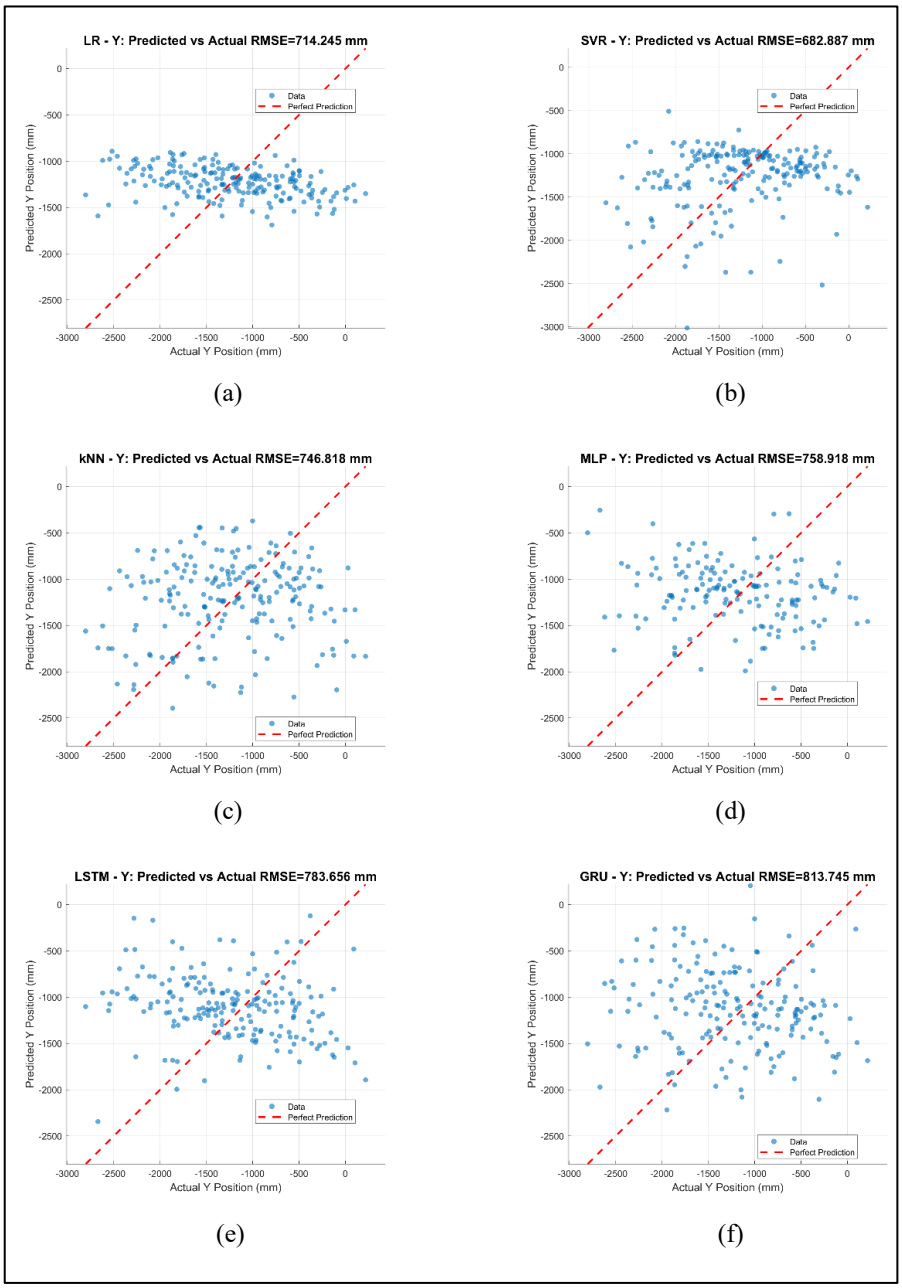

Figure 4.54 Actual versus Predicted Y position for D3 situation in ICU using (a) LR (b) SVR (c) kNN (d) MLP (e) LSTM (f) GRU.

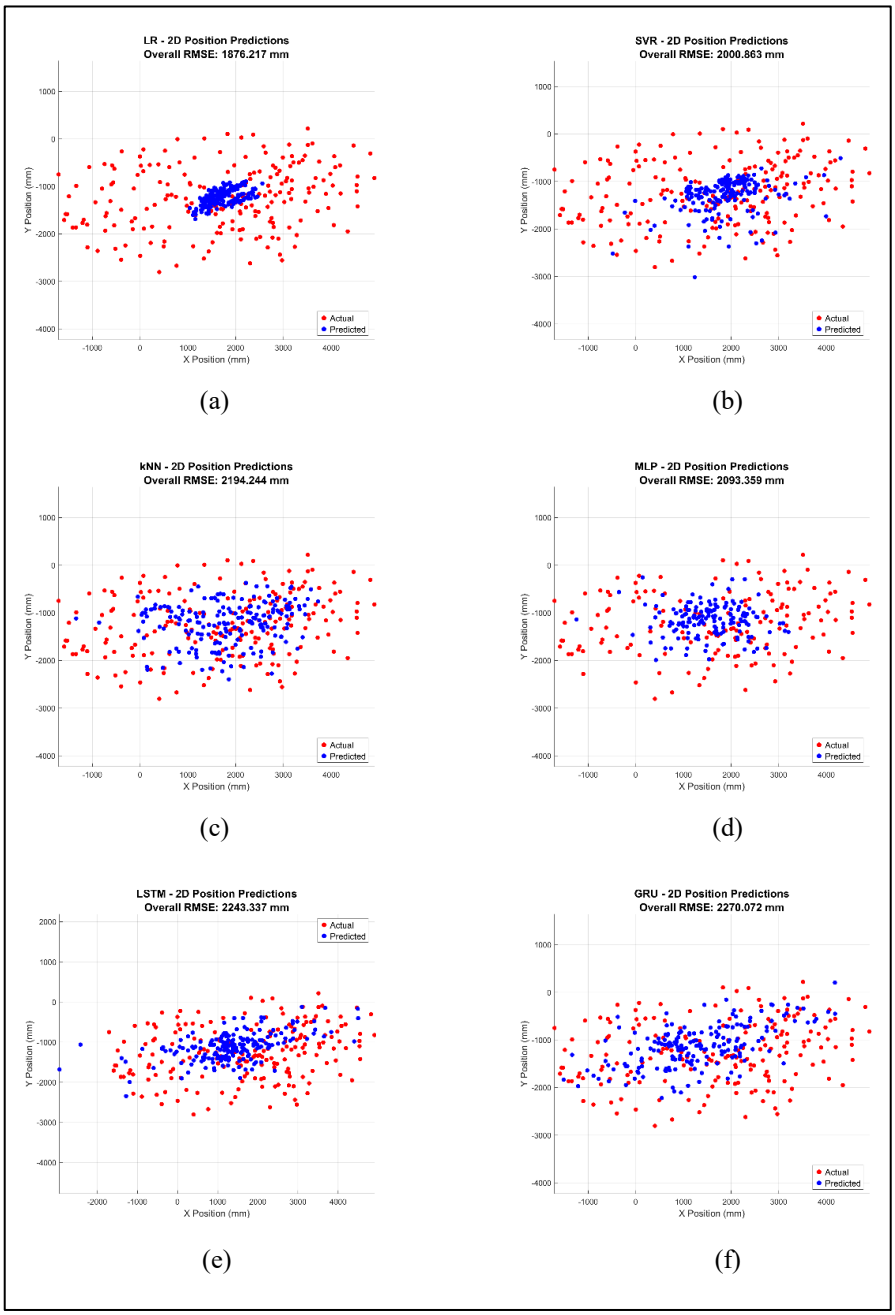

Figure 4.55 2D position predictions for D3 situation in ICU using (a) LR (b) SVR (c) kNN (d) MLP (e) LSTM (f) GRU.

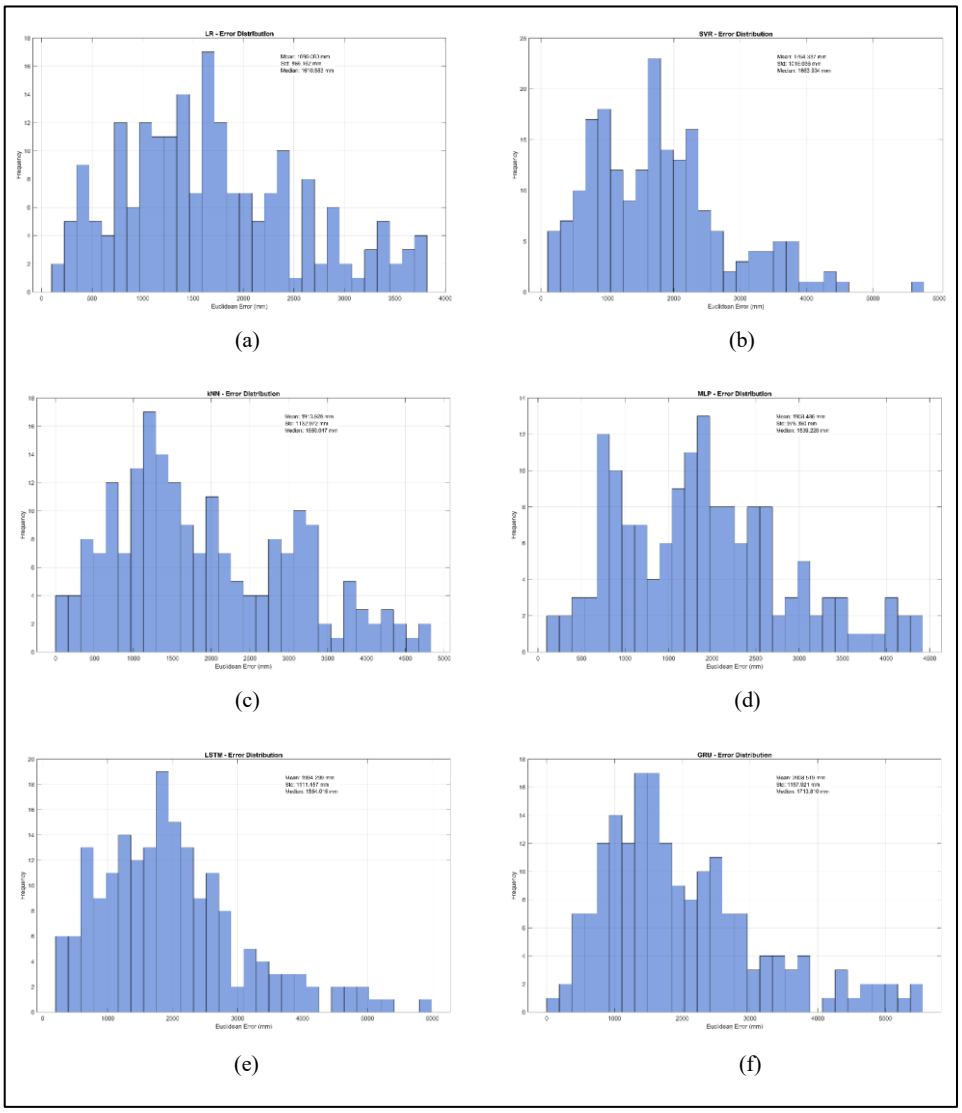

Figure 4.56 Error Distribution for D3 situation in ICU using (a) LR (b) SVR (c) kNN (d) MLP (e) LSTM (f) GRU.

CONCLUSION AND SUGGESTIONS

This paper presents practical statistical channel models tailored for hospital settings, along with ML-based algorithms for adaptive modulation and channel parameter estimation in VLC-based MBSNs. The proposed approach takes into account wavelength dependency, random movement trajectories, and real-world hospital environments.

This study explored various modulation strategies to enhance SE, including Q-learning-based adaptive modulation, KNN-based adaptive modulation, and a fixed non-adaptive scheme used as a benchmark. The Q-learning method showed strong adaptability to system and environmental variations without depending on explicit CSI. By managing the trade-off between exploration and exploitation, the Q-learning agent steadily improved its performance and successfully reached the target SER. While the KNN approach provided better SE than the non-adaptive baseline, it occasionally failed to satisfy the SER condition. On the other hand, Q-learning reliably met the SER target but sometimes yielded slightly lower SE due to quantization limitations and cautious decisions near the SER boundary. Increasing the quantization resolution could offer more accuracy, though it would raise the system's complexity. Future improvements may focus on refining quantization methods or adopting neural network-based solutions. Other adaptive modulation approaches could also support SE gains in VLC-based MBSNs. For environments requiring fast data transmission and minimal delay, more sophisticated RL models may be needed to handle user mobility more effectively.

Beyond that, the study also explored channel parameter estimation to support dependable VLC communication. Among the tested ML models, LSTM networks proved most effective. Simulation findings showed that in the ICU, node D1 yielded the highest RMSE for PL (1.6797 dB) and RMS delay spread

(1.0567 ns). Meanwhile, in the Family-Type Patient Room (FTPR), node D3 had the highest RMSE for PL (1.0652 dB) and delay spread (0.7657 ns). Precise estimation of VLC channel metrics such as DC gain and RMS delay spread is critical for ensuring communication robustness, and ML plays a key role in enhancing both accuracy and system efficiency. The results underscore that the performance of these ML-based estimators in VLC-based MBSNs is highly dependent on the location of the PD and the spatial layout of the deployment area—factors that are fundamental to effective VLC channel modeling.

The comprehensive position estimation analysis identified MLP as the optimal architecture for practical deployment across diverse healthcare environments. In FTPR scenarios, MLP achieved positioning accuracies of 58.6 cm for the combined D1-D2-D3 configuration, 63.0 cm for D1-D2, 61.0 cm for D1-D3, and 67.5 cm for D2-D3, demonstrating consistent sub-meter accuracy essential for patient tracking applications. Individual sensor configurations yielded accuracies of 63.5 cm, 75.0 cm, and 73.1 cm for D1, D2, and D3 respectively, maintaining acceptable precision even with reduced sensor diversity. In the more challenging ICU environment, MLP sustained reliable performance with accuracies of 217.1 cm for D1-D2-D3, 202.1 cm for D1-D2, 216.3 cm for D1-D3, and 227.5 cm for D2-D3, while individual sensors achieved 213.0 cm, 219.6 cm, and 209.3 cm for D1, D2, and D3 respectively. These results, combined with MLP's 35-48% reduction in computational requirements compared to sequential models and its ability to maintain spatial variance unlike classical approaches, establish it as the preferred solution for VLC-based positioning in medical facilities.

Compared to results from other papers, the accuracy is relatively low mainly because of the lack of data available for training. Since there is extremely insufficient amount of data for training ML models, particularly deep learning models. Also, the channel simulation outputs a single channel for the LED array, which makes the use of trilateration not possible. Having only one overall channel resulted in low confidence in position estimation. Moreover, the

standard deviation in features are extremely low, which causes trouble in predicting the position, even with multiple sensors.

Compared with results from other papers, the accuracy is relatively low mainly because of the lack of data available for training. Since there is an extremely insufficient amount of data for training ML models, particularly deep learning models, the standard deviation in features remains extremely low, which creates difficulties in predicting the position even with multiple sensors. We also noticed that in ICU, more light is captured by the sensors due to the higher illumination level. As D1 is placed on the shoulder, it collects the most rays compared to D2 on the wrist and D3 on the ankle, which barely receives light. Consequently, D1 exhibits greater variance and higher prediction error. The observation that error more than doubled between FTPR and ICU further validates this outcome, as also verified by Donmez et al. (2021). Moreover, results consistently confirm that using more sensors improves accuracy, with D1–D2–D3 outperforming any single or paired sensor configuration, and paired sensor configuration produce higher accuracy compared to single sensor configuration.

For future work, it is essential to explore additional ML algorithms, including hybrid and ensemble models that can better leverage limited datasets. Extending the evaluation to a broader range of hospital scenarios, such as emergency rooms, operating theaters, and corridors, will allow the framework to generalize more effectively across diverse clinical environments. Another important direction is investigating the direct relationship between feature variance and positioning error. Real-world implementation and data collection should also be prioritized to assess the feasibility of the system under operational constraints and to compare measured outcomes against simulations. Finally, since feature variance is low, incorporating additional channel characteristics beyond PL and RMS delay spread may lead to more robust estimators and improved accuracy, thereby bringing VLC-based MBSNs closer to practical deployment in next-generation healthcare systems.

REFERENCES

Abtahi, M., & Hashemi, H. (1995). Simulation of indoor propagation channel at infrared frequencies in furnished office environments. *Proceedings of 6th International Symposium on Personal, Indoor and Mobile Radio Communications*. https://doi.org/10.1109/pimrc.1995.476903

Alkandari, Y., Ijaz, M., Ekpo, S., Adebisi, B., Soto, I., Zamorano-Illanes, R., & Azurdia, C. (2023). Optimization of Visible Light Positioning in Industrial Applications using Machine Learning. *2023 South American Conference on Visible Light Communications (SACVLC)*, 141–146. https://doi.org/10.1109/sacvlc59022.2023.10347641

Al-Kinani, A., Wang, C., Haas, H., & Yang, Y. (2016a). Characterization and Modeling of Visible Light Communication Channels. *2016 IEEE 83rd Vehicular Technology Conference (VTC Spring)*, 1–5. https://doi.org/10.1109/vtcspring.2016.7504160

Al-Kinani, A., Wang, C., Haas, H., & Yang, Y. (2016b). A geometry-based multiple bounce model for visible light communication channels. *2016 International Wireless Communications and Mobile Computing Conference (IWCMC)*, 31–37. https://doi.org/10.1109/iwcmc.2016.7577029

Al-Kinani, A., Wang, C., Zhou, L., & Zhang, W. (2018). Optical wireless communication channel measurements and models. *IEEE Communications Surveys & Tutorials*, *20*(3), 1939–1962. https://doi.org/10.1109/comst.2018.2838096

Alnaim, A. K., & Alwakeel, A. M. (2023). Machine-Learning-Based IoT–Edge Computing healthcare solutions. *Electronics*, *12*(4), 1027. https://doi.org/10.3390/electronics12041027

Alsulami, O., Hussein, A. T., Alresheedi, M. T., & Elmirghani, J. M. H. (2018). Optical wireless communication systems: A survey. *arXiv preprint arXiv*:1812.11544. Retrieved July 9, 2025, from https://arxiv.org/abs/1812.11544

Alwahedi, F., Aldhaheri, A., Ferrag, M. A., Battah, A., & Tihanyi, N. (2024). Machine learning techniques for IoT security: Current research and future vision with generative AI and large language models. *Internet of Things and Cyber-Physical Systems*, *4*, 167–185. https://doi.org/10.1016/j.iotcps.2023.12.003

Antaki, B., Dalloul, A. H., & Miramirkhani, F. (2025). Intelligent health monitoring in 6G networks: Machine Learning-Enhanced VLC-Based medical Body sensor networks. Sensors, 25(11), 3280. https://doi.org/10.3390/s25113280

Arfaoui, M. A., Soltani, M. D., Tavakkolnia, I., Ghrayeb, A., Safari, M., Assi, C. M., & Haas, H. (2020). Physical layer security for visible light communication Systems: a survey. *IEEE Communications Surveys & Tutorials*, *22*(3), 1887–1908. https://doi.org/10.1109/comst.2020.2988615

Arnon, S., Barry, J., & Karagiannidis, G. (2012). *Advanced optical wireless communication systems* (1st ed.). Cambridge University Press.

Bariah, L., Mohjazi, L., Muhaidat, S., Sofotasios, P. C., Kurt, G. K., Yanikomeroglu, H., & Dobre, O. A. (2020). A prospective look: key enabling technologies, applications and open research topics in 6G networks. *IEEE Access*, *8*, 174792–174820. https://doi.org/10.1109/access.2020.3019590

Barry, J., Kahn, J., Krause, W., Lee, E., & Messerschmitt, D. (1993). Simulation of multipath impulse response for indoor wireless optical channels. *IEEE Journal on Selected Areas in Communications*, *11*(3), 367–379. https://doi.org/10.1109/49.219552

Bayat Rizi, R., Forouzan, A. R., Miramirkhani, F., & Sabahi, M. F. (2024). Machine Learning-Driven Adaptive Modulation for VLC-Enabled Medical Body Sensor Networks. *IJEEE*, *20*(4). https://doi.org/10.22068/IJEEE.20.4.3407

Bergstra, J., & Bengio, Y. (2012). Random search for hyper-parameter optimization. *Journal of Machine Learning Research*, *13*(1), 281–305.

Bhat, J. R., & Alqahtani, S. A. (2021). 6G ecosystem: current status and future perspective. *IEEE Access*, *9*, 43134–43167. https://doi.org/10.1109/access.2021.3054833

Bian, R., Tavakkolnia, I., & Haas, H. (2019). 15.73 Gb/s Visible Light Communication With Off-the-Shelf LEDs. *Journal of Lightwave Technology*, *37*(10), 2418–2424. https://doi.org/10.1109/jlt.2019.2906464

Bo, C., Jung, T., Mao, X., Li, X., & Wang, Y. (2016). SmartLoc: sensing landmarks silently for smartphone-based metropolitan localization. *EURASIP Journal on Wireless Communications and Networking*, *2016*(1). https://doi.org/10.1186/s13638-016-0603-7

Bobrov, E., Kropotov, D., Lu, H., & Zaev, D. (2021). Massive MIMO adaptive modulation and coding using online deep learning algorithm. *IEEE Communications Letters*, *26*(4), 818–822. https://doi.org/10.1109/lcomm.2021.3132947

Boric-Lubecke, O., Gao, X., Yavari, E., Baboli, M., Singh, A., & Lubecke, V. M. (2014). E-healthcare: Remote monitoring, privacy, and security. *2014 IEEE MTT-S International Microwave Symposium (IMS2014)*, 1–3. https://doi.org/10.1109/mwsym.2014.6848602

Buzzi, S., D'Andrea, C., Li, D., & Feng, S. (2019). MIMO-UFMC Transceiver schemes for Millimeter-Wave wireless communications. *IEEE Transactions on Communications*, *67*(5), 3323–3336. https://doi.org/10.1109/tcomm.2019.2896122

Byun, J., Cho, Y., Im, T., Ko, H., Shin, K., Kim, J., & Jo, O. (2021). Iterative learning for reliable link adaptation in the internet of underwater things. *IEEE Access*, *9*, 30408–30416. https://doi.org/10.1109/access.2021.3058981

Cao, Z., Cheng, M., Yang, Q., Tang, M., Liu, D., & Deng, L. (2021). Experimental investigation of environmental interference mitigation and blocked LEDs using a memory-artificial neural network in 3D indoor visible light positioning systems. *Optics Express*, *29*(21), 33937. https://doi.org/10.1364/oe.441540

Caputo, S., Borghini, G., Jayousi, S., Rashid, A., & Mucchi, L. (2023). Visible Light Communications for Healthcare Applications: Opportunities and Challenges. *2023 IEEE 17th International Symposium on Medical Information and Communication Technology (ISMICT)*, 1–6. https://doi.org/10.1109/ismict58261.2023.10152290

Carruthers, J., & Kahn, J. (1997). Modeling of nondirected wireless infrared channels. *IEEE Transactions on Communications*, *45*(10), 1260–1268. https://doi.org/10.1109/26.634690

Carruthers, J., & Kannan, P. (2002). Iterative site-based modeling for wireless infrared channels. *IEEE Transactions on Antennas and Propagation*, *50*(5), 759–765. https://doi.org/10.1109/tap.2002.1011244

Chen, C., Basnayaka, D., & Haas, H. (2016). Non-line-of-sight channel impulse response characterisation in visible light communications. *2016 IEEE International Conference on Communications (ICC)*, 1–6. https://doi.org/10.1109/icc.2016.7511382

Chen, H., Li, F., & Wang, Y. (2017). EchoTrack: Acoustic device-free hand tracking on smart phones. *IEEE INFOCOM 2022 - IEEE Conference on Computer Communications*. https://doi.org/10.1109/infocom.2017.8057101

Chi, N. (2018). *LED-based visible light communications* (1st ed.). Springer.

Chi, N., Jia, J., Hu, F., Zhao, Y., & Zou, P. (2020). Challenges and prospects of machine learning in visible light communication. *Journal of Communications and Information Networks*, *5*(3), 302–309. https://doi.org/10.23919/jcin.2020.9200893

Cho, S., Chen, G., & Coon, J. P. (2021). Cooperative beamforming and jamming for secure VLC system in the presence of active and passive eavesdroppers. *IEEE Transactions on Green Communications and Networking*, *5*(4), 1988–1998. https://doi.org/10.1109/tgcn.2021.3092146

Chowdhury, M. I. S., Zhang, W., & Kavehrad, M. (2014). Combined Deterministic and modified Monte Carlo method for calculating impulse responses of indoor optical wireless channels. *Journal of Lightwave Technology*, *32*(18), 3132–3148. https://doi.org/10.1109/jlt.2014.2339131

Chowdhury, M. Z., Hossan, M. T., Islam, A., & Jang, Y. M. (2018). A Comparative Survey of Optical Wireless Technologies: Architectures and Applications. *IEEE Access*, *6*, 9819–9840. https://doi.org/10.1109/access.2018.2792419

Chowdhury, M. Z., Shahjalal, M., Ahmed, S., & Jang, Y. M. (2020). 6G Wireless Communication Systems: applications, requirements, technologies, challenges, and research directions. *IEEE Open Journal of the Communications Society*, *1*, 957–975. https://doi.org/10.1109/ojcoms.2020.3010270

Dalloul, A. H., Miramirkhani, F., & Kouhalvandi, L. (2023). A review of recent innovations in remote health monitoring. *Micromachines*, *14*(12), 2157. https://doi.org/10.3390/mi14122157

Dastgheib, M. A., Beyranvand, H., Salehi, J. A., & Maier, M. (2018). Mobility-Aware resource allocation in VLC networks using T-Step Look-Ahead Policy. *Journal of Lightwave Technology*, *36*(23), 5358–5370. https://doi.org/10.1109/jlt.2018.2872869

Dharmarathne, G., Jayasinghe, T. N., Bogahawaththa, M., Meddage, D., & Rathnayake, U. (2024). A novel machine learning approach for

diagnosing diabetes with a self-explainable interface. *Healthcare Analytics*, *5*, 100301. https://doi.org/10.1016/j.health.2024.100301

Dhatchayeny, D. R., Arya, S., & Chung, Y. H. (2019). Infrared-Based Multiple-Patient monitoring in indoor optical wireless healthcare systems. *IEEE Sensors Journal*, *19*(14), 5594–5599. https://doi.org/10.1109/jsen.2019.2906898

Dimitrov, S., & Haas, H. (2015). *Principles of LED light communications* (1st ed.). Cambridge University Press.

Dimitrov, S., Mesleh, R., Haas, H., Cappitelli, M., Olbert, M., & Bassow, E. (2009). On the SIR of a cellular infrared optical wireless system for an aircraft. *IEEE Journal on Selected Areas in Communications*, *27*(9), 1623–1638. https://doi.org/10.1109/jsac.2009.091212

Ding, J., I, C., & Xu, Z. (2015). Indoor optical wireless channel characteristics with distinct source radiation patterns. *IEEE Photonics Journal*, *8*(1), 1–15. https://doi.org/10.1109/jphot.2015.2508420

Dissanayake, S. D., & Armstrong, J. (2013). Comparison of ACO-OFDM, DCO-OFDM and ADO-OFDM in IM/DD systems. *Journal of Lightwave Technology*, *31*(7), 1063–1072. https://doi.org/10.1109/jlt.2013.2241731

Donmez, B., & Miramirkhani, F. (2021). Channel modeling and characterization for VLC-based MBSNs impaired by 3D user mobility. *2021 13th International Conference on Electrical and Electronics Engineering (ELECO)*, 485–489. https://doi.org/10.23919/eleco54474.2021.9677662

Donmez, B., & Miramirkhani, F. (2022). Path Loss and RMS Delay Spread Model for VLC-based Patient Health Monitoring System. *2022 4th West Asian Symposium on Optical and Millimeter-wave Wireless Communications (WASOWC)*, 1–5. https://doi.org/10.1109/wasowc54657.2022.9798434

Donmez, B., Mitra, R., & Miramirkhani, F. (2021). Channel Modeling and Characterization for VLC-Based Medical Body Sensor Networks: Trends and Challenges. *IEEE Access*, *9*, 153401–153419. https://doi.org/10.1109/access.2021.3127941

Du, P., Zhang, S., Alphones, A., & Chen, C. (2021). Faster deployment for indoor visible light positioning using XGBoost algorithms in industrial Internet-of-Things. *IECON 2020 the 46th Annual Conference of the IEEE Industrial Electronics Society*, 1–7. https://doi.org/10.1109/iecon48115.2021.9589151

Du, P., Zhang, S., Chen, C., Yang, H., Zhong, W., Zhang, R., Alphones, A., & Yang, Y. (2019). Experimental demonstration of 3D visible light positioning using received signal strength with Low-Complexity trilateration assisted by deep learning technique. *IEEE Access*, *7*, 93986–93997. https://doi.org/10.1109/access.2019.2928014

Elwekeil, M., Jiang, S., Wang, T., & Zhang, S. (2018). Deep convolutional neural networks for link adaptations in MIMO-OFDM wireless systems. *IEEE Wireless Communications Letters*, *8*(3), 665–668. https://doi.org/10.1109/lwc.2018.2881978

Eroglu, Y. S., Guvenc, I., Pala, N., & Yuksel, M. (2015). AOA-based localization and tracking in multi-element VLC systems. *2015 IEEE 16th Annual Wireless and Microwave Technology Conference (WAMICON)*. https://doi.org/10.1109/wamicon.2015.7120424

Fath, T., & Haas, H. (2013). Performance comparison of MIMO techniques for optical wireless communications in indoor environments. *IEEE Transactions on Communications*, *61*(2), 733–742. https://doi.org/10.1109/tcomm.2012.120512.110578

Feng, L., Hu, R. Q., Wang, J., & Qian, Y. (2018). Deployment Issues and performance study in a Relay-Assisted Indoor Visible Light Communication system. *IEEE Systems Journal*, *13*(1), 562–570. https://doi.org/10.1109/jsyst.2018.2869073

Fernando, N., Hong, Y., & Viterbo, E. (2012). Flip-OFDM for unipolar communication systems. *IEEE Transactions on Communications*, *60*(12), 3726–3733. https://doi.org/10.1109/tcomm.2012.082712.110812

Fu, Q., & Song, A. (2018). Adaptive Modulation for Underwater Acoustic Communications Based on Reinforcement Learning. *OCEANS 2018 MTS/IEEE Charleston*, 1–8. https://doi.org/10.1109/oceans.2018.8604746

Garg, D., & Nain, A. (2021). Next generation optical wireless communication: a comprehensive review. *Journal of Optical Communications*, *44*(s1), s1535–s1550. https://doi.org/10.1515/joc-2020-0254

Gfeller, & Bapst, U. (1979). Wireless in-house data communication via diffuse infrared radiation. *Proceedings of the IEEE*, *67*(11), 1474–1486. https://doi.org/10.1109/proc.1979.11508

Ghassemlooy, Z., Popoola, W., & Rajbhandari, S. (2017*). Optical wireless communications: System and channel modelling with MATLAB®* (2nd ed.). CRC Press.

Giordani, M., Polese, M., Mezzavilla, M., Rangan, S., & Zorzi, M. (2020). Toward 6G networks: use cases and technologies. *IEEE Communications Magazine*, *58*(3), 55–61. https://doi.org/10.1109/mcom.001.1900411

Gizzini, A. K., & Chafii, M. (2023). RNN based channel estimation in doubly selective environments. *IEEE Transactions on Machine Learning in Communications and Networking*, *2*, 1–18. https://doi.org/10.1109/tmlcn.2023.3332021

Gu, W., Aminikashani, M., Deng, P., & Kavehrad, M. (2016). Impact of multipath reflections on the performance of indoor visible light positioning systems. *Journal of Lightwave Technology*, *34*(10), 2578–2587. https://doi.org/10.1109/jlt.2016.2541659

Guo, J., Zhao, Y., Zhang, Q., & Jiang, Y. (2019). RNN-Test: Towards adversarial testing for recurrent neural network systems. *arXiv preprint arXiv*:1911.06155. Retrieved July 3, 2025, from https://arxiv.org/abs/1911.06155

Hadjidj, A., Souil, M., Bouabdallah, A., Challal, Y., & Owen, H. (2012). Wireless sensor networks for rehabilitation applications: Challenges and opportunities. *Journal of Network and Computer Applications*, *36*(1), 1–15. https://doi.org/10.1016/j.jnca.2012.10.002

Hakeem, S. a. A., Hussein, H. H., & Kim, H. (2022). Vision and research directions of 6G technologies and applications. *Journal of King Saud University - Computer and Information Sciences*, *34*(6), 2419–2442. https://doi.org/10.1016/j.jksuci.2022.03.019

Hamza, A. S., Deogun, J. S., & Alexander, D. R. (2018). Classification Framework for free space Optical Communication links and Systems. *IEEE Communications Surveys & Tutorials*, *21*(2), 1346–1382. https://doi.org/10.1109/comst.2018.2876805

Hassan, N. M., Olaniyi, O. M., Ahmed, A., & Dogo, E. M. (2013). Wireless sensor networks for remote healthcare monitoring in Nigeria: Challenges and way forward. *2013 IEEE International Conference on Emerging & Sustainable Technologies for Power & ICT in a Developing Society (NIGERCON)*, 182–187. https://doi.org/10.1109/nigercon.2013.6715654

Hayasaka, N., & Ito, T. (2007). Channel modeling of nondirected wireless infrared indoor diffuse link. *Electronics and Communications in Japan (Part I Communications)*, *90*(6), 9–19. https://doi.org/10.1002/ecja.20352

Hazas, M., & Hopper, A. (2006). Broadband ultrasonic location systems for improved indoor positioning. *IEEE Transactions on Mobile Computing*, *5*(5), 536–547. https://doi.org/10.1109/tmc.2006.57

Hong, Y., Feng, F., Bottrill, K. R. H., Taengnoi, N., Singh, R., Faulkner, G., O'Brien, D. C., & Petropoulos, P. (2020). Beyond Terabit/s WDM Optical Wireless Transmission using Wavelength-transparent Beam Tracking and Steering. *Optical Fiber Communication Conference (OFC) 2022*, *36*, W1G.4. https://doi.org/10.1364/ofc.2020.w1g.4

Hong, Y., Wu, T., & Chen, L. (2016). On the Performance of Adaptive MIMO-OFDM Indoor Visible Light Communications. *IEEE Photonics Technology Letters*, *28*(8), 907–910. https://doi.org/10.1109/lpt.2016.2517192

Hsu, L., Chow, C., Liu, Y., Chang, Y., Tsai, T., Hung, T., Lin, Y., Jian, Y., & Yeh, C. (2022). Utilizing single light-emitting-diode (LED) lamp and silicon solar-cells visible light positioning (VLP) based on angle-of-arrival (AOA) and long-short-term-memory-neural-network (LSTMNN). *Optics Communications*, *524*, 128761. https://doi.org/10.1016/j.optcom.2022.128761

Huang, B., Liu, J., Sun, W., & Yang, F. (2019). A Robust Indoor Positioning Method based on Bluetooth Low Energy with Separate Channel Information. *Sensors*, *19*(16), 3487. https://doi.org/10.3390/s19163487

Hussein, H. H., & El-Kader, S. M. A. (2017). Enhancing signal to noise interference ratio for device to device technology in 5G applying mode selection technique. *2017 Intl Conf on Advanced Control Circuits Systems (ACCS) Systems & 2017 Intl Conf on New Paradigms in Electronics & Information Technology (PEIT)*, 187–192. https://doi.org/10.1109/accs-peit.2017.8303040

Hutter, F., Kotthoff, L., & Vanschoren, J. (2019). *Automated machine learning: Methods, systems, challenges* (1st ed.). Springer.

Interim amendment for the 2018 residential guidelines. (2020). Guidelines for design and construction of residential health, care, and support facilities. https://fgiguidelines.org/wp-content/uploads/2020/08/FGI-2018-RES-Interim-Amendment-ResidentRooms\2020-08-28.pdf

International Telecommunication Union. (2022). *Future technology trends of terrestrial IMT systems towards 2030 and beyond*. https://www.itu.int/md/R19-WP5D-C-1295/en

ISO/IEEE International Standard Health Informatics-Point-of Care Medical Device Communication-Transport Pro Le-Infrared (document ISO/IEEE 11073-30300:2004(E)). (2004). IEEE.

ISO/IEEE international standard health informatics-Point-of-care medical device communication-Transport profile-Infrared (ISO/IEEE 11073-30300:2004(E)). (2004).

ITU-R. (2015). *IMT Vision – Framework and overall objectives of the future development of IMT for 2020 and beyond*. https://www.itu.int/dms_pubrec/itu-r/rec/m/R-REC-M.2083-0-201509-I!!PDF-E.pdf

Jativa, P. P., Becerra, R., Azurdia-Meza, C. A., Zabala-Blanco, D., Soto, I., & Canizares, M. R. (2021). Extreme Learning Machine Based Channel Estimator and Equalizer for Underground Mining VLC Systems. *2021 IEEE Latin-American Conference on Communications (LATINCOM)*, 1–6. https://doi.org/10.1109/latincom53176.2021.9647737

Jebur, B. A., Alkassar, S. H., Abdullah, M. a. M., & Tsimenidis, C. C. (2021). Efficient Machine Learning-Enhanced channel estimation for OFDM systems. *IEEE Access*, *9*, 100839–100850. https://doi.org/10.1109/access.2021.3097436

Ji, S., & Thompson, J. (2023). Robust Machine Learning for Channel Estimation with Varying Delay and Doppler Shift Conditions. *2022 IEEE 95th Vehicular Technology Conference: (VTC2022-Spring)*, *4*, 1–5. https://doi.org/10.1109/vtc2023-spring57618.2023.10199352

Jovicic, A., Li, J., & Richardson, T. (2013). Visible light communication: opportunities, challenges and the path to market. *IEEE Communications Magazine*, *51*(12), 26–32. https://doi.org/10.1109/mcom.2013.6685754

Julien-Vergonjanne, A., Sahuguède, S., & Chevalier, L. (2016). Optical wireless body area networks for healthcare applications. In *Signals and communication technology* (pp. 569–587). https://doi.org/10.1007/978-3-319-30201-0_26

Jung, S., Hann, S., & Park, C. (2011). TDOA-based optical wireless indoor localization using LED ceiling lamps. *IEEE Transactions on Consumer Electronics*, *57*(4), 1592–1597. https://doi.org/10.1109/tce.2011.6131130

Jungnickel, V., Pohl, V., Nonnig, S., & Von Helmolt, C. (2002). A physical model of the wireless infrared communication channel. *IEEE Journal on Selected Areas in Communications*, *20*(3), 631–640. https://doi.org/10.1109/49.995522

Kao, Y., & Wu, K. (2022). A Low-Complexity channel estimation based on a Least-Squares algorithm in OFDM systems. *Applied Sciences*, *12*(9), 4258. https://doi.org/10.3390/app12094258

Karsanti, H. T., Ardiyanto, I., & Nugroho, L. E. (2019). Deep Learning-Based Patient Visits Forecasting Using Long Short Term Memory. *2019 International Conference of Artificial Intelligence and Information Technology (ICAIIT)*. https://doi.org/10.1109/icaiit.2019.8834634

Karunatilaka, D., Zafar, F., Kalavally, V., & Parthiban, R. (2015). LED based indoor visible light communications: state of the art. *IEEE Communications Surveys & Tutorials*, *17*(3), 1649–1678. https://doi.org/10.1109/comst.2015.2417576

Khalaf-Allah, M. (2015). Time of arrival (TOA)-based direct location method. *2015 16th International Radar Symposium (IRS)*. https://doi.org/10.1109/irs.2015.7226229

Khalighi, M. A., & Uysal, M. (2014). Survey on Free Space Optical Communication: A Communication Theory Perspective. *IEEE Communications Surveys & Tutorials*, *16*(4), 2231–2258. https://doi.org/10.1109/comst.2014.2329501

Khan, L. U., Yaqoob, I., Imran, M., Han, Z., & Hong, C. S. (2020). 6G Wireless Systems: a vision, architectural elements, and future directions. *IEEE Access*, *8*, 147029–147044. https://doi.org/10.1109/access.2020.3015289

Kizilirmak, R. C., Narmanlioglu, O., & Uysal, M. (2015). Relay-Assisted OFDM-Based visible light communications. *IEEE Transactions on Communications*, *63*(10), 3765–3778. https://doi.org/10.1109/tcomm.2015.2464815

Komine, T., & Nakagawa, M. (2004). Fundamental analysis for visible-light communication system using LED lights. *IEEE Transactions on Consumer Electronics*, *50*(1), 100–107. https://doi.org/10.1109/tce.2004.1277847

Konings, D., Faulkner, N., Alam, F., Noble, F., & Lai, E. M. (2017). The effects of interference on the RSSI values of a ZigBee based indoor localization system. *2021 27th International Conference on Mechatronics and*

Machine Vision in Practice (M2VIP). https://doi.org/10.1109/m2vip.2017.8211460

KS, A., Mani, V. V., & Sellathurai, M. (2023). Mitigating nonlinear distortions of high-powered LEDs for VLC using deep neural networks. *Optics Communications*, *550*, 129997. https://doi.org/10.1016/j.optcom.2023.129997

Kurunathan, H., Indhumathi, R., Gaitán, M. G., Taramasco, C., & Tovar, E. (2023). VLC-enabled monitoring in a healthcare setting: Overview and Challenges. *2023 South American Conference on Visible Light Communications (SACVLC)*, 135–140. https://doi.org/10.1109/sacvlc59022.2023.10347546

Lashkari, B., Rezazadeh, J., Farahbakhsh, R., & Sandrasegaran, K. (2018). Crowdsourcing and Sensing for Indoor Localization in IoT: A review. *IEEE Sensors Journal*, *19*(7), 2408–2434. https://doi.org/10.1109/jsen.2018.2880180

Lebas, C., Sahuguede, S., Julien-Vergonjanne, A., Combeau, P., & Aveneau, L. (2018). Infrared and visible links for medical body sensor networks. *2018 Global LIFI Congress (GLC)*, *26*, 1–6. https://doi.org/10.23919/glc.2018.8319120

Lecerf, U., Yemdji-Tchassi, C., Aubert, S., & Michiardi, P. (2022). Automatically Learning Fallback Strategies with Model-Free Reinforcement Learning in Safety-Critical Driving Scenarios. *Proceedings of the 2022 7th International Conference on Machine Learning Technologies (ICMLT)*, 209–215. https://doi.org/10.1145/3529399.3529432

Lee, D., Sun, Y. G., Kim, S. H., Sim, I., Hwang, Y. M., Shin, Y., Kim, D. I., & Kim, J. Y. (2020). DQN-Based Adaptive Modulation Scheme over wireless communication channels. *IEEE Communications Letters*, *24*(6), 1289–1293. https://doi.org/10.1109/lcomm.2020.2978390

Lee, H. W., & Choi, S. W. (2023). A Light-Weighted machine learning approach to channel estimation for New-Radio Systems. *Electronics*, *12*(23), 4740. https://doi.org/10.3390/electronics12234740

Lee, J., & Lee, H. (2008). A photon modeling method for characterization of indoor optical wireless system. *The Journal of Korean Institute of Electromagnetic Engineering and Science*, *19*(6), 688–697. https://doi.org/10.5515/kjkiees.2008.19.6.688

Lee, K., Park, H., & Barry, J. R. (2011). Indoor channel characteristics for visible light communications. *IEEE Communications Letters*, *15*(2), 217–219. https://doi.org/10.1109/lcomm.2011.010411.101945

Lent, D. M. B., Novaes, M. P., Carvalho, L. F., Lloret, J., Rodrigues, J. J. P. C., & Proenca, M. L. (2022). A gated Recurrent unit deep learning model to detect and mitigate distributed denial of service and portscan attacks. *IEEE Access*, *10*, 73229–73242. https://doi.org/10.1109/access.2022.3190008

Letaief, K. B., Chen, W., Shi, Y., Zhang, J., & Zhang, Y. A. (2019). The Roadmap to 6G: AI empowered Wireless Networks. *IEEE Communications Magazine*, *57*(8), 84–90. https://doi.org/10.1109/mcom.2019.1900271

Li, H., Huang, Z., Xiao, Y., Zhan, S., & Ji, Y. (2019). A power and spectrum efficient NOMA scheme for VLC network based on Hierarchical Pre-Distorted LACO-OFDM. *IEEE Access*, *7*, 48565–48571. https://doi.org/10.1109/access.2019.2908524

Li, J., Xie, Z., Liang, C., Xu, C., Ge, C., Xu, Z., Wang, J., Ruan, L., Gui, W., Liang, X., & Ding, W. (2024). Indoor Health Monitoring with VLC-based Passive Posture Monitoring. *2022 Photonics &Amp; Electromagnetics Research Symposium (PIERS)*, 1–8. https://doi.org/10.1109/piers62282.2024.10618552

Li, X., Cao, Y., & Chen, C. (2018). Machine Learning Based High Accuracy Indoor Visible Light Location Algorithm. *Proc. IEEE Int. Conf. Smart Internet Things (SmartIoT)*. https://doi.org/10.1109/smartiot.2018.00043

Lichtenegger, F., Leiner, C., Sommer, C., Weiss, A. P., & Wenzl, F. P. (2019). *Ray-tracing based channel modeling for the simulation of the performance of visible light communication in an indoor environment*. IEEE. https://doi.org/10.1109/blj.2019.8883669

Lighting for hospitals and healthcare facilities (aNSI/IES RP-29-16). (2016). Illuminating engineering society (IES) of North America.

Ling, X., Wang, J., Ding, Z., Zhao, C., & Gao, X. (2018). Efficient OFDMA for LiFi Downlink. *Journal of Lightwave Technology*, *36*(10), 1928–1943. https://doi.org/10.1109/jlt.2018.2796120

Liu, X., Guo, L., & Wei, X. (2021). Indoor visible light applications for communication, positioning, and security. *Wireless Communications and Mobile Computing*, *2021*(1). https://doi.org/10.1155/2021/1730655

Long, S., Khalighi, M. A., Wolf, M., Bourennane, S., & Ghassemlooy, Z. (2014). Channel characterization for indoor visible light communications. *2014 3rd International Workshop in Optical Wireless Communications (IWOW)*, 75–79.

López-HernáNdez, F., & Betancor, M. (1997). DUSTIN: Algorithm for calculation of impulse response on IR wireless indoor channels. *Electronics Letters*, *33*(21), 1804–1806. https://doi.org/10.1049/el:19971224

López-HernáNdez, F., Pérez-JiméNez, R., & SantamaríA, A. (1998a). Monte Carlo calculation of impulse response on diffuse IR wireless indoor channels. *Electronics Letters*, *34*(12), 1260–1262. https://doi.org/10.1049/el:19980825

López-HernáNdez, F., Pérez-JiméNez, R., & SantamaríA, A. (1998b). Modified Monte Carlo scheme for high-efficiency simulation of the impulse response on diffuse IR wireless indoor channels. *Electronics Letters*, *34*(19), 1819–1820. https://doi.org/10.1049/el:19981173

Lu, Y., & Zheng, X. (2020). 6G: A survey on technologies, scenarios, challenges, and the related issues. *Journal of Industrial Information Integration*, *19*, 100158. https://doi.org/10.1016/j.jii.2020.100158

Luo, J., Fan, L., & Li, H. (2017). Indoor positioning systems based on visible light communication: state of the art. *IEEE Communications Surveys & Tutorials*, *19*(4), 2871–2893. https://doi.org/10.1109/comst.2017.2743228

Ma, S., Li, H., He, Y., Yang, R., Lu, S., Cao, W., & Li, S. (2018). Capacity bounds and interference management for interference channel in visible light communication networks. *IEEE Transactions on Wireless Communications*, *18*(1), 182–193. https://doi.org/10.1109/twc.2018.2878585

Ma, Z., Jia, P., Han, D., Zhang, M., Ghassemlooy, Z., & Wang, L. (2022). Deep-Learning-Based Channel Estimation for Multi-wavelength Visible Light Communication System. *2022 4th West Asian Symposium on Optical and Millimeter-wave Wireless Communications (WASOWC)*, 01–04. https://doi.org/10.1109/wasowc54657.2022.9798444

Mao, S., & Sejdić, E. (2022). A review of Recurrent Neural Network-Based Methods in Computational Physiology. *IEEE Transactions on Neural Networks and Learning Systems*, *34*(10), 6983–7003. https://doi.org/10.1109/tnnls.2022.3145365

Mapunda, G. A., Ramogomana, R., Marata, L., Basutli, B., Khan, A. S., & Chuma, J. M. (2020). Indoor Visible Light Communication: a tutorial and survey. *Wireless Communications and Mobile Computing*, *2020*, 1–46. https://doi.org/10.1155/2020/8881305

Marzencki, M., Lin, P., Cho, T., Guo, J., Ngai, B., & Kaminska, B. (2011). Remote health, activity, and asset monitoring with wireless sensor networks. *2021 4th International Conference on Bio-Engineering for Smart Technologies (BioSMART)*, 98–101. https://doi.org/10.1109/health.2011.6026796

Mashhadi, S., Ghiasi, N., Farahmand, S., & Razavizadeh, S. M. (2021). Deep reinforcement learning based adaptive modulation with outdated CSI. *IEEE Communications Letters*, *25*(10), 3291–3295. https://doi.org/10.1109/lcomm.2021.3098419

Maulud, D., & Abdulazeez, A. M. (2020). A review on Linear Regression comprehensive in Machine Learning. *Journal of Applied Science and Technology Trends*, *1*(2), 140–147. https://doi.org/10.38094/jastt1457

MEDICAL ELECTRICAL EQUIPMENT — Part 1-2: General requirements for basic safety and essential performance — Collateral standard: Electromagnetic disturbances — Requirements and tests. (2014). In *IEC 60601-2*. https://doi.org/10.2345/9781570205248.ch1

Mettiti, A. E., & Oumsis, M. (2022). A survey on 6G networks: vision, requirements, architecture, technologies and challenges. *Ingénierie Des Systèmes D Information*, *27*(1), 1–10. https://doi.org/10.18280/isi.270101

Mia, M. M. H., Mahfuz, N., Habib, M. R., & Hossain, R. (2021). An Internet of Things Application on Continuous Remote Patient Monitoring and Diagnosis. *2021 4th International Conference on Bio-Engineering for Smart Technologies (BioSMART)*, 1–6. https://doi.org/10.1109/biosmart54244.2021.9677715

Miramirkhani, F., Narmanlioglu, O., Uysal, M., & Panayirci, E. (2017). A mobile channel model for VLC and application to adaptive system design. *IEEE Communications Letters*, *21*(5), 1035–1038. https://doi.org/10.1109/lcomm.2017.2651800

Miramirkhani, F., & Uysal, M. (2015). Channel modeling and characterization for visible light communications. *IEEE Photonics Journal*, *7*(6), 1–16. https://doi.org/10.1109/jphot.2015.2504238

Miramirkhani, F., & Uysal, M. (2020). Channel modelling for indoor visible light communications. *Philosophical Transactions of the Royal Society a Mathematical Physical and Engineering Sciences*, *378*(2169), 20190187. https://doi.org/10.1098/rsta.2019.0187

Mitra, R., & Kaddoum, G. (2022). Random Fourier Feature-Based deep learning for wireless communications. *IEEE Transactions on Cognitive Communications and Networking*, *8*(2), 468–479. https://doi.org/10.1109/tccn.2022.3164898

Mossaad, M. S. A., Hranilovic, S., & Lampe, L. (2015). Visible light communications using OFDM and multiple LEDs. *IEEE Transactions on Communications*, *63*(11), 4304–4313. https://doi.org/10.1109/tcomm.2015.2469285

Mucchi, L., Jayousi, S., Caputo, S., Paoletti, E., Zoppi, P., Geli, S., & Dioniso, P. (2020). How 6G Technology Can Change the Future Wireless Healthcare. In *2020 2nd 6G Wireless Summit (6G SUMMIT)* (pp. 1–6). IEEE. https://doi.org/10.1109/6gsummit49458.2020.9083916

Musumeci, F., Rottondi, C., Nag, A., Macaluso, I., Zibar, D., Ruffini, M., & Tornatore, M. (2018). An overview on application of machine learning techniques in optical networks. *IEEE Communications Surveys & Tutorials*, *21*(2), 1383–1408. https://doi.org/10.1109/comst.2018.2880039

Na, Z., Wang, Y., Xiong, M., Liu, X., & Xia, J. (2018). Modeling and throughput analysis of an ADO-OFDM based Relay-Assisted VLC system for 5G networks. *IEEE Access*, *6*, 17586–17594. https://doi.org/10.1109/access.2018.2817487

Narmanlioglu, O., Kizilirmak, R. C., Baykas, T., & Uysal, M. (2017). Link adaptation for MIMO OFDM Visible Light communication systems. *IEEE Access*, *5*, 26006–26014. https://doi.org/10.1109/access.2017.2771333

Naser, S., Bariah, L., Muhaidat, S., Sofotasios, P. C., Al-Qutayri, M., Damiani, E., & Debbah, M. (2022). Toward Federated-Learning-Enabled visible light communication in 6G systems. *IEEE Wireless Communications*, *29*(1), 48–56. https://doi.org/10.1109/mwc.005.00334

Nguyen, H., Choi, J., Kang, M., Ghassemlooy, Z., Kim, D. H., Lim, S., Kang, T., & Lee, C. G. (2010). A MATLAB-based simulation program for indoor visible light communication system. *2010 7th International Symposium on Communication Systems, Networks Digital*

Signal Process Ing (CSNDSP 2010). https://doi.org/10.1109/csndsp16145.2010.5580355

Nidhi, N., Khan, B., Mihovska, A., Prasad, R., & Velez, F. J. (2021). Trends in standardization towards 6G. *Journal of ICT Standardization*. https://doi.org/10.13052/jicts2245-800x.932

Nirmalathas, A., Song, T., Edirisinghe, S., Wang, K., Lim, C., Wong, E., Ranaweera, C., & Alameh, K. (2020). Indoor optical wireless access networks—recent progress [Invited]. *Journal of Optical Communications and Networking*, *13*(2), A178. https://doi.org/10.1364/jocn.403485

Noor-A-Rahim, M., John, J., Firyaguna, F., Sherazi, H. H. R., Kushch, S., Vijayan, A., O'Connell, E., Pesch, D., O'Flynn, B., O'Brien, W., Hayes, M., & Armstrong, E. (2022). Wireless communications for smart manufacturing and industrial IoT: existing technologies, 5G and beyond. *Sensors*, *23*(1), 73. https://doi.org/10.3390/s23010073

O'Brien, D. C. (2011). Visible Light Communications: Challenges and potential. *IEEE Photonic Society 24th Annual Meeting*. https://doi.org/10.1109/pho.2011.6110579

O'Brien, D. C., Zeng, L., Le-Minh, H., Faulkner, G., Walewski, J. W., & Randel, S. (2008). Visible light communications: Challenges and possibilities. *2008 IEEE 19th International Symposium on Personal, Indoor and Mobile Radio Communications*. https://doi.org/10.1109/pimrc.2008.4699964

Pachpande, P. G., Khadr, M. H., Hussein, A. F., & Elgala, H. (2018). Visible Light Communication Using Deep Learning Techniques. *IEEE 39th Sarnoff Symposium*, 1–6. https://doi.org/10.1109/sarnof.2018.8720493

Pathak, P. H., Feng, X., Hu, P., & Mohapatra, P. (2015). Visible Light Communication, Networking, and Sensing: A Survey, Potential and challenges. *IEEE Communications Surveys & Tutorials*, *17*(4), 2047–2077. https://doi.org/10.1109/comst.2015.2476474

Petkovic, M. (2009). Remote patient monitoring: Information reliability challenges. *2009 9th International Confer Ence on Telecommunication in Modern Satellite, Cable, and Broadcasting Services*, 295–301. https://doi.org/10.1109/telsks.2009.5339520

Photo-Biological Safety of Lamps and Lamp Systems (Identical With CIE S009) (document IEC 62471). (2006).

Pillai, B. (2024). 6G Network – A Literature Review. *International Research Journal of Engineering and Technology (IRJET)*, *11*(11), https://www.irjet.net/archives/V11/i11/IRJET-V11I1117.pdf.

Priyadharsini, R., & Kunthavai, A. (2022). Implementation of digital filters for Real-Time PPG signal Processing in VLC. *Fluctuation and Noise Letters*, *22*(01). https://doi.org/10.1142/s0219477523500013

Qiu, Y., Chen, H., & Meng, W. (2016). Channel modeling for visible light communications-a survey. *Wireless Communications and Mobile Computing*, *16*(14), 2016–2034. https://doi.org/10.1002/wcm.2665

Rahman, M., Sarwar, H., Kader, M. A., Gonçalves, T., & Tin, T. T. (2024). Review and Empirical analysis of Machine Learning-Based Software Effort Estimation. *IEEE Access*, *12*, 85661–85680. https://doi.org/10.1109/access.2024.3404879

Rajagopal, S., Roberts, R., & Lim, S. (2012). IEEE 802.15.7 visible light communication: modulation schemes and dimming support. *IEEE Communications Magazine*, *50*(3), 72–82. https://doi.org/10.1109/mcom.2012.6163585

Ramesh, M. V., Anand, S., & Rekha, P. (2012). A mobile software for health professionals to monitor remote patients. *2012 Ninth International Conference on Wireless and Optical Communications Networks (WOCN)*. https://doi.org/10.1109/wocn.2012.6335565

Rasmussen, C. E., & Williams, C. K. I. (2005). *Gaussian processes for machine learning* (1st ed.). MIT Press.

Razaz, M. A., Algaolahi, A. Q., Makarem, M. A., & Alwardy, E. H. (2024). VLC channel estimation for indoor environment using lstm. *2024 4th International Conference on Emerging Smart Technologies and Applications (eSmarTA)*, 1–4. https://doi.org/10.1109/eSmarTA62850.2024.10638984

Rodríguez, S. P., Jiménez, R. P., Mendoza, B. R., Hernández, F. J. L., & Alfonso, A. J. A. (2013). Simulation of impulse response for indoor visible light communications using 3D CAD models. *EURASIP Journal on Wireless Communications and Networking*, *2013*(1). https://doi.org/10.1186/1687-1499-2013-7

Rufo, J., Rabadan, J., Guerra, V., & Perez-Jimenez, R. (2017). BRDF models for the impulse response estimation in indoor optical wireless channels. *IEEE Photonics Technology Letters*, *29*(17), 1431–1434. https://doi.org/10.1109/lpt.2017.2723543

Saad, W., Bennis, M., & Chen, M. (2019). A Vision of 6G Wireless Systems: applications, trends, technologies, and open research problems. *IEEE Network*, *34*(3), 134–142. https://doi.org/10.1109/mnet.001.1900287

Safety of Laser products Part 1: Equipment classi cation and Requirement (document IEC 60825-1). (2007).

Sagahyroon, A. (2017). Remote patients monitoring: Challenges. *2017 IEEE 7th Annual Computing and Communication Workshop and Conference (CCWC)*, 1–4. https://doi.org/10.1109/ccwc.2017.7868460

Salama, W. M., Aly, M. H., & Amer, E. S. (2022). Deep learning based channel estimation optimization in VLC systems. *Optical and Quantum Electronics*, *55*(1). https://doi.org/10.1007/s11082-022-04363-7

Santo, H., Maekawa, T., & Matsushita, Y. (2017). Device-free and privacy preserving indoor positioning using infrared retro-reflection imaging. *IEEE International Conference on Pervasive Computing and Communications (PerCom)*. https://doi.org/10.1109/percom.2017.7917860

Saxena, A. K., Dixit, R. R., & Aman-Ullah, A. (2022). An LSTM Neural Network approach to resource allocation in hospital management systems. *International Journal of Applied Health Care Analytics*, *7*(2), 1–12. https://moodle.net/.pkg/@moodlenet/ed-resource/dl/ed-resource/3eyM1Ehp/967_An_LSTM_Neural_Network_Approach_to_Resource_Allocation_in_Hospital_Management_Systems.pdf

Saxena, V. N., Dwivedi, V. K., & Gupta, J. (2023). Machine Learning in Visible Light Communication System: A survey. *Wireless Communications and Mobile Computing*, *2023*, 1–12. https://doi.org/10.1155/2023/3950657

Saxena, V., Tullberg, H., & Jalden, J. (2021). Reinforcement learning for efficient and Tuning-Free link adaptation. *IEEE Transactions on Wireless Communications*, *21*(2), 768–780. https://doi.org/10.1109/twc.2021.3098972

Schiller, J., & Voisard, A. (2004). *Location-based services* (1st ed.). Elsevier.

Schulze, H. (2016). Frequency-Domain simulation of the indoor wireless optical communication channel. *IEEE Transactions on Communications*, *64*(6), 2551–2562. https://doi.org/10.1109/tcomm.2016.2556684

Serpi, H., & Politi, C. (2023). Radio environment maps for indoor visible light communications aided by machine learning. *AEU - International Journal*

of Electronics and Communications, *170*, 154866. https://doi.org/10.1016/j.aeue.2023.154866

Sharma, A., Keshari, P., & Bhatia, V. (2023). LSTM-based Channel Estimator for Optical IRS-Assisted non-Linear VLC Systems. *2023 IEEE International Conference on Advanced Networks and Telecommunications Systems (ANTS)*, 114–119. https://doi.org/10.1109/ants59832.2023.10468699

Shehab, M., Abualigah, L., Shambour, Q., Abu-Hashem, M. A., Shambour, M. K. Y., Alsalibi, A. I., & Gandomi, A. H. (2022). Machine learning in medical applications: A review of state-of-the-art methods. *Computers in Biology and Medicine*, *145*, 105458. https://doi.org/10.1016/j.compbiomed.2022.105458

Shu, Y., Chang, Y., Lin, Y., & Chow, C. (2024). Real-Time Indoor Visible Light Positioning (VLP) Using Long Short Term Memory Neural Network (LSTM-NN) with Principal Component Analysis (PCA). *Sensors*, *24*(16), 5424. https://doi.org/10.3390/s24165424

Simon, M. K., & Alouini, M. (2002). *Digital communication over fading channels*. https://doi.org/10.1002/0471200697

Slalmi, A., Chaibi, H., Chehri, A., Saadane, R., & Jeon, G. (2020). Toward 6G: Understanding network requirements and key performance indicators. *Transactions on Emerging Telecommunications Technologies*, *32*(3). https://doi.org/10.1002/ett.4201

Snoek, J., Larochelle, H., & Adams, R. P. (2012). Practical Bayesian optimization of machine learning algorithms. *arXiv preprint arXiv*:1206.2944. Retrieved September 9, 2025, from https://arxiv.org/abs/1206.2944

Sohn, I., Jang, Y. H., & Lee, S. H. (2020, May 1). *Ultra-Low-Power Implantable Medical Devices: Optical Wireless Communication approach*. IEEE Journals & Magazine | IEEE Xplore. https://ieeexplore.ieee.org/stamp/stamp.jsp?tp=&arnumber=9112747

Song, H. (2021). Terahertz Wireless Communications: Recent developments including a prototype system for Short-Range data downloading. *IEEE Microwave Magazine*, *22*(5), 88–99. https://doi.org/10.1109/mmm.2021.3056935

Song, S., Lin, D., Liu, Y., Chow, C., Chang, Y., Lin, K., Wang, Y., & Chen, Y. (2021). Employing DIALux to relieve machine-learning training data

collection when designing indoor positioning systems. *Optics Express*, *29*(11), 16887. https://doi.org/10.1364/oe.422851

Strinati, E. C., Barbarossa, S., Gonzalez-Jimenez, J. L., Ktenas, D., Cassiau, N., Maret, L., & Dehos, C. (2019). 6G: the next frontier: from holographic messaging to artificial intelligence using subterahertz and visible light communication. *IEEE Vehicular Technology Magazine*, *14*(3), 42–50. https://doi.org/10.1109/mvt.2019.2921162

Su, W., Lin, J., Chen, K., Xiao, L., & En, C. (2019). Reinforcement Learning-Based adaptive modulation and coding for efficient underwater communications. *IEEE Access*, *7*, 67539–67550. https://doi.org/10.1109/access.2019.2918506

Sutton, R. S., & Barto, A. G. (2018). Re*inforcement learning: An introduction* (2nd ed.). MIT Press.

Tiemann, J., Schweikowski, F., & Wietfeld, C. (2015). Design of an UWB indoor-positioning system for UAV navigation in GNSS-denied environments. *IEEE International Conference on Indoor Positioning and Indoor Navigation (IPIN)*. https://doi.org/10.1109/ipin.2015.7346960

Tran, H. Q., & Ha, C. (2019). Fingerprint-Based Indoor Positioning System using Visible Light Communication—A Novel method for Multipath Reflections. *Electronics*, *8*(1), 63. https://doi.org/10.3390/electronics8010063

Tran, H. Q., & Ha, C. (2021). Reducing the burden of data collection in a fingerprinting-based VLP system using a hybrid of improved co-training semi-supervised regression and adaptive boosting algorithms. *Optics Communications*, *488*, 126857. https://doi.org/10.1016/j.optcom.2021.126857

Trong-Hop, N., DO, Hwang, N. J., & Yoo, N. M. (2013). TDoA based indoor visible light positioning systems. *2013 Fifth International Conference on Ubiquitous and Future Networks (ICUFN)*. https://doi.org/10.1109/icufn.2013.6614860

Ullah, A., Choi, W., & Coleri, S. (2023). Path loss Estimation and jamming detection in hybrid RF-VLC Vehicular Networks: a Machine-Learning Framework. *IEEE Sensors Journal*, *23*(24), 31325–31336. https://doi.org/10.1109/jsen.2023.3329490

Uysal, M. (2019). Visible Light Communications: From Theory to Industrial Standardization. *Optical Fiber Communication Conference (OFC) 2022*, Th3I.4. https://doi.org/10.1364/ofc.2019.th3i.4

Uysal, M., Capsoni, C., Ghassemlooy, Z., Boucouvalas, A., & Udvary, E. (2016). *Optical wireless communications: An emerging* technology (1st ed.). Springer.

Uysal, M., Miramirkhani, F., Narmanlioglu, O., Baykas, T., & Panayirci, E. (2017). IEEE 802.15.7R1 Reference Channel models for visible light communications. *IEEE Communications Magazine*, *55*(1), 212–217. https://doi.org/10.1109/mcom.2017.1600872cm

Van Houdt, G., Mosquera, C., & Nápoles, G. (2020). A review on the long short-term memory model. *Artificial Intelligence Review*, *53*(8), 5929–5955. https://doi.org/10.1007/s10462-020-09838-1

Wang, C., You, X., Gao, X., Zhu, X., Li, Z., Zhang, C., Wang, H., Huang, Y., Chen, Y., Haas, H., Thompson, J. S., Larsson, E. G., Di Renzo, M., Tong, W., Zhu, P., Shen, X., Poor, H. V., & Hanzo, L. (2023). On the Road to 6G: Visions, Requirements, Key Technologies, and Testbeds. *IEEE Communications Surveys & Tutorials*, *25*(2), 905–974. https://doi.org/10.1109/comst.2023.3249835

Wang, K., Song, T., Wang, Y., Fang, C., He, J., Nirmalathas, A., Lim, C., Wong, E., & Kandeepan, S. (2022). Evolution of Short-Range optical wireless communications. *Journal of Lightwave Technology*, *41*(4), 1019–1040. https://doi.org/10.1109/jlt.2022.3215590

Wang, N. Y., & Haas, H. (2015). Dynamic load balancing with handover in hybrid Li-Fi and Wi-Fi networks. *Journal of Lightwave Technology*, *33*(22), 4671–4682. https://doi.org/10.1109/jlt.2015.2480969

Wang, X., Kong, L., Kong, F., Qiu, F., Xia, M., Arnon, S., & Chen, G. (2018). Millimeter Wave Communication: A Comprehensive survey. *IEEE Communications Surveys & Tutorials*, *20*(3), 1616–1653. https://doi.org/10.1109/comst.2018.2844322

Wang, X., Yu, Z., & Mao, S. (2019). Indoor Localization Using Smartphone Magnetic and Light Sensors: a Deep LSTM Approach. *Mobile Networks and Applications*, *25*(2), 819–832. https://doi.org/10.1007/s11036-019-01302-x

Wei, L., Zhang, H., & Song, J. (2016). Experimental demonstration of a Cubic-Receiver-Based MIMO visible light communication system. *IEEE*

Photonics Journal, *9*(1), 1–7. https://doi.org/10.1109/jphot.2016.2636752

World Economic Forum. (2019). *Fourth Industrial Revolution Beacons of Technology and Innovation in Manufacturing*. White Paper.

Wu, J. (2022). Development paradigms of cyberspace endogenous safety and security. *Science China Information Sciences*, *65*(5). https://doi.org/10.1007/s11432-021-3379-2

Wu, L., Zhang, Z., Dang, J., & Liu, H. (2014). Adaptive modulation schemes for visible light communications. *Journal of Lightwave Technology*, *33*(1), 117–125. https://doi.org/10.1109/jlt.2014.2374171

Wu, X., Hu, F., Zou, P., Lu, X., & Chi, N. (2019). The performance improvement of visible light communication systems under strong nonlinearities based on Gaussian mixture model. *Microwave and Optical Technology Letters*, *62*(2), 547–554. https://doi.org/10.1002/mop.32080

Yahia, S., Meraihi, Y., Ramdane-Cherif, A., Gabis, A. B., Acheli, D., & Guan, H. (2021). A survey of channel modeling techniques for visible light communications. *Journal of Network and Computer Applications*, *194*, 103206. https://doi.org/10.1016/j.jnca.2021.103206

Yakovlev, A., Kim, S., & Poon, A. (2012). Implantable biomedical devices: Wireless powering and communication. *IEEE Communications Magazine*, *50*(4), 152–159. https://doi.org/10.1109/mcom.2012.6178849

Yang, S., Kim, H., Son, Y., & Han, S. (2014). Three-Dimensional visible light indoor localization using AOA and RSS with multiple optical receivers. *Journal of Lightwave Technology*, *32*(14), 2480–2485. https://doi.org/10.1109/jlt.2014.2327623

Ying, Yu, Z., Baxley, R., Qian, H., Chang, G., & Zhou, G. (2015, April 1). *Nonlinear distortion mitigation in visible light communications*. IEEE Journals & Magazine | IEEE Xplore. https://ieeexplore.ieee.org/stamp/stamp.jsp?arnumber=7096283

You, X., Wang, C., Huang, J., Gao, X., Zhang, Z., Wang, M., Huang, Y., Zhang, C., Jiang, Y., Wang, J., Zhu, M., Sheng, B., Wang, D., Pan, Z., Zhu, P., Yang, Y., Liu, Z., Zhang, P., Tao, X., . . . Liang, Y. (2020). Towards 6G wireless communication networks: vision, enabling technologies, and new paradigm shifts. *Science China Information Sciences*, *64*(1). https://doi.org/10.1007/s11432-020-2955-6

Yu, H., Lu, J., & Zhang, G. (2020). An online robust support vector regression for data streams. *IEEE Transactions on Knowledge and Data Engineering*, 1. https://doi.org/10.1109/tkde.2020.2979967

Yuan, T., Xu, Y., Wang, Y., Han, P., & Chen, J. (2018). A tilt receiver correction method for visible light positioning using machine learning method. *IEEE Photonics Journal*, *10*(6), 1–12. https://doi.org/10.1109/jphot.2018.2880872

Yuan, Z., Zha, X., & Zhang, X. (2020). Adaptive Multi-Type Fingerprint indoor positioning and localization method based on Multi-Task learning and weight coefficients K-Nearest neighbor. *Sensors*, *20*(18), 5416. https://doi.org/10.3390/s20185416

Zafari, F., Gkelias, A., & Leung, K. K. (2019). A survey of indoor localization Systems and technologies. *IEEE Communications Surveys & Tutorials*, *21*(3), 2568–2599. https://doi.org/10.1109/comst.2019.2911558

Zengeya, T., & Fonou-Dombeu, J. V. (2024). A review of state of the art deep learning models for Ontology Construction. *IEEE Access*, *12*, 82354–82383. https://doi.org/10.1109/access.2024.3406426

Zhang, S. (2021). Challenges in KNN classification. *IEEE Transactions on Knowledge and Data Engineering*, *34*(10), 4663–4675. https://doi.org/10.1109/tkde.2021.3049250

Zhang, Y., Yang, L. T., & Chen, J. (2009). *RFID and sensor networks: Architectures, protocols, security, and integrations* (1st ed.). CRC Press.

Zhang, Y., Zhu, J., Wang, H., Shen, X., Wang, B., & Dong, Y. (2022). Deep Reinforcement Learning-Based Adaptive Modulation for Underwater Acoustic Communication with Outdated Channel State Information. *Remote Sensing*, *14*(16), 3947. https://doi.org/10.3390/rs14163947

Zhang, Z., Xiao, Y., Ma, Z., Xiao, M., Ding, Z., Lei, X., Karagiannidis, G. K., & Fan, P. (2019). 6G Wireless Networks: vision, requirements, architecture, and key technologies. *IEEE Vehicular Technology Magazine*, *14*(3), 28–41. https://doi.org/10.1109/mvt.2019.2921208

Zhao, X., Chen, H., & Sun, J. (2018). On Physical-Layer security in multiuser visible light communication systems with Non-Orthogonal multiple access. *IEEE Access*, *6*, 34004–34017. https://doi.org/10.1109/access.2018.2847744

Zhou, C., Yu, W., Huang, K., Zhu, H., Li, Y., Yang, C., & Sun, B. (2021). A new model transfer strategy among spectrometers based on SVR

parameter calibrating. *IEEE Transactions on Instrumentation and Measurement*, *70*, 1–13. https://doi.org/10.1109/tim.2021.3119129

Zhu, N. Y., Liang, N. W., Zhang, N. J., & Zhang, N. Y. (2015). Space-Collaborative constellation designs for MIMO indoor visible light communications. *IEEE Photonics Technology Letters*, *27*(15), 1667–1670. https://doi.org/10.1109/lpt.2015.2435009

Zong, B., Fan, C., Wang, X., Duan, X., Wang, B., & Wang, J. (2019). 6G technologies: key drivers, core requirements, system architectures, and enabling technologies. *IEEE Vehicular Technology Magazine*, *14*(3), 18–27. https://doi.org/10.1109/mvt.2019.2921398

Zou, H., Jin, M., Jiang, H., Xie, L., & Spanos, C. J. (2017). WINIPS: WiFi-Based Non-Intrusive Indoor Positioning System with online radio map construction and adaptation. *IEEE Transactions on Wireless Communications*, *16*(12), 8118–8130. https://doi.org/10.1109/twc.2017.2757472

CURRICULUM VITAE